Biochemical and genetic characterisation of ciliary transition zone transmembrane proteins in cystic kidney disease and ciliopathies

Ekram Abdullah Shoaib

Submitted in accordance with the requirements for the degree of
Doctor of Philosophy

The University of Leeds
Leeds Institute of Medical Research at St James's
School of Medicine

May 2020

The candidate confirms that the work submitted is her own and that appropriate credit has been given where reference has been made to the work of others.

This copy has been supplied on the understanding that it is copyright material and that no quotation from the thesis may be published without proper acknowledgement.

The right of Ekram Abdullah Shoaib to be identified as Author of this work has been asserted by her in accordance with the Copyright, Designs and Patents Act 1988.

Acknowledgements

First of all, praise is due to almighty ALLAH with His compassion and mercifulness to allow me finalizing this thesis. Without his blessings, this achievement would not have been possible. Undertaking this PhD has been a truly life-changing experience for me and it would not have been possible to do without the support and guidance that I received from many people which support my work presented in this thesis.

Special mention goes to my main supervisor, Prof. Colin A. Johnson for his academic support, professional guidance, patience, and for giving me opportunities and encouragements to attend conferences and club meetings throughout my PhD journey. This is attested by me winning the Best Poster Prize at the international conference "Cilia in Disease and Development", Amsterdam, October 2016. Similar, profound gratitude goes to Dr Sandra Bell, for her moral support, patience, and especially for being so dedicated to her role as my secondary supervisor. I am also hugely appreciative to Dr Ewan Morrison, who has been very helpful and thanks for his patience, encouragement, and guidance.

I would like to acknowledge the help kind support of Dr Brian Jackson (for FPLC guidance and assistance), Dr. James Poulter (for his kind help to use DNA sequencing facility), Dr. Dorus Mans (for Gateway cloning guidance and assistance), Julie Higgins and Alice lake (for operetta high content imaging system guidance), Dr. Karsten Boldt and Nicola Horn (for TAP-MS analysis).

I also appreciate the help and support from all persons who were directly or indirectly involved in my project. I would like to thank Team Meckel members and all staff and students from the Department of Ophthalmology and Neuroscience at Leeds Institute of Medical Research at St James's. Thanks must go to the many MKS/JSRD families for participating in the study, described in Chapter 2.

Thanks also must go to King Abdullah Scholarships Program and Ministry of Education for funding my scholarship and their investment in me.

Finally, but by no means least, I would like to thank my husband and my children (Elyas, Jasser, and Maria) for listening to me at times of despair and thank you endlessly for being a constant source of inspiration in my life. In addition, thanks and love go to my parents, my brothers and sisters, and friends for all the unconditional support through this process. They are the most important people in my world and I dedicate this thesis to them.

Abstract

Meckel-Gruber syndrome (MKS) and Joubert syndrome (JBTS) are rare autosomal recessive genetic disorders caused by genetic defects in proteins responsible for primary cilia formation, maintenance or function. Primary cilia regulate essential cellular and developmental processes and have a complex compartmentalized organization. This project focuses on transmembrane proteins (TMEMs) that form the "MKS/JBTS functional module" at the ciliary transition zone compartment. These include TMEM17 TMEM67, TMEM138, TMEM216, TMEM231 and TMEM237 that, when mutated, cause MKS or JBTS. The detailed biochemical and genetic interactions that form this functional module remain unclear.

This project describes biochemical and cell biological approaches to understand the functional roles of ciliary TMEMs. Biochemical interactions were defined through a series of co-immunoprecipitation assays of epitope-tagged and endogenous ciliary TMEM proteins. This showed that TMEM17 interacts with TMEM138, TMEM237, TMEM216, TMEM67 and the intraflagellar transport protein IFT88. Tandem affinity purification (TAP) followed by mass spectroscopy confirmed that TMEM17 interacted with TMEM237. In addition, reciprocal biochemical interactions confirmed novel interactions between TMEM237-TMEM216 and TMEM237-TMEM17. TMEM17 also interacted with the pre-mRNA splicing factors (PRPF8 and PRPF6) that do not have an established role in the ciliary apparatus.

Genetic interactions were also determined between ciliary TMEMs and other ciliary proteins (RPGRIP1L, CEP290 and IFT88) chosen because they localize to different ciliary compartments and appear to form distinct functional modules. Genetic interactions were inferred from co-localization studies in 3D reconstituted confocal microscopy images following a series of RNAi knockdowns. This highlighted the significance of the TMEM17-TMEM67 genetic interaction in organizing ciliary sub-compartments. Finally, both biochemical and genetic interactions delineated the existence of a novel complex between TMEM237, TMEM17 and TMEM138 with the ciliary protein IFT88. These results provide new insights into how ciliary trafficking and ciliogenesis could be mediated through interactions with TMEM components at the ciliary transition zone.

Contents

Table of Figures

List of Tables

Abbreviations

AAV	Adeno-associated virus
ADPKD	Autosomal dominant polycystic kidney disease
ALMS	Alström Syndrome
ANXA2	Annexin A2
APC	Adenomatous polyposis coli
ATP	Adenosine triphosphate
AURKA	Aurora kinase A
Axial SMD	Axial spondylometaphyseal dysplasia
B9D1	B9 domain-containing protein 1
B9D2	B9 domain-containing protein 2
BBS	Bardet-Biedl syndrome
BCC	Basal cell carcinomas
BioID	Proximity-dependent biotin identification
bps	Base pairs
BSA	Bovine serum albumin
βDM	-dodecyl maltoside
β-TrCP	Beta-transducin repeats-containing proteins
C21orf2	Chromosome 21 open reading frame 2
CCA	Cholangiocarcinoma
CCD	Coiled-coil domain
CC2D2A	Coiled-coil and C2 domain-containing protein 2A
CDC42	Cell division control protein 42 homolog
cDNA	Complementary DNA
CK1	Casein kinase 1
CKIα	Casein kinase Iα
CED	Cranioectodermal dysplasia
CEP41	Centrosomal protein 41 kDa
CEP131	Centrosomal protein 131 kDa
CEP135	Centrosomal protein 135 kDa
CEP290	Centrosomal protein of 290 kDa
CSPP1	Centrosome and spindle pole associated protein 1
COACH	Cerebellar vermis hypoplasia-oligophrenia-congenital ataxia-coloboma-hepatic fibrosis
CORS2	Cerebello-oculo-renal syndrome 2
DAPI	4',6-Diamidino-2-phenylindole dihydrochloride
dH$_2$O	Distilled water
DI water	Deionised water
DLL1	Delta Like Canonical Notch Ligand 1
DNA	Deoxyribonucleic acid
DMEM	Dulbecco's Modified Eagle Medium
DMSO	Dimethyl sulfoxide
dNTPs	Deoxynucleotide triphosphates
DPBS	Dulbecco's Phosphate buffered saline
DPBST	DPBS+ 0.1% Tween 20
DVl	Dishevelled

DVL (1-3)   Dishevelled (1-3)
DYNLT1   Dynein light chain Tctex-type 1
EDTA   Ethylenediaminetetraacetic acid
EHD1   EH Domain Containing 1
ESRD   End-stage renal disease
EVC   EIlis-Van Creveld Syndrome
EXOC3L4   Exocyst Complex Component 3 Like 4
eYFP   Enhanced yellow fluorescent protein
FBS   Fetal bovine serum
FGF   Fibroblast growth factors
FZD   Frizzled
g   Gram
GFP   Green fluorescent protein
GLI   Glioma-associated oncogene homologue
GPCR   G-coupled protein receptors
GSK3 β-   Glycogen synthase kinase-3 beta
GEF   Guanine nucleotide-exchange factor
HDAC6   Histone deacetylase 6
HEK-293   Human embryonic kidney 293
HEPES   4-(2-hydroxyethyl)-1-piperazineethanesulfonic acid
HH   Hedgehog
HNPCC   Hereditary non-polyposis colorectal cancers
HRP   Horseradish peroxidase
IFT   Intraflagellar transport
IFT-A   Intraflagellar transport-A
IFT-B   Intraflagellar transport-B
IFT46   *Intraflagellar transport protein 46*
IFT52   *Intraflagellar transport protein 52*
IFT57   *Intraflagellar transport protein 57*
IFT80   *Intraflagellar transport protein 80*
IFT88   *Intraflagellar transport protein 88*
IFT172   *Intraflagellar transport protein 172*
INL   Inner nuclear layer
INPP5E   Inositol Polyphosphate-5-Phosphatase E
INVS   Inversin
JATD   Jeune asphyxiating thoracic dystrophy
JBTS   Joubert syndrome
JSRD   JBTS and related disorders
KIF7   Kinesin Family Member 7
KV   Kupffer's vesicle
LB   Lysogeny broth
LCA   Leber congenital amaurosis
LRP5   The low-density lipoprotein receptor-related protein 5
LRP6   The low-density lipoprotein receptor-related protein 6
M   Molar
MES   2-(N-morpholino) ethanesulfonic acid
mIMCD-3   Mouse inner medullary collecting duct

MIM	Mendelian inheritance in man
MKS	Meckel-Gruber syndrome
MKS1	Meckel-Gruber syndrome type1
mM	Millimolar
Ms	Mouse
MS	Mass spectrometry
MST1/2	Mammalian Ste20-like 1 and 2 in mammals
mTOR	Mechanistic target of rapamycin
MTS	Molar tooth sign
NEDD9	Neural precursor cell expressed, developmentally down-regulated 9
NDE1	NudE neurodevelopment protein 1
NICD	Notch intracellular domain
NIMA	(Never in mitosis gene a)-related kinase 1
NP40	Nonidet P-40
NPHP	Nephronophthisis
Nt	N-terminus
OFDI	Oral-facial-digital syndrome type I
OSNs	Olfactory sensory neurons
P/S	Penicillin and streptomycin
PCD	Primary ciliary dyskinesia
PCL	Procentriole-like
PCM1	Pericentriolar Material 1
PCR	Polymerase chain reaction
PCP	Planar cell polarity
PDGFRα	Platelet-derived growth factor receptor α
PFA	Paraformaldehyde
PGRMC1	Progesterone receptor component 1
Pifo	Pitchfork
PKD	Polycystic kidney disease
PLK	Polo family protein kinase
PLK4	Polo-like kinase 4
PLK1	Polo-like kinase 1
PTCH	Patched
PVDF	Polyvinylidene fluoride
RCC	Renal cell carcinomas
RDMS	Retinal dystrophy with macular staphyloma
Rb	Rabbit
RPGR	Retinitis pigmentosa GTPase regulator
RPGRIP1L	Retinitis pigmentosa GTPase regulator interacting protein 1-like
RPM	Revolutions per minute
RT	Room temperature
SAS-5	Spindle assembly abnormal protein 5
SAS-6	Spindle assembly abnormal protein 6
SDS	Sodium dodecyl sulfate
SDS-PAGE	Sodium dodecyl sulfate polyacrylamide gel electrophoresis
SHH	Sonic hedgehog
siRNA	Small interfering RNA

SLS	Senior Løken syndrome
SMO	Smoothened
SNP	Single nucleotide polymorphism
SOC	Super optimal broth with catabolite repression
SF-TAP	Strep-tag/FLAG tandem affinity purification
STIL	SCL-interrupting locus protein
SUFU	Suppressor of fused
TAP	Tandem affinity purification
TAP-MS	Tandem affinity purification-mass spectroscopy
TAZ	transcriptional coactivator with PDZ-binding motif
TCNT1	Tectonic Family Member 1
TCTN3	Tectonic Family Member 3
TE	Tris/EDTA
TEM	Transmission electron microscopy
TMEMs	Transmembrane proteins
TMEM17	Transmembrane Protein 17
TMEM67	Transmembrane Protein 67
TMEM107	Transmembrane Protein 107
TMEM138	Transmembrane Protein 138
TMEM216	Transmembrane Protein 216
TMEM218	Transmembrane Protein 218
TMEM231	Transmembrane Protein 231
TMEM237	Transmembrane Protein 237
TGF-β	Transforming growth factor- beta
TTC21B	Tetratricopeptide Repeat Domain 21B
TULP3	Tubby-like protein-3
TXNDC15	Thioredoxin Domain Containing 15
VHL	Von Hippel-Lindau
WB	Western blot
WCE	Whole cell extract
Wdr35	WD Repeat Domain 35
Wnt	Wingless-type MMTV integration site
x *g*	number of times gravitational force
YAP-	Yes-associated protein
λex	Excitation wavelength
λem	Emission wavelength

Chapter 1 Introduction

1.1 History of cilia

The cilium or flagellum is the oldest known cellular organelle and was first observed at the end of the seventeenth century by the Dutch microscope maker Antoni van Leeuwenhoek. The first time that he saw ciliated protozoa he described them as having 'thin little feet' as defined in Leeuwenhoek's 1677 paper (Lane, 2015, Dobell, 1932). The term "cilium" (from the Latin, meaning hair or eyelash), was most likely used by Otto Müller in 1786 (Beales and Jackson, 2012, Müller, 1786). Cilia were originally defined by their motile function and this was thought to be the only function of these little hair-like structures. In 1834, Purkinje and Valentin were the first to describe ciliary motility in mammals in which cilia found lining most of the respiratory tract moved mucus out of the airways (Wang et al., 2010, Purkinje JE, 1834). It was not until the end of the nineteenth century, that Zimmermann (1898) first observed another class of solitary cilium in mammalian cells, referring to them as central flagella (Bloodgood, 2010, Zimmermann, 1898). They were renamed "primary cilia" in 1968 (Sorokin, 1968); Zimmermann was also the first scientist to hypothesize a sensory function for these organelles but they received little attention thereafter (Bloodgood, 2010, Zimmermann, 1898). In the 1950s, interest in cilia rapidly grew and increased further from the late 1970s. A ground-breaking observation in 1976 was the association of motile cilia with primary ciliary dyskinesia (PCD) by Bjorn Afzelius (Afzelius, 1976, Praveen et al., 2015). Considerable progress was made at that time in understanding ciliary structure by using electron microscopy techniques (Satir, 2017, Moser et al., 2014).

Although motile cilia were studied intensively in previous decades, primary 'non-motile' cilia were widely considered to play a very minor role in cellular events and were thought to be a vestigial structure (Ke and Yang, 2014). However, in the last twenty years, research has emphasized the importance of primary cilia, which are now thought to play an essential role in sensing and transducing cellular signals. For instance, primary cilia, also called sensory cilia, play a crucial role in vertebrate development (Chih et al., 2011) and can sense and mediate a wide variety of signals such as Sonic hedgehog (SHH) signalling,

Wingless-type MMTV integration site (Wnt) signalling and other paracrine signalling pathways (Lee et al., 2012). Therefore, primary cilia appear to perform crucial functions for human health and their dysfunction causes human disease.

1.2 The classification of cilia

Cilia, with their hair-like structure, are highly conserved microtubule-based organelles that protrude from the surface of most vertebrate animal cells (Czarnecki and Shah, 2012) and are conserved in a wide variety of eukaryotic species throughout their evolution (Sasai and Briscoe, 2012). Primary cilia occur on the apical surface of most mammalian cells in G0/G1 of the cell cycle (Szymanska and Johnson, 2012) and their structure is distinct from the surrounding cytosol and plasma membrane (Yoder, 2007). Although cilia are present in many eukaryotic animal cells (Takeda and Narita, 2012), they appear to have been lost in many seed plants, most *Fungi* and *Amoebozoa* even though spermatozoa in some of these species have motile cilia in the form of flagellae (Nevers et al., 2017). Cilia are classified according to their microtubule components and functions as described in Figure1.1 and discussed below in sections (1.2.1) and (1.2.2).

A. Motile cilia **B. Sensory non-motile cilium**

Tissue/cell type	Disorder
Conducting airways	Airway disease
Ependymal cells	Hydrocephalus
Fallopian tubes	Ectopic pregnancy
Sperm cells	Infertility

Multiciliated/ Sperm cell

Tissue/cell type	Disorder
Embryonic node	Heterotaxia

Nodal cell

Tissue/cell type/process	Disorder
Rods; cones	Blindness
Renal Epithelium	Cysts
Brain	Cognitive impairment
Defective HH signalling	Polydactyly skeletal abnormalities
Hypothalamic	Obesity
Pancreatic β-cells	Type2 diabetes

Photoreceptor cell/ Epithelial cell

Figure 1. 1: A comparison of the cross-sectional diagram of motile and primary cilia and system location. Examples of tissue and cell types associated with disorders of each type of cilium indicate in tables. Examples of cell types harbouring each type of cilium show in black rectangles. References are giving in the text. **(A)** Two cross-sectional views of motile cilia seen from the proximal end containing the canonical nine doublet microtubules and two central pair microtubules features with outer/inner dynein arms and radial spokes (left panel) and nodal cilium seen from the proximal end containing a 9 + 0 arrangement that lack the central pair of microtubules (left panel). **(B)** A cross-sectional view of a sensory non-motile cilium showing the nine doublet microtubules and lack of dynein arms and central pair microtubules (right panel). The figure is adapted from (Bernabe-Rubio and Alonso 2017).

1.2.1 Motile cilia

An organized microtubule-based axoneme is the core of a motile cilium. Most motile cilia consist of a so-called "9+2" configuration of microtubules by which nine peripheral microtubules surround a central inner pair (Chilvers and O'Callaghan, 2000, Fretzayas and Moustaki, 2016). The nine peripheral doublets connect to the central pair by radial spokes; this connection is called nexin links (Fretzayas and Moustaki, 2016) as shown in Figure 1.1 A. Motile cilia have also motor proteins, the outer and inner dynein arms, link to the outer microtubules and provide energy for cilia motility and only present in specific tissue or cells (Hsiao et al., 2012, Satir and Christensen, 2007) (see Figure 1.1 A). Each cell can display up to 200–300 motile cilia, enabling a powerful and co-ordinated motion of the extracellular

fluid (van Reeuwijk et al., 2011) or move mucus such as a ciliated epithelium cell which beats in a coordinated fashion providing the respiratory epithelial defence mechanisms (Fretzayas and Moustaki, 2016). In general most motile cilia or flagella only move back and forth with a whip-like motion (Hirokawa et al., 2006). They are found on multiciliated cells: epithelial cells in the lungs and brain ependymal cells, in the olfactory bulb, and in the female reproductive system as well as in male sperm cells; Figure 1.1 shows some examples of tissues and phenotypic manifestations of the disease in each types of cilium (Huang et al., 2009b) and the figure is adapted from Bernabe-Rubio and Alonso (2017).

Since the structures of the motile cilia are known to be conserved, many studies have identified a clear link between motile ciliary function and human inherited disease: Mutations that affect proteins that are components of specific ciliary compartments (such as the basal bodies, microtubules and intraflagellar transport) tend to manifest as inherited disease phenotypes that reflect the function of both the disrupted compartment and the category of cilium. For example, mutations in dynein arms in motile cilia, or components that assemble dyneins, result in a more limited range of disease phenotypes, specifically primary ciliary dyskinesia (PCD) (MIM: 244400) (Ostrowski et al., 2011) that is distinct to the broader and more severe phenotypes of other ciliopathy phenotypes (see section 1.6.1.1; Figure 1.7). In addition, 50% of PCD patients have situs inversus totalis and, less commonly, heterotaxy and congenital heart disease which reflect a dysfunction of embryological nodal cilia (Leigh et al., 2009) that are critical for left-right axis determination (Garcia-Gonzalo et al., 2011). Situs inversus totalis (type 1) is also called situs inversus dextrocardia and is characterized by a complete left-right mirror reversal of the visceral organs: the heart and other internal organs. This is usually a recessive disorder: PCD in association with situs inversus totalis, known as Kartagener syndrome. Situs inversus type 2 is characterized by levocardia, when the heart lies on the left side of the body and the liver and spleen lie on the right and is usually associated with cardiac anomalies (Abdullah et al., 2015).

Furthermore, male infertility is a common clinical feature of most PCD patients (Bisgrove and Yost, 2006) which reflects defects in sperm tail axonemes. Moreover, most PCD patients (70-80%) present in the neonatal period with respiratory distress, indicating

that motile cilia are essential for pulmonary mucus clearance of fetal lung fluid (Leigh et al., 2009, Hossain et al., 2003).

Motile cilia have sensory functions, in addition to motility, in order to detect the external environment. (Braiman and Priel, 2008, Gheber et al., 1995) and Braiman and Priel, 2008 supported this notion by indicating that motile ciliary beat changes in response to viscous load, phorbol esters and adenosine triphosphate (ATP). However, these observations do not provide an explanation of any underlying mechanisms. Shah et al. (2009) suggested that motile cilia had a sensory function by demonstrated that motile cilia of human airway epithelia have a unique chemosensory role. They indicated that motile cilia co-localized to these cells and express sensory bitter taste receptors. These receptors increased intracellular Ca^{2+} concentration and stimulated ciliary beat frequency; according to Mitchison and Valente (2017), the associations between motile and non-motile sensory ciliopathies are unclear, but clinical investigations indicated overlapping features that include embryonic left-right axis patterning, infertility and congenital hydrocephalus. Therefore, motile and non-motile cilia are now thought to act as the "antennae" of the cell (Ke and Yang, 2014). It is notable that both motile and primary cilia share some ciliary components. Proteomic analyses of mammalian primary cilia (or sensory cilia) (see section 1.2.2) versus motile cilia have identified about 152 shared ciliary proteins (Narita et al., 2012). For instance, they possess the same intraflagellar transport system (see section: 1.2.4.5 and 1.2.4.5.1) though they differ in their axonemal structure and motility.

1.2.2 Sensory primary cilia

In contrast to motile cilia, most primary (non-motile or sensory) cilia lack the additional central pair of microtubules, have a "9+0" axonemal arrangement of microtubules, and are devoid of inner and outer dynein arms. They usually found to be present at a ratio of one per cell, for example in photoreceptor cells and epithelial cells (Figure 1.1 B). The primary cilium has a conserved basic morphology, but this varies considerably in shape and size. For instance, it measures 1 to 5 µm in length and 0.2 µm in width (Scherft and Daems, 1967) and recently, Dummer et al. (2016) reported that the length of the cilium can vary between 1 and 9 µm within various cell types, including kidney epithelial cells (5–6 µm) (Besschetnova et al., 2010), neurons (4–9 µm)(Broekhuis et al.,

2013, Miyoshi et al., 2014), vascular endothelial cells (1–5 µm)(Van der Heiden et al., 2008), osteoblasts (3–4 µm)(Delaine-Smith et al., 2014, Qiu et al., 2012), and chondrocytes (2 µm)(Wann and Knight, 2012). Primary cilia are required for mechano-sensory functions that detect both environmental and intercellular stimuli (Leightner et al., 2013); for instance, those on the dendritic knob of the olfactory neuron are essential for chemo-sensing functions and also act as a mechano-sensory system in cerebral-spinal fluid in the nervous system (Satir and Christensen, 2007). It performs diverse biological roles, principally to control and maintain cellular and tissue homeostasis (Cardenas-Rodriguez and Badano, 2009). Primary cilia also mediate chemosensory, mechanosensory and photosensory roles (Goetz and Anderson, 2010), particularly during embryonic development. They are critical for the development and function of many tissue types and cells including stem, neurons, epithelial, endothelial, connective tissue and muscle cells (Satir et al., 2010, Abou Alaiwi et al., 2009, Anderson et al., 2008). As a consequence, cilia mediate diverse signalling pathways that include SHH, non-canonical and canonical Wnt, PDGF, Hippo and Notch (see section 1.5).

In addition, the role of primary cilia is well-established in and essential for photoreception. In the photoreceptor, the cells in the retina that respond to light, primary cilia are specialized structures with four distinct compartments, including distal cilium/axoneme, the so-called connecting cilium (comprising the transition zone), basal body, and periciliary complex/ciliary pocket. The light-detecting protein machinery passes through the connecting cilium on its way to the outer segment, so defects in cilia-mediated transport are associated with blindness. For instance, Centrosomal protein of 290 kDa (CEP290) and Retinitis pigmentosa GTPase regulator (RPGR) are central proteins in the connecting cilium of the photoreceptor (Rachel et al., 2012) and mutations in the genes that encode them are major causes of ciliopathies (see section 1.6) with retinal involvement, ranging from leber congenital amaurosis (LCA) to multiorgan Joubert syndrome (JBTS) (Hollander et al., 2006, Sayer et al., 2006, Valente et al., 2006). Therefore, studying primary cilia provides critical information to understand the pathogenesis of the different phenotypes that characterize human ciliopathies (Cardenas-Rodriguez and Badano, 2009).

There are other specific types of non-motile cilia with a microtubule structure similar to motile cilia that adopt the 9+2 configuration, such as olfactory neurons (associated with anosmia) and kinocilium of hair cells (linked to deafness disorder) (Falk et al., 2015, Pruski and Lang, 2019, Bernabe-Rubio and Alonso, 2017).

1.2.3 Other cilia types

Nodal cilia have a 9+0 microtubule arrangement that includes nine peripheral doublets and dynein arms but lacks the central pair of microtubules (Baker and Beales, 2009, Fretzayas and Moustaki, 2016) (Figure 1.1 A, right panel). Nodal cilia are motile and are present in the ventral embryonic nodes of vertebrates. Hirokawa et al. (2006) discovered the nodal monocilia movement which was described as "vigorously rotating" or a clockwise rotation: a sloping rotational movement that is essential for establishing left–right asymmetry by generating leftward flow of extraembryonic fluid as well as determining of the laterality of visceral organs in mammals during embryogenesis (Bernabe-Rubio and Alonso, 2017, Shinohara et al., 2015, Yoshiba and Hamada, 2014). Although nodal cilia have both motility and sensory functions, some nodal cilia in the peripheral region of the ventral node are immotile and act as a sensor for the direction of flow (Tabin and Vogan, 2003).

Herein the core structure and function of primary cilia are described in detail, as this type of cilia module is the main focus of this project.

1.2.4 The core structure of sensory primary cilia
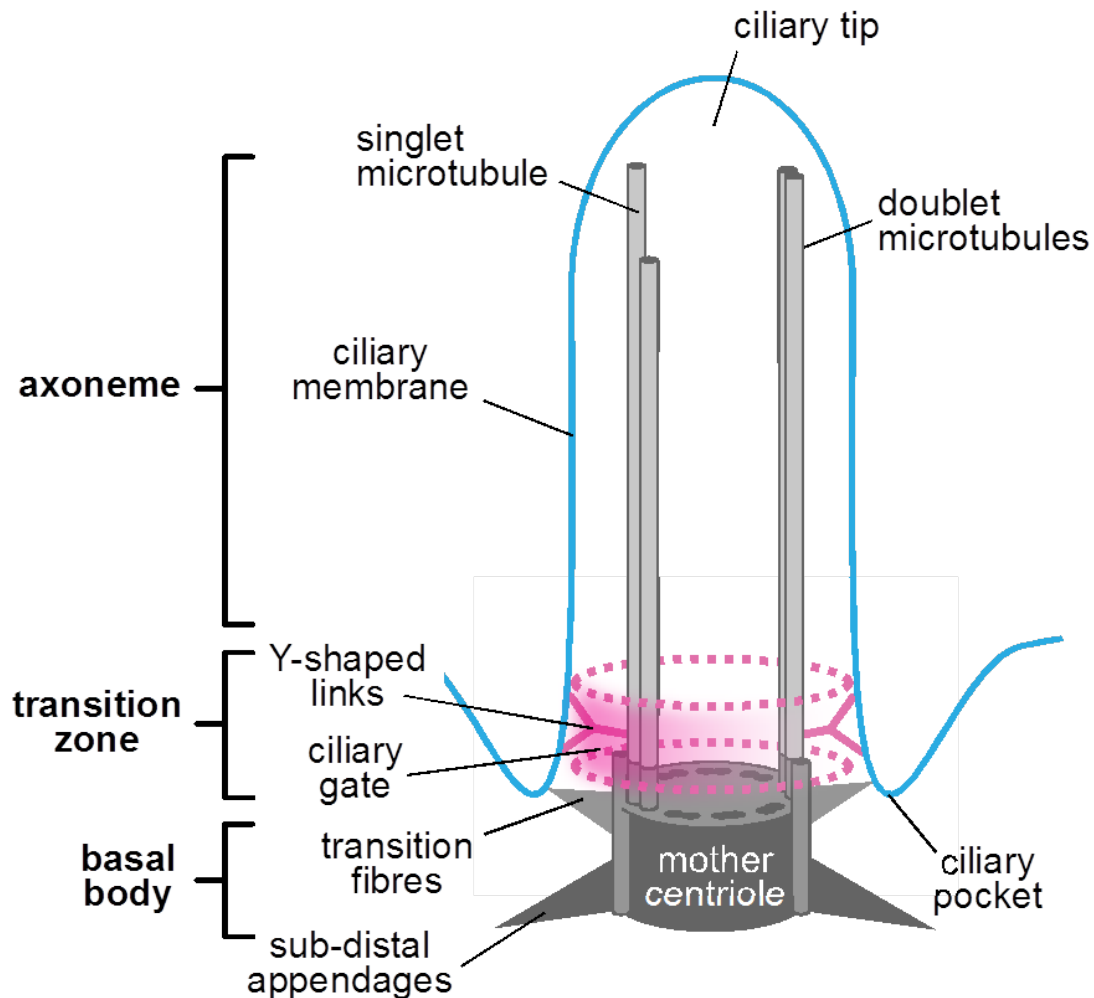
Figure 1. 2: Architecture of a primary (9+0) cilium. The microtubule-based axoneme of the primary cilium originates from the basal body (Mother centriole) which is organized in cylinders of nine microtubule triplets. The mother centriole converts into the axonemal doublet microtubular structure and forms the transition zone. The ciliary gate consists of transition fibres and transition zone sections. The transition zone is characterized by the presence of Y-links, which connect the axoneme to the ciliary membrane and are located at the beginning of the axoneme. Transition fibres connect the distal basal body to the base of the ciliary membrane and plays key roles in ciliary assembly and trafficking. A cup-like structure, the ciliary pocket, is a depression of the plasma membrane surrounding the axoneme in which the primary cilium is rooted and the cilium is covered by the ciliary membrane. Adapted from (Malicki and Johnson, 2017, Garcia-Gonzalo and Reiter, 2017, Molla-Herman et al., 2010).

1.2.4.1 Basal body

Cilia have been dissected into at least two distinct sub-structural zones, including the basal body and the transition zone (Czarnecki and Shah, 2012) (Figure 1.2). The basal body is derived from the cytosolic microtubule-organizing centre and mother centriole during interphase. During cell division, the mother centriole migrates to the apical surface of the cell and acts as the basal body to assemble primary cilia during interphase (Kobayashi and Dynlacht, 2011). According to Malicki and Johnson (2017), the mother centriole matures into the basal body by the addition of distal accessory appendages, which are thought to then form the transition fibres that root the transition zone to the ciliary membrane in the mature cilium. The basal body is composed of microtubules, which are assembled as a set of nine triplets in a structure 0.5 μm long, and 0.2 μm in diameter (Ovalle, 2013). Each triplet contains three microtubules, categorized A, B and C, attached to each other along their lengths. The basal body plays several roles important to ciliary activity, providing the template for building the axoneme, dictating the orientation and position of the cilium for the correct movement of extracellular fluids, regulating the entry of proteins into the cilium and playing a role in cell division (Marshall, 2008). Furthermore, there is a fundamental relationship between the cell cycle and the basal body–centriole transition, since the mother centriole is converted into a basal body and mediates assembly of a primary cilia in interphase. The conversion between centrioles and basal bodies is therefore reversible and cell cycle dependent, but the mechanistic basis of this functional relationship remains unclear (Kobayashi and Dynlacht, 2011).

Recent studies have indicated that basal body/centriole assembly is tightly regulated by the spindle assembly abnormal protein 6 (SAS-6), Polo-like kinase 4 (PLK4), and the SCL-interrupting locus protein (STIL, also known as SAS-5). These key players also play important roles in regulating centriole duplication during early S phase (Yamamoto and Kitagawa, 2019). SAS-6 is a basal body protein and considered a marker of the new-born centriole which regulates assembly of all types of cilia. SAS-6 plays a role in establishment of centriolar nine-fold symmetry (cartwheel) and the formation of a procentriole-like structure (PCL) (Blachon et al., 2009) which is the first structure of the centriole to be assembled. Centrosomal protein 135 (CEP135) and STIL amongst other proteins are also associated with the PCL (Nakazawa et al., 2007, Kitagawa et al., 2011, Lin et al., 2013). SAS-6 and CEP135 can

self-assemble *in vitro* to generate the cartwheel (Guichard et al., 2017). SAS-6 is also necessary for centriolar duplication and function; its functional disruption causes cilia-related disorders in eukaryotes (Marques et al., 2015) as well as centriole reduplication and de novo assembly of centrioles in cells (Peel et al., 2007). In *Caenorhabditis elegans (C. elegans)*, SAS-6 is required for the central tube formation, which is functionally related to the cartwheel that appears at the beginning of centriole formation (Pelletier et al., 2006). According to Qiao et al. (2012) mutations in the SAS-6 coiled-coil domain (CCD) disrupt centriolar recruitment and function in *C. elegans* embryos. In addition, SAS-6 is functionally related to a number of protein kinases that regulate cell cycle processes, such as PLK, the master key regulator of centriole duplication that plays roles in centrosome function (Lee et al., 2014). SAS-6 requires PLK4 to phosphorylate components in the procentriole in *Drosophila* and human cells (Dzhindzhev et al., 2014); centriolar biogenesis is triggered by active PLK4 which recruits and phosphorylates STIL, which then recruits SAS-6 (Arquint et al., 2012, Moyer et al., 2015).

Recently Denu et al. (2019) indicated that PLK4 (UniProt ID: O00444) maintains centriolar satellite integrity by phosphorylation of centrosomal protein 131 (CEP131). These satellites are essential for the recruitment of proteins involved in microtubule organization (Dammermann and Merdes, 2002), ciliogenesis (Lopes et al., 2011), and centriole duplication (Kodani et al., 2015).

In addition, the basal body consists of several other hundred proteins that are implicated in the generation of cilia, such as *CEP290* which works with and functionally overlaps with Talpid3. Both play distinct roles in ciliary vesicle formation through regulation of centriolar satellite accretion and Rab8a (Kobayashi et al., 2014). The centrosomal protein Talpid3 is essential for primary cilia formation and is involved in both ciliogenesis and HH signalling (Keeling et al., 2016, Yin et al., 2009).

In addition, Gerhardt et al. (2015) found that there are different proteasomal components localized to the basal body of cilia and that they play a role in ciliary function. They identified a proteasomal 19S subunit component, PSMD2, at the basal body and showed its interaction with retinitis pigmentosa GTPase regulator interacting protein 1-like (RPGRIP1L). Their data showed RPGRIP1L deficiency causes decreased proteasomal activity

at primary cilia, but the functional consequence of this association was not clear because the target(s) of potential protein degradation in the ciliary apparatus were not identified.

1.2.4.2 Ciliary pocket

Ciliogenesis, initiates when Golgi-derived ciliary vesicles attach to the distal ends of the mother centriole (Keeling et al., 2016). The extended centriole vesicle builds a ciliary membrane, which fuses with the cell membrane, forming a cup-like structure called the ciliary pocket in which the primary cilium is rooted (van Reeuwijk et al., 2011). Ciliary proteins are transported from the basal body to the ciliary pocket. Transmembrane proteins are then transported into the ciliary membrane and cytosolic proteins are transported by intraflagellar transport (Szymanska and Johnson, 2012). Molla-Herman et al. (2010) used mIMCD-3 kidney epithelial cells as a model to study the structure of the primary cilium in kidney epithelial cells. Transmission electron microscopy (TEM) showed the basal body was located underneath the base of this depression. A ciliary pocket was present with low frequency in kidney epithelial cells but was linked with nearly all primary cilia in retinal pigment epithelial cells. Recent insights have suggested that the ciliary pocket mediates ciliary endocytic activity which suggests dynamic and intense vesicular trafficking activity through endocytic recycling of transmembrane proteins, specifically ciliary receptors (Malicki and Johnson, 2017) (see section: 1.2.4.5.1 and 1.5). In addition, the ciliary pocket appears to interact with the actin cytoskeleton (Malicki and Johnson, 2017) (Figure 1.2) but the functional relevance of this for ciliary trafficking is unclear.

1.2.4.3 Transition zone

A short region of length 0.5 μm in most mammalian cilia is called the ciliary transition zone. It is located between the basal body and the axoneme (Gerhardt et al., 2016). TEM studies of cilia have hinted at the exquisite morphology and organization of the transition zone (Goncalves and Pelletier, 2017, Czarnecki and Shah, 2012). The transition zone has been suggested to act as a "ciliary gate" (Sanchez and Dynlacht, 2016) that mediates selective permeability during trafficking into and out of the cilium. The ciliary gate consists of at least 2 structures that include the transition zone, transition fibres (TFs) and perhaps nuclear pore components (Malicki and Johnson, 2017). The ciliary transition zone

forms when the basal body transitions into an axoneme, which forms the skeleton of the cilium (Lodish et al., 2007). The beginning of the TFs is formed by terminating the C microtubules of the basal body, whilst the nine sets of A and B tubules extend through the transition zone and help to form the axoneme (Lodish et al., 2007). Even though the transition zone is a region between the basal body and the axoneme, it is a highly complex structure that contains many proteins that contribute to the generation, function and maintenance of the cilia (Szymanska and Johnson, 2012). It plays a key role in regulating ciliary protein composition in many cell types, including mammalian cells, unicellular organisms such as *Chlamydomonas* and invertebrates such as *C. elegans* (Garcia-Gonzalo et al., 2011).

Transmembrane proteins and cytoplasmic proteins are selectively loaded on to the intraflagellar transport complexes because the access into and out of cilia is strictly controlled. Therefore, the proteins are not free to diffuse from the plasma membrane through the ciliary pocket into the ciliary membrane (Garcia-Gonzalo and Reiter, 2012). Sections through the transition zone have revealed Y-shaped linkers between the microtubules and the ciliary membrane that appear to be associated with characteristic bumps known as the ciliary necklace, that are revealed by freeze-fracture EM to be on the external surface of the ciliary membrane at the transition zone. The Y-shaped linkers are also associated with the TFs, and in combination these are proposed to act as the filter for the ciliary gate (Bisgrove and Yost, 2006). The TFs also encourage ciliogenesis by recruiting intraflagellar transport components to the basal body (Garcia-Gonzalo and Reiter, 2012) (Figure 1.2).

1.2.4.4 Diffusion barrier

As noted above, a diffusion barrier is located at the base of the cilia, the ciliary gate (Figure 1.2). The effectiveness of this barrier is that it restricts movement between the ciliary membrane and the plasma membrane. Hu and Nelson (2011) hypothesized that once membrane proteins are transported into the ciliary membrane, they are prevented from diffusing into the surrounding apical plasma membrane by a physical barrier.

There are two factors that affect ciliary trafficking by promoting retention inside cilia; a lipid barrier at the base of the cilia and a diffusion barrier- the septin-based gate. Vieira et al. (2006) proposed that there are distinct lipid barriers between cilia and rest of the plasma membrane, whilst Hu et al. (2010) and Chih et al. (2011) indicated that the base of cilia contains a septin (SEPTs), a group of GTP-binding proteins that oligomerize to form cytoskeletal filaments and higher-order structures. In particular, a member of the septin family Septin-2 contributes to the diffusion barrier at the base of primary cilia and it essential for retaining ciliary membrane proteins in the primary cilium ((Hu et al., 2010). Hu et al. (2010) showed that SEPT2 depletion caused loss of ciliary membrane protein localization and SHH signal transduction, as well as repressing ciliogenesis. SEPT7 and SEPT9 appear to be present along most of the length of the primary cilium (Ghossoub et al., 2013).

In addition, cilia were shown to use the septin-dependent diffusion barrier and transition zone proteins as a gate to regulate membrane protein passage, since proteins in the MKS module contain transmembrane or lipid-binding domains and these proteins are largely immobile at the transition zone, implying that this module forms a barrier and regulates the ciliary gate (Takao and Verhey, 2016). This observation was supported with the assembly of protein scaffolds that included the B9 domain containing proteins Meckel-Gruber syndrome type1 (MKS1), Tectonic-1 (TCTN1) and Tectonic-2 (TCTN2) as well as TMEM231 at the transition zone. These components appeared to localize with SEPT2 and formed the "ciliary gate" by contributing to transition zone barrier function (Mukhopadhyay et al., 2017, Francis et al., 2011).

1.2.4.5 The axoneme and intraflagellar transport

Cilia require large protein complexes and motors for the distal addition of tubulin and extension of the ciliary membrane. The basal body acts as the matrix for microtubule nucleation for the growth of the axoneme and connects the base of the cilium to its tip. This axoneme, a complex cylindrical structure, is encased by ciliary membrane that harbours receptors for crucial signalling cascades (Rohatgi and Snell, 2010) continuous with the plasma membrane of the cells (Figure 1.2). The ciliary axoneme is composed of nine doublets of fused microtubules arranged in a ring. The axoneme is arrayed in the 9+0

configuration in primary cilia or the 9+2 configuration in motile cilia, as discussed above (see section 1.2; Figure 1.1) (Plotnikova et al., 2009). These structural differences dramatically affect the mechanics of each. For instance, the ciliary axoneme location on the plasma membrane as it emerges from the cell and its orientation in three-dimensional space has a critical role in the proper function of both motile cilia and nodal cilia (Farnum and Wilsman, 2011).

Intraflagellar transport, a microtubule-based conveying system, is responsible for the bidirectional motility of proteins along the ciliary axonemal microtubules (Singla and Reiter, 2006). During ciliogenesis, the intraflagellar transport system traffics tubulin as well as other ciliary building blocks (Chih et al., 2011). Therefore, both intraflagellar transport and microtubule assembly help the axoneme to elongate (Conduit et al., 2012). In addition, small GTPases of the Rab family regulate membrane trafficking. Rab8 is essential for membrane trafficking from the trans-Golgi network and recycling of endosomes to the plasma membrane. Briefly, active forms of Rab8 control the transport of proteins and membrane receptors into the primary cilium. The intraflagellar transport system continues the trafficking of these proteins up and down the ciliary axoneme (Hsiao et al., 2012). Therefore, Rab8 together with the intraflagellar transport system is essential for ciliogenesis (Pedersen and Rosenbaum 2008; Patrussi and Baldari 2016), (see section 1.4).

1.2.4.5.1 Trafficking in and to the primary cilium

The intraflagellar transport system is involved in cilia assembly, ciliary sensory perception, and cilia signalling (Yoder, 2007). Its particles carry ciliary receptors and channels, and deliver signals that emerge from the cilia into the cytoplasm in response to environmental stimuli (Yoder, 2007). For example, the glioma-associated oncogene homologue (GLI) family of zinc finger transcription factors control the output of the SHH pathway. *GLI2* and *GLI3* were shown to be recruited to the tip of primary cilia by intraflagellar transport upon SHH stimulation (Rohatgi et al., 2007, Chen et al., 2009). Accordingly, the role of intraflagellar transport is not limited to constructing cilia and intraflagellar transport appears to play a distinguishable function in signal transduction events. The knock-out of intraflagellar transport proteins in various mouse models demonstrates their importance in the assembly, production, maintenance and the transport

of other proteins into and out of cilia (Garcia-Gonzalo and Reiter, 2012). For example, mice with an alteration in the *Ift88* gene have renal abnormalities and retinal degeneration due to defects in photoreceptor outer segment development (Pazour et al., 2002).

Researchers have used the 2 flagella of the unicellular green algae *Chlamydomonas reinhardtii* as a model to investigate how ciliary proteins are transported. The ciliary intraflagellar transport system consists of two multi-subunit particles that consist of intraflagellar transport-B (IFT-B) for anterograde transport and intraflagellar transport-A (IFT-A) for retrograde transport (Figure 1.3). The intraflagellar transport particles move between the ciliary membrane and the axonemal microtubules. IFT-B transports proteins toward the ciliary tip in a process driven by the kinesin-2 motor, whilst IFT-A transports the proteins towards the ciliary base in a process driven by the cytoplasmic dynein 2/1b motor (Follit et al., 2009). Intraflagellar transport protein trafficking is of crucial importance in the control of cilium length which depends upon the balance between IFT-B anterograde and IFT-A retrograde trafficking (Ishikawa and Marshall, 2011, Hirano et al., 2017).

All IFT-B proteins, that were initially identified in *Chlamydomonas*, have also been subsequently described in mouse by biochemical methods (co-immunoprecipitation and mass spectrometry). For instance, studies of mouse mutant or knock-out models have established the critical role of kinesin-2 and most of the IFT-B proteins in the SHH pathway. Analysis of mouse ciliary mutations in *Ift172, Ift88, Ift52, Ift57*, and *Ift46* as well as genetic inactivation of kinesin-2 resulted in a range of phenotypes, including absence of cilia, loss of SHH-dependent ventral neural cell types and lack of all response to the SHH ligand (He et al., 2017, Goetz and Anderson, 2010). Furthermore, this study also revealed that genetic inactivation of mouse IFT-A proteins caused embryonic lethality. IFT-A subunits have been suggested to promote trafficking of G protein-coupled receptors (GPCRs) into primary cilia (Mukhopadhyay et al., 2010) as well as regulate SHH signalling pathway through intraflagellar transport machinery at the primary cilium (Liem et al., 2012). The IFT-A complex was not only involved in intraflagellar transport and ciliogenesis, but may also bind, anchor and transport ciliary precursors in the cell body towards the ciliary base (Zhu et al., 2017). Novel functions were also described for WD Repeat Domain 35 (Wdr35), an IFT-A

subunit, that appears to mediate fusion of Rab8 vesicles at the nascent cilium, protein exit from the cilium, and centriolar satellite organization (Fu et al., 2016).
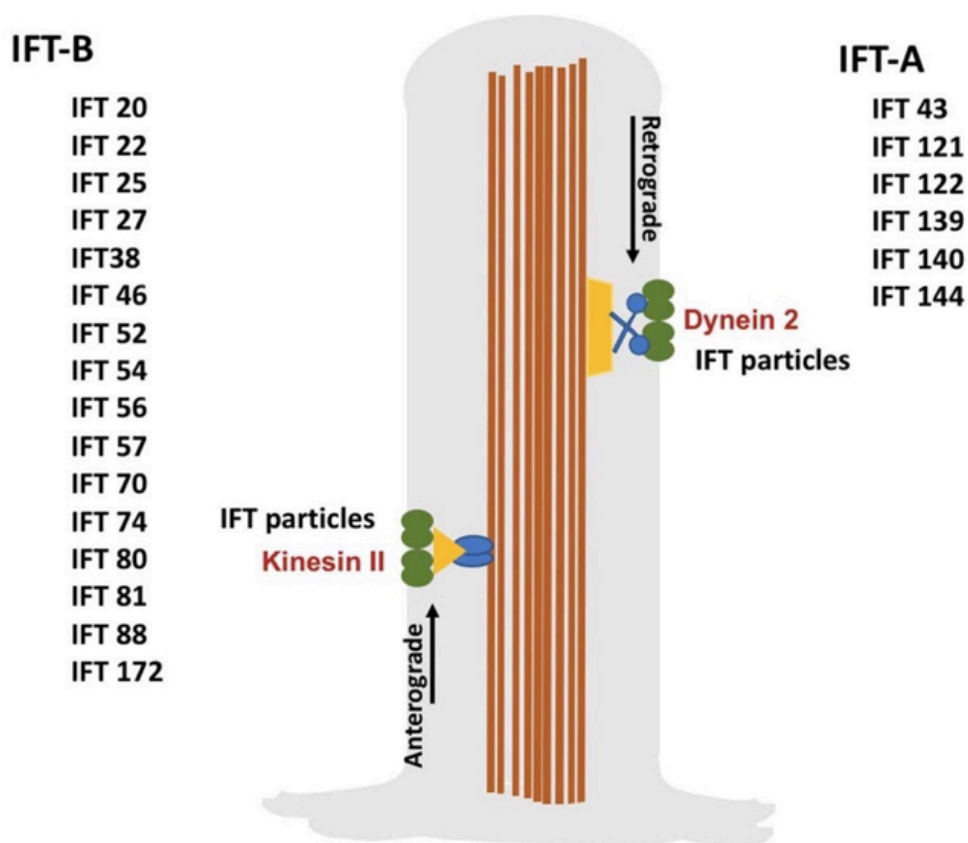
Figure 1. 3: List of intraflagellar transport complex ciliary proteins. The intraflagellar transport complex is composed of sub-complex A (IFT-A), connected to a dynein motor for transport towards the ciliary base (retrograde transport), and sub-complex B (IFT-B) linked to a kinesin motor for transport towards the ciliary tip (anterograde transport). The IFT-A and IFT-B complexes assemble to form intraflagellar transport particles (Nachury, 2014).

1.2.5 Centriolar satellites

Centriolar satellites are small granules that cluster around centrosomes and contain proteins directly involved in centrosome maintenance, ciliogenesis, and neurogenesis (Tollenaere et al., 2015). The first component of centriolar satellites, Pericentriolar Material 1 (PCM1), was identified by (Kubo et al., 1999). This study described PCM1 as specific component of centriolar satellites, morphologically characterized as electron-dense granules 70–100 nm in diameter, scattered around centrosomes. PCM1-containing centriolar satellites moved along microtubules toward centrosomes in an ATP-dependent

manner (Kubo et al., 1999), suggesting that centriolar satellites have a possible association with centriolar replication.

A previous study in 2011 suggested that centriolar satellites might function in communication between the centrosomes and the cytoplasm and appear to surround the core of the centrosome in most animal cells as "busy orbits around the centrosome" (Barenz et al., 2011). Recently several studies have identified many new centriolar satellite components, however the regulatory mechanisms that control centriolar satellite status and function are not yet understood, and further components need to be identified in order to fully understand the mechanisms that mediate satellite formation (Kim et al., 2012, Quarantotti et al., 2019, Tollenaere et al., 2015). Defects in centriolar satellite components are linked to a wide spectrum of human diseases (Tollenaere et al., 2015). For instance, *CEP290*, a gene which encodes a centrosomal protein involved in ciliary assembly and ciliary trafficking, interacts with the centriolar satellite protein PCM1, which is implicated in *BBS4* function (Kim et al., 2008). CEP290 co-immunoprecipitated with PCM1 (Chang et al., 2006) and depletion of *CEP290* disrupted subcellular distribution and protein complex formation of PCM1. The association of both *CEP290* and *PCM1* was required for ciliogenesis, since both proteins were required for the ciliary localization of Rab8 (Kim et al., 2008).

1.3 The functional significance of the ciliary transition zone

Significant progress has been made during the past decade in understanding the constituents and architecture of the primary cilia, particularly the transition zone, and to comprehending the functions of transition zone proteins. The disruption of transition zone proteins by mutations cause a group of inherited conditions: the ciliopathies (Leightner et al., 2013). Mutations can disrupt the control of protein entry and exit from the cilium, the trafficking of proteins to the cilium, and in the regulation of signalling pathways. Figure 1.4 summarizes the localization of ciliary proteins based on the results of different research teams who investigated the composition of protein complexes at the transition zone and other ciliary compartments.

Sang et al. (2011) identified and showed the localization of *NPHP1*, *NPHP4*, and *RPGPIP1L* at the transition zone and described a compartment that they named the

nephronophthisis NPHP module. Garcia-Gonzalo et al. (2011) showed the importance of *CEP290* in cilia formation, identified mutations in TCTN1 as a cause of Joubert syndrome, and showed the physical interaction between these proteins in the Joubert (JBTS) module. For example, TCTN1 is required for the transition zone localization of *MKS1* and *TMEM67/Meckel*. Also, *RPGRIP1L* regulated the transition zone amount of *NPHP4* by ensuring the correct amount of *CEP290/NPHP6* at the transition zone (Wiegering et al., 2018a).

Moreover, *RPGRIP1L* localizes independently (Figure 1.4) and influences proper transition zone localization of the *NPHP1-4* and *MKS/B9* complexes. The third module, the MKS module, described by Williams et al. (2011), showed that *MKS1*, coiled-coil and C2 domain-containing protein 2A (*CC2D2A)*, and *TCTN2* are involved in neural tube development and the SHH pathway. Other CEP290-dependent transition zone proteins include transmembrane proteins such as Tmem17, Tmem138, and Tmem231 (Li et al., 2016) delineating a possible new compartment of the cilium that was termed the inversin compartment. Although many proteins were found to be localized to this compartment, their function remains unclear. In a fourth study, Huang et al. (2011) identified mutations in the novel gene *TMEM237* as a cause of Joubert syndrome-related disorders. Their research on *C. elegans*, zebrafish and ciliated mouse (mIMCD-3) cells showed that *TMEM237* localized to the transition zone and had biochemical and genetic interactions with several other ciliary TMEM proteins, including *TMEM216* and *TMEM67*. They also confirmed that TMEM237 requires RPGRIP1L for correct localization to the transition zone. Subsequent studies suggested that RPGRIP1L functions at the base of a hierarchy during assembly of the transition zone (Wiegering et al., 2018a), thereby regulating the proper number of components of the *NPHP* module at the ciliary transition zone. However, there are some obvious inconsistencies between the studies. These differences could be due to the fact that the 4 groups used different tissues or cell-lines with different cilia structures with possible inconsistencies in the dynamic nature of ciliogenesis or ciliary trafficking.
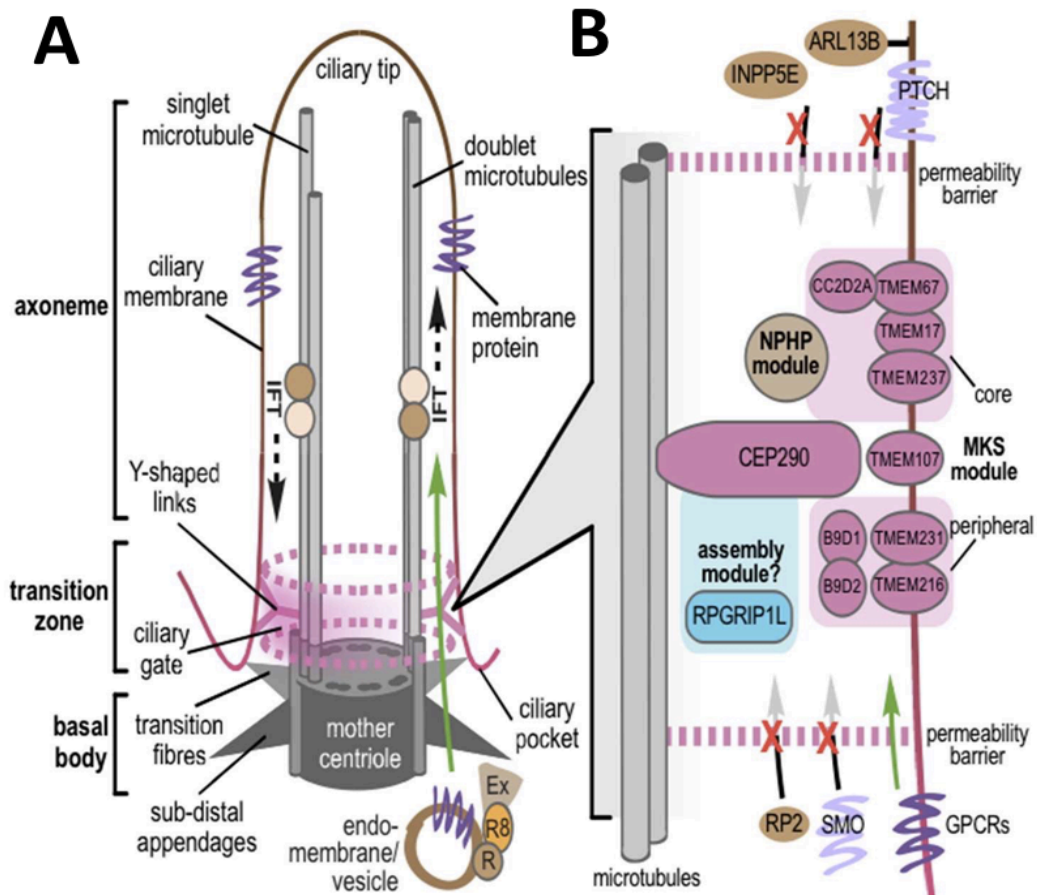
Figure 1. 4: An overview of the primary cilium, transition zone molecular organization and ciliary protein complexes. (A) Key structures of cilia and the transition zone. Ciliary receptor (purple) is trafficked into the cilium (green arrow) through a permeability barrier (pink). **(B)** Models of hierarchical transition zone protein organisation within functional modules (MKS, NPHP, assembly modules) at the transition zone. The MKS module consists of core, intermediate and peripheral layers. RPGRIP1L localizes independently and influences proper transition zone localization of the NPHP and MKS complexes. Selective permeability barriers prevent trafficking of key signalling proteins (red crosses) to maintain compartmentalization. Smoothened (SMO) (light purple) plays a role in an intercellular communication in development Localized lipid composition in the ciliary membrane is indicated by a brown-magenta gradient, adapted from (Hartill et al., 2017).

1.4 Ciliogenesis

Recent evidence suggests that cilium assembly and disassembly links to the cell cycle (Ke and Yang, 2014), as well as vesicular trafficking and ciliary extension (Avasthi and Marshall, 2012). As previously noted, the formation of primary cilia depends on the cell cycle and is initiated in G1 by the addition of Golgi-derived vesicles to the distal end of the mother centriole (Sanchez and Dynlacht, 2016). When a cell forms a primary cilium in G0,

the centrosome migrates to the cortex of the cell. Then, Golgi-derived vesicles produce a centriolar vesicle that caps the distal end of the mother centriole. Once docked, the extended centriolar vesicle forms a ciliary membrane, which fuses with the cell membrane, forming the ciliary pocket. Early studies confirmed that polarized vesicular transport involving Rab8 and its guanine nucleotide-exchange factor (GEF) Rabin8 is essential for primary ciliogenesis. For example, Knodler et al. (2010) have suggested that Rab GTPases coordinate with each other in the regulation of vesicular trafficking during primary ciliogenesis.

The trafficking pathway of Rab8-dependent primary cilium assembly in RPE cells was investigated by Westlake et al. (2011), who suggested that a Rab11–Rab8 cascade functions in primary cilium assembly. They proposed that Rab11 delivers Rabin8 to the centrosome to activate Rab8 and Rab11 vesicles are converted into the Rab8 ciliary compartment (Westlake et al., 2011). According to Knodler et al. (2010), Rab11 is enriched at the base of primary cilia and inhibition of its function by a dominant-negative mutant or siRNA blocks ciliogenesis. Activated Rab8 participates in the formation of primary cilia and regulates the transport of Smoothened (SMO) and fibrocystin receptors (Boehlke et al., 2010, Follit et al., 2010). Rabin8 has been shown to associate with the BBSome, a basal body protein complex implicated in Bardet-Biedl Syndrome, and to regulate cilia formation. BBSome proteins modulate the activity and the ciliary entry of Rab8, through its interaction with Rabin8 via BBS1 (Nachury et al., 2007). Recently, Lu et al. (2015) suggested that Rab-GTPase functioned at a later stage of ciliary vesicle membrane elongation. They found that Rab8 was unessential for initial docking of ciliary vesicles to the mother centriole and, interestingly, Rab8 was recruited to ciliary vesicles after the recruitment of other ciliary proteins linked to ciliary vesicle formation, including the endocytic transport regulator EH Domain Containing 1(EHD1), the ciliary transition zone protein B9D2 (B9 domain-containing protein 2) and Golgi-associated IFT20.

Another study demonstrated that the centrosome then differentiates into the basal body and localizes at the base of the primary cilia, which results in early formation of the ciliary bud. The ciliary bud is continuous with the centriole and surrounded by the ciliary vesicle. The ciliary bud then extends by microtubule assembly and the ciliary vesicle merges with the plasma membrane (Conduit et al., 2012). CEP110, CEP97, and CEP290 play a vital

role in centrosome duplication and cytokinesis: these proteins interact with each other at the mother centriole/basal body to regulate ciliary assembly (Tsang et al., 2008). In addition, the centriolar kinesin Kif24 was found to control the stability of *CP110* at the distal end of the mother centriole localized in the centrosome/basal body. This is a key spindle assembly checkpoint protein, whose insufficiency leads to cell cycle dysregulation and ciliogenesis defects (Kobayashi and Dynlacht, 2011).

A normal differentiated cell has a pair of centrioles within the centrosome that differ functionally and morphological (Pierce and Nachury, 2013). A normal centriole number is maintained by duplication and segregation mechanisms synchronized to the cell cycle. However, additional centrioles within the centrosome can result in super-numerary cilia on the cell surface, so that the cell then exhibits a "cilia-diluted" phenotype with reduced signalling molecules (Mahjoub and Stearns, 2012). This phenotype has been suggested to cause a signalling dysfunction that underlies oncogenesis. Avasthi and Marshall (2012) have suggested that accurate timing also plays a crucial part in cilia formation during cell cycle regulation and blocking cancer phenotypes, emphasizing that it is essential to understand the inductive cues that link ciliogenesis to the cell cycle (Sanchez and Dynlacht, 2016).

1.4.1 Cilia disassembly

Disassembly of cilia occurs prior to mitosis. Cells re-enter the cell cycle in G1 and then the centrioles duplicate in S-phase and the basal body detaches itself from the plasma membrane (Santos and Reiter, 2008). The scaffolding protein neural precursor cell expressed, developmentally down-regulated 9 (NEDD9)/HEF1, vital for ciliary disassembly, interacts with Aurora kinase A (AURKA) at the mother centriole and controls the disassembly of cilia by inducing phosphorylation and thereby activation of Histone deacetylase 6 (HDAC6), a tubulin deacetylase that triggers ciliary disassembly (Pugacheva et al., 2007). AAURKA, polo-like kinase 1 (PLK1), and never in mitosis gene a-related kinase 1 (NIMA) also have non-mitotic functions by inducing cell cycle progression through the stimulation of primary cilia disassembly (Ke and Yang, 2014). Other proteins have been identified that regulate ciliary disassembly, including the basal body and ciliary necklace protein Pitchfork (Pifo) which activates AURKA, resulting in ciliary disassembly (Kinzel et al., 2010). Furthermore, the inhibition of ciliogenesis by nudE neurodevelopment protein 1

(NDE1) stimulates and accelerates cell cycle re-entry (Kim and Tsiokas, 2011). Moreover, the activity of Dynein light chain Tctex-type 1 (DYNLT1) (also known as TCTEX1), a cytoplasmic dynein subunit regulates ciliary disassembly and S-phase entry (van Reeuwijk et al., 2011).

More recent studies have tested the hypothesis that the regulation of DYNLT1/TCTEX1's ciliary resorption function is linked to the G1-S transition during the cell cycle (Saito et al., 2017). This work showed that phospho- (T94) DYNLT1/TCTEX1 was recruited to the ciliary transition zone during the G1-S transition and that this regulated actin polymerization which appeared to control ciliary resorption (Saito et al., 2017, Li et al., 2011). The molecular mechanism of this regulatory process involved the direct binding of DYNLT1/TCTEX1 to F-actin, forming multivalent, cooperative protein-protein interactions with three actin polymerization regulators including Annexin A2 (ANXA2), actin-related protein 2/3 complex subunit 2 (ARPC2) and cell division control protein 42 homolog (CDC42). Furthermore, cytochalasin D, an inhibitor of actin polymerization, suppressed ciliary resorption mediated by DYNLT1/TCTEX1, whereas stimulating actin polymerization by over-expression of CDC42 prevented resorption defects caused by knockdown of DYNLT1/TCTEX1. This was supported by previous work from this group, showing that knockdown of DYNLT1/TCTEX1 blocked both ciliary resorption and G1-S progression (Li et al. 2011). Their finding suggested that when the phosphomimic mutant T94E, Tctex1^{T94E}, was overexpressed in the human immortalized retinal pigmented epithelial (RPE1) cells, it represented a functionally active form of Tctex-1 in ciliary disassembly which accelerated cilium disassembly and S-phase entry (Saito et al., 2017, Li et al., 2011).

1.5 Primary cilium-dependent signalling mechanisms

The primary cilium plays a vital role in sensing the extracellular environment by conveying the signalling events from extracellular space into the cell (Ke and Yang, 2014). The ciliary compartment harbours many receptors and components of key signalling cascades, including Hedgehog, non-canonical Wnt, Hippo, Notch, planar cell polarity (PCP), fibroblast growth factors (FGF), mechanistic target of rapamycin (mTOR), platelet-derived growth factor receptor α (PDGFRα), transforming growth factor (TGF)-β and Hippo signalling (Ke and Yang, 2014, Eggenschwiler and Anderson, 2007). Cilia therefore play critical roles in signalling pathways that are important for both embryonic development and tissue

homeostasis. In addition, cilia regulate proliferation, differentiation, transcription, migration, polarity and tissue morphology. Therefore, disruption of ciliary function has severe consequences (van Reeuwijk et al., 2011). Receptors are enriched at the primary cilium and many events of signalling mechanisms are concentrated at the cilium, making it an importance structure for receiving and transducing a variety of signals (Hsiao et al., 2012).

1.5.1 SHH signalling and the primary cilium

Primary cilia are essential for SHH signalling in vertebrates, with the pathway in mice and zebrafish found to have fundamental roles in both embryonic development and cancer. The mammalian SHH signalling pathway controls processes associated with tumorigenesis and vertebrate cells rely on primary cilia to respond to Hedgehog family ligands (Huangfu et al., 2003, He et al., 2017). Hedgehog signalling is essential for stem cell maintenance and embryonic development (Jiang and Hui, 2008, Beachy et al., 2004) and many consequences of perturbation of primary ciliary proteins can be explained by dysregulation of SHH signalling (He et al., 2017). For instance, during embryonic development the SHH pathway is a critical component of neural tube closure and organ patterning. Disruption of these embryonic processes causes neural tube defects that are a clinical feature of severe ciliopathies such as Meckel-Gruber syndrome. Moreover, absence of cilia in the chick blocks the ability of cells to receive Hedgehog signals (Yin et al., 2009). SHH signalling can be regulated by either preventing accumulation of SMO within the cilium or by inhibiting its activation (Rohatgi et al., 2009). SHH signalling proteins are enriched in cilia and these proteins alter their localization within the cilium in response to ligand (Goetz and Anderson, 2010). For instance, SHH signalling and ciliogenesis defects have been reported in the *Tmem231* knock-out mouse. These defects included disruption of a complex of 9 proteins (including TMEM231, B9D1 (B9 domain-containing protein 1) and CC2D2A: see Figure 6.1) at the transition zone and a reduction in cilia formation. This study highlighted the importance of SHH signalling, particularly in early embryonic developmental processes, in maintaining and regulating transition zone cilia sup-compartments (Chih et al., 2011). This study also contributed to the emerging understanding that the transition zone is a key regulator of cilium composition and signalling by establishing diffusion barriers that restrict cytosolic

protein entry in a size-dependent manner and the lateral exchange of proteins between ciliary and non-ciliary membranes (Chih et al., 2011). Taking this into account, more emphasis is now being placed on understanding the molecular mechanisms underlying the signalling pathways responsible for primary ciliary-related diseases.

SHH, the secreted ligand protein, plays an important role in activation of the glioma-associated oncogene (GLI) family of transcriptional regulators (Wilson and Stainier, 2010). GLI proteins work as either transcriptional activators or truncated transcriptional repressors. The formation of either repressor or activator forms of GLI3 can be controlled by their interaction with suppressor of fused (SUFU) protein. Prior studies have proposed that SUFU function can either stimulate GLI proteins in the cytoplasm or repress GLI transcriptional activity in the nucleus (Humke et al., 2010). SHH signalling is therefore regulated by the dynamic association between SUFU and the GLI proteins, which will be discussed in the following sections.

Ramsbottom and Pownall (2016) argued that input from other environmental signals should be considered to understand a potential general mechanism of how SHH signalling is regulated during the cellular response. They believed that multiple levels of regulation of specific signals will influence SHH signalling. For instance, Notch enhances the effect of SHH by up-regulating SMO activity (Stasiulewicz et al., 2015). The latter study found that Notch signalling modulates SHH signalling by regulating the localization of key ciliary components of its transduction machinery; they showed *in vivo* evidence supporting a novel role for the Notch pathway in modulating ciliary architecture and localisation of SMO in cilia (Stasiulewicz et al., 2015). Furthermore, supporting data from others, Kong et al. (2015) also demonstrated that Notch activity plays an essential role in the SHH pathway by regulating the subcellular localization of the receptor Patched1 (PTCH1), influencing the ciliary trafficking of PTCH1 and SMO and the downstream activation of GLI transcription factors. Together, these data provide important insights into the interactions between Notch and SHH signalling pathways in cilia.

1.5.1.1 In the absence of SHH signalling

Cubitus interuptus (Ci) in *Drosophila* and GLI proteins in vertebrates are transcriptional regulators that act as repressors in the absence of SHH signalling (Wilson and Stainier, 2010). The process begins when a GPCR, the seven-pass transmembrane protein, SMO, is repressed by Patched (PTCH) resulting in repression of target gene transcription (Humke et al., 2010). PTCH1 is the SHH receptor and is a 12-pass transmembrane receptor protein that is localized within the ciliary membrane of vertebrates (Ingham et al., 1991). In the absence of SHH ligands, SUFU interacts with all three GLI proteins and mediates their nuclear export (Haycraft et al., 2005). SUFU restricts GLI3 in the cytoplasm and converts its function to a repressive form. Protein kinase A (PKA) starts a phosphorylation cascade (Humke et al., 2010), with both GLI2 and GLI3 phosphorylated at the basal body by PKA. PKA prepares GLI2 and GLI3 for additional phosphorylation by glycogen synthase kinase 3β (GSK3β) and casein kinase 1 (CK1). This process delivers a high-affinity binding site for β-transducin repeat-containing protein (TrCP). Then β-TrCP induces the SCF (Skp1/Cullin1/F-box) ubiquitin ligase complex to target full-length, 190 kDa GLI3 and 185 kDa GLI2 for the ubiquitin-proteasome pathway. Phosphorylation selects GLI3 for ubiquitination, and the N-terminal repressor forms of 83 kDa GLI3 (GLI3R) and 78 kDa GLI2 (GLI2R) are produced. The C-terminus is thought to be completely degraded (Wen et al., 2010). Figure 1.5 shows a simplified diagram of SHH signalling pathway in the presence or absence of SHH.

1.5.1.2 In the presence of SHH signalling

SHH signalling triggers the activities of GLI proteins by translocating these proteins to the nucleus and activating target genes. This process occurs as a result of the activity of SMO (Wilson and Stainier, 2010). First of all, the secreted SHH binds to the receptor PTCH1. PTCH1 releases SMO from inhibition, and the latter translocates into the primary cilium (Chen et al., 2009). The accumulation of SMO drives an increased level of the GLI proteins: SMO activates the production of the three GLI protein transcription factors (GLI complex) by relieving the inhibition of SUFU. This means that the presence of SHH protein causes the dissociation of the SUFU-GLI complex and allows GLI to enter the nucleus and initiate transcription of a target gene. In addition, SHH signalling causes the dissociation of SUFU from GLI3 through the action of a kinesin motor (KIF3A), which prevents the formation of

the repressor isoform and allows GLI3 to enter the nucleus (Humke et al., 2010). The full-length GLI3FL isoform, in the presence of signalling, is altered into transcriptional activator protein isoforms (GLI3A), although the biochemical mechanism of this activation process is still ambiguous in flies as well as mammals (Tukachinsky et al., 2010) (Figure 1.5).
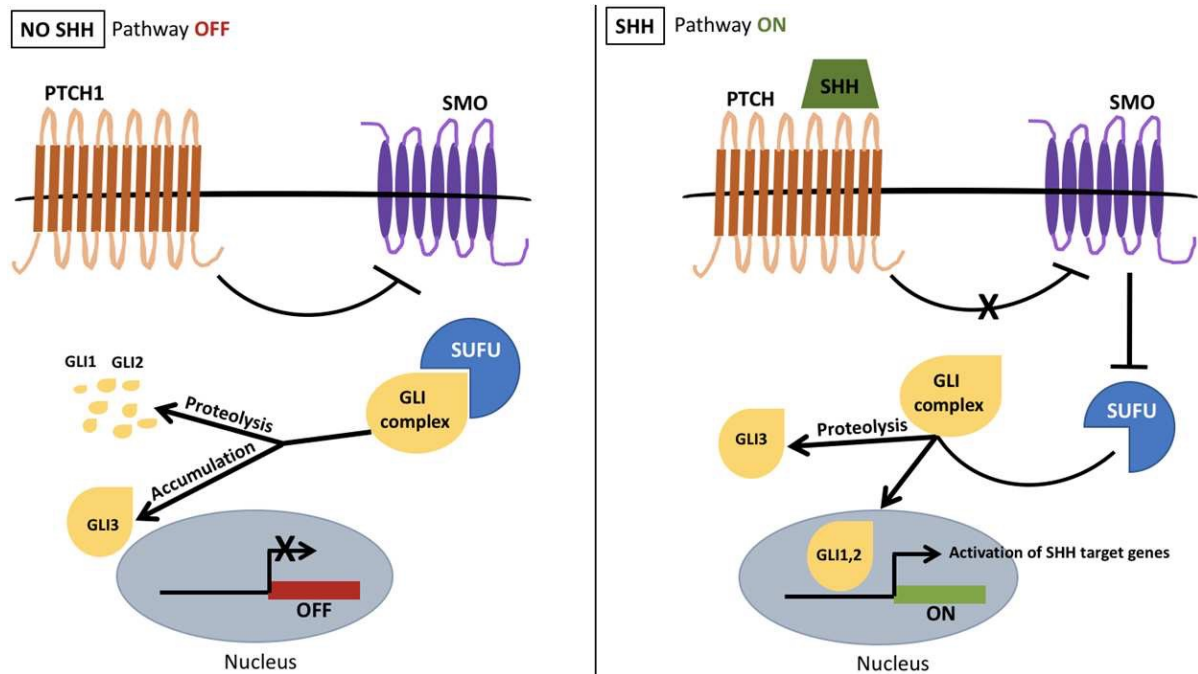
Figure 1. 5: A simplified diagram of SHH signalling pathway. Pathway OFF, in the absence of SHH ligand: PTCH1 inhibits the activity of SMO, which stops the suppressor of SUFU complex from entering the nucleus and promotes GLI3 nuclear accumulation, resulting in low expression of SHH target genes (right panel). Pathway ON, in the presence of SHH ligand: SHH binding to PTCH1 activates the SHH signalling pathway by promoting GLI1/2 expression by entering the nucleus (left panel).

1.5.1.3 Basal body proteins required for SHH signalling

Genetic studies have indicated that basal body proteins are required for SHH signalling. Mutations in the centrosomal/basal body protein Talpid3 are associated with cilia loss and disruption of the SHH signalling pathway in mouse mutant embryos, which results in developmental abnormalities in the limbs: a polydactyly ciliopathy phenotype (Goetz and Anderson, 2010). Furthermore, CEP290, a basal body and transition zone protein (Goncalves and Pelletier, 2017, Garcia-Gonzalo et al., 2011, Arts et al., 2007), has been suggested to control the transport of distinct SHH signalling proteins.

Shimada et al. (2017) examined the SHH signalling pathway in JSRD patient and control fibroblasts using serum-starved cells with the SMO agonist SAG and defined the expression of PTCH and GLI1/2. SAG-dependent expression of PTCH and GLI1 was high and cilia number was lower in JSRD fibroblasts compared to the control cells. In addition, Kilander et al. (2018) showed that a rare human *CEP290* variant disrupted the molecular integrity of the primary cilium and impaired SHH machinery. Cells expressing R1747Q mutant *Cep290* in mouse revealed a defect in SHH signalling response, mis-localisation of the SMO receptor and dysregulation of ciliary protein mobility. Therefore, they demonstrated that CEP290 is essential for positioning the molecular components that are necessary for correct processing of SHH signalling in the primary cilium.

A further example is *RPGRIP1L*, which localizes to both the ciliary transition zone and basal body (Goncalves and Pelletier, 2017, Arts et al., 2007, Garcia-Gonzalo et al., 2011). Recently Lin et al. (2018) argued that RPGRIP1L is a central protein of the transition zone. A mouse knock-out of *Rpgrip1l* had defective patterning of the neural tube and the limbs, as well as a disrupted ratio of GLI3 activator to GLI3 repressor, suggesting that Rpgrip1l is required for SHH signalling (Vierkotten et al., 2007).

1.5.1.4 Intraflagellar transport system and SHH signalling

Intraflagellar transport proteins are required for cilia assembly and play a crucial role in embryonic development in vertebrates. Early studies showed that mouse ethylnitrosourea (ENU) mutants in genes encoding Intraflagellar transport proteins had perturbed SHH signalling (Huangfu et al., 2003) with low production of GLI protein activators and repressors (Chen et al., 2009). In addition, any disruption of Intraflagellar transport appeared to inhibit the formation of GLI3R and reduced GLI2/3A function in embryos (Huangfu et al., 2003, Huangfu and Anderson, 2005, Liu et al., 2005). It is notable that GLI3 processing appears to mainly affect limb development, and for proper digit number and identity the appropriate ratio of GLI3FL and GLI3R must be maintained (Wen et al., 2010).

Many genetics studies have suggested that IFT proteins are essential for SHH signalling. In mouse for instance, many mutations in IFT components resulted in embryonic mid or late-gestation arrest with mis-patterning of SHH-dependent tissues (Bangs and

Anderson, 2017) such as the neural tube and limb buds. In humans, mutations in IFT genes cause ciliopathies that often affect the skeletal system such as Jeune asphyxiating thoracic dystrophy, cranioectodermal dysplasia (CED) and short-rib polydactyly syndrome (Gilissen et al., 2010, Arts et al., 2011, Schmidts et al., 2013, Gholkar et al., 2015, Moosa et al., 2016). Yuan et al. (2016) demonstrated that IFT80, an Intraflagellar transport protein in IFT-B, is required for osteoblast differentiation by balancing canonical Hh–Gli and non-canonical Hh–Gαi–RhoA pathways and represent a therapeutic target for craniofacial and skeletal abnormalities. They showed that loss of *IFT80* prevents SMO localization to the cilium resulting in inhibition of canonical HH signalling and increased noncanonical HH-GI-RHO Hh–Gαi–RhoA–stress fibre signalling by increasing SMO and Gαi binding.

1.5.2 Wnt signalling pathways

Signalling by the Wnt family of glycoproteins also appears to be mediates, in part, by primary cilia. The Wnt signalling pathway is a conserved pathway in many species, ranging from flies to human (Pala et al., 2017). Wnt was named by a fusion of the name of the *Drosophila* segment polarity gene wingless and its vertebrate homolog, integrated or int-1 (Wodarz and Nusse, 1998, Komiya and Habas, 2008). Wnt signalling functions in a range of cellular processes, including cell migration, PCP, neural patterning, skeletal system development, and organogenesis (Pala et al., 2017, Corbit et al., 2008, Ross et al., 2005, Simons et al., 2005). Mutations in this signalling pathway result in developmental disorders and cancer.

Wnt signalling can be divided into β-catenin dependent (canonical) and β-catenin independent (non-canonical) signalling (Park et al., 2019, Oh and Katsanis, 2013, Berbari et al., 2009). In recent years, canonical and non-canonical Wnt signalling pathways have been shown to be associated with the primary cilium, which has been suggested to act as a switch between the 2 (May-Simera and Kelley, 2012, Goggolidou et al., 2014). For instance, primary cilia modulate the balance between canonical and non-canonical signalling responses in the injured kidney (Saito et al., 2015), with renal repair and progressive renal fibrosis linked to increased canonical and decreased non-canonical Wnt signalling. Simons et al. (2005) first demonstrated that Inversin (INVS), which localized in cilium, acts as a molecular switch between types of Wnt signalling pathways by inhibiting the canonical Wnt pathway during

renal development by targeting *DVL1* for degradation. They demonstrated that fluid flow increases INVS levels in ciliated tubular epithelial cells and therefore regulates the switch between Wnt pathways. They concluded that this inhibition or modulation of canonical Wnt signalling is required for normal kidney development. This is supported by the observation that ciliopathy patients with mutations in *INVS* developed NPHP type 2, an autosomal recessive cystic kidney disease. Moreover, a study suggested that PCP is also involved in the switch between canonical and non-canonical Wnt signalling (Eggenschwiler and Anderson, 2007). PCP signalling appears to act as a molecular switch from canonical to PCP signalling in renal cystic disease and more recent work has indicated that PCP signalling is necessary for vertebrate renal tubular formation and is disrupted in renal cystic disease (Papakrivopoulou et al., 2014).

In relation to Wnt signalling, primary cilia have been demonstrated to play a significant role in cystic renal disease (Goggolidou et al., 2014) and it has been discovered that many of the proteins needed for the correct formation and function of kidney structures are located in the cilia.

1.5.2.1 Canonical Wnt signalling and cystic kidney disease

Canonical Wnt signalling control of cell proliferation and differentiation is critical for early kidney development. Mutations in this pathway are implicated in cancer development and renal cyst formation. Numerous studies have suggested that the loss of cilia leads to increased canonical Wnt signalling that causes severe disruption in early development (Eggenschwiler and Anderson, 2007). More recent studies have shown that the signalling pathways that require the primary cilium in the kidney are LKB1/AMPK, regulator of cell metabolism, growth and proliferation, Wnt and SHH developmental signalling pathways. These signalling pathways are dysregulated in renal cystic disease (Avasthi et al., 2017) and ciliopathies have been implicated in the negative regulation of the canonical Wnt pathway (Lancaster et al., 2011, Corbit et al., 2008, Simons et al., 2005). However, it remains unclear if disrupted Wnt signalling causes or is a consequence of defective ciliogenesis. There is also evidence of an association between PCP-related mechanisms and the cause of renal disease. Therefore, it is vital to understand the regulation of this pathway in order to develop

treatments for these diseases (Lancaster et al., 2011). Table 1.1 lists some important components in renal ciliopathies that are involved in Wnt signalling.

A parallel group of studies also highlighted the connections between cilia and the canonical Wnt pathway by demonstrating that nephrocystin 2 (also called INVS) localized to cilia and physically interacted with the core Wnt pathway component *DVL1* (Wallingford and Mitchell, 2011, Simons et al., 2005, Otto et al., 2003, Watanabe et al., 2003). Therefore, *DVL1* is believed to act as a molecular switch to activate canonical or non-canonical signalling (Oh and Katsanis, 2013). Knock-out of *DVL* orthologues cause disorders that resemble human ciliopathies in animal models. For instance, the knock-down of all three zebrafish *DVL (1-3)* genes led to defects in asymmetric basal body localization in floor plate cells. This occurs because *DVL* is important for zebrafish convergence-extension cell movements, which is a polarized cell movement during embryonic development (Mahuzier et al., 2012, Angers et al., 2006). When an embryo is restructured to converge (narrow) and elongate along the mediolateral axis and extend (elongate) along a intercalate toward the midline (convergence), leading to extension of the anterior/posterior axis, this is achieved by regulation of cellular movement (Veeman et al., 2003, Wallingford et al., 2002). This developmental process is regulated by the non-canonical Wnt/PCP pathway during vertebrate gastrulation (Wallingford and Habas, 2005, Myers et al., 2002).

Important mediators of Wnt signalling include the Dishevelled (DVL) proteins, classified into Dishevelled1 (DVL1), Dishevelled 2 (DVL2) and Dishevelled3 (DVL3) in mammals. The canonical Wnt pathway has a two-state model of activation (with Wnt ligand binding) and inactivation (without Wnt), which then controls subcellular β-catenin levels and localization (Figure 1.6). In the activated state, a canonical Wnt ligand binds to the seven-pass transmembrane receptor Frizzled (FZD) in the presence of the single-pass low-density lipoprotein receptor-related protein 5 or 6 (LRP5 or LRP6), which are co- receptors in vertebrates (He et al., 2004). This creates a Wnt–FZD–LRP5/6 trimeric complex that recruits and binds the cytoplasmic protein DVL and Axin. In turn, this triggers the activation of the canonical Wnt signalling pathway and initiates signal transduction. Signal transduction appears to be largely mediated through DVL and ultimately effected through β-catenin-mediated transcription. DVL also inhibits the large multiprotein β-catenin destruction

complex, that includes glycogen synthase kinase-3 beta (GSK3 β), adenomatous polyposis coli (APC), casein kinase 1 (CK1) and Axin, all of which act a repressor for β-catenin by targeting it for degradation (Avasthi et al., 2017). As a result, the active state of Wnt/β-catenin signalling triggers the stabilization and accumulation of cytoplasmic β-catenin, inhibition of β-catenin phosphorylation and activation of the transcriptional factors of Wnt target genes (MacDonald and He, 2012). When the pathway is inactive, cytoplasmic β-catenin is targeted through phosphorylation for proteasomal degradation (Goggolidou and Wilson, 2016) by two proteins, Axin and APC. They also facilitate the amino-terminal phosphorylation of β-catenin via the kinases Glycogen synthase kinase-3β (GSK3β) and casein kinase Iα (CKIα). Phosphorylated β-catenin is recognized by the E3 ubiquitin ligase β-Trcp and is ubiquitinated and degraded by the proteasome, resulting in low levels of free β-catenin in the cytoplasm and nucleus (MacDonald et al., 2009).

Surprising, de novo and heterozygous mutations in human Disheveled-1 (*DVL1*), a key component of the Wnt/PCP pathway, cause the rare developmental disorder autosomal dominant Robinow syndrome type 2 (MIM: 616331) (White et al., 2016) that affects the development of many parts of the body, particularly the skeleton (specifically, short-limbed dwarfism). However, it is seemingly unrelated to ciliopathies and maybe as a simple of different patterns of inheritance; perhaps it's the difference between gain-of-function mutations in RS2 and loss-of-function mutations as the predominant cause for recessive ciliopathies.
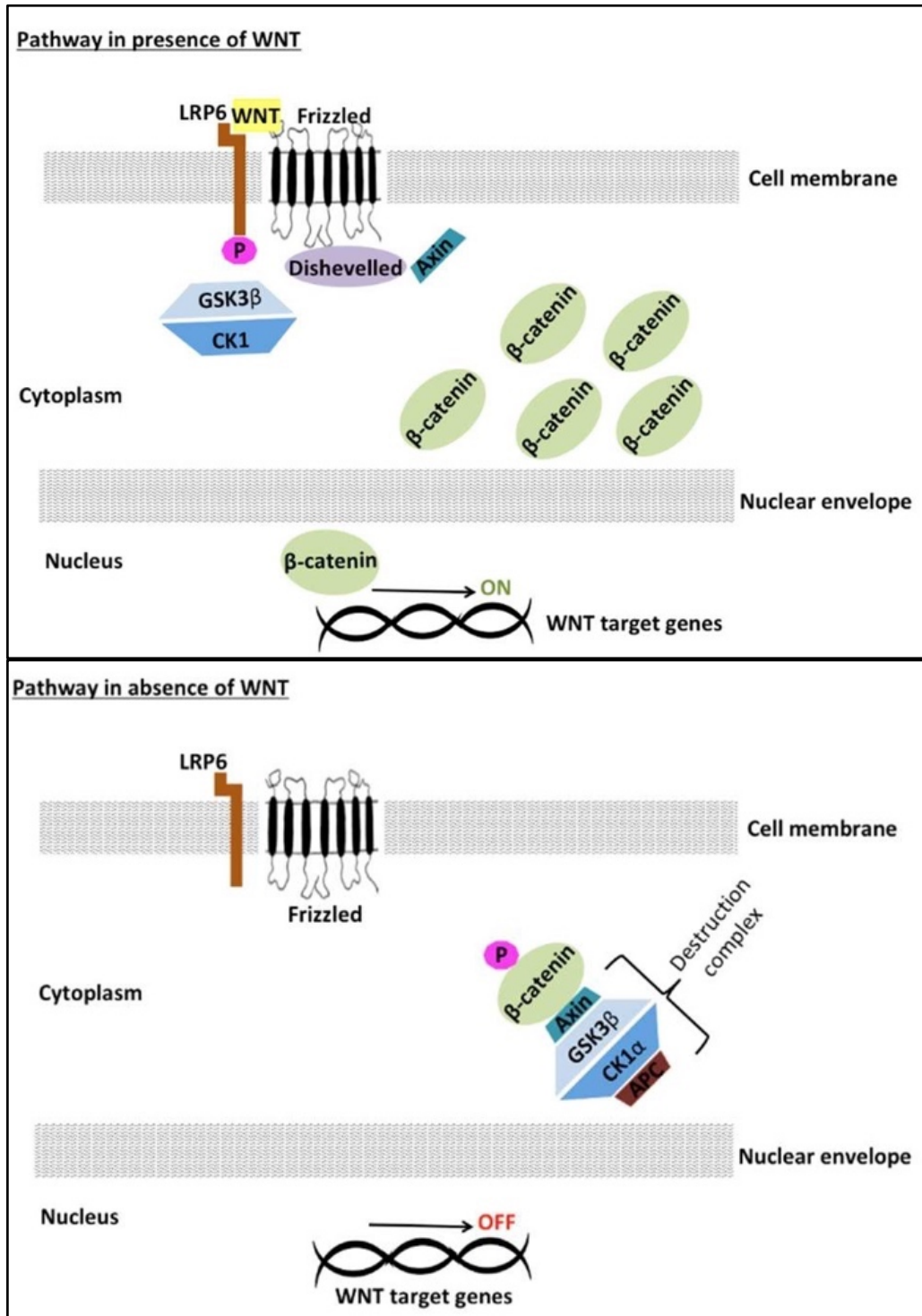
Figure 1. 6: Summary of the canonical Wnt signalling pathway. Wnt pathway activation: Wnt ligand binds to FZD which results in a signal to activate FZD and LRP: this causes CK1 and GSK3 to phosphorylate LRP. Dishevelled and Axin are recruited to LRP and FZD: β-catenin accumulates in the cytoplasm and moves into the nucleus enabling target genes to be expressed (top panel). Wnt pathway inactivation: β- catenin is bound by a destruction complex which result in its phosphorylation, targeting it for ubiquitination and degradation. As a result, it is not free to move into the nucleus (bottom panel).

1.5.2.2 Non-canonical Wnt signalling (Planar Cell Polarity/PCP)

Non-canonical Wnt signalling organizes cell movements and establishment of tissue polarity (Tanaka et al., 2011). The non-canonical or β-catenin-independent pathways are divided into the Wnt/planar cell polarity (PCP) and the Wnt/Ca^{2+} pathways, although both are less well understood than the canonical pathway. Several studies have proposed that normal ciliogenesis is essential for PCP signalling (Wheway et al., 2018, Gomez-Orte et al., 2013, Hua and Ferland, 2018) since ciliogenesis depends on cell polarity being correctly established during migration of the basal body to the apical cell surface to define apicobasal polarity (Jones et al., 2008). A recent study by Hua and Ferland (2018) hypothesized that polarity-driven pathways are not only necessary for the construction of a primary cilium but are also important for the assembly of other polarized cellular protrusions. Hua and Ferland (2018) suggested that ciliogenesis is a consequence of polarity, in which they considered cilia proteins as global regulators to establish polarity. They hypothesized that PCP signalling is essential for ciliogenesis, in which this signalling affects the assembly of a polarized cilium, further highlighting the potential links between polarity and ciliogenesis proteins.

PCP is also required for the directional beating of motile cilia which generates directional fluid flow in different tissues (Wallingford and Mitchell, 2011). *INVS* localizes to primary cilia of renal tubular cells and is important in regulating the process of mitotic cell division in this tissue. Disruption or loss of *INVS* and IFT88 was shown to cause defects in mitotic spindle orientation which result in incorrect orientation of cell division, consistent with defects in PCP. Studies also showed Vangl, a PCP protein, was disrupted in some animal models of PKD (Kunimoto et al., 2017, Saburi et al., 2008, Simons et al., 2005, Otto et al., 2003, Karner et al., 2009).

In addition, PCP proteins have been demonstrated to play a direct function in cilia with Vangl2, Fat4, and Fuzzy localizing to the cilia basal body (Papakrivopoulou et al., 2014, Ross et al., 2005, Saburi et al., 2008, Zilber et al., 2013). One principle function of the PCP pathway is the mediation and regulation of actin-dependent polarized cell behaviour such as ciliogenesis (Park et al., 2006) and morphogenic cell movements (Wallingford et al., 2000). DVL2 is required to control basal body docking (Wallingford and Mitchell, 2011), ciliogenesis and planar cell polarity (Park et al., 2008, Wallingford and Habas, 2005). In

addition, DVL plays a role in influencing both the planar orientation and assembly of motile cilia in multi-ciliated cells (Wallingford and Mitchell, 2011, Park et al., 2008, Mitchell et al., 2009, Hirota et al., 2010). DVL2 is only localized to the basal bodies of cilia, suggesting divergent functions (Vladar et al., 2012).

Wnt stimulates Wnt-Frizzled (FZD) signalling independent of LRP5/6, resulting in the activation of DVL. DVL and Disheveled-associated activator of morphogenesis 1 (DAAM1) mediate activation of RHO, which in turn activates RHO kinase (ROCK) and leads to cytoskeletal rearrangements through downstream phosphorylation of DVL (Sharma et al., 2018, Habas and He, 2007). DAAM1 also mediates actin polymerization through the actin binding protein profilin (Komiya and Habas, 2008). DVL mediates activation of RAC, which in turn activates JNK. These events regulate tissue polarity in *Drosophila* and gastrulation movements and cardiogenesis in vertebrates (Komiya and Habas, 2008). Less is understood about the Wnt/Ca^{2+} signalling pathway. One key difference with the other Wnt pathways is that Wnt ligand binding to the FZD receptor activates phospholipase C via G proteins, resulting in excessive intracellular Ca^{2+} levels and activation of downstream effectors such as protein kinase C (PKC). The Wnt/Ca^{2+} pathway appears to play an important role in development and is implicated in cancer (Kohn and Moon, 2005), but the molecular mechanisms that mediate and regulate this pathway remain unclear.

1.5.3 Similarities in SHH and Wnt signalling mechanisms at the cell surface

The SHH and the canonical Wnt signalling pathways both rely on serpentine receptors including SMO and Frizzled for pathway initiation. Both pathways also rely on the regulation of proteosome-dependent events including processing of GLI3 and regulation of β-catenin degradation (Eggenschwiler and Anderson, 2007). The Wnt and SHH ligands are unrelated classes of proteins, but both are lipid-modified, probably by the action of enzymes that are associated with each other (Nusse, 2003). In the absence of ligand, both pathways use the protein kinases GSK3 and CK1 to facilitate proteolysis of transcription factors such as β-catenin for Wnt and GLI for SHH (Nusse, 2003). In contrast, in the presence of ligand their signal prevents phosphorylation-dependent proteolysis of GLI or β-catenin and switches a DNA-binding protein from a transcriptional repressor to a transcriptional activator

(Kalderon, 2002). Selected examples of key proteins or receptors in SHH and Wnt signalling pathways are listed in Table 1.1.

Table 1. 1: List of key proteins or receptors in SHH and Wnt signalling pathways.

SHH components	Function and diseases associated
GLI	GLI proteins localize to cilia in vertebrate limb bud cells; these proteins are required to recruit SUFU to cilia
SUFU	A cytoplasmic protein suppressor of Fused and a major Hedgehog regulator in mammals; it inhibits GLI proteins by preventing their nuclear translocation.
SMO	Accumulates in the ciliary membrane when cells receive the Hedgehog signal and an essential positive mediator of the HH signal.
PTCH1	A tumour suppressor gene inhibits the activity of SMO Somatic mutations in the *PTCH1* gene are the main cause Gorlin syndrome and basal cell carcinomas (BCC).
Wnt components	**Function and diseases associated**
INVS	Mutated in NPHP type 2; required for normal renal development and establishment of left-right axis; acts as a molecular switch between canonical and non-canonical Wnt signalling pathways
DVL	Key effector molecule of the Wnt signalling pathway transduces signals into three separate branches, the canonical, non-canonical and Ca^{2+} pathways.
AHI1	Encodes jouberin; binds to b-catenin; deficiency in kidney tissue can impair Wnt and cause cystic kidney disease.
APC	Tumour suppressor gene; component of Wnt/β-catenin signalling; Mutations of the *APC* gene cause hereditary familial adenomatous polyposis (FAP) colorectal cancers.

1.5.4 Hippo signalling

Several studies have indicated that the actin cytoskeleton is involved in the regulation of ciliogenesis. YAP (Yes-associated protein) and its paralogue TAZ (transcriptional coactivator with PDZ-binding motif) are transcriptional coactivators of the Hippo pathway (Kim et al., 2015). Both are regulated by actin cytoskeleton architecture that in turn regulates ciliary vesicle trafficking and ciliogenesis (Kim et al. 2015). Mechano-transduction by YAP/TAZ can independently function without the Hippo pathway but it requires Rho GTPase and actin cytoskeletal tension; Rho GTPases regulate the actin cytoskeleton and promote cell proliferation (Jaffe and Hall, 2005).

Habbig et al. (2011) demonstrated that the cilia-associated protein, NPHP4 negatively regulates the Hippo pathway and promoted nuclear targeting of TAZ. More recent work has shown that the mammalian Ste20-like 1 and 2 (MST1/2) in mammals, a Hippo signalling mediator kinase, co-localized to the base of cilia and was required for ciliogenesis. MST1/2 is required for phosphorylation of AURKA to prevent it from complexing with HDAC6 to disassemble cilia, as described previously (see section 1.4.1). NPHP ciliary proteins bound MST1/2 at the basal body and promoted ciliogenesis by targeting ciliary cargoes into IFT for transport into the cilium(Wheway et al., 2018, Kim et al., 2014).

1.5.5 Notch Signalling

Notch signalling is initiated when Notch receptors bind to their membrane-bound ligands (for example, Jagged and Delta-like) which induce cleavage and release of the Notch intracellular domain (NICD). This is the intracellular part of the receptor that translocates to the nucleus to regulate gene transcription (High and Epstein, 2008). Cilia appear to mediate Notch signalling by regulating cell differentiation and proliferation, for example during skin development (Ezratty et al., 2011), although the mechanistic details remain unclear. Notch signalling components associate with ciliated areas of the heart during development and defective Notch signalling leads to cardiac phenotypes reminiscent of cilia-related phenotype (High and Epstein, 2008). Notch signalling may also be involved in the establishment of the left-right axis which is evolutionary conserved among vertebrates. In the murine embryonic node and the zebrafish embryo, Notch signalling activates nodal expression as an essential step during left-right patterning (Krebs et al., 2003). Furthermore, Lopes et al. (2010) demonstrated that decreased Notch signalling resulted in shorter cilia whilst hyperactivation resulted in longer cilia. As a result, short cilia generated a weaker fluid flow inside the embryonic node/Kupffer's vesicle as well as ultimately in left-right defects, indicating that proper cilia length regulation is crucial for the establishment of left-right asymmetries.

1.6 Ciliopathies: clinical aspects and molecular mechanisms

Ciliopathies refer to a group of developmental disorders that are characterized by multi-organ system disorders, resulting in very significant morbidity and mortality for many patients, particularly in the perinatal and paediatric age ranges. These result from defects in cilia structure and function, caused by a variety of different inherited mutations that occur in more than 150 different genes (Wheway et al., 2019). In addition, autosomal dominant polycystic kidney disease (ADPKD) is considered to be an adult-onset ciliopathy. The aetiology of this class of genetic conditions is caused by defects in the structure or function of the primary cilium, and it is strongly associated with defects in ciliary signal- transduction proteins and pathways (Reiter and Leroux, 2017) or with defects in the formation of the cilium (Shaheen et al., 2013a), particularly those forming the ciliary transition zone. Ciliopathies show a very wide range of clinical phenotypes and but also have considerable phenotypic overlap (Ke and Yang, 2014), although cystic kidney disease appears to be an invariable clinical feature of many of these conditions (Tables 1.2 and 1.3). These conditions range from relatively mild, organ-specific conditions such as retinitis pigmentosa and other inherited retinal conditions, to perinatal-lethal disorders such as Meckel- Gruber syndrome that involve defects in multiple organs including the brain (see details in Figure 1.7).

Defects of primary cilia and their related proteins cause the dysregulation of cell proliferation and embryonic development that lead to phenotypes that include Bardet-Biedl Syndrome (BBS), Senior-Løken Syndrome (SNLS), Alström Syndrome (ALMS), Oral-Facial-Digital Syndrome Type I (OFD I), Jeune Syndrome (also known as asphyxiating thoracic dystrophy; JATD), EIIis-Van Creveld Syndrome (EVC), LCA (Tobin and Beales, 2009), polycystic kidney disease (PKD) (Nonaka et al., 1998), randomization of left-right asymmetry leading to heterotaxy and congenital heart defects (Eley et al., 2005), nephronophthisis (NPHP) (Sang et al., 2011), sensorineural deafness (Eley et al., 2005), Joubert syndrome (JBTS) (Gerdes et al., 2009) and Meckel-Gruber syndrome (MKS) (Sang et al., 2011).

Figure 1. 7: Scale of the severity of primary ciliopathies. Distribution of known ciliopathy disorders across a spectrum of severity based on the major organ(s) involved, from relatively mild to lethal. For example, BBS is among the mildest ciliopathies (see section 1.6.1.4). Joubert syndrome is a moderately severe disease amongst the range of ciliopathies (Rachel et al., 2012)(see section 1.6.1.2) while the lethal ciliopathy, MKS comes at the end of this spectrum (see section 1.6.1.1). Image adapted from (Mitchison and Valente, 2017).

Since there are hundreds of ciliary proteins, defining the clinical overlap of phenotypes between the many ciliopathies remains a significant challenge while mutations in many of the same genes are responsible for the phenotypic overlap in the ciliopathies. This refers to pleiotropic ciliopathy conditions for which mutations in individual genes can be associated with ciliopathies with dramatically different phenotypes. For instance, mutations in the ciliary protein *CEP290* affect many tissues resulting in a very wide range of phenotypes that include neurodevelopmental phenotypes (as part of Joubert syndrome), renal cystic dysplasia and renal failure, obesity, polydactyly or retinitis pigmentosa.

Tables 1.2 and 1.3 show examples of phenotypic overlaps between the ciliopathies caused by mutations in many ciliary genes (Gerdes et al., 2009). For example, significant genetic overlap is noted between MKS and JBTS (Waters and Beales, 2011)(Table 1.2 and 1.3) and the pleiotropic autosomal recessive ciliopathy Bardet-Biedl Syndrome type 14 (BBS14) showed significant phenotypic and molecular overlap with other ciliopathies (Leitch et al., 2008). This last study described phenotypic overlap between BBS and MKS which showed that mutation in MKS-related genes (including *CEP290*, *TMEM67* and *MKS1*) were also a rare cause of BBS. The most significant example of pleiotropy in the ciliopathies is the identification of more than 80 mutations in the *TMEM67* gene associated not only with MKS but also with a specific sub-type of JBTS, cerebellar vermis hypoplasia-oligophrenia-congenital ataxia-coloboma-hepatic fibrosis (COACH) syndrome (see section 1.6.3.1) involving liver fibrosis in which missense mutations predominate (Novarino et al., 2011, Brancati et al., 2009, Iannicelli et al., 2010). The question remains; how could mutations in

individual genes produce such pleiotropic phenotypic effects in patients? The reasons for the overlap in phenotypes remain unclear but it may be that all these conditions represent a spectrum of the same underlying disorder, due to a congenital dysfunction of embryonic signalling, overlaid by tissue-specific differences, and the effect of modifier alleles. To illustrate, given the complexity of ciliopathy phenotypes, Louie et al. (2010) anticipated the role of modifiers in phenotypic expressivity of ciliopathies. This is the action of pleiotropy-modifier genes that cause individuals that are discordant for a modifier allele to show a range of phenotypes. Their data suggested the involvement of a hypomorphic mutation in *AHI1* as a modifier of retinal degeneration in the context of causative mutations leading to NPHP.

A previous report Leitch et al. (2008) hypothesized that MKS might represent a more severe variant of BBS. Mutation of *MKS1* (MIM: 609883) was associated with a novel phenotype; seizures in BBS-affected subjects with mutations in *BBS1* (MIM:209901), *BBS9* (MIM:607968), or *BBS10* (MIM:610148), which indicated that the *MKS* gene was modifying the effect of mutations in the *BBS* genes and might represent a more severe variant of BBS. A similar effect was presented by Zaki et al. (2011), who reported significant clinical variability among siblings who carry the same genetic mutations in two consanguineous Egyptian families, each with non-overlapping ciliopathy spectrum disorders; family number 1 had one child affected by NPHP and polydactyly but not the Molar Tooth Sign (MTS), while another affected child displayed only the MTS of JBTS but not NPHP. In a second branch of this family two other children were affected by NPHP but not the MTS. Family number 2 had one child who displayed typical features of BBS but not the MTS, while the other two children presented the MTS without typical features of BBS. These families underline the degree of phenotypic variability that can be seen within the ciliopathy spectrum, suggesting genetic modifiers as a possible explanation for these differences.

NPHP has less severe involvement of organ systems, principally the kidney and retina (Hildebrandt and Zhou, 2007), causing end stage renal failure in the paediatric or juvenile age ranges, and is therefore has a milder phenotype than BBS or MKS. JBTS, MKS, and NPHP have a high degree of genetic and phenotypic overlap depending on allelic effects, genetic background and genetic complexity due to extreme genetic heterogeneity (Leightner et al.,

2013). In addition, BBS has more multi-organ involvement, which makes it an informative phenotype to study the effect of ciliary dysfunction in many different organ systems (Tobin and Beales, 2009), but without the significant early embryonic lethality in MKS or severe structural neurodevelopmental defects in JBTS. Both MKS and JBTS are the most severe types of ciliopathies (Figure 1.7): MKS invariably causes intrauterine or neonatal death shortly after birth (Tobin and Beales, 2009, Hildebrandt and Zhou, 2007). However, the variability of the MKS phenotypes may also display the possible effect of strong modifier alleles. For example, in one MKS family, five affected foetuses had a broad variability of central nervous system involvement ranging from severe enchephalocele to completely normal despite the fact that all five fetuses had biallelic pathogenic *TMEM67* mutations (Ben-Salem et al., 2014, Smith et al., 2006). This variability indicates that other genetic variants could modify or influence the phenotype caused by pathogenic mutations in the causative ciliopathy gene (Ware et al., 2011, Consugar et al., 2007).

Previous studies by (Williams et al., 2011, Jensen et al., 2015, Yee et al., 2015) signified some components of different complexes, including the transition zone and BBS have overlapping functions in ciliogenesis in *C. elegans* and mice model organisms; these observations imply that the type of alleles, the modifiers that present in different genetic backgrounds, overlapping protein functions, and cell -type specificity can all influence the phenotypic outcome which such genetic complexities may underline human ciliopathies (Reiter and Leroux, 2017).

Given the examples above, understanding the disease mechanism of ciliopathies requires insights into ciliary interaction networks (van Reeuwijk et al., 2011) and the structure-function relationships between ciliary proteins. Although the majority of genes that are mutated as causes of ciliopathies appear to have been identified (Tables 1.2 and 1.3), surprisingly little is known about the structure of ciliary proteins and their organization within ciliary compartments. Therefore, the biggest challenge to the ciliary biology field is to understand the intricate organization and ultrastructure that underlies the functional complexity of ciliary-related processes.

Table 1. 2: Common clinical features of the ciliopathies and phenotypic overlap in the ciliopathies, modified from (Waters and Beales, 2011).

Phenotype	MKS	JBTS	NPHP	BBS	LCA	SLS
Cerebellar		✓	✓	✓		
Obesity		✓		✓		
Polydactyly	✓	✓	✓			
Renal disease	✓	✓	✓	✓		✓
Situs inversus	✓	✓	✓	✓		✓
Retinopathy		✓	✓	✓	✓	✓
Hepatic disease	✓		✓	✓		✓

Table 1. 3: Genetic pleiotropy and phenotypic overlap in a range of ciliopathies, modified from (Waters and Beales, 2011, Rachel et al., 2012).

Phenotype	MKS	JBTS	NPHP	BBS	LCA	SLS	OFD	COACH
CEP290	✓	✓	✓	✓	✓	✓		
RPGRIP1L	✓	✓	✓		✓			✓
TMEM67	✓	✓	✓	✓				✓
TMEM216	✓	✓					✓	
BBS (2,4,6)	✓			✓				
MKS1	✓			✓				
NPHP (1,4,5)			✓			✓		
NPHP3	✓		✓			✓		
CC2D2A	✓	✓						✓

1.6.1 Ciliopathy phenotype and mechanisms of disease

1.6.1.1 Meckel–Gruber Syndrome (MKS)

Meckel–Gruber Syndrome (MKS) (MIM:249000) is a rare autosomal recessive disorder, first described in 1822 by Johann Meckel. MKS is a genetically heterogeneous severe ciliopathy with a wide variety of overlapping phenotypic features with JBTS and other ciliopathies. It is an important systemic malformation syndrome leading to death of the fetus *in utero* or shortly after birth (Paavola et al., 1995) and it is the most severe ciliopathy (Leightner et al., 2013) (Figure 1.7). MKS is characterized by developmental defects of the central nervous system including occipital encephalocele, bilateral renal cystic dysplasia, hepatic ductal proliferation, fibrosis and cysts, and polydactyly (Smith et al., 2006)

(see details in Figure 1.8). MKS is considered to be the most frequent syndromic cause of neural tube defects (Simpson et al., 1991).

The most common clinical features of MKS comprise a triad that consist of occipital encephalocele, post-axial polydactyly, and bilateral enlarged multicystic kidneys. These clinical features are useful for ultrasound diagnosis before the 14th gestational week. The genetic heterogeneity of MKS has been established by the description, to date, of mutations in at least 13 MKS disease genes. These genes include *MKS1*, *TMEM216* (as a cause of MKS type 2), *TMEM67 (MKS3), CEP290 (MKS4), (RPGRIP1L), (MKS5), CC2D2A (MKS6), NPHP3 (MKS7), Tectonic2 (TCTN2) (MKS8), B9D1 (MKS9), B9D2 (MKS10), TMEM237, C5orf42 and TMEM231 (MKS11)* (Shaheen et al., 2013a) (Table 1.4). Worldwide, the occurrence of this disorder is 1 per 13,250-140,000 live births (Kheir et al., 2012), but can be higher in specific ethnic groups with higher rates of consanguinity or endogamy. Szymanska et al. (2012) estimated that the frequency of MKS was as high as 1 in 3000 in consanguineous Pakistani families, caused by extensive genetic heterogeneity and allelism. For example, 3 different causal homozygous founder mutations in *CEP290* were identified in the same ethic group. The incidence of MKS in the Finnish population, which has high levels of endogamy, has been estimated to be 1 in 9000 births (Barisic et al., 2015) and appears to be caused by founder mutations in *MKS1* (the "Finn major" mutation) and CC2D2A (*MKS6*) (Tallila et al., 2008, Kyttala et al., 2006) (Table 1.4).
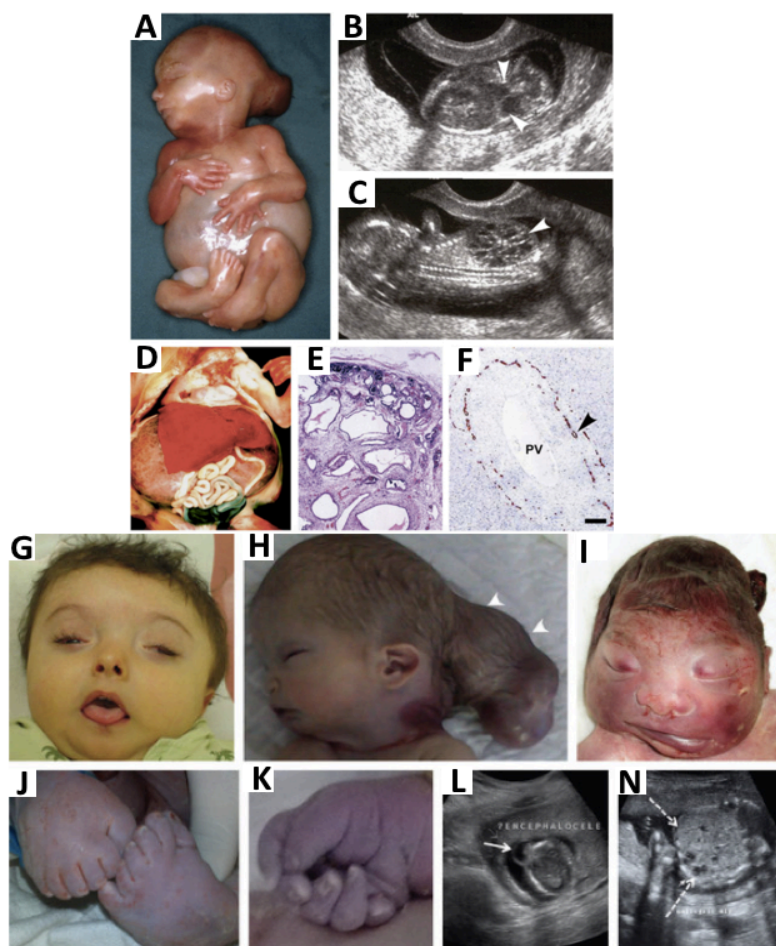
Figure 1. 8: Clinical features of Meckel–Gruber syndrome (MKS). (A) Typical external features for a fetus with MKS at gestation age 16/40, showing typical clinical features comprising occipital encephalocele, massive flank masses due to bilateral renal cystic dysplasia, postaxial hexadactyly of all limbs, and a typical Potter's sequence facies with a slanting forehead and flattened nose. **(B, C)** Ultrasound findings at 14+/40 weeks of gestation for MKS showing **(B)** encephalocele (arrowheads), and **(C)** large cystic kidneys (arrowhead). **(D)** Massive swelling of the abdomen of a fetus at gestation age 18+/40 with MKS due to grossly enlarged, cystic kidneys. **(E)** Hematoxylin-eosin staining of MKS fetal kidney at gestation age 18+/40 showing cystic dysplasia, comprising large, fluid- filled cysts, small cysts, and cystic swelling of the proximal tubules and glomeruli, with the absence of normal renal parenchyma. **(F)** Immunohistochemical staining of MKS fetal liver at gestation age 18+/40 for cytokeratin-19, showing the retention of embryonic bile duct structures (the ductal plate malformation) without the formation of patent bile ducts (arrowhead). PV, hepatic portal vein. Images **(A-F)** adapted from (Hartill et al., 2017) with the kind permission of Dr. Riitta Salonen (Rinnekoti Foundation, Helsinki, Finland) from the Robert J. Gorlin Slide Collection. JBTS, Joubert syndrome. **(G- I)** Facial features of some MKS patients MKS_F1, F2, and F8, respectively, showing: microcephaly, sloping forehead, hypertelorism, micrognathia, potter-like facies, and severe occipital encephalocele (black arrows). **(J, K)** Representative hand and foot images showing postaxial polydactyly in MKS_F2. **(L, N)** Antenatal ultrasound for MKS_F12 patient showed encephalocele (white arrow) and enlarged polycystic kidney (dashes arrows) **(G-N)** adapted from (Shaheen et al., 2013b).

Table 1. 4: List of gene mutated in human MKS.

Locus	Gene	Aliases	Founder mutation	Reference
MKS1	*MKS1*	MKS, BBS13, JBTS28	Finnish c.1408-35_1408-7del29	(Kyttala et al., 2006)
MKS2	*TMEM216*	JBTS2, CORS2	Ashkenazi c.218G>T (p.R73L)	(Valente et al., 2010)
MKS3	*TMEM67*	JBTS6, NPHP11, Meckelin, MKS3, TMEM67	Pakistani c.1575+1G>A	(Smith et al., 2006)
MKS4	*CEP290*	KIAA0373, 3H11AG, JBTS5, SLSN6, LCA10, BBS14, NPHP6, MKS4		(Baala et al., 2007)
MKS5	*RPGRIP1L*	KIAA1005, JBTS7, CORS3, FTM, NPHP8, MKS5	European c.1843A>C (p.T625P)	(Delous et al., 2007)
MKS6	*CC2D2A*	KIAA1345, JBTS9, MKS6	Finnish c.1762C>T	(Tallila et al. 2008)
MKS7	*NPHP3*	SLSN3, NPHP3, NPH3, RHPD1, MKS7		(Bergmann et al. 2008)
MKS8	*TCTN2*	C12orf38, TECT2, JBTS24, MKS8		(Shaheen et al. 2011)
MKS9	*B9D1*	MKSR1, JBTS27, MKS9		(Hopp et al. 2011)
MKS10	*B9D2*	MKSR2, MKS10		(Dowdle et al. 2011)
MKS11	*TMEM231*	JBTS20, MKS11		(Shaheen et al. 2013)
MKS12	*KIF14*	KIAA0042		(Filges et al. 2014)
MKS13	*TMEM107*	JBTS29, PRO1268		(Shaheen et al., 2015)

1.6.1.2 Joubert syndrome (JBTS)

JBTS is a rare, recessive ciliopathy with overlapping phenotypic features, first identified in 1969 by Marie Joubert (MIM: 213300) (Joubert et al., 1968). The incidence of this condition is estimated to be 1:100.000 (Parisi, 2009). It is characterized by a distinctive brain malformation, known as the "molar tooth sign" (MTS) visible on brain magnetic resonance imaging, and variable multi- organ involvement (Parisi et al., 2007). The common syndromic features in many patients are retinal dystrophy, renal defects, cystic dysplastic kidneys, and congenital hepatic fibrosis (Romani et al., 2013) (see details in Figure 1.9). Mutations in at least 27 causative genes for JBTS have been recognized and reported to the present date (see Table 1.5). For instance, *AHI1* (Abelson helper integration-1), encoding the protein jouberin, is the most frequently mutated gene in 10-15% of cases of autosomal recessive JBTS (Wolf et al., 2007). Jouberin is localized to basal bodies and cell-cell junctions (Tuz et al., 2013) and is essential for cerebellar and cortical development in humans since *AHI1* mutations cause both abnormal cerebellar development and axonal decussation

(Ferland et al., 2004). It is notable that there is a significant genetic overlap between JBTS and MKS, since mutations in at least 12 genes seem to cause either JBTS or MKS (Slaats et al., 2016). Tables 1.2 and 1.3 summarize the ciliary genes that have been identified to have causal mutations for MKS and JBTS, as well as those that display genetic pleiotropy between the two conditions.
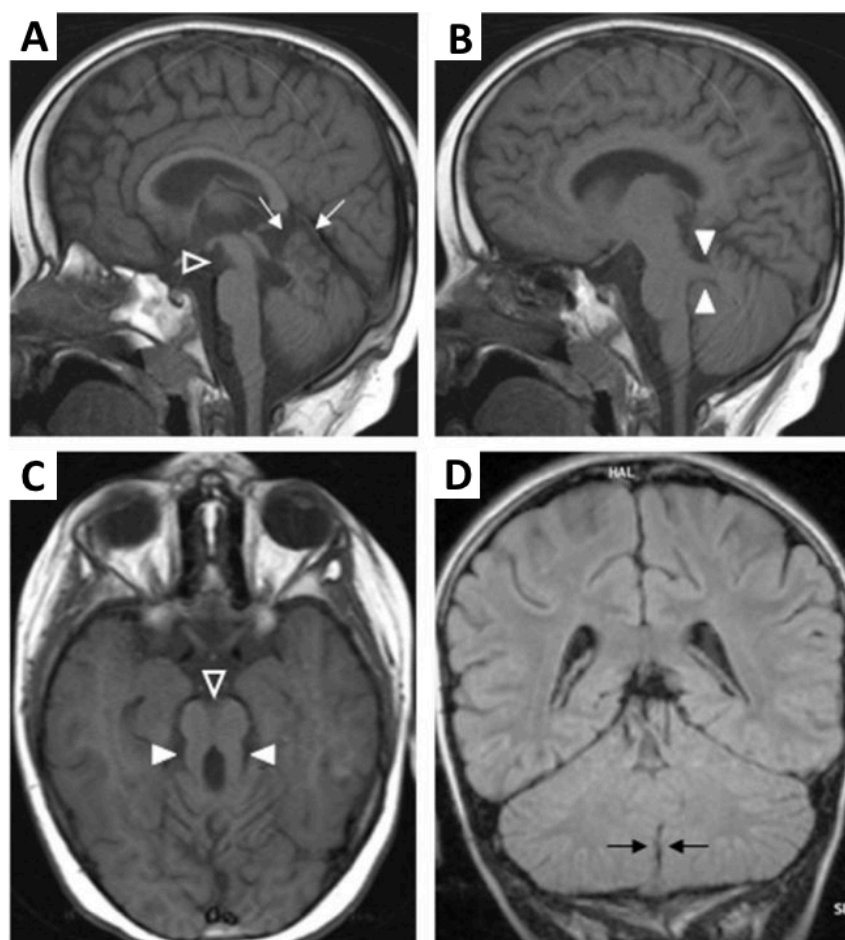
Figure 1. 9: Clinical features of Joubert syndrome (JBTS). Brain MRI sections in patients with JSRD. **(A)** mid-sagittal T1-weighted image shows a thin midbrain with corresponding enlargement of the interpeduncular fossa (open arrowhead). There is concurrent superior vermian dysplasia (thin arrows); **(B)** parasagittal T1-weighted image shows thickened and maloriented superior cerebellar peduncle (thick arrowheads); **(C)** axial T1-weighted image confirms the deepened interpeduncular fossa (open arrowhead) and abnormal superior cerebellar peduncles (thick arrowheads), comprising the "molar tooth sign"; **(D)** coronal FLAIR image shows midline cerebellar cleft (black arrows) indicating agenesis of the inferior vermis. Images **(A-D)** adapted from (Brancati et al., 2010).

Table 1. 5: List of selected genes mutated in human JBTS and MKS.

Locus	Gene	Aliases	Founder mutation	Reference
JBTS1	*AHI1*			
JBTS2	*TMEM216*	HSPC244	Ashkenazi p.R73L	(Valente et al., 2010)
JBTS4	*NPHP1*	*JBTS4, NPH1, SLSN1*		(Parisi et al., 2004)
JBTS5	*CEP290*	3H11Ag, JBTS5, LCA10, BBS14, NPHP6, CT87, MKS4, POC3, SLSN6, rd16		(Sayer et al., 2006)
JBTS6	*TMEM67*	JBTS6, MECKELIN, MKS3, NPHP11, TMEM67		(Baala et al., 2007)
JBTS7	*RPGRIP1L*	JBTS7, CORS3, FTM, NPHP8, MKS5		(Delous et al., 2007)
JBTS8	*ARL13B*	ARL2L1, JBTS8		(Cantagrel et al., 2008)
JBTS9	*CC2D2A*	Mks6, JBTS9		(Noor et al., 2008)
JBTS14	*TMEM237*	ALS2CR4, JBT14		(Huang et al., 2011)
JBTS16	*TMEM138*	HSPC196		(Lee et al., 2012)
JBTS20	*TMEM231*	UNQ870/PRO1886, ALYE870, JBTS20, MKS11, PRO1886		(Srour et al., 2012)
JBTS21	*CSPP1*	CSPP, JBTS21		(Tuz et al., 2014)

1.6.1.3 Nephronophthisis

NPHP (MIM: 256100) is an autosomal recessive cystic kidney disease first described by Smith and Graham in 1945. It is the most frequent genetic cause of end-stage renal disease (ESRD) in children and young adults (O'Dea et al., 1996, Waters and Beales, 2011). Previous studies have identified mutations in over 20 genes that are associated with this ciliopathy, although there is considerable genetic pleiotropy and phenotypic overlap with other ciliopathies. NPHP is primarily a kidney disease, but it can be associated with retinitis pigmentosa (SLS) and cerebellar vermis aplasia (JBTS) in approximately 15% of patients (Hildebrandt and Zhou, 2007). Mutations in NPHP genes have also been found in patients with MKS (Fleming et al., 2017) and an association with hepatic fibrosis in NPHP type 11 is consistently observed with *TMEM67* mutations (Otto et al., 2009), more usually a cause of MKS. Consistent with this genetic finding, mutations in this the NPHP group of genes are proposed to cause defects in the non-canonical Wnt and SHH signalling pathways (Hildebrandt et al., 2009).

1.6.1.4 Bardet-BiedI syndrome (BBS)

BBS (MIM: 209900) is an autosomal recessive rare, heterogeneous disorder that affects many parts of the body. Its prevalence in Europe and North America is estimated to be below 1 in 100,000 (Forsythe and Beales, 2013). BBS is among the mildest ciliopathies (see Figure 1.7), and the major features of this syndrome are loss of vision, obesity (with hypogonadism in males), developmental delay (intellectual impairment) and post-axial polydactyly, and genital and renal malformations (Mitchison and Valente, 2017, Khan et al., 2016). Mutations in 21 genes have been recognized as causal for BBS, although there is considerable phenotypic overlap and genetic pleiotropy with other ciliopathies such as NPHP and MKS (Suspitsin and Imyanitov, 2016, Redin et al., 2012). Mutations in the majority of BBS genes lead to problems in the structure and function of cilia or ciliary-related signalling processes. Ten BBS proteins (BBS1, 2, 4, 5, 6, 7, 8, 9, 17 and 18) appear to contribute to the formation of a multiprotein complex called the BBSome. The BBSome has been proposed to work as an adapter for IFT complexes that cross the transition zone barrier to transport ciliary proteins between the ciliary membrane and the plasma membrane (Nachury et al., 2007). A second complex of additional BBS proteins, containing BBS6, BBS10 and BBS12, forms a possible chaperonin complex that is assumed to mediate BBSome assembly (Seo et al., 2010).

1.6.2 Primary cilia and oncogenesis

Recent work connected dysfunction of primary cilia with tumour formation. These studies have been shown that primary cilia could play a critical role in tumorigenesis and tumour progression by acting as a "tumour suppressor organelle". For example, the incidence of primary cilia was reduced in cholangiocarcinoma (CCA) *in vivo* as well as *in vitro* (Gradilone et al., 2013) and the molecular mechanisms and significance of this effect remain to be elucidated (Gradilone et al., 2017). However, some insights have recently emerged which have shown that ciliary number was decreased in ovarian cancer cells, in a mechanism linking ciliogenesis with over-expression of Aurora A kinase (AURKA), a protein implicated in cilia assembly (see section 1.4.1) (Gradilone et al., 2017, Egeberg et al., 2012). In addition, the ciliary-associated gene, von Hippel Lindau (VHL) is a tumour suppressor, dysregulated in VHL disease and clear cell renal carcinoma (Arjumand and Sultana, 2012).

Furthermore, Esteban et al. (2006) suggested that VHL regulates ciliogenesis in the renal epithelium and is involved in microtubule stabilization and subsequent cilia maintenance. Thoma et al.(2010) suggested that VHL is involved in the regulation of microtubule dynamics and confirmed the previous suggestion that VHL interacts with the ciliary motor kinesin-2 (Mans et al., 2008, Lolkema et al., 2007) as well as potentially being implicated in maintenance of the primary cilium. In support of this observation, human renal cell carcinomas (RCC) tumours lacking functional VHL displayed reduced ciliary frequency compared with matched, normal tissues (Basten et al., 2013). The molecular mechanism that explains these observations has been suggested to be control of microtubule growth by VHL during ciliogenesis (Schermer et al., 2006). In this study, VHL was shown to be essential for the oriented growth of microtubules toward the cell periphery, a prerequisite for the formation of cilia. VHL interacts with the kinase that phosphorylates components of a cell polarity complex (Par3, Par6, and atypical protein kinase C aPKC), implying that VHL links the polarity complex proteins to microtubule capture and ciliogenesis.

1.6.3 Ciliopathy proteins and functions: Ciliopathy-associated genes encoding ciliary transition zone transmembrane proteins

A number of protein complexes that include MKS, JBTS, and NPHP proteins have been defined by biochemical or genetic means, but the ultrastructure that underlies this functional complexity is unknown. Three studies (Chih et al., 2011, Garcia-Gonzalo et al., 2011, Sang et al., 2011) suggested 3 core ciliopathy-associated multiprotein modules within the transition zone, including MKS, NPHP and JBTS, each of which are composed of proteins that are involved in ciliary assembly and the selective permeability of the "ciliary gate" in the transition zone. However, the organization of these proteins within this ciliary compartment remains to be determined. In particular, the complexes have been suggested to regulate ciliary membrane protein composition (Garcia-Gonzalo et al., 2011, Garcia-Gonzalo and Reiter, 2012), with each of the 3 modules mediating protein translocation event during SHH signalling (Sang et al., 2011). The following section describes the functions of selected examples of proteins that are components of the MKS, JBTS and NPHP functional modules and Figure 1.10 shows 2 examples of important ciliary transmembrane proteins.
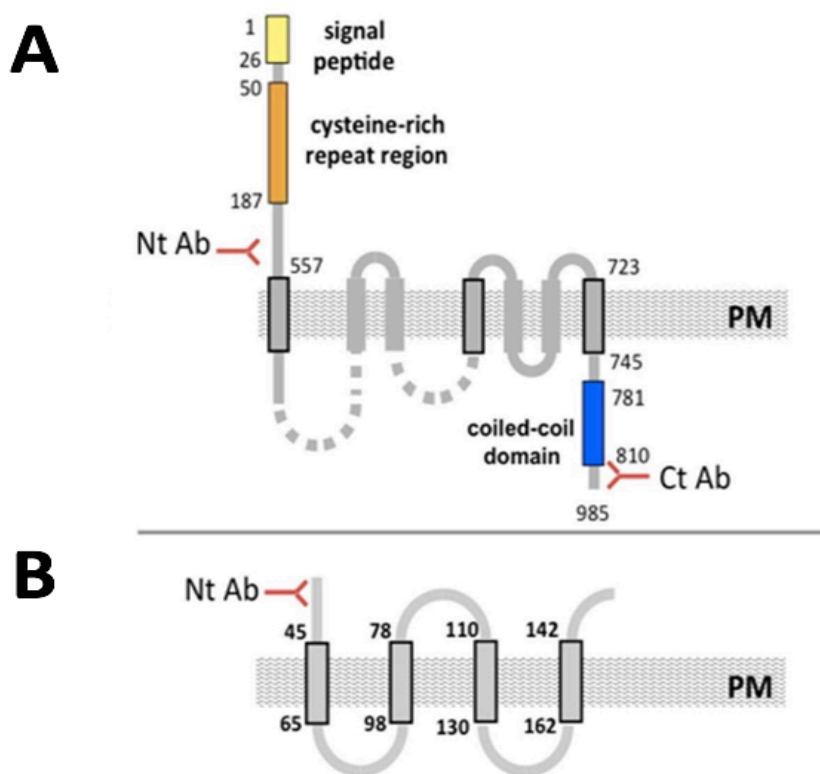
Figure 1. 10: Domain structure of transition zone components: TMEM67 and TMEM17. Numbering indicates the amino-acid residue. **(A)** Reference TMEM67 sequence is NCBI accession number NP_714915.3. Schematic diagrams of conserved domains and structural motifs within TMEM67: TMEM67 N-terminus includes a signal peptide (outlined rectangle yellow) in the extracellular loops, conserved cysteine residues (outlined rectangle orange), and coiled-coil domain (outlined rectangle blue) in the C-terminus. Strongly predicted transmembrane alpha-helices are shown as grey rectangles with black outlines; weakly predicted ones are shown in grey only. Plasma membrane (PM): Regions of β-sheet periodicity (grey), seven predicted transmembrane helices (grey). **(B)** TMEM17 sequence is NCBI accession number NP_498542.2 and the predicted transmembrane helices are shown as grey rectangles with black outlines. Red symbols show epitopes of antibodies (Ab) used in this research thesis.

1.6.3.1 TMEM67

Transmembrane protein 67 (*TMEM67*, MIM: 609884) mutations are the most frequent cause of MKS, and mutations in this gene cause 16% of all MKS cases (Iannicelli et al., 2010). The Frizzled-like orphan receptor TMEM67 is a 995 amino-acid transmembrane protein with structural similarity to Frizzled receptors (Smith et al., 2006) (Figure 1.10; Table 1.6). In both mouse and human kidney cell-lines, *TMEM67* (also known as meckelin) localized at the base of the primary cilium (Smith et al, 2006). Subsequent studies implicated *TMEM67* as a component in a complex containing *TCTN1*, *TCTN3* and six MKS proteins

(MKS1, TMEM216, CEP290, CC2D2A, B9D1 and TCTN2) (Garcia-Gonzalo et al., 2011). This complex localized to the ciliary transition zone and regulated ciliogenesis and ciliary membrane composition in a tissue-dependent manner, suggesting that TMEM67 is a membrane ciliary protein that contributes to selective permeability at the ciliary transition zone (Leightner et al., 2013). In addition, as part of determining the MKS complex of proteins at the transition zone, *TMEM67* is essential for other components such as *MKS1*. Protein-protein interaction studies show that MKS1 interacts with *TMEM67* and both are required for mother centriole migration to the apical membrane and the subsequent formation of the primary cilia (Dawe et al., 2007). In addition, mutations in *TMEM67* cause the related ciliopathies JBTS (Baala et al., 2007), COACH syndrome (Joubert syndrome with congenital hepatic fibrosis) (see section 1.6), BBS syndrome (Leitch et al., 2008) and NPHP (Otto et al., 2009). *TMEM67* has similar protein domains to the frizzled group of transmembrane receptors that are involved in Wnt and PCP signalling (Tobin and Beales, 2009) (see section 1.5.2). *TMEM67* has 7 predicted transmembrane domains and an N-terminal extracellular cysteine-rich region, possibly an ectodomain, as well as a highly conserved intracellular coiled-domain at the C-terminus (Smith et al., 2006).

The suggested role of *TMEM67* in the PCP pathway was derived from zebrafish embryo "morphant" phenotypes following morpholino oligonucleotide (MO) knockdown of *mks3* (the zebrafish orthologue of human T*MEM67*). The morphant phenotypes included defects in gastrulation movements that included a shortened body axis, broad notochords and misshapen somites that are suggestive of defects in the PCP pathway (Leitch et al., 2008, Badano et al., 2006). *TMEM67* may also have a role in the basal-body/centrosome compartment since it appears to have a significant role in controlling primary ciliary length and number through modulating centrosome duplication (Tammachote et al., 2009). For instance, mutations in *Tmem67* lead to cilium elongation in renal collecting duct cells and PKD in the rat *wpk* model (Tammachote et al., 2009) but loss of cilia in other tissues, indicating that *TMEM67* mediates tissue-specific ciliogenesis.

1.6.3.2 TMEM216

Transmembrane protein 216 (*TMEM216*, MIM: 613277) encodes a tetraspanin-like transmembrane protein, characterized by 4 predicted transmembrane domains. *TMEM216*

localizes to the base of primary cilia, most likely at the transition zone (Hartill et al., 2017)(Table 1.6). Knockdown or loss of this gene in mutant fibroblasts resulted in defects in ciliogenesis and docking of the centrosome to the apical cell surface in polarized cells (Lee et al., 2012, Valente et al., 2010) suggesting that *TMEM216* is required for centrosome/basal body docking to initiate ciliogenesis at the transition zone (Garcia-Gonzalo et al., 2011, Szymanska and Johnson, 2012). *TMEM216* appears to be part of the MKS complex that mediates the link between the transition zone and the ciliary membrane (Kim et al., 2018). Mutations in *TMEM216* cause pleiotropy between both JBTS (JBTS type 2) and MKS (MKS type 2) (Edvardson et al., 2010, Valente et al., 2010), as well as an intermediate phenotype known as "cerebello-oculorenal syndrome 2" (CORS2). CORS2 was the original locus name but that the associated phenotype is better described as COACH.

1.6.3.3 TMEM231

Transmembrane protein 231 (*TMEM231*, MIM: 614949) is a pleiotropic ciliopathy gene for which mutations cause variable phenotypic consequences. Shaheen et al. (2013a), first identified a splicing mutation in *TMEM231* in 2 consanguineous families with phenotypes ranging between JBTS and MKS syndromes. Affected children had the typical constellation of JBTS features that included oculomotor apraxia, molar tooth sign on brain MRI, breathing abnormalities and developmental delay. Other affected individuals had early lethality, occipital encephalocele, polydactyly and PKD consistent with MKS (Table 1.6). *TMEM231* mutations were subsequently associated with both MKS (Hopp et al., 2011) and JBTS type 14 (Srour et al., 2012), further emphasizing the genetic pleiotropy between these conditions and shared molecular patho-mechanisms for these two phenotypes (Shaheen et al., 2013a). *TMEM231* encodes a tetraspanin-like transmembrane protein that localizes to the transition zone (Reiter et al., 2012).

The first clues about function came from studies of the *TMEM231* orthologue in *C. elegans* (Roberson et al., 2015). This study investigated whether *TMEM231* localization to the transition zone was conserved in this organism and if *TMEM231* localization required other transition zone proteins. This study confirmed that *TMEM231* was a component of the MKS complex since it interacted with both B9D1 and *MKS1*. Thus, *TMEM231* localised to the transition zone and controlled ciliary protein composition and function (Roberson et al.,

2015). In parallel, Chih et al. (2011) confirmed that *TMEM231*, *B9D1*, *CC2D2A* and *TMEM17* localized at the ciliary transition zone and formed a multiprotein complex. Furthermore, this study demonstrated that the localizations of these proteins are dependent on one another and on the septin SEPT2. It also demonstrated that knock-outs of both the *B9d1* and *Tmem231* genes in mice caused defects in SHH signalling and ciliogenesis, suggesting that TMEM231 contributes to selective permeability at the ciliary transition zone.

Roberson et al. (2015) also described mutations in *TMEM231* causing both orofaciodigital syndrome type 3 (OFD3) and MKS, further supporting the hypothesis that TMEM231 is a member of the MKS complex and that the basis of genetic pleiotropy in ciliopathies may be due to a shared molecular pathogenesis. This is supported by a loss-of-function *Tmem231* mutation in homozygous mutant mouse embryos (Roberson et al., 2015). This revealed polycystic kidneys, polydactyly and hepatic ductal plate malformations, which are all clinical signs characteristic of MKS-like phenotypes. In support of a functional role for *Tmem231* in regulating ciliary composition, in particular the MKS complex, loss of *Tmem231* in the mutant resulted in increased accumulation of NPHP1 at the transition zone, as well as loss of the MKS complex (specifically, MKS1 and TMEM67) from the transition zone (Roberson et al., 2015). These data indicate that TMEM231 is required for the assembly of the MKS complex at the transition zone.

1.6.3.4 CEP290

Centrosomal protein 290 (*CEP290*, MIM: 610142) encodes a large multi-domain transition zone /centrosomal protein and its localization to the centrosome is dynamic and dependent on the cell cycle (Sayer et al., 2006) (Table 1.6). CEP290 localizes, in particular, to mother and daughter centrioles as well as pericentriolar satellites. However, CEP290 is also a component of the transition zone and may contribute to selective permeability at the base of the cilium (Betleja and Cole, 2010). Surprisingly, CEP290 also contains a nuclear localization signal and may also localize to the nucleus (Baala et al., 2007, Sayer et al., 2006, Valente et al., 2010), but the functional purpose of this localization remains unclear.

In photoreceptors, *CEP290* localizes to the connecting cilium and appears to function in controlling entry and trafficking of ciliary proteins as well as regulating cilium assembly (Chang et al., 2006, Barbelanne et al., 2013). Consistent with these functions, mutations in

CEP290 have been implicated in retinal degeneration in human ciliopathies and mouse models (Chang et al., 2006). Moreover, loss of this gene causes supernumerary centrioles in kidneys in a *Cep290* mouse knock-out (Slaats et al., 2015). Mutations in *CEP290* causes a broad range of human ciliopathies, including the second major cause of MKS (Sayer et al., 2006), JBTS (Valente et al., 2006), NPHP, BBS, Leber congenital amaurosis (LCA type 10) and Senior-Løken syndrome (SLS) (Dooley et al., 2018) (Figure 1.7). As an example of phenotypic range, SLS is characterized by severe loss of vision and renal failure (kidney cyst formation and end-stage renal disease) (Coppieters et al., 2010).

1.6.3.5 TMEM17

Transmembrane protein 17 (*TMEM17*, MIM: 614950) encodes a small tetraspanin-like transmembrane protein (TMEM), 198 amino acid residues in length (Figure 1.10; Table 1.6). *TMEM17* may localize to the ciliary necklace alongside TCTN and TMEM231 in mIMCD-3 cells (Satir, 2017), and consistent with this localization *TMEM17* biochemically interacts with components of a TMEM complex that included *TCTN2*, T*CTN3*, *TMEM67*, *TMEM231* and *TMEM237* (Garcia-Gonzalo and Reiter, 2012). *TMEM17* is required for localization of *TMEM231* and *B9D1* to the ciliary transition zone (Chih et al., 2011). Despite the evidence that *TMEM17* is implicated in the MKS module, the expression pattern and clinicopathological relevance of this ciliary gene is still unclear. Mutations in *TMEM17* have not yet been conclusively implicated in a human ciliopathy. In a single family, a homozygous missense mutation in *TMEM17* was reported as causal for Oral-Facial-Digital syndrome type 6 (OFD6) and patient fibroblasts had ciliogenesis defects (Li et al., 2016).

1.6.3.6 TMEM138

Mutations in the transmembrane protein 138 (*TMEM138,* MIM: 614459) are implicated in JBTS (Chih et al., 2011, Lee et al., 2012) but have not been described as a cause of MKS (Szymanska et al., 2014) (Table 1.6). Lee et al. (2012) revealed that *TMEM138* and *TMEM216* have an interdependent role in ciliary assembly since the genes are adjacent and co-regulated, and mutation in either of these genes causes JBTS. *TMEM138* is required for ciliogenesis in both mIMCD-3 cells and in patient-derived mutated fibroblasts (Lee et al., 2012). Interestingly, *TMEM138* interacts genetically with *CEP290* but not with other

components of either the MKS or the NPHP modules (Li et al., 2016), but the functional significance of this interaction is unclear.

1.6.3.7 TMEM237

Transmembrane protein 237 *(TMEM237*, MIM: 614423), a MKS complex component, is a ciliopathy protein associated with JBTS-related disorders and is localized to the transition zone. Mutations in this gene result in defective ciliogenesis and deregulation of Wnt signalling (Huang et al., 2011) (Table 1.6). Consistent with the functional roles of other TMEMs, *TMEM237* also appears to be required for regulation of the protein composition of the ciliary membrane. Biochemical interactions showed that *TMEM237* is necessary for *TMEM231*, *B9D1* and *B9D2* to localize to the ciliary transition zone (Chih et al., 2011), whilst within the transition zone *RPGRIP1L* was required for the proper localisation of *TMEM237* to the ciliary transition zone of mIMCD-3 cells (Huang et al., 2011).

1.6.3.8 RPGRIP1L

RPGRIP1-Like (*RPGRIP1L* (also known as MKS5 or NPHP8)), MIM: 610937) is located at the ciliary transition zone. Mutations in *RPGRIP1L* causes JBTS (Arts et al., 2007) and MKS (Delous et al., 2007) (Table 1.6). *C. elegans* genetic studies suggest that it is a "master regulator" of ciliogenesis for both the MKS and JBTS complexes. *RPGRIP1L* appears to be a key structural component of the ciliary transition zone, in particular the Y-shaped axoneme-to-membrane linkers, and it is essential for the correct localization of *NPHP1*, *NPHP4*, *TMEM17* and *TMEM138* (Jensen et al., 2015). In contrast, a second study has suggested that *RPGRIP1L* controls ciliary length and ciliary signalling by regulating proteasomal activity at the cilium (Gerhardt et al., 2016, Gerhardt et al., 2015, Liu et al., 2014) although the mechanistic basis of this regulation remains unknown.

Table 1. 6: List of ciliary genes and encoded proteins investigated in this project describing the associated human syndromic disorders.

OMIM	Gene name used in this project	Cytogenetic location	Related ciliopathies	Protein-Sub-cellular ciliary localization	Function	Renal Phenotypes	Category
614950	TMEM17	2p15	(OFD6)	Transition zone (Chih et al., 2011)	Ciliogenesis (Li et al., 2016)		
609884	TMEM67	8q22.1	COACH, JBTS6, MKS3, NPHP11, RHYNS, modifier of BBS14	Transition zone (Williams et al., 2011, Garcia-Gonzalo et al., 2011)	Ciliogenesis (Abdelhamed et al., 2015) required for centriolar migration to the apical membrane (Dawe et al., 2007)	Renal cystic dysplasia, (micro)cystic kidneys, nephronophthisis	Neurodevelopmental ciliopathy
614459	TMEM138	11q12.2	JBTS16	Ciliary axonemes / Basal body (Lee et al., 2012)	Ciliogenesis (Lee et al., 2012)	Renal cystic dysplasia, nephronophthisis	
613277	TMEM216	11q12.2	JBTS2, MKS2	Post-Golgi vesicles along microtubules, Golgi apparatus, and surrounding the base of cilium (Lee et al., 2012)	Ciliogenesis (Lee et al., 2012)	Renal cystic dysplasia, cystic kidneys, nephronophthisis	
614949	TMEM231	16q23.1	JBTS20, MKS11	Transition zone (Chih et al., 2011)	Organizing the MKS complex and controlling ciliary composition (Roberson et al., 2015)	Retinal and kidney involvement	
614423	TMEM237	2q33.1	JBTS14	Transition zone (Huang et al., 2011)	Ciliogenesis and function as a module with TMEM216, and TMEM67 to regulate Wnt signalling (Huang et al., 2011).	Cystic kidneys	
610142	CEP290	12q21.32	JBTS5, SLSN6, LCA10, MKS4, BBS14,	Centriolar satellites (Tsang et al., 2008, Kim et al., 2008), Transition zone (Garcia-Gonzalo et al., 2011, Craige et al., 2010)	Ciliary assembly and ciliary trafficking (Coppieters et al., 2010)	Multicystic dysplastic kidneys, nephronophthisis	
610937	RPGRIP1L	16q12.2	JBTS7, MKS5, COACH	Basal body (Arts et al., 2007) Transition zone (Williams et al., 2011)	Ciliogenesis: Assemble of the vertebrate ciliary transition zone/ Regulate proteasomal activity at the base of primary cilia (Wiegering et al., 2018b)		
613979	*PRPF6	20q13.33	*RP60	Proximal/basal body of primary cilia and nuclear speckles in mIMCD-3/Base of the retinal photoreceptor connecting cilium and nuclei of *INL (Wheway et al., 2015)	Cell division (Neumann et al., 2010) Ciliogenesis (Wheway et al., 2015)		Isolated retinal ciliopathy
607300	*PRPF8	17p13.3	*RP13	Proximal/basal body of primary cilia and nuclear speckles in mIMCD-3 /Base of the retinal photoreceptor connecting cilium and nuclei of *INL (Wheway et al., 2015)	Implicating in the process of centriolar under-duplication (Balestra et al., 2013). Important effectors of cell division (Neumann et al., 2010). Ciliogenesis (Wheway et al., 2015)		
603191	C21orf2	21q22.3	*JATD, *RDMS, *axial SMD	Basal body in mIMCD-3/RPE1 (Wheway et al., 2015)/ the connecting cilium of the cone and rod photoreceptors (Wang et al., 2016)	Ciliogenesis (Suga et al., 2016)	Role in cilia formation and/or maintenance	Ciliopathies with major skeletal involvement

*Oral-Facial-Digital type 6 (OFD6), *Pre-mRNA processing factor 8 (PRPF8), Pre-mRNA processing factor 6 (PRPF6), *Retinitis pigmentosa 60 (RP60), *Retinitis pigmentosa 13 (RP13), * Inner nuclear layer (INL) *Jeune asphyxiating thoracic dysplasia (JATD), *Retinal dystrophy with macular staphyloma (RDMS), *Axial spondylometaphyseal dysplasia (axial SMD), Progesterone Immunomodulatory Binding Factor 1 (PIBF1). (Falk et al., 2015, Wheway et al., 2019). Online Mendelian Inheritance in Man, OMIM®. McKusick-Nathans Institute of Genetic Medicine, Johns Hopkins University (Baltimore, MD), (Andreu-Cervera et al.). World Wide Web URL: https://omim.org/.

1.7 Therapies for ciliopathies

There are considerable limitations and challenges to gene therapies that face researchers, such as the complex pleiotropy of ciliopathies. These are very heterogeneous conditions which may be attributed to allelic heterogeneity, locus heterogeneity, reduced penetrance, variable expressivity, impact of modifier genes and/or environmental factors (as is the case in cystic kidney diseases; (Lemaire and Parekh, 2017, Konig et al., 2018). This complexity must be overcome (McIntyre et al., 2013). Therefore, Gainotti et al. (2018) claimed that clinicians should encourage patients to describe their own phenotype. The earlier involvement of patients and more specific diagnoses are needed to enable delivery of effective care and treatments (James et al., 2010, Groopman et al., 2018).

Modern next-generation sequencing (NGS) of gene panels is used instead of testing single ciliopathy genes, since these genes have the large phenotypic overlap between different diseases and wide genetic heterogeneity. Arts and Knoers (2013) argued that such testing will promote diagnostics, prognosis, and genetic counselling. However, significant consideration must be taken to improve the issues in bioinformatic analysis and variant interpretation. Furthermore, strict ethical regulation will be required to enable our understanding of conditions such as renal ciliopathies to be improved. A number of ethical issues remain to be resolved such as what to do with incidental genetic findings, identified by genomic sequencing but unrelated to the disease being investigated, which have major implications for both patients and their relatives. For renal ciliopathies, should exomes be sequenced or should a selected set of known ciliopathy genes be included in an NGS panel in order to avoid this ethical issue? What should be done if variants of unknown significance are identified (Arts and Knoers, 2013)?

Recently, Wheway et al. (2019) reported a comprehensive overview discussing the opportunities and challenges for molecular understanding of ciliopathies. This shed the light on some approaches to data analysis within the UK, the EU, the USA, China, Saudi Arabia and other countries. For instance, the Saudi Human Genome Program was established in December 2013 to sequence 100,000 individuals. The database was set up with a specific focus on understanding the most common Saudi Arabian rare inherited diseases since consanguineous marriage between cousins is very common. Additional genome projects are the USA's $215 million Precision Medicine Initiative set up in January 2015, and China's

Genomic Medicine Initiative, launched in 2016, which aimed to sequence 1 million genomes. It should be noted that whilst these current genome programmes have different specific aims they share some similarities. If these global efforts were combined into one platform, in which data and resources could be shared worldwide including standardizing phenotypic descriptions, data standards, analysis pipelines and mechanisms for data-sharing and discovery, then this would contribute to increased diagnostic outputs and may facilitate targeted therapies for ciliopathy patients (Wheway et al., 2019).

Over the past two decades, there were no approved drugs or therapeutic interventions available for the syndromic ciliopathies, as is the case for most rare genetic disorders. Recently however, there has been extensive discussion and review of gene therapy studies that demonstrate the introduction of wild-type genes through viral transduction can correct cilia dysfunction, including immotility, defective ciliogenesis/maintenance and altered protein trafficking. Several studies have highlighted promising approaches to the development of effective treatments for one of the multiorgan disorders ciliopathies: childhood blindness (Shivanna et al., 2019, McIntyre et al., 2013). Since ciliopathies are in most instances due to loss of wild-type protein, gene therapies consisting of gene replacement or augmentation are realistic prospects for disease processes that are degenerative or later onset. The exceptions are, of course, neurological manifestations or the structural neurodevelopmental anomalies observed in ciliopathies which are too severe to benefit from this approach. This is exemplified by recent current clinical trials for *CEP290*-related disorders that target retinal degeneration. CEP290-associated disease caused by the IVS26 c.2991+1655 A>G mutation, which is a single common nucleotide change in intron 26, caused the introduction of an aberrant exon that reduces the amount of CEP290 protein. Garanto et al. (2016) reported the development of a gene-editing approach for therapeutic treatment of CEP20. This and subsequent studies (Gerard et al., 2012, Collin et al., 2012) have shown that transfection of naked antisense oligonucleotides (AONs) restored normal *CEP290* splicing in cultured cells of LCA patients with homozygous intronic *CEP290* mutations. The AONs treatment strategy has been developed using oligonucleotides that bind to their target mRNA in a complementary fashion and subsequently can interfere with pre-mRNA splicing.

In addition, Garanto et al. (2016) developed the strategy using naked and adeno-associated virus (AAV)-packaged AONs which were replication-defective, followed by AAV

transduction into retinal cells. Their results indicated the efficacy of using AAV-mediated delivery of AONs in *CEP290*-mutated patients for whom protein levels were restored. In a humanized *Cep290* mouse model that carries the LCA mutation, AON treatment reduced the amount of aberrant *Cep290* transcripts. A similar technique used intraretinal injection of AAV vectors carrying full-length *Bbs4* to slow progression of retinal degeneration in *Bbs4* knock-out mice. This treatment prevented photoreceptor death and improved both retinal electrophysiological responses and visually-guided behaviours in the *Bbs4* mutants (McIntyre et al., 2013, Simons et al., 2011). Recently, however, adverse events occurred during AAV treatment. Several issues related to AAV gene transfer treatment were discussed in detail by Colella et al. (2018), including immunogenicity, potency and efficacy, genotoxicity, and persistence side effects. For instance, the random integration of AAV vector genomes into the host DNA could result in gain-of-function mutations that could alter cellular homeostasis and cell function, suggesting an issue of AAV-related genotoxicity.

On the other hand, recent research has revealed a therapy to slow cyst growth in adult patients with the ciliopathy ADPKD using the cAMP-targeting drug tolvaptan (Torres et al., 2017). Tolvaptan, a vasopressin 2 receptor blocker, has been shown to slow the growth in total kidney volume. The V2 receptors targeted by tolvaptan reduce cAMP levels, renal weight, cystic volume, fibrosis, and apoptotic and mitotic indices. (Torra, 2008, Torres et al., 2012). However, the treatment was associated with adverse events. For instance, the sort-term effectiveness of tolvaptan was tested in clinical trials (Sans-Atxer and Joly, 2018). Patients who were at risk of or with evidence of rapidly progressing disease received tolvaptan and their symptoms included thirst, polyuria, nycturia and polydipsia (Sans-Atxer and Joly, 2018, Torres et al., 2017). The long-term effectiveness of the drug remains to be determined (Torres et al., 2017). Despite the risks of this drug, it helps in slowing the progression of ADPKD in these patients. It is worth mentioning that nephronophthisis patients could benefit from this treatment since the ADPKD and nephronophthisis-associated genes are involved in similar ciliary pathways (Arts and Knoers, 2013).

As an alternative approach, drug screening and early preclinical testing (Kim et al., 2018) has identified a potential lead compound, eupatilin, for treatment of retinal degeneration, which is a notable example of using a small molecule as a therapeutic intervention for a genetic disorder. Importantly, preclinical studies showed clinical efficacy in the *rd16* mouse model of CEP290-related retinal degeneration. The *rd16* mouse has a

Cep290 in-frame deletion, and homozygotes exhibit blindness due to complete degeneration of photoreceptors (Chang et al., 2006). In the normal transition zone, *CEP290* forms a complex with *NPHP5* and facilitate the function of the ciliary transition zone. In the *rd16* photoreceptor, the lack of full-length *CEP290* appears to be rescued by eupatilin through direct binding to NPHP5, leading to partial restoration of function for the complex and NPHP5. This prevented retinal degeneration in the *rd16* model (Kim et al., 2018) but it is unclear if this intervention will be effective for other *CEP290* in-frame deletions or for null mutations that cause complete absence of the protein.

In 2009, Chin and colleagues showed successful *ex vivo* gene therapy when ciliary beating was rescued in recovered in DNAI1-deficient human airway epithelial cells after lentivirus transduction. Respiratory epithelial cells were harvested from PCD patients with *DNAI1* mutations, and a wild-type copy of DNAI1 was introduced by lentiviral transduction. This example demonstrated a gene therapy technique that was sufficient to repair endogenous machinery in existing cilia and suggested that gene augmentation is a viable future approach (Chhin et al., 2009, McIntyre et al., 2013).

More recent studies (McIntyre et al., 2012, Lehman et al., 2008) have revealed that restoration of cilia function is possible using adenovirus-mediated gene delivery for gene and cell-based therapies. In this study, the *Ift88^{Tg737Rpw}* homozygous mouse model of human ciliopathies (Lehman et al. 2008) has olfactory sensory neurons (OSNs) in the nasal cavity that were unable to build or maintain cilia due to a hypomorphic mutation of *Ift88*. McIntyre et al. (2012) performed adenoviral-mediated gene delivery that resulted in restoration of *Ift88* expression and was sufficient to produce functional olfactory cilia. Again, this work demonstrates that gene augmentation is a therapeutic approach worth future investigation.

To sum up, as mentioned in this section that the NGS and high-throughput technologies in the last decade has significantly improved the understanding of the biological basis of ciliopathy disorders. Ongoing projects are needed to better understand the molecular causes of disease, and to determine the possible reasons for the extensive overlap in their symptoms and genetic aetiologies. This knowledge is essential before the potential of targeted therapeutic interventions can be realized for this group of important genetic conditions.

1.8 An overview of recent research projects 'the research rationale' and aims of investigation

The specialized proximal region of the primary cilium known as the transition zone has been a focus of study in recent years, but there is still little known about the biochemical and genetic interactions in the transition zone that could underlie ciliopathy disease mechanisms. Further detail about these transition zone interactions could therefore provide new insights into the pathogenic mechanisms of cystic kidney disease in ciliopathies, as well as provide further understanding of the molecular architecture, interactions and functions of the ciliary proteins in this compartment.

A previous study has highlighted the potential genetic interactions between *C. elegans* and mammalian transition zone components, that presumably influence the function of macromolecular complexes that are required for early stages of ciliogenesis (Williams et al., 2011). Williams et al. (2011) showed that transition zone modules such as MKS and NPHP are likely to share common biological functions within predicted macromolecular complexes signifying a common cellular mechanism as the basis of their etiology. This hypothesis was supported by a previous study, again in *C. elegans* (Williams et al., 2008), which demonstrated that B9 domain-containing proteins (including *MKS1*, *B9D1* and *B9D2* as components of the MKS module), functionally interact with components of the NPHP module in particular *NPHP1* and *NPHP4*. These genetic interactions were essential for ciliogenesis and will be placed in context with my own work in Chapters 4 and 5.

One of the overall aims of this project therefore is to determine whether similar genetic interactions occur between selected transmembrane ciliary transition zone genes. Ciliary transition zone proteins for this project comprised the transmembrane proteins *TMEM17*, *TMEM67*, *TMEM138*, *TMEM216*, *TMEM218*, *TMEM231* and *TMEM237* from the MKS complex. The reasons for considering the selected transition zone proteins is that most of these proteins are required for primary cilia formation and have medical relevance (pathogenic mutations in the encoding genes have been described as causes of MKS or JBTS; see section 1.6) as well as available of relevant reagents. For example, *TMEM67* and *TMEM216* are essential for basal body docking, ciliogenesis and PCP and they are mutated in Joubert syndrome and Meckel-Gruber syndrome (Dawe et al., 2007, Dawe et al., 2009,

Valente et al., 2010). Mapping the locations of these transition zone proteins using biochemical approaches for characterizing protein-protein interactions will enhance our knowledge to clarify the potential relations leading to their tethering and anchoring functions.

A standard biochemical method, co-immunoprecipitation, was used at the beginning of the study to identify the interacting proteins since protein-protein interactions are crucial in many biological processes in living cells (Lin and Lai, 2017). This relied on the availability of specific antibody reagents. As the study developed, I also used over-expression of Strep/FLAG (SF-TAP) tag construct contains a 3xFLAG tag (SF-TAP-tagged proteins) in order to develop mass spectrometry-based proteomics of TMEM proteins. This approach has been used in previous studies to gain insights into ciliary protein function. In this work, I used a MS-based comparative proteomics approach to investigate the expressed selected ciliary transition zone proteins as well as the purified N-terminal region of the TMEM67 protein.

RNA interference (RNAi)-based gene knockdown "reverse genetics" approaches allow for rapid and efficient assessment of potential genetic interactions of ciliopathy genes. My work leads on from a whole genome short interfering RNA (siRNA) reverse genetics screen (Wheway et al., 2015) that sought to identify regulators of ciliogenesis and cilia maintenance, which exemplified the utility of using acute knockdown as an approach to gain insights into mechanism but without complete ablation of protein levels. This study identified 194 candidate genes for ciliogenesis and ciliopathies from an initial screen in the mouse inner medullary collecting duct (mIMCD-3) ciliated cell-line that was further refined by studies in the hTERT-RPE1 cell-line. In Chapter 4, I summarize a number of experiments targeting ciliated cell line mIMCD-3 with the aid of RNAi which aims to analyse the organization of components of the ciliary transition zone, basal body and axoneme. Thus, I hypothesize that even partial reduction of TMEM gene expression using siRNA approaches will give rise to quantifiable defects in ciliary incidence or organization.

1.8.1 Specific objectives of the study comprised:

1. Sanger sequencing for causative mutations in *TMEM218* and *TMEM17*, in a large cohort of MKS patients and families already pre-screened and confirmed to be mutation-negative in known MKS genes.

2. Biochemical characterization of TMEM proteins including protein purification and protein colocalization identifying new interacting proteins of TMEMs and protein-protein complexes involved in facilitating ciliogenesis at the ciliary transition zone; and detecting potential ligands of the orphan receptor TMEM67.

3. RNA interference-based studies to characterize genetic and potential functional interactions between TMEM genes in order to identify novel ciliopathy genes and mediators of ciliogenesis.

Chapter 2 Mutation Screening of *TMEM17* and *TMEM218*

2.1 Introduction

The ciliopathy MKS syndrome is a lethal neurodevelopmental condition that is characterized by occipital encephalocele, PKD and polydactyly (see section 1.6.1.1). MKS syndrome comprises the severe end of a phenotypic spectrum that includes JBTS syndrome and the two conditions are allelic at several loci such as *TMEM216*, which is mutated as a cause of both of these pleiotropic ciliopathies. Homozygous missense mutations were found in *TMEM216* in patients with JBTS and related disorders (JSRD), while frameshift mutations were found in *TMEM216* in two Palestinian families with MKS (Waters and Beales, 2011, Valente et al., 2006). These pleiotropic ciliopathies have defects in particular molecular complexes and structures that are critical for ciliogenesis and cilia maintenance (see section 1.6). Many studies have identified ciliopathy disease genes; Table 1.2 and Table 1.3 show some examples, but more recent findings have described only private mutations in single families (Hartill et al., 2017).

To substantiate the role of these putative ciliary genes in ciliopathy disease, and to try to establish if there are any genotype-phenotype correlations, I sequenced two such genes, *TMEM17* (NM_198276.3) and *TMEM218* (NM_001258241.2).

Therefore, a cohort of families affected with MKS, already known to be mutation-negative for variants in the known ciliary MKS genes (Table 2.1), were selected for further molecular genetic studies. In this chapter, I therefore screened the ciliary genes *TMEM17* and *TMEM218*, since mutations in both genes have been implicated in ciliopathies (Vogel et al., 2015, Li et al., 2016) although neither encoded TMEM protein has been functionally characterized. Furthermore, both *TMEM218* and *TMEM17* are considered to be potential regulators during the formation of the primary cilia compartment in *C. elegans* (Li et al., 2016). In this study, the transition zone proteins *RPGRIP1L* and *CEP290* appear to function as assembly factors for *TMEM17*, *TMEM218* and other proteins in the MKS module. *TMEM17* and *TMEM218* are therefore strong functional candidate disease genes for new genetic causes of ciliopathies. I therefore prioritized sequencing of cases that were mutation-negative for known MKS genes (n=36), from a larger cohort of MKS patient DNA samples (n=395). These had already been screening for pathogenic variants in the following

ciliopathy genes: *MKS1*, *TMEM216*, *TMEM67*, *RPGRIP1L*, *CEP290*, *CC2D2A*, *NPHP3*, *TMEM138*, *TMEM231*, *TMEM237*, *C2orf42*, *TULP3*, *KIF7*, *EXOC3L4*, *TXNDC15*, *CSPP1*, *TTC21B*, *INPP5E*, *TCTN1*, *TCTN3*, *DLL1*, *TMEM107* and *CEP41*. Most of these genes are known to be involved in the formation and assembly processes of the transition zone.

The tetraspan transmembrane 17 protein (TMEM17; Figure 1.10) is characterized by 4 hydrophobic, putative transmembrane domains. The encoded protein is thought to regulate ciliogenesis, but there is little mechanistic insight into this process other than the observation that *Tmem17* is necessary for *Tmem231* and *B9d1* to localize to the transition zone in mouse ciliated cells (Chih et al., 2011). Both human proteins TMEM216 and TMEM80 also contain a so-called "transmemb_17 domain" (Lee et al., 2012), highlighting the close sequence similarities between these proteins.

The transmembrane protein 218 protein (TMEM218) encodes a small protein with 3 predicted transmembrane domains that is conserved across metazoans, including *C. elegans* and humans. Subsequent work by (Li et al., 2016) and colleagues, as mentioned in (see section 1.6.3.5), identified one private mutation in TMEM218 in a family with OFD6 (Li et al., 2016); they studied the composition, assembly and function of the *C. elegans* transition zone. They found that Tmem218 localized at the transition zone protein of *C. elegans* which, in addition to genetic interactions with other ciliary gene mutations, suggested that Tmem218 is a new MKS module component (Li et al., 2016). This study suggested but did not confirm that a private mutation in human *TMEM218* may be causative for retinal degeneration and may be a possible rare cause of NPHP, since the main pathogenic features of the *Tmem218*$^{-/-}$ knockout mice were progressive cystic kidney disease and retinal degeneration (Vogel et al., 2015).

The aim of this chapter was therefore to screen for recessive mutations in the *TMEM17* and *TMEM218* ciliary genes as possible causes of MKS. This aim was addressed by carrying out Sanger sequencing of "mutation negative" MKS patients for predicted causative mutations in *TMEM17* and *TMEM218*.

2.2 Materials and methods

In this Chapter, unless stated otherwise all reagents were kept on ice. Relative centrifugal force (rcf) is expressed as *xg*.

2.2.1 Patient DNA

Families with affected foetuses or children diagnosed with Meckel-Gruber or Meckel-Gruber-like syndromes were ascertained and recruited to the study following informed consent for research. DNA samples were obtained from NHS diagnostic centres for UK families and patients, or from referring clinicians and collaborators for non-UK individuals. Ethical approval for the study entitled "Molecular genetic investigations of autosomal recessive conditions", was granted by the South Yorkshire Research Ethics Committee on 18th February 2011 for five years (REC ref. number 11/H1310/1). NHS Permission for Research at Leeds Teaching Hospitals NHS Trust was granted on 29th April 2011 (LTHT R&D number CG11/9764) (see Appendix A.1).

2.2.2 Primer design

PCR primers were designed to amplify the exons and flanking intronic sequences of *TMEM17* and *TMEM218* using Primer3 software (http://bioinfo.ut.ee/primer3/). Primers were designed for regions across intron-exon boundaries to avoid amplification from contaminating genomic DNA. Primers were designed to avoid common single nucleotide polymorphisms (SNPs) and parameters were set to produce primers with an optimum annealing temperature of approximately 60°C and with products of between 250-600 base pairs (bps). Data were visualized using SeqScape software or SnapGene Viewer software. Primer sequences used in this Chapter are listed in Appendix A.2.

2.2.3 Polymerase chain reaction (PCR)

2.2.3.1 Standard PCR

PCR reactions were set up in a total volume of 10 μl containing 20-50 ng genomic DNA with the following reagents at the specified concentrations: 10 μM of forward and reverse primers (Sigma-Aldrich), 0.1 unit of Taq DNA polymerase (ABgene), 0.25 μM

deoxynucleotide triphosphates (dNTPs) (Thermo Fisher Scientific) and 1x PCR reaction buffer (75 mM Tris-HCl buffer (pH8.8) (Sigma-Aldrich), 20 mM $(NH_4)_2SO_4$, 0.01% Tween-20 and 1.5 mM $MgCl_2$). Reactions were performed in a Veriti Thermal Cycler (Thermo Fisher Scientific). Thermal cycling was performed on this mixture with an initial denaturing step at 95°C for 5 minutes, followed by 45 cycles of 94°C for 15 seconds, the appropriate annealing temperature (55-65°C) for 15 seconds, and 72°C for 30 seconds (extension). The final extension step was performed at 94°C for 30 seconds. PCR products were visualized by agarose gel electrophoresis (see section 3.2.3.5).

2.2.3.2 Hot-Shot PCR master mix

If the standard method did not give successful PCR results, Hot-Shot Diamond PCR Master Mix (Clent Life Science) was used as an alternative. 20 ng of genomic DNA was amplified in a 10 µl reaction volume, and combined with 0.5 µl of each 10 µM forward and reverse primers and the 5 µl Hot-Shot Diamond PCR Master Mix (Clent Life Science). This was made up to 10 µl with distilled water (dH$_2$O). After gentle mixing, the mixture was subjected to the same thermocycling conditions as in the standard PCR method.

2.2.4 Purification with ExoSAP

Prior to sequencing, DNA samples were purified with ExoSAP-IT® (Affymetrix, Thermo Fisher Scientific) which contains both exonuclease I and shrimp alkaline phosphatase to remove unused primers and unincorporated dNTPs. For 2.5 µl of PCR product, 1 µl of ExoSAP-IT was added. Samples were incubated on a thermocycler for 30 minutes at 37°C and then inactivated for 15 minutes at 80°C.

2.2.5 Sanger sequencing

ExoSAP-IT purified PCR products were sequencing using the BigDye® Terminator v3.1 Cycle Sequencing Kit (Thermo Fisher Scientific). This method is suitable for testing a small number of exons and samples. Cycle sequencing was performed in 10 µl reactions consisting of 1 µl of the ExoSAP-IT purified product, 0.5 µl BigDye® terminator v3.1 (Applied Biosystems), 1.5 µl 5x BigDye® sequencing buffer (Applied Biosystems), 1 µl forward or reverse primer at a final concentration of 2 µM, and 6 µl dH$_2$O, giving a final reaction

volume of 10 µl. The mixture was kept on ice during the reaction set-up. Sequencing reactions were performed in a Veriti Thermal Cycler (Thermo Fisher Scientific). Denaturation was at 96°C for 1 minute, followed by 45 cycles of 96°C for 10 seconds, annealing at 50°C for 15 seconds, and extension at 60°C for 4 minutes. Temperatures were ramped at 1°C /second. Sequencing products were ethanol precipitated by adding 5 µl 125 mM ethylenediaminetetraacetic acid (EDTA) (pH 8.0) (Sigma-Aldrich) and 60 µl of absolute ethanol to each product, followed by mixing and centrifugation at 3000 *xg* for 30 minutes at 4°C. The plate was then inverted onto tissue and spun upside down at 200 *xg* for 5 seconds. Next, 60 µl of 70% (v/v) ethanol was added and the plate was centrifuged at 3900 *xg* for 15 minutes. Then the plate was inverted and spun at 200 *xg* for 5 seconds. The plate was then left to air dry for 30 minutes at RT under foil or placed on a hot block at 37°C for 15 minutes. The purified reactions were dissolved in 10 µl of deionized HiDi-formamide loading buffer (Applied Biosystems; Thermo Fisher Scientific) and sequenced at 60°C on an ABI 3130xl Genetic Analyzer (Applied Biosystems) using polymer POP7 (Applied Biosystems). Data was analysed using Sequence Analysis v5.2 and SeqScape v2.5 software (Applied Biosystems).

2.3 Screening results

Mutational screening of *TMEM17* and *TMEM218* was performed by direct Sanger sequencing of PCR products of the coding exons from families with MKS. Sequencing results for "mutation negative" MKS patients of *TMEM17* and *TMEM218* are listed in Table 2.1, respectively. Sequencing was designed to cover all coding exons and about 30 bp of intronic sequence that flanked each exon. Both the exonic sequence of *TMEM17* and *TMEM218* in the selected MKS patients did not indicate any biallelic variants that could be interpreted as pathogenic. Furthermore, sequencing of parental DNA samples, under the assumption that they were carriers for an autosomal recessive condition, did not carry any heterozygous variants that could be interpreted as pathogenic.

In total, n=36 affected individuals or parents were sequenced for *TMEM17* (Table 2.1). Figure 2.1 shows exemplar results for *TMEM17* sequencing. Specifically, the figure provides examples of Sanger sequencing electropherograms that demonstrate several *TMEM17* variants in MKS families. In particular, pathogenic biallelic mutations were not identified in *TMEM17*, but a G>C nucleotide substitution c.59G>C (p.Ser20Thr) resulted in

heterozygous variants in sample 35 (Figure 2.1 D; substitution indicated by red box). This individual was already identified to carry a homozygous *INPP5E* mutation (Table 2.1). The same individual had a homozygous G>A nucleotide substitution c.54G>A causing a synonymous variant p.Val18= (Figure 2.1 C). This variant replaced a GTG codon (encoding valine) with GTA (encoding valine) (Figure 2.1 C). Furthermore, a novel heterozygous missense TMEM17: NM_198276.3:c.76G>A: (p.Gly26Ser) variant was identified in individual sample ID 222, 291 and 222 (Figure 2.1 H). Individual 222 was affected with corpus callosum agenesis, unilateral multicystic kidneys, epileptic (Table 2.1). Moreover, a second novel heterozygous missense TMEM17: NM_198276.3: c.64T>A: (p.Ser22Thr) variant was identified in individual 364 (Figure 2.1 I; Table 2.1).

Screening also identified several known variants in *TMEM17*. The G>A nucleotide substitution c.12G>A (p.Pro4=) resulted in recurrent heterozygous variants in 9 candidates (Table 2.1 and Figure 2.1 A; substitution indicated by red box). The A>G nucleotide substitution c.216A>G (p.Leu72=) resulted in heterozygous variants in 9 candidates (Table 2.1 and Figure 2.1 B). Affected individual had a C>T nucleotide substitution c.24C>T resulting in the synonymous change p.Arg8= (Figure 2.1 E) and affected individual 278 had a C>T nucleotide substitution c.264C>T also resulting in the synonymous change p.Thr88= (Figure 2.1 F). Sequence analysis of *TMEM17* and *TMEM218* were performed for all family members when high-quality DNA were available, or for at least one parent in each family to screen for possible carrier status (see Table 2.1). In general, Agilent Bioanalyzer traces were poor with either severe fragmentation or low DNA concentration for some samples that had failed PCRs, so further analyses were discontinued for these samples, (see trace examples in appendix A.3). Mutation analysis of *TMEM218* was performed in n=7 MKS patients. However, the sequencing results did not reveal any variants that could be interpreted as pathogenic (Table 2.1).

Table 2. 1: Summary of all sequence variants identified in TMEM17 (NM_198276.3) and TMEM218 (NM_001258241.2). Sanger sequencing results of consanguineous and non-consanguineous patients with MKS and MKS-like phenotypes are listed, showing clinical data for the affected fetus or patient with variants listed by dbSNP ID number.

Sample			Consanguineous?	Variants in known ciliopathy genes (zygosity)	Gene screened	Rsnumber and variant type\class	RefSeqID: Mutation	Predicted amino acid change HGVSp	Phenotype of affected proband						
ID	Ethnicity	family relationship							OE	PK	PD	DPM	MCDK	BM	other
1	Pakistani	Mother	+	Not determined	TMEM17	Not determined	Not determined	Not determined							
					TMEM218										
8	Pakistani	Father	+	Not determined	TMEM218	Not determined	Not determined	Not determined							
14	Pakistani	Father	+	Not determined	TMEM17	rs11676567(Synonymous)	NM_198276.3: c.12G>A (exon 1)	p.Pro4=							
						rs4672527 (Synonymous)	NM_198276.3: c.216A>G (exon 3)	p.Leu72=							
35	Gujarati	Mother	-	INPP5E c.1750C>T p.H584Y (het)	TMEM17	Rs753028662 (Indel Insertion and Deletion)	t NM_198276.3:c.-20_-2=	Not determined							
						rs758254535 (Synonymous)	NM_198276.3: c.54G>A (exon 1)	p.Val18=							
						rs72885228 (Missense)	NM_198276.3: c.59G>C (exon 1)	p.Ser20Thr							
113	Pakistani	Mother	+	IFT144 c.910G>A p.V304I (het)	TMEM17	rs11676567 (Synonymous)	NM_198276.3: c.12G>A (exon1)	p.Pro4=							
						rs4672527 (Synonymous)	NM_198276.3: c.216A>G(exon3)	p.Leu72=							
					TMEM218	Not determined	Not determined	Not determined							
129	Pakistani	Father	+		TMEM17	Not determined	Not determined	Not determined							
					TMEM218										
134	Pakistani	Affected fetus	+	RPGRIP1L c.1350+86G>A (hmz) CEP290 rs71082425 (Intron variant) (Insertion) NG_008417.1:g.18170_18171insG	TMEM17	Not determined	Not determined	Not determined							
136	Brazilian	Affected patient		Not determined	TMEM17	Not determined	Not determined	Not determined			+				Two accessory spleens, adrenal hypoplasia, anencephaly, thymic hypoplasia
138	Brazilian	Affected patient		Not determined	TMEM17	Not determined	Not determined	Not determined							
140	Brazilian	Affected patient		Not determined	TMEM17	Not determined	Not determined	Not determined							
					TMEM218										
175	Bangladesh	Affected fetus	-	CSPP1 c.2219G>A p.R740H (het) CEP164 c.3268T>C p.Y1090H (het)	TMEM17	Not determined	Not determined	Not determined	+		+	+	+		small disrupted left cerebral hemispheredysmorphic facies part of the hard palate, postaxial large cystic dysplasia,

															bowed limbs curved femora and only 11 thoracic vertebral bodies (autopsy)
200	No information	Father	-	**TMEM67** c.1810A>G p.Met604Val (het)	TMEM17	rs11676567 (Synonymous)	NM_198276.3: c.12G>A (exon1)	p.Pro4=							
				CC2D2A c.685_687delGAA p.E229del (het); c.3893T>A p.V1298D (het)		rs4672527 (Synonymous)	NM_198276.3: c.216A>G (exon3)	p.Leu72=							
201	No information	Mother	-	Not determined	TMEM17	Not determined	Not determined								
211	No information	Mother	-	Not determined	TMEM17	rs4672527 (Synonymous)	NM_198276.3: c.216A>G (exon3)	p.Leu72=							
216	Spanish	Father	-	**TMEM67** c.1810A>G p.Met604Val (hmz)	TMEM17	Not determined	Not determined	Not determined							
220	No information	Mother	-	**TMEM67** c.1810A>G p.Met604Val (hmz)	TMEM17	Not determined	Not determined	Not determined							
222	No information	Affected	-	Not determined	TMEM17	rs17854454 (Missense variant)	NM_198276.3:c.76G>A (exon1)	p.Gly26Ser					+		corpus callosum agenesis, unilateral multicystic kidneys, epileptic??
229	No information	Mother	+	**INPP5E** c.1897_1898delCA,p.Q633EfsX (het)	TMEM17	Not determined	Not determined	Not determined							
232	No information	Mother	-	Not determined	TMEM17	rs11676567 (Synonymous)	NM_198276.3: c.12G>A (exon1)	p.Pro4=							
234	No information	Mother	+	Not determined	TMEM17	Not determined	Not determined	Not determined							
237	No information	Unaffected twin	+	Not determined	TMEM17	rs1216848114 (Synonymous)	NM_198276.3: c.24C>T (exon1)	p.Arg8=							
242	Spanish	Affected fetus	-	**TTC21B** c.2588G>A p.R863Q (het)	TMEM17	Not determined	Not determined	Not determined			+				encephalocele
245	No information	Father	-		TMEM17	rs11676567 (Synonymous)	NM_198276.3: c.12G>A (exon1)	p.Pro4=							
278	No information	Unaffected sibling	-	**CEP290** c.678_680delGA p.E227SfsX2 (het)	TMEM17	rs772164894 (Synonymous)	NM_198276.3:c.264C>T (exon3)	p.Thr88=							
287	No information	Affected fetus	-	**DLL1** c.1802_1804del, p.D601_I602delinsV (het)	TMEM17	Not determined	Not determined	Not determined							

291	Pakistani	Mother	+	Not determined	*TMEM17*	rs17854454 (Missense variant)	NM_198276.3:c.76G>A (exon1)	p.Gly26Ser						
293	No information	Mother	+	**CEP290** c.954delT p.S318fs16X (het)	*TMEM17*	Not determined	Not determined	Not determined						
295	No information	Affected baby	+	Not determined	*TMEM17*	Not determined	Not determined	Not determined						
305	Turkish	Father	+	Not determined	*TMEM17*	rs6713096 (Synonymous)	NM_198276.3:c.237T>C (exon3)	p.Ile79=						
327	Pakistani	Father	+	Not determined	*TMEM17*	Not determined	Not determined	Not determined						
361	Dutch	Affected	-	Not determined	*TMEM17*	Not determined	Not determined	Not determined	+		+		+	structural brain malformations, very large kidneys with cystic dysplasia, small uterus, lung hypoplasia
364	No information	Mother	No information	Not determined	*TMEM17*	rs11676567 (Synonymous)	NM_198276.3: c.12G>A (exon1)	p.Pro4=						
						rs4672527 (Synonymous)	NM_198276.3: c.216A>G (exon3)	p.Leu72=						
						rs78110679 (Missense variant)	NM_198276.3:c.64T>A (exon1)	p.Ser22Thr						
						rs17854454 (Missense variant)	NM_198276.3:c.76G>A (exon1)	p.Gly26Ser						
						rs6713096 (Synonymous)	NM_198276.3:c.237T>C (exon3)	p.Ile79=						
365	No information	Father	No information	**PIBF1** c.1567C>A, p.H523N (het)	*TMEM17*	rs11676567 (Synonymous)	NM_198276.3: c.12G>A (exon1)	p.Pro4=						
				CEP290 c.5850delT p.F1950LfsX15 (het)		rs4672527 (Synonymous)	NM_198276.3: c.216A>G (exon3)	p.Leu72=						
366	No information	Affected fetus	No information	Not determined	*TMEM17*	Not determined	Not determined	Not determined						
375	Pakistani	Father	+	Not determined	*TMEM17*	Not determined	Not determined	Not determined						
391	Pakistani	Father	+	**KIF7** c.2654C>T p.A885V (het) **TCTN3** c.1074T>G,p.Y358X (hmz)	*TMEM17*	rs11676567 (Synonymous)	NM_198276.3: c.12G>A (exon1)	p.Pro4=						
393	No information	Mother	-	Not determined	*TMEM17*	Not determined	Not determined	Not determined						

Abbreviations: + indicates the presence of consanguinity and – indicates non-consanguineous families; hmz, homozygous; het, heterozygous; OE, occipital encephalocele; PK, polycystic kidneys; PD, polydactyly; DPM, ductal plate malformation; MCDK, multicystic dysplastic kidney; BM, brain malformations; + indicates the presence of a clinical feature.

A) c.12G>A

ID: 1   ID: 113   ID: 200   ID: 211

ID: 222   ID: 232   ID: 245   ID: 364

ID: 365   ID: 366   ID: 391

B) c.216A>G

ID: 14   ID: 113   ID: 200

ID: 211   ID: 305   ID: 327

ID: 364   ID: 365   ID: 366

C) c.54G>A D) c.59G>C E) c.24C>T

F) c.264C>T G) c.237T>C

H) c.76G>A
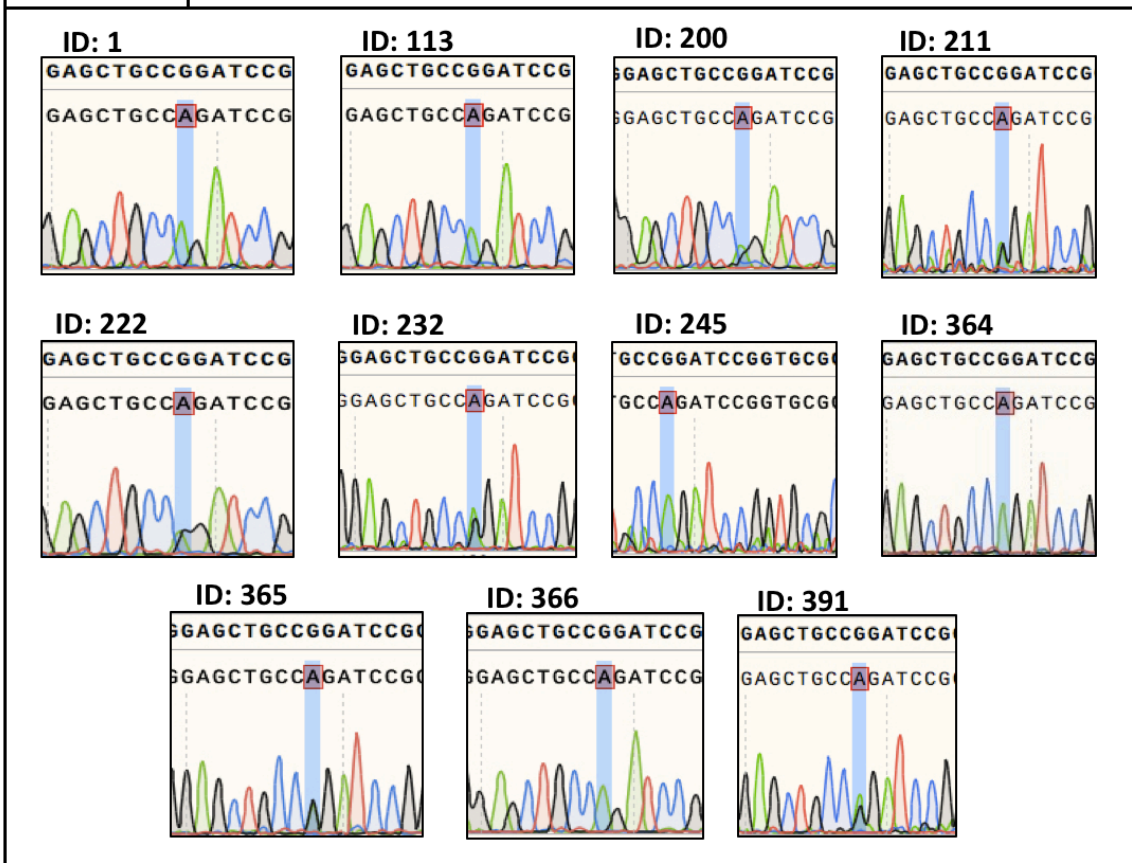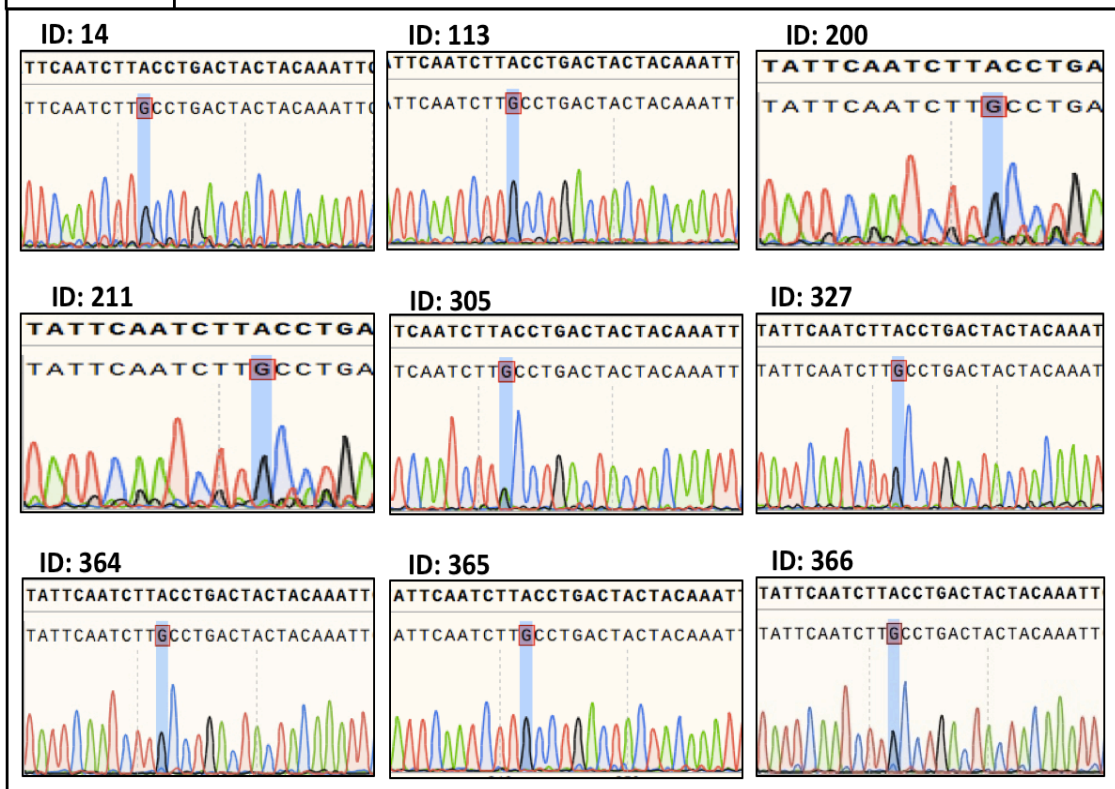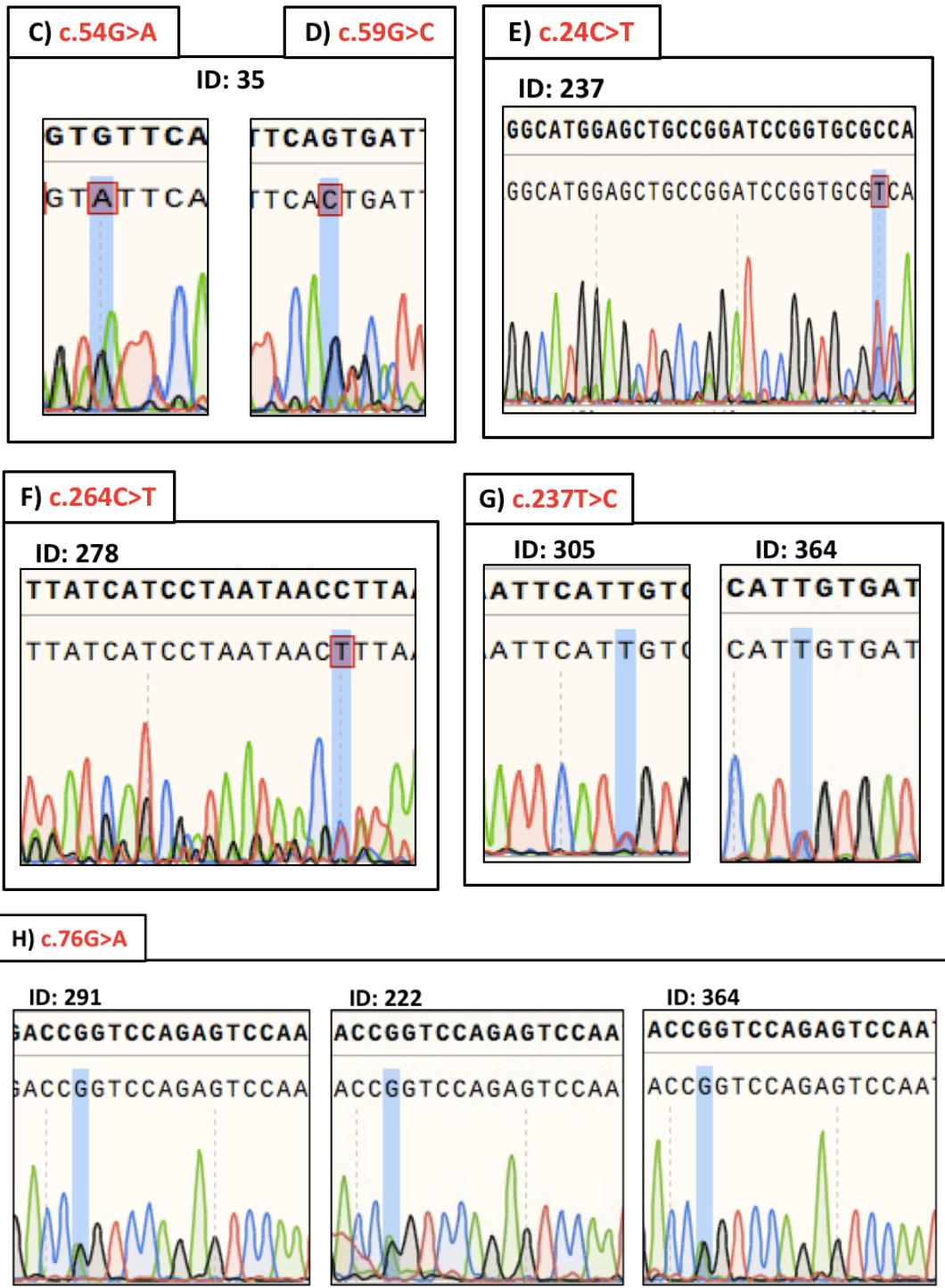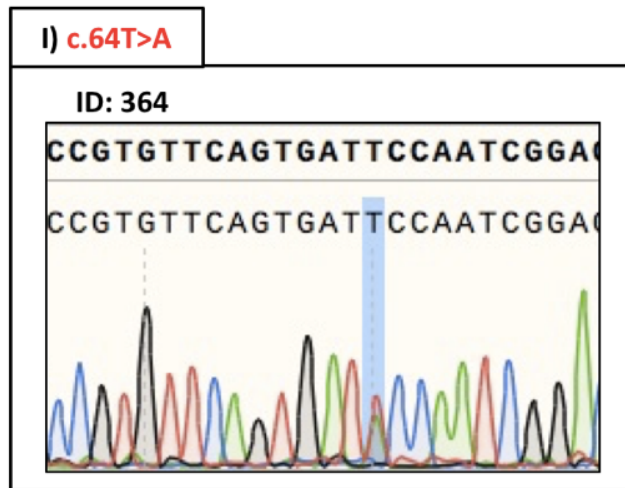
Figure 2. 1: Examples of electropherograms showing variants in *TMEM17* identified in selected MKS families multiple. Blue highlighting and the red box indicate the position and identity of the variant compared to the reference sequence. The ID number indicates the individual sequenced (either affected patient/fetus or parent; refer to Table 2.1 for further details). **(A)** Sanger sequencing electropherograms to show the c.12G>A variant in *TMEM17* for individuals ID 1, 113, 200, 211,222, 232, 245, 364, 365, 366 and 391. **(B)** *TMEM17* c.216A>G variant in individuals ID 14, 113, 200, 211, 305, 327, 364, 365 and 366. **(C, D)** *TMEM17* c.54G>A and c.59G>C variants for individual ID 35. **(E)** *TMEM17* c24C>T variant in individual ID 237. **(F)** *TMEM17* c.264C>T variant in individual ID 278. **(G)** *TMEM17* c.237T>C variant in individuals 305 and 364. **(H)** *TMEM17* c.76G>A variants for individuals ID 291, 222, and 364. **(I)** *TMEM17* c.64T>A for individuals ID 364. MKS samples were also screened for TMEM218, but no further variants were identified in predicated open reading frame of this gene for individuals ID 1,8,113,129,136, and 138.

2.4 Discussion

TMEM17 and *TMEM218* represent potential functional candidate genes for MKS, since mutations are a possible cause for OFD6 and other ciliopathies. Vogel et al. (2015) suggested that *TMEM218* has a role in maintaining normal structure and function in the kidney and retina of mice and it is possible that human *TMEM218* mutations will be associated with human ciliopathies in the future. Other groups have strong data that places TMEM17 at the transition zone and that mutations in *TMEM17* are likely to be found in human patients with ciliopathies (Chih et al., 2011). The selected samples from MKS families examined here were confirmed to be mutation-negative in the known MKS genes. Despite poor coverage of some exons, due to low DNA quality and yield, there were no biallelic variants identified that could be interpreted as pathogenic mutations in these genes (Table 2.1). It remains possible that pathogenic mutations in this cohort were missed because they

occur in the gene promoter or deeper in introns or non-coding regions that were not covered by the exon-based sequencing.

Furthermore, fetal DNA or DNA derived from post mortem tissue samples, typically extracted from formalin-fixed paraffin embedded (FFPE) clinical material, was often of poor quality and quantity. Indeed, the number of high-quality DNA samples screened was limited to 36 or 7 DNA samples for *TMEM17* and *TMEM218*, respectively.

2.4.1 Further investigations and experimental limitations

Intronic variants can affect gene expression levels by introducing or eliminating enhancer activity, or variants in the promoter can affect gene expression. These possibilities were not fully explored in the mutation screens because sequencing primers were designed to cover all coding exons and about 30 bp of intronic sequence that flanked each exon, and they are not a routine part of diagnostic or research gene screening. Furthermore, families apparently confirmed to be mutation negative by whole exome sequencing, could have harboured variants in the intronic sequences or promoters of known MKS genes and have been misidentified as false negatives. In the future, better WES reagents with more complete coverage of non-coding sequences or whole genome sequencing (WGS) may be able to identify "missing mutations" in these MKS families that could then be uploaded to the Matchmaker Exchange website (http://www.matchmakerexchange.org) via Decipher (https://decipher.sanger.ac.uk), in an attempt to identify other families with similar phenotypes and variants in the same gene. However, the work in this chapter confirms that these families are likely to be mutation negative for *TMEM17* and *TMEM218*, two genes that are strong functional candidates for ciliopathies.

In a very recent study, Shamseldin et al. (2020) identified a single-nucleotide homozygous variant in *TMEM17* (NM_198276:c.302G > T:p.Gly101Val) in a Saudi Arabian child with Joubert syndrome. The authors suggest that this is a probable pathogenic *TMEM17* mutation, sufficient to explain the clinical phenotype in this family. The functional study of (Chih et al., 2011) strongly implicates TMEM17 as a functional candidate gene, and I would recommend that *TMEM17* is included in all targeted sequencing panels for MKS, JBTS and other ciliopathies.

Chapter 3 Construction and expression of TMEM plasmids and purification of the TMEM67 N-terminal region (Nt-TMEM67) in mammalian cell lines

3.1 Introduction

This chapter describes the production and use of expression constructs for a selection of genes that encode members of ciliary transition zone complexes. These genes were selected from the current literature (Huang et al., 2011, Williams et al., 2011, Chih et al., 2011, Li et al., 2016); therefore, TMEM17, TMEM67, TMEM138, TMEM216, TMEM231, and TMEM237 were studied. All of the selected ciliary transition zone genes encode proteins that have important biological function and are mutated as a cause of ciliopathies including JBTS, JSRDs, and MKS (Ben-Salem et al., 2014, Leightner et al., 2013) (see Table: 1.4, 1.5, and 1.6). The initial biochemical characterization of these TMEM proteins, and the description of their protein-protein interactions in complexes, therefore provides insights into how ciliogenesis is facilitated at the ciliary transition zone and could further explain the pathogenic mechanisms in ciliopathies and cystic kidney disease.

To accomplish these goals, "Gateway" cloning technology (Invitrogen Life Technologies) was used to make expression constructs by cloning selected complementary DNA (cDNAs) encoding transition zone TMEM proteins into multiple vector systems. "Gateway" cloning technology is based on a site-specific recombination system which involves a 2-step process. The first step is cloning the gene of interest into an "Entry" vector using a BP clonase reaction (Figure 3.1). This involves the BP clonase catalysing the recombination of the attB sites flanking the insert PCR products or sub-cloning DNA and the attP sites of the donor vector. As a by-product of this reaction, the entry clone contains the DNA of interest flanked by *att*L sites and the gene for kanamycin resistance. The *ccdB* gene was excised from the donor vector. The next step is sub-cloning the gene of interest from the Entry clone into a "Destination" vector using the LR clonase reaction to produce the expression clone (Figure 3.1).

The full-length open reading frame (ORF) cDNA for selected TMEM genes were cloned into "Gateway" destination vectors to enable fusion with an N- or C-terminus of an epitope tag, Strep/FLAG (SF-TAP) tag or eYFP. Constructs encoding either SF-TAP, eYFP or 3xFLAG-tagged TMEMs were transfected into HEK-293 and mIMCD-3 cells and the exogenous expression of each protein was verified by western blot (WB). The HEK-293 cell line was used in this study (Table 3.1) due to its high transfection efficiency (Liste-Calleja et al., 2015). Then, the subcellular localization of each TMEM was examined by confocal fluorescence microscopy using the ciliated mIMCD-3 cells (see section 4.3.1) followed by co-immunoprecipitation experiments (see section 4.3.2) in order to identify protein-protein interactions by biochemical methods. In this study, Entry clones including TMEM17, TMEM138, TMEM216, TMEM231 and TMEM237 were the kind gift of Prof. Ronald Roepman, Radboud University Medical Centre, Nijmegen, The Netherlands, whilst TMEM67 was purchased as a Gateway PLUS shuttle plasmid construct for TMEM67 (NM_153704.5) from GeneCopoeia. The manufacturer's protocol was followed for all cloning steps (see section 3.2.3.1).

The SF-TAP-tag construct contains a 3xFLAG tag: the GW331 and GW306 Destination vectors were used to produce SF-TAP N-terminal fusions, and the GW332 and GW311 vectors for C-terminal fusions (Table 3.2). These vectors were suitable for studying the subcellular localization of ciliary proteins due to the small epitope size compared to green Fluorescent Protein (GFP) (Appendix B.1). Analysis by the SignalP program http://www.cbs.dtu.dk/services/SignalP/ of TMEM17, TMEM138, TMEM216, TMEM231 and TMEM237 protein sequences did not show any evidence of a predicted signal peptide though this was not considered unusual since the first transmembrane helix can be used as a signal peptide during membrane insertion of type 2 and multi-span membrane proteins (H. Lodish, 2007, Zimmermann et al., 2011). Therefore, these TMEMs were N- terminal tagged. No evidence of mis-localization for these N-terminal tagged TMEMs was observed and alternative C-terminal tagged versions were therefore not constructed. In the case of *TMEM67*, this receptor protein has a clear prediction of a signal peptide and it was therefore C-terminal tagged. The GW315 vector was used for eYFP C-terminal fusions while GW332 was used for Strep/FLAG C-terminal tagging (Table 3.2).

In this chapter, I also describe the expression and purification of the extracellular N-terminal region of TMEM67, a ciliary-associated transmembrane protein which is essential to a wide range of cell biological processes, particularly Wnt signal transduction pathways (see section 1.6.3.1). Therefore, in this Chapter, I hypothesized that the extracellular domain is critical for cell surface expression and secretion (Figure 1.10). This domain may not only be essential for junctional localization but may also have a role in ligand binding and/or protein-protein interaction networks. Immunodetection of the TMEM67 extracellular N-terminal (Nt) domain indicates that it is localized in the cellular and ciliary membranes (Dawe et al., 2007). The domain is rich in cysteine residues, similar to the cysteine-rich domain of Frizzled receptors (Dawe et al., 2007). Abdelhamed et al. (2015) suggested that TMEM67 binds to the Wnt5a ligand using the extracellular cysteine-rich domain to mediate downstream non-canonical Wnt signalling, with ROR2 acting as a co-receptor. The extracellular cysteine-rich domain is encoded by exons 8 to 15, spanning amino acids 30-187 of the protein, in which most missense mutations cluster that cause a range of ciliopathies (Iannicelli et al., 2010).

The main purpose for producing purified N-terminal (Nt)-TMEM67 was to generate "Affimers", artificial non-antibody binding proteins (Roovers et al. 2007; Tamaskovic et al. 2012; Sha et al. 2017) specific for the extracellular domain of TMEM67. These are useful in localization studies or as potential chaperones for the optimization of protein crystallization. Antibodies have long been vital tools for research, however concerns have been raised over their lack of validation and renewability (Bordeaux et al., 2010; Bradbury and Plückthun, 2015). By contrast, the purification success rate of Affimers is more than 95%, their concentration range is between 50-100 mg/l, they are cheap and easy to produce and purify, and they can have high specificity for the target protein (Tiede et al., 2014). Nt-TMEM67 was able to be secreted into culture medium via a secretion leader and could be detected by immunofluorescence images and immunoblotting analysis.

Membrane proteins have proven to be difficult to study. Transmembrane proteins are embedded in a complex and dynamic lipid bilayer that makes them difficult to extract and purify from cells by mechanical methods or chemical buffers. This section highlights the issues associated with biochemical isolation and purification of the transmembrane protein

TMEM67, as well as providing an overview of the techniques used to successfully purify the extracellular domain of TMEM67 (see section 3.3).

The aims of this chapter were to:

- Produce expression constructs using 'Gateway' cloning for analysis of the subcellular localization and biochemical interactions of TMEM proteins.
- Optimise and utilise a method for generating stably-transfected mammalian cell lines for protein expression.
- Develop an artificial binding protein reagent (Affimer), for the *N*-terminal extracellular domain of TMEM67 for *in vivo* or *ex vivo* detection of ciliary localization.

3.2 Materials and methods

Unless otherwise stated, all common chemicals and reagents were purchased from Sigma-Aldrich, Invitrogen, Dako, Bio-Rad, Roche and Thermo Fisher Scientific. Corning® tissue culture plastics were purchased from Sigma-Aldrich unless otherwise specified. Cell culture work was performed under sterile conditions in a NuAire Labgard 437 ES Class II Biosafety Cabinet. Unless otherwise stated, solutions were made up in dH_2O or deionised water (DI water) (Milipore) and stored at room temperature (RT) between 20- 22°C. General solutions such as Dulbecco's phosphate-buffered saline (DPBS) (Sigma-Aldrich #P4417) was made by dissolving one tablet in 200 ml dH_2O at RT to obtain 1x DPBS solution. DPBS-T was prepared by adding 0.1% (v/v) Tween20 (Sigma-Aldrich) to 1x DPBS. In this Chapter, unless stated otherwise all solutions were kept on ice. PCR reagents and programmes were described in more detail elsewhere (see section 2.2.3). Buffers used in this study are listed and detailed in the next section.

3.2.1 Buffers used in this study

3.2.1.1 CHAPS Lysis buffer*

TrisCl pH7.6	50 mM
NaCl	150 mM
CHAPS	10 mM

3.2.1.2 NONIDET-P40 (NP40) Lysis buffer*

Tris-HCl pH8	20 mM
NaCl	150 mM
Glycerol (Sigma-Aldrich)	10 %
EDTA	0.5 M
NP40 (IPEGAL CA-630) (Sigma-Aldrich)	1 % (v/v)

* x100 dilution of "Halt" Protease/Phosphatase Inhibitor Cocktail (Thermo Fisher Scientific #78442) supplemented buffers immediately before use

3.2.2 Cell culture

mIMCD-3 and HEK-293 cell lines were used in this study Table 3.1. Early passage cells were obtained from the American Tissue-type Cell Collection (ATCC) and cultured according to standard mammalian tissue culture protocols provided by the supplier, employing sterile technique. mIMCD-3 cells were maintained in Dulbecco's Modified Eagle Medium: Nutrient Mixture F-12 (DMEM/F-12) while HEK-293 cells were maintained in Dulbecco's Modified Eagle's Medium (DMEM). All culture medium was supplemented with 10% (v/v) foetal calf serum (FCS) (Sigma-Aldrich #7524) unless stated otherwise and 1% penicillin and streptomycin (P/S) (Thermo Fisher Scientific #15140122). The latter was used as a bacterial and fungal antibiotic to avoid contamination but was not added to the medium during cell transfection in order to avoid toxicity effects. Cells were grown in Corning® 25cm^2 (T25), 75 cm^2 (T75), and 150 cm^2 (T150) cell culture flasks (Sigma-Aldrich respectively #430639, #431464U, #430825).

Table 3. 1: Cell lines, origin, medium, and suppliers used in this thesis.

Cell line (Suppliers)	Origin	Split frequency	Culture medium (Suppliers)
mIMCD-3 (CRL-2123, ATCC)	Mouse kidney, medulla/collecting duct (epithelial adherent)	Twice/week* (1 in 10)	DMEM/F12 (GIBCO)
HEK-293 (ATCC)	Human embryonic kidney (epithelial non-adherent)	Twice/week* (1 in 10)	DMEM (Sigma-Aldrich)

* Split frequency and ratio were for T75 flasks but can be scaled up or down to accommodate flask size.

3.2.2.1 Harvesting and passage of cells

In general, a T75 flask was used when culturing cells. Cells were sub-cultured at 72 hours intervals (when monolayers were 90% confluent) by removing the old culture medium and gently washing with 10 ml of 1x DPBS (Sigma-Aldrich #D8537) modified without calcium chloride and magnesium chloride. Cells were then detached using 1x trypsin-EDTA solution (0.5 g/L trypsin and 0.2g/L EDTA), stock 10x (Sigma-Aldrich #T4174) diluted 1:10 in DPBS to 1x concentration. Cells then were briefly incubated in a cell incubator (Sanyo MCO 20A/C set at 37°C with 5% CO_2) until cells rounded and began to detach from the substrate during

light microscopic observation (4-15 minutes). Trypsin was then inactivated with 10 ml of culture medium and the cells pelleted by centrifugation for 5 min at 200 x*g*, RT. The cell pellet was resuspended in 10 ml fresh medium. Cell suspension was dispensed into fresh flasks containing culture medium at a ratio of 1:10. The flask was gently rocked back and forth, side to side, to distribute the cells evenly. Then flask was placed in a horizontal position in the incubator.

3.2.2.2 Cell count and viability

Before placing cells into plates or flasks for experimental work, a Countess automated cell counter was used to calculate the viable cell density in order to determine the number of cells in the cell suspension and allow an accurate cell per volume seeding density. This used the Trypan Blue exclusion method. In a micro-centrifuge tube, 10 µl of cell suspension was mixed with 10 µl 0.4% trypan blue (Thermo Fisher Scientific #T10282). 10 µl of this mixture was then loaded onto a Countess^{TM} cell counting chamber slide (Invitrogen™ #C10228) and inserted into the Countess Automated Cell Counter for analysis.

3.2.2.3 Freezing cell lines

Mycoplasma testing was performed prior to freezing or every 3 months. Supernatant was collected from confluent cells, centrifuged for 5 minutes at 400 *xg* RT and 1 ml of the supernatant was collected and stored at - 20°C prior to examination by Dr Sarah Perry, Senior Laboratory Manager, Leeds Institute of Medical Research.

Cells were harvested (see section 3.2.2.1) and resuspended in chilled freezing solution [70% FCS, 20% medium, 10% dimethyl sulfoxide (DMSO) (Sigma-Aldrich #D4540)]. The suspension was added to 1 ml cryovials (Thermo Fisher Scientific # 368632); T25, T75, and T150 flasks were enough to generate 1, 3, and 7, 1 ml cryovials per flask respectively. The vials were slowly frozen to -80°C overnight in a Mr Frosty container (Thermo Fisher Scientific # 5100-0001). On the following morning, the vials were moved to a liquid nitrogen cryo-store for long-term storage.

3.2.2.4 Thawing frozen cells

Vials were defrosted at 37°C in a water bath for 1 minute, and then disinfected thoroughly using 70% ethanol (Sigma-Aldrich # 32221). The contents were transferred into 15 ml centrifuge tube (Sigma-Aldrich #430790) and gradually diluted by drop-wise addition of 10 ml of warmed growth medium followed by centrifugation for 5 minutes at 200 *xg*, RT to remove any traces of DMSO. Spent medium was removed by aspiration and cells resuspended with 5 ml fresh growth medium then added to a T25 flask. The flask was tilted to evenly disperse cells and placed in the incubator.

3.2.3 Microbiology

Luria Bertani (LB) broth was made up with 20 g LB powder (Sigma-Aldrich) in 1 litre of dH$_2$O and autoclaved in a bench top autoclave (Prestige Medical, Coventry UK) in a dedicated microbiology lab. Agar plates were made by dissolving 15 g of agar powder (Merck) into 1 litre LB. This was autoclaved in a bench top autoclave (Prestige Medical, Coventry UK) and cooled to around 50°C. Ampicillin (final concentration 50 µg/ml) or kanamycin (final concentration 50 µg/ml) was added to the mixture from stock solutions (100 mg/ml, kept frozen at -20°C until immediately before use). Approximately 25 ml of the prepared agar was plated per 100 mm x 15mm polystyrene Petri dish, left to cool and then stored upside-down at 4°C for up to a month wrapped in Parafilm.

3.2.3.1 Gateway Cloning

"Gateway" cloning technology (Thermo Fisher Scientific) is a universal cloning method that based on the highly specific integration and excision reactions of bacteriophage λ into and out of the *Escherichia coli* genome at specific sites of recombination ("*att*" sites). This technology allows shuttling of a gene of interest into multiple vector systems (Figure 3.1). The BP Clonase II reaction generates "Entry" constructs which were either received as gifts or purchased (Section 3.2), and this reaction is not described further in this study. The LR Clonase gateway reaction was performed as described in the manufacturer's protocol to sub-clone cDNAs into the "Destination" vectors GW306, GW311, GW315, GW331 and GW332 (see Table 3.2 for further details). The following components were added and mixed in a 1.5 ml Eppendorf micro-centrifuge tube

at RT: 150 ng of Entry clone, 150 ng Destination vector, 2 µl 5x LR Clonase™ Reaction Buffer, and 4 µl 1x TE buffer pH8.0 (10 mM Tris-HCl,1 mM EDTA; Thermo Fisher Scientific). The LR Clonase enzyme mix was thawed on ice for 2 minutes and vortexed briefly once. 2 µl of LR Clonase™ enzyme added to each reaction and mixed by vortexing briefly. The mixture reaction was then incubated for 1 hour at RT. Afterward, 1 µl proteinase K solution (2 µg/µl) (Roche) was added to each reaction and vortexed briefly twice to terminate the reaction and incubated at 37°C for 10 minutes. The reaction generates an expression clone with the DNA of interest flanked by *att*B sites and the *ccdB* gene excised from the Destination vector (Figure 3.1). All cDNA clone sequences were confirmed by Sanger sequencing. For primer sequences see Appendix B.2.

Table 3. 2: Gateway vectors (GW) used in this study. Abbreviation: Cytomegalovirus (CMV); Ampicillin (Amp); Neomycin (Neo).

GW vector	Tags	Description
GW 306	p3xFLAG_CMV/DEST (tag at N-terminus)	Mammal; CMV; 3xFLAG; Amp; 8025
GW 311	pDEST-510 (tag at C-terminus)	Mammal; CMV; Amp/Neo; based on pDEST47; 7569
GW315	pDEST-504 (tag at C-terminus)	Mammal; CMV; Amp/Neo; e YFP; 7569
GW331	Strep/FLAG (tag at N-terminus)	Mammal; CMV; Amp; Nt-TAP
GW332	Strep/FLAG (tag at C-terminus)	Mammal; CMV; Amp; Ct-TAP
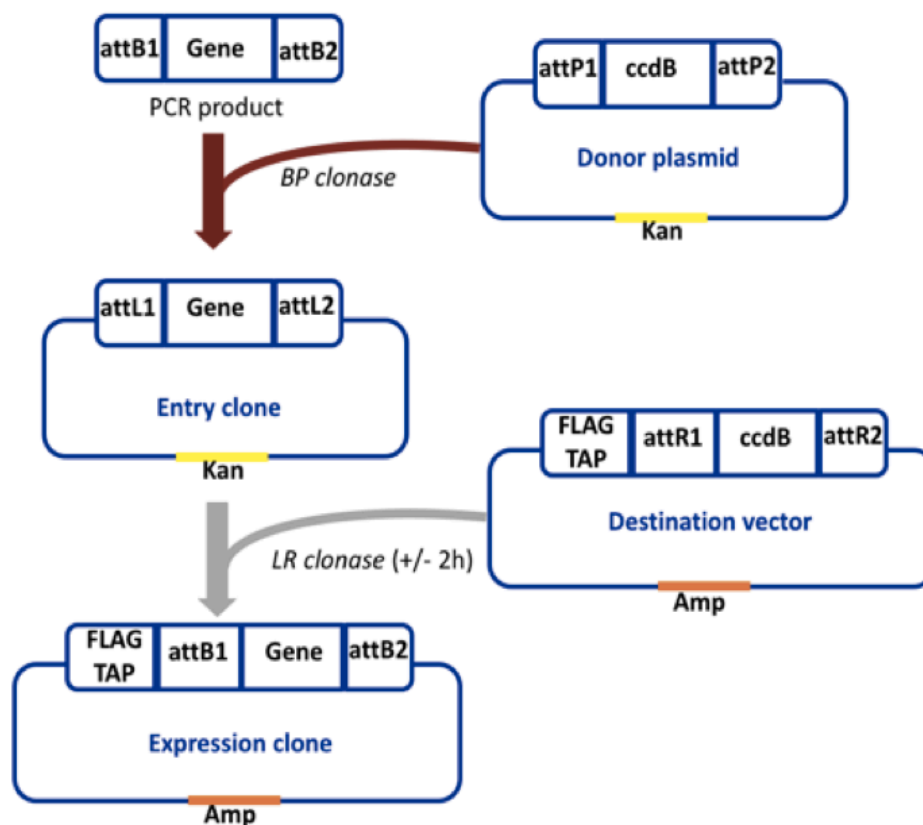
Figure 3. 1: Gateway cloning methods. The Gateway LR reaction (grey arrows) was performed in this study which allows the gene of interest within an Entry clone to be combined with the Destination vector to create the desired expression clone. In this study, full-length cDNAs of the selected TMEM genes were successfully Gateway cloned with N- or C-terminal SF-TAP- eYFP or 3xFLAG epitope tags for use in expression studies. Schematics of the N-terminal TAP TMEM138, TMEM216, and TMEM237 constructs are shown in Appendix B.1.

3.2.3.2 Transformation

Frozen α-Select Chemically Competent cells (50 µl, Bioline) were thawed on wet ice. In a micro-centrifuge tube, 10 to 50 ng of plasmid DNA were added into the competent cells. The mixture was incubated for 30 minutes on ice, then the tube was placed in 42°C water bath for 45 second, without shaking; the tube that contained the transformed cells was then replaced on ice for 2 minutes. 150 µl super optimal broth with catabolite repression (SOC) recovery medium (New England Biolabs) (without antibiotics) was added into the transformed cells. The tube was then placed on a temperature-controlled shaker at 37°C for 1 hour at 270 revolutions per minute (rpm) to allow recovery of cells after heat shock and transformation.

100 µl and 50 µl aliquots of the bacteria were plated by spreading onto selective LB agar plates containing the appropriate antibiotic(s) at 50 µg/ml (see section 3.2.3) and incubated at 37°C overnight and inverted to prevent water condensation from accumulating and disturbing colony growth.

Isolated colonies were picked using a plastic loop and grown in Corning 50 ml centrifuge tubes (#CLS430828) or 30 ml universal containers plain label (#SL7504) containing Luria-Bertani (LB) medium with appropriate antibiotic (see section 3.2.3). The bacterial culture medium was then placed in a temperature-controlled shaker at 37°C, 230 rpm, overnight unless otherwise stated. The following day, overnight cultures were used to inoculate a larger culture volume at a 1/200 dilution. Cultures were grown at 37°C, 230 rpm overnight.

The culture was harvested in a bench-top micro-centrifuge at 12000 xg for 3 minutes, RT. After the culture had been pelleted, QIAprep Spin Miniprep Kit (QIAGEN) was carried out using 1.5 ml of the culture to isolate plasmid DNA following the manufacturer's instructions. The plasmid was then digested to confirm the size of the insert, followed by a sequencing reaction. For high-copy plasmids, 1 ml of bacterial culture was transferred to aerated conical flasks containing 200 ml broth and expanded for 16 hours on a temperature-controlled shaker for 2 hours, 270 rpm at 37°C. A QIAfilter Plasmid Midi and Maxi Kit (QIAGEN) was used to isolate plasmid DNA following the manufacturer's instructions. DNA plasmid concentrations were determined by photo spectrometric means using the 260/280 nm measurements on a NanoDrop ND-1000 spectrophotometer.

3.2.3.3 Small and large-scale plasmid DNA purification

Mini and maxi-prep followed the same basic protocol with changes in volumes and times as indicated by mini/maxi protocol. Briefly, a colony grown on LB plates was picked and grown overnight at 37°C, 230 rpm in 5 ml of LB with the appropriate selection antibiotic. Plasmid purification was performed using QIAGEN Plasmid QIAprep Midi and Maxi Kit (QIAGEN) according to the manufactures' instructions. DNA was eluted in the appropriate volume of 1x TE buffer and stored at -20°C.

3.2.3.4 Restriction endonuclease digests

All restriction endonucleases used were purchased from New England Biolabs, or Promega and used with the appropriate NEB buffer and bovine serum albumin (BSA) according to the manufacturer's instructions in a total volume of 50 µl: 1 U restriction enzyme(s), 500 ng DNA, 1x NEBuffer, 1x BSA, dH$_2$O added to 50 µl. All digests in this study were performed in a heat block at 37°C. In general, up to 500 ng of DNA was used for digestion. The unit number required of the restriction enzymes was calculated based on the amount of DNA but in general 10-20 units were added per µg of DNA in each reaction. The samples were cleaved with a restriction enzyme having a known restriction site position, followed by sequencing analysis methods (see section 2.2.5). The restriction enzymes used in this study are shown in section 3.3.1.

3.2.3.5 Agarose gel electrophoresis

Plasmid DNA, PCR products, and digested PCR products were separated using agarose gel electrophoresis. The gel was composed of molecular biology grade agarose powder (Bioline) and suspended in 1x TRIS-acetate-EDTA (TAE) buffer [2M Tris HCl, 50 mM EDTA (pH 8), 0.97 M glacial acetic acid (Sigma-Aldrich)] at the requisite concentration and boiled until the agarose dissolved. The agarose concentration varied from 0.7% to 4% (w/v) depending on the predicted size of the DNA fragments. The agarose gel was then cooled and mixed with 0.5 µg/ml of ethidium bromide (Sigma-Aldrich) or 5 µl/100 ml of Midori Green (Geneflow). A multiwall comb was then inserted and the gel was allowed to solidify. DNA samples were mixed with an appropriate volume of 10x DNA loading buffer [30% (v/v) glycerol (Sigma-Aldrich), 0.25% (w/v) Orange G (Sigma-Aldrich)]. DNA samples were loaded alongside 1 kb DNA Ladder (Promega) or Easy Ladder I (Bioline) depending on the estimated size of the products. Electrophoresis was performed in a Mini-Sub Cell GT apparatus (Bio-Rad) in 1x TAE buffer and the DNA samples were run at 90 volts (v) for 45 minutes. Bands were visualised on a UV transilluminator and displayed using Image Lab (v. 4.0) analysis software (Bio-Rad).

3.2.4 Preparing plasmid DNA-lipid complex for transient mammalian cell transfection

1 μg plasmid DNA was mixed with 100 μl of Opti-MEM reduced serum medium (Gibco #31985-047) in a centrifuge tube. 10 μl of the transfection reagent, Lipofectamine 2000 (Thermo Fisher Scientific) was mixed with 90 μl of Opti-MEM medium in a centrifuge tube. Both centrifuge tubes were mixed thoroughly and incubated for 20 minutes at RT. The transfection mixture was then added into 70% confluent cells containing 1.8 ml of Opti-MEM medium/well. Cells were then incubated in an atmosphere of 5% CO_2 at 37°C in full humidity 98%. To remove transfection complexes, the medium was replaced with fresh medium the next morning and the cells were incubated for an additional 56 hours. Cells were then visualized and analysed using confocal microscopy or western blotting.

3.2.5 Immunofluorescence
3.2.5.1 Preparation of slides and staining for confocal microscopy visualization

Coverslips (22x22mm) (Scientific Laboratory Supplies #MIC3346) were sterilized by sequential washing with 70% ethanol, and absolute acetone, followed by air-drying in a laminar flow hood. The sterilised coverslips were placed into each well in Corning® Costar® 6-well flat-bottom plates (Sigma-Aldrich #3506). An average yield of cells from a confluent culture was subsequently seeded into each well; 80% confluency was achieved by plating $1x10^5$ cells per well, 48 hours prior to transfection (see section 3.2.2.2) and growth medium was added to a total volume of 2 ml/well and the plate was placed horizontally in the incubator overnight (see section 3.2.2.1). Following DNA transfection (see section 3.2.4), after the incubation period, the transfected cells were washed 3 times with 1x DPBS (Sigma-Aldrich #P4417, see section 3.2.1). After aspirating the DPBS, the cells on the coverslips were fixed with ice cold methanol (Sigma-Aldrich #32213) and incubated for 5 minutes in a freezer. Alternatively, cells were fixed with 4% (w/v) para-formaldehyde (PFA) (Sigma-Aldrich) was dissolved in 1x DPBS for 20 minutes at RT; afterwards, the PFA/DPBS solution was aspirated and cells were permeabilized by treatment with 0.1% (v/v) Triton x-100 (Sigma-Aldrich) in DPBS for 5 minutes in order to facilitate antibody penetration. The fixed cells were washed 3 times with 1x PBS, blocked in a solution of [1% (w/v) Marvel non-fat dried milk (Marvel) diluted in DPBS-0.01% (w/v) Tween-20 (DPBS-T)] on a plate mixer for 15

minutes. The blocking solution was clarified by centrifugation immediately before use to remove any particulates.

Cells adhering to the cover-slips were labelled with labelling solution as follows. Briefly, primary antibodies, which were optimized (Table 4.1 in Chapter 4) were diluted in the 1% (w/v) "Marvel" blocked milk solution and centrifuged at 1000 xg for 2 minutes to precipitate any insoluble substance. Cells were incubated for 1 hour in a humidity chamber in a dark cabinet by inverting the coverslips into 100 µl of the diluted primary antibody solution. The coverslips were then washed 3 times with 1x DPBS-T. Fluorophore-conjugated secondary antibodies (1:500) were also diluted in blocking solution and clarified by centrifugation (Table 4.2 in Chapter 4). Cover-slips were inverted onto 100 µl of the secondary antibody solution and incubated in a humidified chamber in darkness for 1 hour. Coverslips were then washed 3 times with DPBS-T and once with dH_2O. A 50 µl drop of Mowiol® (Sigma-Aldrich) mounting solution was placed in the centre of each marked slide. The coverslips were removed with forceps and the underside (non-cell side) was gently wiped. Then the coverslip was carefully mounted, cell-side down, onto the mounting solution. Slides were left to allow the Mowiol to solidify overnight in the dark. The cells were visualized using a confocal laser-scanning microscope (Nikon A1R) using 60x and/or 100x oil-immersion objectives.

3.2.5.1.1 Confocal microscopy

Confocal images of immunofluorescent staining of ciliated cell-line (see section 3.2.5.1) were visualized using a 100x oil-immersion objective using a Nikon A1R confocal microscope, processed by NIS-Elements Confocal 4.5 (Nikon) software. Slides were viewed using wide-field epifluorescence with DAPI blue filter, violet diode (laser excitation (λex) = 340-380 nm and emission λem 400 nm); FITC green filter, argon laser (λex = 460-500 nm and λem 505 nm); TRITC red filter, HeNe543 laser (λex = 528-553 nm and λem 565 nm). Confocal images were processed using Nikon EZ-Cl 3.50 software.

3.2.6 SDS-PAGE western blot analysis of cell lysates

3.2.6.1 Lysate preparation

Confluent transfected and non-transfected HEK-293 cells were washed with cold 1x DPBS (Sigma-Aldrich #P4417) and pelleted by centrifugation. Cells then were incubated for 10 minutes at 4°C in an appropriate cold lysis buffer. The lysis buffers contained a variable degree of detergents, salts, and enzymatic inhibitors, including Protease/phosphatase Inhibitor Cocktail (Thermo Fisher Scientific). Lysed cells were scraped off the plate, transferred into a micro-centrifuge tube and kept on ice. To break apart cells and solubilize proteins, cells were then sonicated for 10 seconds at 40% power using a Sanyo Soniprep 150 Sonicator to ensure total cell lysis and membrane disruption, reduction of sample viscosity and increased protein yield. Subsequently, the cell lysates were micro-centrifuged for 10 minutes at 12000 *xg*, 4°C. When the lysate was not required immediately, the supernatant was frozen at -80°C.

3.2.6.2 Protein blotting

Each protein sample was mixed with an equal volume of 2x sodium dodecyl sulphate (SDS) loading buffer [100 mM Tris-HCl pH 6.8; 4% (w/v) SDS (BDH); 20% (v/v) glycerol (Sigma-Aldrich); 20 mM β – mercaptoethanol (BDH); 0.004% (v/v) Bromophenol Blue (Sigma-Aldrich)] and 40 µl/sample of the mixture was heated at 95°C for 5 minutes. An XCell SureLock electrophoresis tank (Invitrogen) was filled with 1x NuPAGE® MES-SDS running buffer (Thermo Fisher Scientific). Approximately 20 µl of a heated protein sample was loaded into 4-12% Sodium dodecyl sulfate polyacrylamide gel electrophoresis (SDS-PAGE) (Life Technologies). Precision Plus Protein™Standards 'All Blue' (Bio-Rad) were loaded onto the gel as a size standard during electrophoresis. Samples were run and separated at 120 v for 90 minutes. After gel electrophoresis, western blotting was performed to transfer proteins from the gel to a polyvinylidene fluoride (PVDF) membrane (Life Technologies #LC2005). The membrane was activated by immersing in absolute methanol (Sigma-Aldrich #32213) for a few seconds before use. A sandwich was made between the SDS-PAGE gel and the activated membrane and 2 filter papers and 8 sponges. The prepared sandwich was then placed into an XCell SureLock electrophoresis tank (Invitrogen) filled with 1x NuPAGE

transfer buffer (Invitrogen) supplemented with 10% (v/v) methanol (Sigma-Aldrich #32213) while the surrounding tank was filled with water. The transfer sandwich was run at 30 v for 90 minutes.

3.2.6.3 Membrane blocking and antibody incubations

After the transfer, the membrane was incubated in 50ml of a blocking buffer (5% (w/v) non-fat dried marvel milk or 5% BSA containing 1x DPBS with 0.1% (v/v) Tween® 20 (1x DPBS-T) for an hour at RT. The membrane then was incubated with primary antibodies, at the appropriate dilution and buffer with gentle agitation overnight at 4°C (Table 4.3 in Chapter 4). Following washes with 1x DPBS+ 0.1% Tween 20 (DPBS-T) (3x, 10 minutes), Horseradish peroxidase (HRP)-conjugated secondary antibody (Dako) was applied at 1:5000 dilution in blocking buffer with gentle agitation for an hour at RT to detect protein bands and the biotinylated protein markers. The membrane was washed with PBS-T (3x, 10 minutes) and the molecular weights of bands were estimated relative to the protein markers over the 10 to 250 kDa range by treating the membrane with SuperSignal West Femto Maximum substrate (Thermo Fisher Scientific) to target antigens and develop the immune-positive bands. Protein bands were quantified by densitometry using Image Lab Software (Bio-Rad).

3.2.7 pSecTag2A_Nt-TMEM67 production and purification

3.2.7.1 Generation of stable cell lines
3.2.7.1.1 pSecTag2A_Nt-TMEM67 linearization and purification from agarose gels

pSecTag2A_Nt-TMEM67 plasmid was linearized with *PuvI* before transfection to increase the chances of productive integration and the linearized plasmid was run on agarose gels as described (see section 3.2.3.5). Following electrophoresis, the agarose gels were visualised on a UV transilluminator in a dark room. The desired DNA fragments were excised from the gel with a clean scalpel. To maintain DNA integrity, UV exposure was kept to a minimum. DNA extraction was performed using the QIAquick gel extraction kit (QIAGEN), following the manufacturer's instructions. The DNA was eluted in 50 µl TE buffer. The eluted DNA was transferred to a fresh micro-centrifuge tube and the purified DNA

quantified using the NanoDrop ND-1000 spectrophotometer (Thermo Fisher Scientific) then stored at -20°C.

3.2.7.1.2 Calcium chloride eukaryotic cell transfection

First, calcium chloride transfection solutions were prepared as follows: 2M $CaCl_2$ (100 ml) was made up by dissolving 29.4 g $CaCl_2$ powder in 100 ml dH_2O and the pH was checked to be near-neutral. The solution was filter sterilized using a 0.2 μm Millipore "Millex" sterile syringe-driven filter. 2x HBS (100 ml) was made up with 1.6 g NaCl, 1.3 g 4-(2-hydroxyethyl)-1-piperazineethanesulfonic acid (HEPES), and 0.07 g $Na_2HPO_4.2H_2O$ in 100 ml dH_2O (adjusted to pH 7 and filter-sterilized). Second, HEK-293 cells were plated in a Corning® Costar® 6-well flat-bottom plate (Sigma-Aldrich #3506). Cells at 20% confluence were grown and incubated for 1-2 hours at 37°C, 5% CO_2 to allow cell adhesion and spreading. 25 μg of pSecTag2A_Nt-TMEM67 was mixed with dH_2O to a volume of 493 μl. 61 μl of 2 M calcium chloride solution was added to the DNA mixture. 500 μl of freshly thawed 2x HEPES-Buffered Saline (HBS) pH7 was added to the DNA mixture drop-wise with constant mixing at RT. The mixture was vortexed briefly and incubated for 20 minutes, RT, to allow plasmid DNA/calcium phosphate precipitates to form. The DNA-calcium chloride mixture was then distributed evenly over the adhered cells prepared in fresh DMEM growing medium (see section 3.2.2). The cultures were incubated at 37°C in 5% CO_2, avoiding any spiralling or swirling motion when putting the plate back, and then the medium was replenished after 24 hours. A time course was performed over 16 hours, 24 hours, 40 hours and 48 hours in order to determine the optimal times for transfection.

3.2.7.1.3 Zeocin selection of HEK-293 cells clones expressing pSecTag2A_Nt-TMEM67 and antibiotic kill curve

HEK-293 cells were subjected to increasing amounts of a selection antibiotic, Zeocin™ (InvivoGen), to determine the minimum concentration that kills all untransfected cells in a specific period of time in order to optimize the protocol for generation of stably-transfected cell lines. HEK-293 culture medium [DMEM (Sigma # RNBG7140) + 10% fetal bovine serum (FBS) + 1% P/S (Gibco)] was prepared and used as growing medium (Table 3.1) and HEK-293 selection medium [DMEM (SIGMA # RNBG7140) + 10% FBS + 1% P/S (Gibco) + 200 μg/ml Zeocin™] respectively.

A kill curve was performed by seeding the transfected cells (see section: 3.2.2.2 and 3.2.4) at a density of 1 x 10^5 cells/ml and plated in Corning® Costar® 6-well flat-bottom plate (Sigma-Aldrich #3506). The cells were directly cultured in DMEM growing medium as described above containing increasing amounts of Zeocin™ (10, 50, 100, 200 and 500 µg/ml) in order to determine the optimal antibiotic concentration for generating stably-transfected cell-lines. The medium was replaced every 2 - 3 days for a week and the cultures were examined every day for signs of toxicity. According to the curve (Figure 3.5 A), the concentration of 200 µg/ml was chosen which showed complete cell death as the minimum antibiotic concentration to use for selection.

The pSecTag2A vector contains a Zeocin resistance gene that was used to select for cells with a genome-integrated construct, to ensure that selection clones will be populated by stably-transfected pSecTag2A_Nt-TMEM67 cells alone. Cells were counted (see section 3.2.2.2) and seeded at a density of 2.5x10^6 cells in 10 ml selection media (200 µg/ml Zeocin) into round Corning 100 mm x 20mm dishes. Selection media was changed every 3-4 days, for 20 days, until cells formed only single colonies. Single colonies consist of several hundred cells growing in a cluster on the plastic substrate. Only colonies with a significant gap between other colonies were chosen for manual picking. Colonies were picked and removed from the dish by using normal sterile blue (P1000) pipette tips with the narrow end cut off. These colonies were transferred into 24-well plates, with one colony per well in 1 ml medium. These cells were grown for approximately 15-20 days, refreshing the selection medium every 3-4 days, until the colonies had become confluent. Afterwards, the surviving clones were transferred into T25, T75 or T150 cell culture flasks (Sigma-Aldrich respectively #430639, #431464U, #430825) for expansion. Transfected cells were maintained under Zeocin selection of 10 µg/ml for several additional days to maintain selection but to ensure cell recovery and were then grown in normal medium. Successful generation of the protein of interest was confirmed using a dot immunoblot assay (dot-blot) and western blotting (see section 3.2.7.1.4; Figure 3.5).

3.2.7.1.4 Dot-blots

The expression capability of the purified pSecTag2A_Nt-TMEM67 was validated using the dot blot assay. 200 µl of the media was vacuum aspirated onto a 0.45 µm

nitrocellulose membrane by using a 24-well dot-blot manifold. Before the membrane dried completely, 400 μl of 1x DPBS (Sigma-Aldrich #P4417, see section 3.2) was poured into the manifold and the membrane was rinsed in DPBS, blocked in 5% (w/v) Marvel non-fat milk and incubated with the primary antibody anti-c-myc mouse monoclonal (Cell signalling #96811). Thereafter, the membrane was washed with DPBS-T and incubated in 1:10000 dilution of horseradish peroxidase- conjugated anti-mouse secondary antibody (Dako #P0447) for 1 hour at RT. Excess block and antibody were removed through washes with DPBS-T. Chemiluminescent HRP-tagged antibodies were visualized using SuperSignal West Femto Maximum substrate (Thermo Fisher Scientific) and detected using a ChemoDoc MP Imaging System with Image Lab (v. 4.0) software (Bio-Rad) (see section 3.2.6.3).

3.2.7.2 Chromatography columns used in this study

His SpinTrap columns (GE Healthcare #GE28-9321-71) were used according to the manufacturer's instructions to confirm the production of a stable clonal cell-line expressing the protein of interest by western blotting (Figure 3.5 C). An AKTA purification system at Leeds Institute of Medical Research was initially used and then subsequently an AKTA chromatography system at the Protein Production Facility, University of Leeds, under the supervision of Dr Brian Jackson, using the following purification columns to purify Nt-TMEM67:

3.2.7.2.1 Affinity chromatography

Tissue culture medium containing secreted protein was filtered and applied to a 1 ml Ni^{2+} Sepharose HisTrap HP column (GE Healthcare) on an AKTA purifier Fast Protein Liquid Chromatography (FPLC) system, equilibrated and washed with phosphate buffer (20 mM sodium phosphate, 0.5 M NaCl) and His-tagged protein was directly eluted using 0.5 M imidazole in phosphate buffer (20 mM sodium phosphate, 0.5 M NaCl, 500 mM imidazole). The maximum binding capacity was 50 mg His-tagged protein per ml resin. 1x DPBS was used as a wash buffer and the column then was then washed with 20 ml of the binding buffer (20 mM sodium phosphate, 500 mM NaCl, pH7.4) and 400 ml of the medium was loaded with a repeat wash and load. Elution fractions were then buffer-exchanged with 10 mM ammonium acetate. The peak fractions were collected, and mixed with an equal volume of (2x sodium dodecyl sulphate (SDS) loading buffer [100 mM Tris-HCl pH 6.8; 4%

(w/v) SDS (BDH, Poole.UK); 20% (v/v) glycerol; 20 mM β – mercaptoethanol (BDH, Poole, UK); 0.004% (v/v) bromophenol Blue (Sigma-Aldrich)] and analysed by SDS-PAGE alongside "All Blue" (Bio-Rad #161-0373) molecular weight marker, whole cell extract and wash fractions. Proteins were then immunoblotted to PVDF membrane (see Section 3.2.6.2), incubated with an anti-cmyc-tag monoclonal antibody (Cell Signaling #96811) (1:1000, overnight at RT) followed by a polyclonal goat anti-mouse HRP-conjugated secondary antibody (Dako #P0447) (1:10000, 1 hour, RT). Western blots were visualized on a ChemiDoc MP Imaging System with Image Lab (v. 4.0) software (Bio-Rad).

In subsequent experiments, the purification and elution protocols were optimized by using Opti-MEM reduced serum medium and a gradient elution method on the FPLC system in order to minimize contaminating bovine serum proteins (Figure 3.8). The elution buffer comprised an increasing gradient of imidazole (0 to 500 mM) in phosphate buffer, [20 mM sodium phosphate NaH_2PO_4, 500 mM NaCl, 500 mM imidazole, pH 7.4], visualised using Coomassie Blue staining and examined by western blotting with an anti-c-myc antibody as described above (Figure 3.8 B).

3.2.7.2.2 Ion exchange chromatography

The column was washed with a wash buffer [20 mM Tris pH 7.4]. The peak (elution 1-12 in total of ~22 ml) eluates from N-NTA column affinity purification were pooled and applied to a HiTrapQ HP Column (GE Healthcare) after concentration and buffer exchange to remove salt using Pierce protein concentrator PES, 10K MWCO (Thermo Fisher Scientific). Fractions were eluted from the ion exchange column by an increasing gradient of NaCl up to 1 M [20 mM Tris pH 7.4, 1 M NaCl].

3.2.7.2.3 Gel filtration chromatography

The fractions were concentrated using a spin column (cut off 10K) to a volume of 2 ml. Gel filtration chromatography on a Superdex 75 FPLC column (GE Healthcare) was used to further separate proteins on the basis of size and shape. The elution buffer [NaP buffer pH 7.4 (500 mM NaCl)] was used. Gels were also stained with InstantBlue stain (Expedeon) (see section 3.2.7.3.1), so that excised bands could be used directly for protein identification studies by MS.

3.2.7.3 Preparation of proteins for mass spectroscopy analysis (MS)

3.2.7.3.1 Coomassie Blue protein staining and InstantBlue staining solution

In order to visualise Nt-TMEM67 protein resolved on an SDS-PAGE gel, the gel was stained with Coomassie Blue staining solution (50% methanol (Sigma-Aldrich #32213), 0.6% Coomassie Brilliant Blue R-250 and 10% (v/v) acetic acid). The gel was fixed for 1 hour at RT in the reagent. The gel was then destained in 50% (v/v) methanol and 10% (v/v) acetic acid with several changes of destaining solution until the bands were visible and then photographed on the ChemoDoc MP Imaging System with Image Lab software (Bio-Rad). Commassie Blue was used after Affinity purification and Ione exchange chromatography.

The InstantBlue staining solution (Expedeon) however, was used to stain the gel after gel filtration chromatography. 20 ml InstantBlue staining was added to cover the gel and left for 15 minutes at RT with gentle shaking.

The gel was sliced and the desired bands were excised from the gel with a clean scalpel. The samples were transferred to a fresh micro-centrifuge tube and stored at -20°C. Samples were sent for mass spectrometry (MS) analysis to the Biomolecular Mass Spectrometry Facility, University of Leeds, unless stated otherwise.

3.2.7.3.2 Methanol/chloroform protein precipitation

The experiment was performed at RT. Four volumes of methanol (Sigma-Aldrich #32213) were mixed with 1 volume of the protein sample, vigorously for 60 seconds. Afterwards, 1 volume of chloroform was added and the mixture was vortexed for 60 seconds. Three volumes of dH_2O were then added to the mixture and vortexed for 60 seconds. The mixture was subsequently centrifuged at 1000 *xg* for 5 minutes. The mixture resolved into 3 phases. The proteins remained at the phase boundary between the upper aqueous methanol layer and the lower chloroform layer. The upper fluid phase was carefully removed and another 4 volumes of methanol (Sigma-Aldrich #32213) was added to wash the precipitate. The mixture was spun at for 15 minutes at 13000 rpm. The supernatant was discarded without disturbing the pellet, and the protein pellet was air dried and then stored at -80°C.

3.2.7.3.3 Acetone protein precipitation

This was performed at 4°C. Four volumes of ice-cold acetone were added to the protein sample and the mixture was briefly vortexed. The mixture was incubated at -20°C for 1 hour then centrifuged at 13,000-15,000 xg for 10 minutes, 4°C. The supernatant was removed carefully to avoid dislodging the protein and the protein pellet was air-dried. The protein was dissolved in PBS, transferred to a fresh micro-centrifuge tube and stored at -20°C. The sample was sent for MS analysis to the Biomolecular Mass Spectrometry Facility, University of Leeds.

3.3 Results
3.3.1 Construction of a series of TMEM gene-based Gateway vectors

The selected TMEM Entry clones were the full open reading frame (ORF) cDNAs of each gene, from the ORFeome Consortium (Invitrogen Life Technologies Inc). In this study, only LR reactions were performed using LR Clonase II Plus enzyme mix (Invitrogen) according to the manufacturer's instructions (see section 3.2.3.1). The method of Gateway cloning is shown in Figure 3.1. LR reactions were achieved and successful cloning was confirmed by restriction enzyme digestion analysis. The *PstI* enzyme was used to validate 3xFLAG-TMEM216, SF-TAP-TMEM216 and SF-TAP-TMEM138 constructs whilst *BamHI* was used to validate the 3xFLAG-TMEM237 and SF-TAP-TMEM237 constructs. The entire cDNA in each entry clone was sequenced, after validation by restriction digestion analysis, using the T7 and SP6 sequencing primers to cover the entire cloned insert for the selected proteins (data not shown). Each of the constructs was transfected into HEK-293 cells (see section 3.2.4) to confirm protein expression by western blotting (see section 3.2.6.2). Whole cell extracts from transfected constructs were prepared (see section 3.2.6.1) and cells were then extracted under mild conditions with CHAPS buffer (see section 3.2.1.1), electrophoresed on a 10% SDS-PAGE gel, followed by transfer to a PVDF membrane (Invitrogen #LC2005) (see section 3.2.6.3). The expression of the selected TMEM proteins were detected by either rabbit polyclonal anti-His$_6$ polyhistidine tag antibody (Cell signalling) against the expressed protein or mouse monoclonal anti-FLAG antibody (Sigma #F3165) against epitope-tagged proteins. The results showed that all TMEM proteins (TMEM17, TMEM138, TMEM216, TMEM231 and TMEM237) were successfully expressed

and clearly detected at their predicted molecular weight (Figure 3.2). In the case of *TMEM67*, an antibody against SF-TAP/FLAG-tagged TMEM67 detected 2 bands, 1 at about 150 kDa and 1 at 25 kDa, whereas the predicted size of *TMEM67* is 111 kDa. The difference between the predicted and actual detected sizes of *TMEM67* can be explained by the presence of possible post-translational modifications in the N-terminal extracellular region of the protein. The band at the lower 25 kDa molecular weight may be due to post-translational cleavage of the N-terminal extracellular region as a separate ectodomain. Validated expression vectors were used for analysis of subcellular localization of TMEM proteins (Chapter 4).
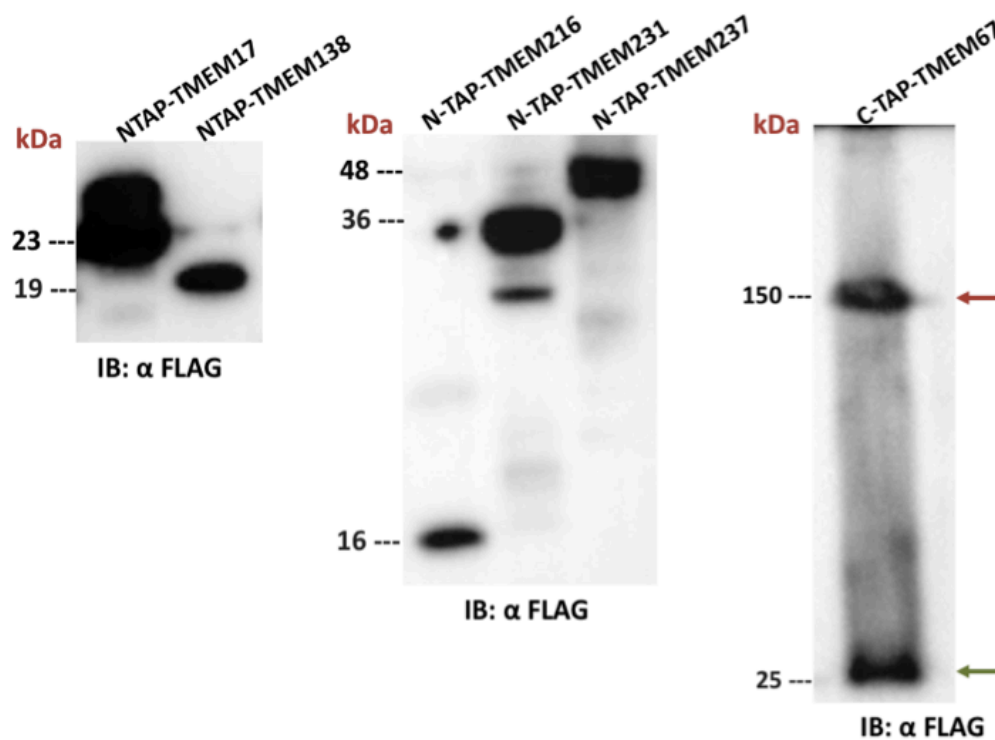
Figure 3. 2: WB analysis of extracts from HEK-293 cells using anti-FLAG antibody (1:2500). Constructs encoding TMEMs were transfected into HEK-293 cells, which were lysed after 48 hours and extracts examined by SDS-PAGE and WB using an anti-FLAG antibody (1:2500). The expected molecular weight (kDa) of each protein is indicated to the left of each blot. WB (left) detected 23 and 19 kDa bands, the expected sizes for tagged TMEM17 and TMEM138 respectively. Tagged TMEM216, TMEM231 and TMEM237 (middle) corresponded to bands of the expected sizes of 16, 36 and 45 kDa respectively. The band of ca. 150 kDa for TMEM67 (red arrow) is the expected molecular weight of the full-length protein with probable post- translational modifications (right). The smaller 25 kDa band (green arrow) indicates the presence of a possible cleaved ectodomain or non-specific band.

3.3.2 Nt-TMEM67 production and purification

A construct was made using the pSecTag2A expression vector (Figure 3.3 A). This construct includes the Ig K-chain leader sequence for extracellular secretion, the cDNA encoding Nt-TMEM67, a c-myc epitope, a polyhistidine tag, and Zeocin resistance gene and ampicillin resistance genes for selection in mammalian and bacterial cells, respectively (Figure 3.3 B). The construct was stably transfected into the HEK-293 cell line (Thomas and Smart, 2005) (see section 3.3.2.1). This expression system allows high yield and correct post-translational modification of Nt-TMEM67, an extracellular part of the receptor, which is secreted into the cell culture medium. Three column chromatography methods were used in order to purify the overexpressed protein from conditioned medium, including affinity column chromatography (HisPrep FF 16/10 column), ion exchange (HiTrapQ HP 1ml column) and gel filtration (HiLoad 16/600 Superdex 75) columns (see section 3.2.7.2).
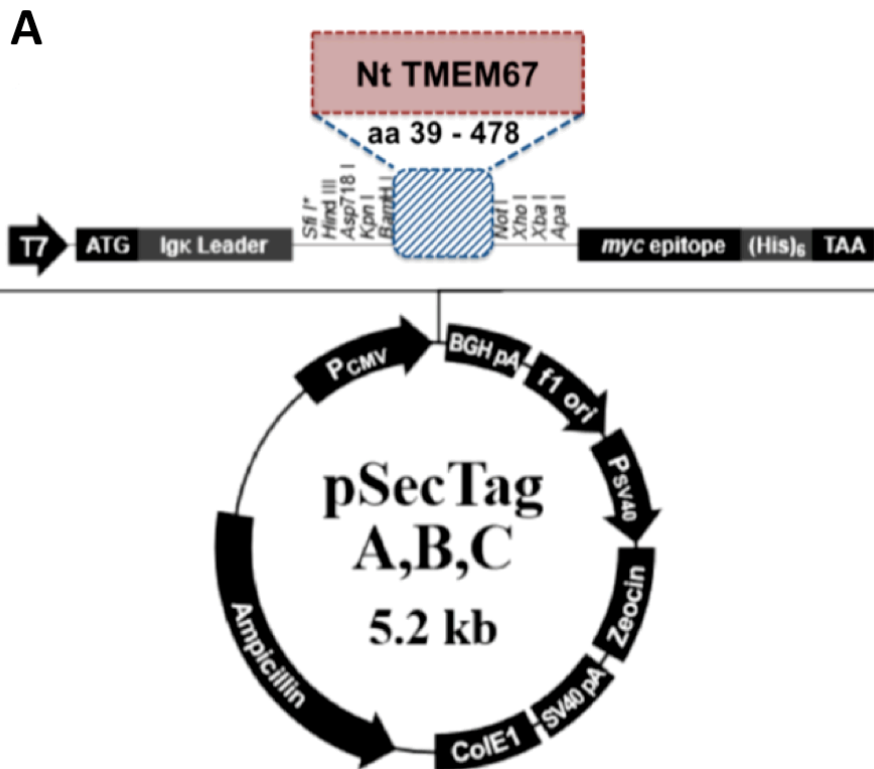
Figure 3. 3: TMEM67 vector and sub-cloned domain. (A) pSecTag2A vector map and sequence alignment of TMEM67 CRD expressed protein. **(B)**The sequence of Nt-TMEM67 sub-cloned to the vector. The protein sequence contains: initiator codon; Ig kappa light chain leader peptide for secretion; TMEM67 N-terminal region (amino acids 39-478); c-myc epitope; Hisx6 epitope; termination codon. Alternating exons are marked in black and blue text, with residues crossing exon-intron boundaries in red. The predicted molecular weight for this 440- residue sequence is 49 kDa (Figure 3.5 C).

Generating the Nt-TMEM67 stable cell line required several steps, including transfection of the plasmid construct (pSecTag2A_Nt-TMEM67) into the HEK-293 cell-line, followed by selection and expansion of clonal populations of the cells (Figure 3.4).
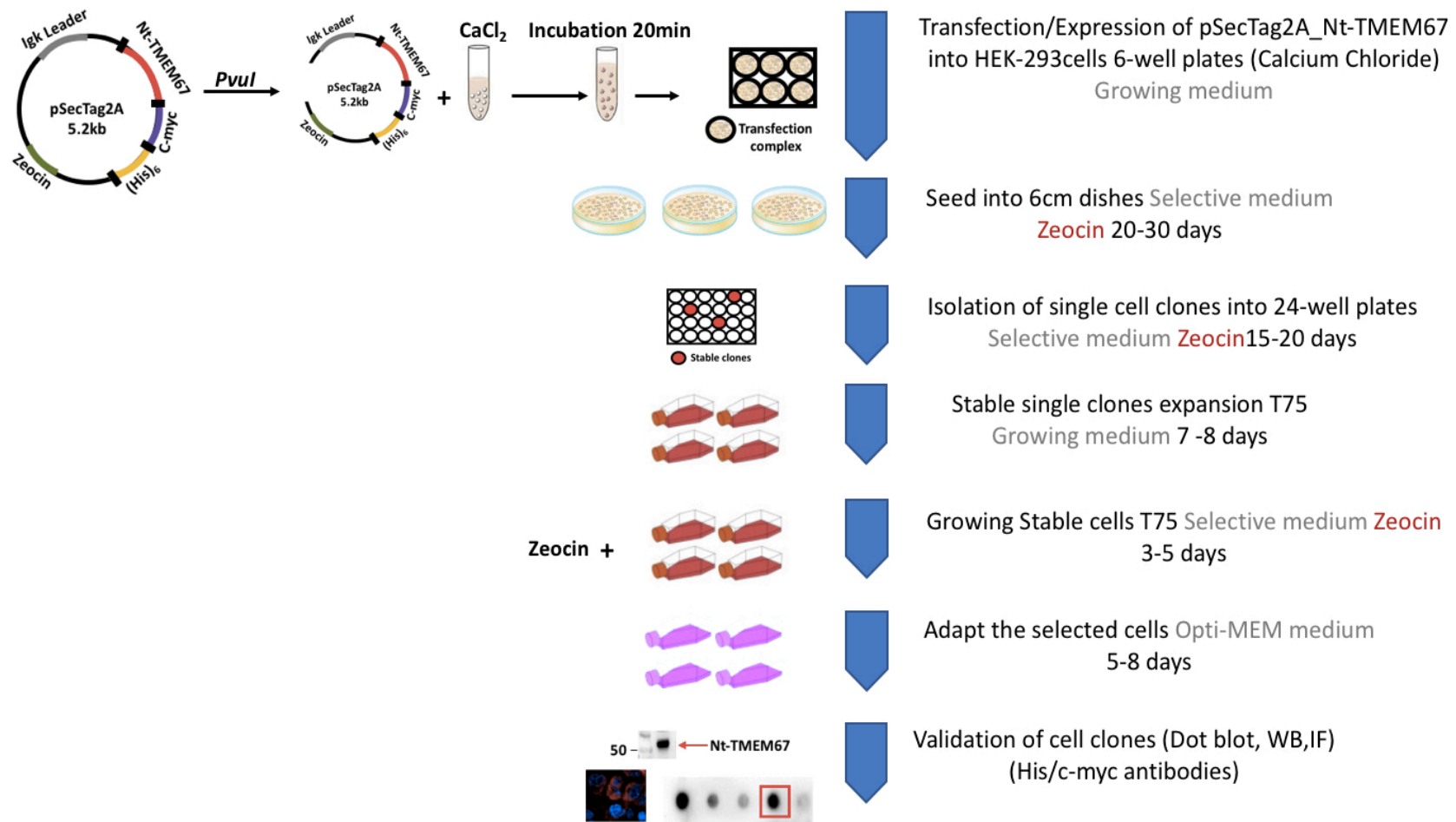
Figure 3. 4: Workflow for production of the stably-transfected Nt-TMEM67 HEK-293 cell-line. The schematic details workflow steps that include transfection, seeding of multi-well plates, isolation and expansion of selected colonies and adaptation of selected mono-clonal colonies to serum-free medium. The final analysis step comprises the collection and processing of cell culture medium by dot-blotting using standard western blotting methodology.

3.3.2.1 Optimization of stable transfection and secreted protein expression

To optimize the efficiency of stable transfection and secreted protein expression, a kill curve for transfected HEK-293 cells was performed in order to determine the optimal concentration of Zeocin antibiotic for efficient transfected cell selection. The kill curves indicated that 200 µl/ml of Zeocin was the optimal concentration to be used for the generation of stably transfected cells (Figure 3.5 A). These experiments showed that cells that did not express the pSecTag2A constructs with the selection marker died, leaving only single colonies of cells expressing the Zeocin resistance gene in these constructs. Single clones were isolated and examined by dot-blot and western blotting to determine the quality and yield of secreted Nt-TMEM67 protein.

First, 200 µl of serial dilutions of colony growth medium were loaded as described in (see section 3.2.7.1.4). The c-myc tagged recombinant protein was immunodetected (see section 3.3.2.7.3) and the result of dot-blots indicated that colony number 34 had the highest expression of N-TMEM67 (Figure 3.5 B). In addition, recombinant protein was purified from medium from colony 34 using a His SpinTrap column (GE Healthcare #GE28-9321-71) following the manufacturer's instructions. Purified Nt-TMEM67 was examined by SDS-PAGE and western blotting. This confirmed that a band of 50 kDa was expressed at the expected molecular weight of Nt-TMEM67 (Figure 3.5 C).
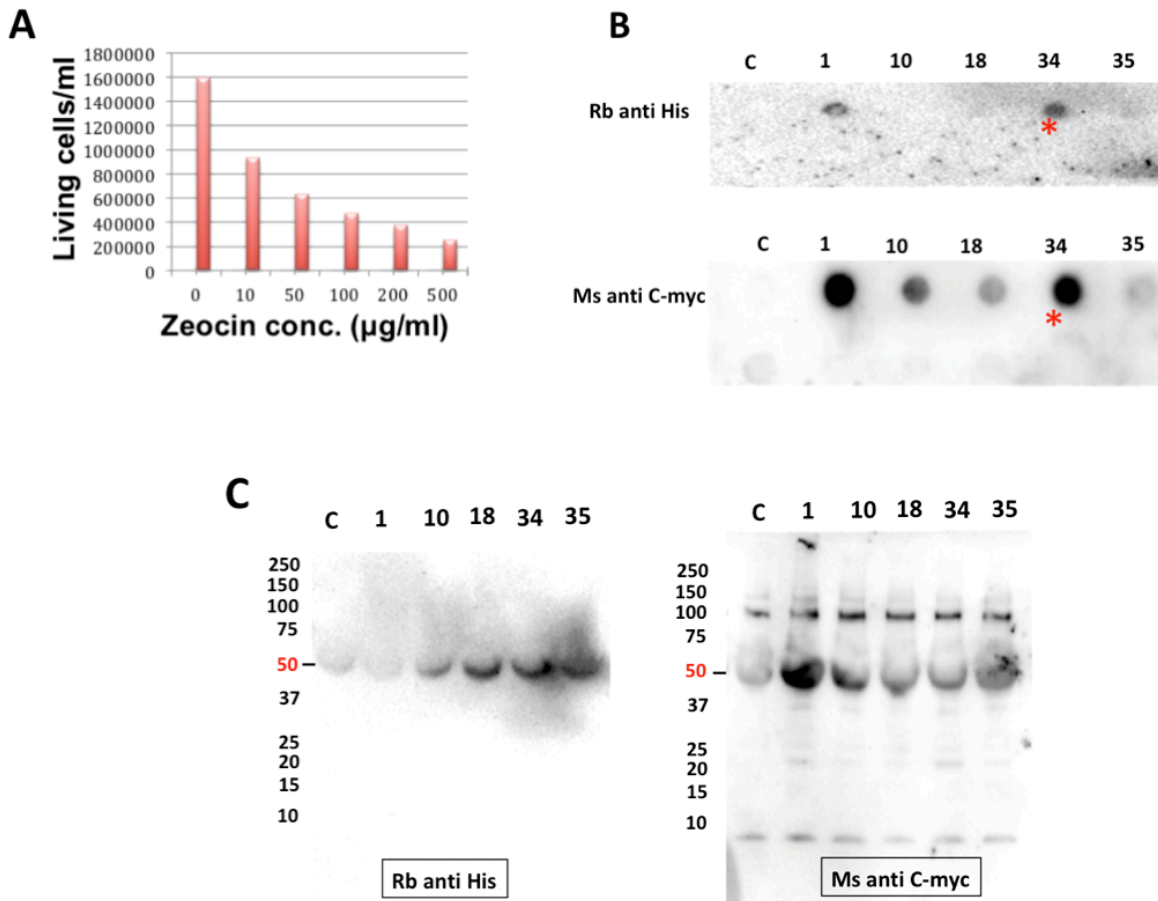
Figure 3. 5: Stably-transfected HEK-293 cell line validation. (A) The bar graph represents the kill curve method that was used to determine the concentration of Zeocin antibiotic required to kill cells within a period of time. The horizontal axis shows the Zeocin concentration whilst the vertical axis shows the living cells/ml. 200 µg/ml of Zeocin concentration was selected. **(B)** Dot blot analysis of pSecTag_Nt-TMEM67 secreted protein. Dot blotting was used to analyse the expression level of different clones after selective growth. Each colony was identified by a number. 200 µl stable medium was added to each well. "C" indicates negative control blots for un-transfected medium. WBs were performed with Ms anti-c-myc and Rb anti-His6 antibodies. Colony 34 was selected as the clone with optimal epitope-tagged protein expression. **(C)** WBs with Ms anti-c-myc and Rb anti-His after SpinHis column purification indicated the correct size of expressed Nt-TMEM67 (50 kDa).

Intracellular localisation studies by indirect immunofluorescence were also performed using either anti-c-myc or anti-His antibodies to visualize protein expression in stably transfected HEK-293 cells. High levels of over-expressed Nt-TMEM67 protein were observed in cells, probably concentrated in the ER (Figure 3.6 A).
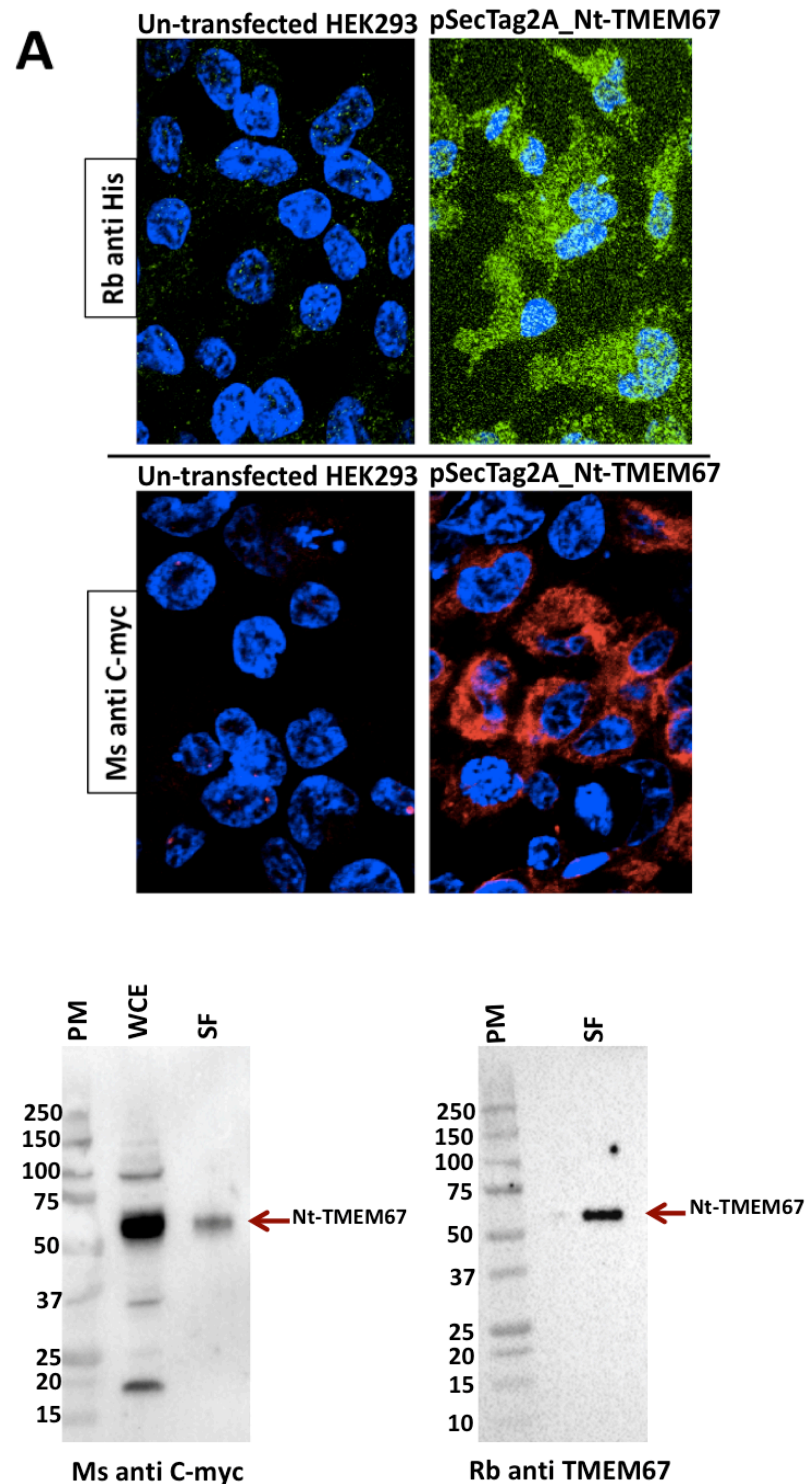
Figure 3. 6: Validation using immunofluorescence and western blotting for the whole cell extracts and secreted protein from colony 34. (A) Cells from colony 34 expressing Nt-TMEM67 were examined using immunofluorescence with Ms anti c-myc (in red) or Rb anti N-TMEM67 (in green) and compared with un-transfected HEK-293 cells. DAPI (Sigma-Aldrich) staining is shown in blue. Scale bar 10 μm. **(B)** HEK-293 cells expressing Nt-TMEM67 analysed by WB. Both anti-c-myc and anti-TMEM67 confirmed protein expression at the expected molecular weight of 50 kDa in conditioned serum-free medium (SF), while anti c-myc antibody also detected Nt-TMEM67 in whole cell extract (WCE).

3.3.2.2 Affinity purification of His-tagged secreted protein

6xHis tagged secreted protein was initially affinity purified from 10% FBS DMEM serum tissue culture medium conditioned by stably-transfected HEK-293 cells (Nt-TMEM67 colony number 34) as described previously (see section 3.3.2.1). There were very likely to be different species present because of glycosylation and this was reflected by the western blots of the protein preparations from eluted fractions (Figure 3.7). Subsequent LC-MS analysis indicated that bovine serum proteins (albumin, alpha-2-HS-glycoprotein and serotransferin) were a major contaminant in the pooled eluted fractions with the highest expression of Nt-TMEM67 (Appendix B.3.1) This precluded the definitive confirmation of correct protein expression by MS analysis since the contaminating serum proteins inhibited the generation of peptides from the human Nt-TMEM67 protein during trypsin digestion of the sample.

In summary, stably-transfected cells from colony 34 expressed and secreted Nt-TMEM67 directly into the tissue culture medium as expected, based on immunofluorescence microscopy and western blotting (Figure 3.6 A). However, affinity purification using a Ni-NTA column did not adequately remove contaminating serum proteins of bovine origin from the medium used to grow the cells. This prevented the identification of Nt-TMEM67 peptides even as minor species in these elutes.
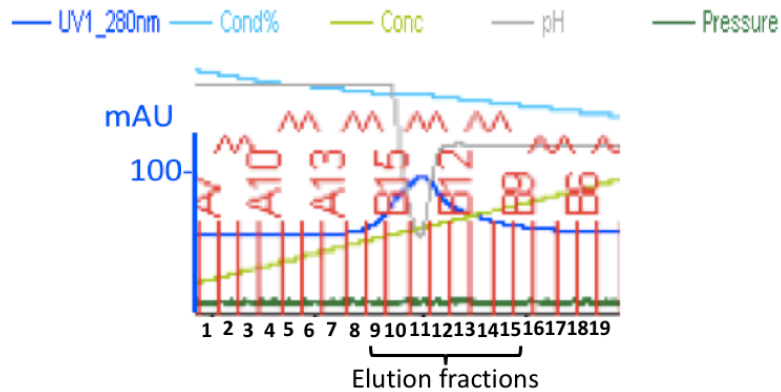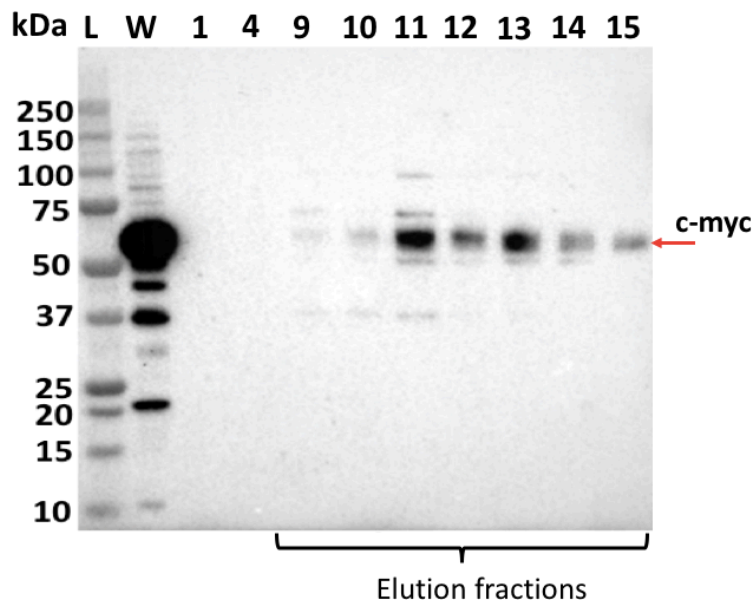
Figure 3. 7: Affinity purification of stabled pSecTag2A_Nt-TMEM67 extracted from HEK-293 cells. (A) Purification of His$_6$ polyhistidine-tagged Nt-TMEM67 with 500 mM imidazole in the sample and binding buffer using an FPLC system. The chromatogram shows fractions comprising flow-through (fractions 1–18) and proteins eluted with increasing imidazole concentrations to a maximum of 500 mM (fractions 9–15). The concentration (Conc; green) trace indicates the increasing imidazole concentration in the buffer flowing through the column. **(B)** SDS-PAGE gel of (His)$_6$- Nt-TMEM67. L: Ladder; W: whole cell extract. Lanes from 9-15 showed the target Nt-TMEM67 detected with anti-c-myc. at the expected molecular weight of 50 kDa.

In subsequent experiments, the purification and elution protocols were optimized by using Opti-MEM reduced serum medium and a gradient elution method on the FPLC system in order to minimize the contaminating bovine serum proteins (Figure 3.8). Nt-TMEM67 protein was successfully eluted from the column by competitive displacement using an elution buffer, comprising an increasing gradient of imidazole (0 to 500 M) in phosphate buffer. The peak fraction of eluted protein was at approximately 0.1 M imidazole and the eluted fractions were collected (Figure 3.8 A), visualised using Coomassie Blue staining (not shown) following resolution on SDS-PAGE gels and finally examined by WB with an anti-c-myc antibody (Figure 3.7 B). The result indicated that contaminating proteins were still present in the peak eluted fractions (Figure 3.8 A, B).
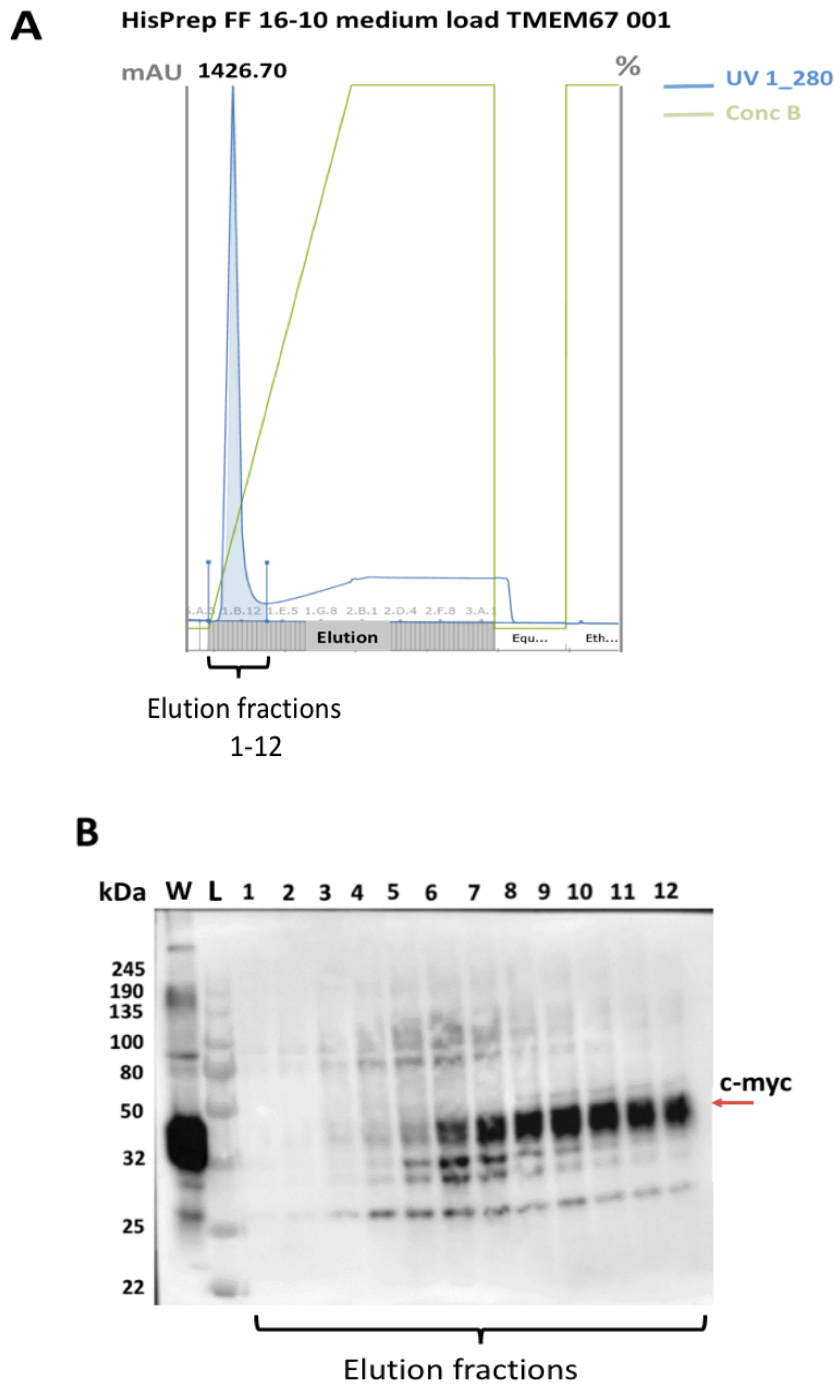
Figure 3. 8: Affinity purification of pSecTag2A_Nt-TMEM67 extracted from HEK-293. (A) A HisPrep FF 16/10 column was used. The conductivity trace (green) indicates the increase of imidazole concentration in the buffer flowing through the column. Absorbance (blue trace) was monitored at 280 nm (mAU, ultraviolet absorbance units). The peak shows proteins eluted when the imidazole concentration was increased from 0 to 500 mM. **(B)** SDS-PAGE and WB analysis of (His)6- Nt-TMEM67 in numbered eluted fractions. L: Ladder; W: Whole cell extract. Eluates containing the target protein were revealed by western blotting with anti-c-myc antibody. Lanes from 9-15 contain Nt-TMEM67 (marked by red arrow) indicating expression at the expected molecular weight of 50 kDa. Other bands of higher or lower MW

were also seen and are likely to represent Nt-TMEM67 degradation products or non-specific labelling of contaminating proteins.

3.3.2.3 Ion exchange purification

To purify recombinant Nt-TMEM67 from contaminating proteins, ion exchange chromatography was used to further separate proteins on the basis of differences in charge. As a result, 4 elution peaks were observed (Figure 3.9 A); Samples from peaks were tested by SDS-PAGE (see section 3.2.6.2) and analysis using an anti-c-myc antibody confirmed that recombinant protein was present in fractions 9 to 20 (Figure 3.9 A, B). Coomassie Blue gel was stained for one-hour Blue staining then destained for two hours; an arrow indicated predicted band since it was difficult to identify the Nt-TMEM67 band in the blue gel. In addition, the SDS-PAGE result showed that peak 1 (samples from fractions 5 to 7) contain truncated forms of the target Nt-TMEM67 and correspond to non-specifically bound protein, whilst peaks 2 and 3 (fractions 9-10 and 12-16, respectively) correspond to the enriched specifically bound Nt-TMEM67. Peak 4 (fraction 24) failed to visualise any bands on SDS-PAGE and Coomassie Blue gels. Therefore, peaks 2 (9-10) and 3 eluting at approx. 150 mM NaCl were selected for further analysis. Peak 2 and 3 fractions containing purified Nt-TMEM67 protein were pooled, concentrated and buffer exchanged into 1xDPBS (Sigma-Aldrich #P4417).
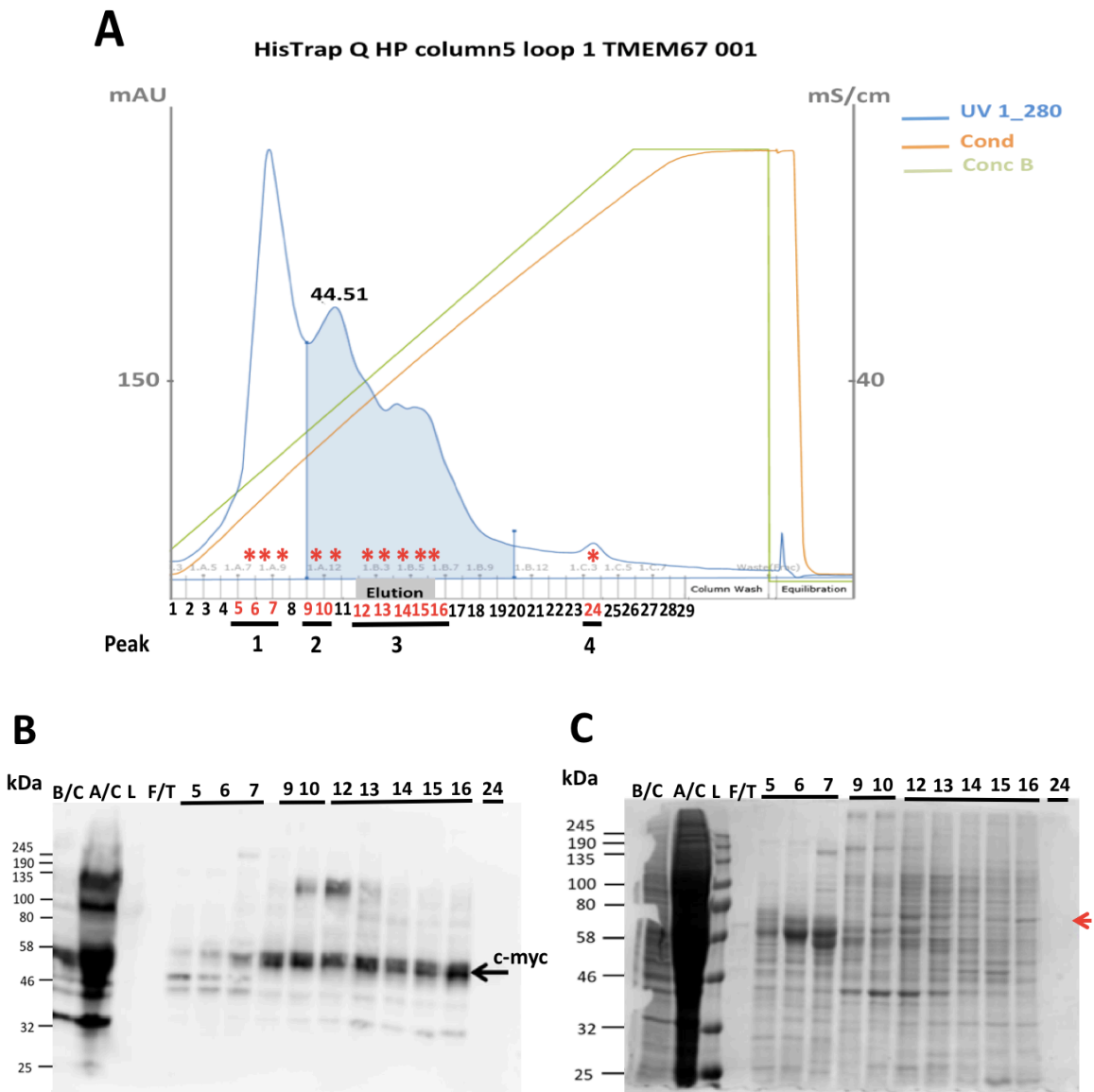
Figure 3. 9: Ion exchange purification of pSecTag2A_Nt-TMEM67. (A) HiTrap Q column 1ml purification of Nt-TMEM67 protein upon applying a NaCl gradient up to 1 M. Absorbance (blue trace) was monitored at 280 nm (mAU, ultraviolet absorbance units). NaCl concentration is indicated by the orange trace. Four elution peaks were observed; Peak 1: samples (5-7); Peak 2: samples (9-10); Peak 3: samples (12-16); Peak 4: sample (24). **(B-C)** selected fractions analysed by SDS-PAGE followed by Coomassie Blue staining. Four elution peaks were observed; Peak 1: samples (5-7) contain truncated forms of the target Nt-TMEM67 and corresponds to non-specifically bound Nt-TMEM67; Peak 2: samples (9-10); Peak 3: samples (12-16) correspond to the enriched specifically bound Nt-TMEM67; Peak 4: (24) failed to visualise any bands on SDS-PAGE and Coomassie Blue gels. Peak 2 and 3 eluting at approx. 150 mM NaCl were selected for further analysis. Lane B/C indicates input material before the elution of affinity-purifed protein. Lane A/C indicates input material after the elution of affinity-purified protein; L, protein ladder; F/T, flow-through. The arrow indicates the relative positions of the eluted Nt-TMEM67 protein in the gels.

3.3.2.4 Gel filtration

Coomassie Blue staining after ion exchange chromatography indicated that contaminating protein was still present in peak fractions that contained Nt-TMEM67 (Figure 3.9 B). Gel filtration chromatography on a Superdex 75 FPLC column was used to further separate proteins on the basis of size and shape. The result showed that gel filtration chromatography resolved the peak pooled ion exchangechromatography fractions into three main peaks (Figure 3.10 A). Selected fractions from these elutions were analysed by SDS-PAGE and western blotting using an anti-c-myc antibody. Gels were also stained with Instant Blue (Expedeon) so that excised bands could be used directly for protein identification studies by MS. Arrows indicate the relative and predicted positions of the eluted Nt-TMEM67 protein in the gels: this indicates that peak 2 (Figure 3.10 B-C) corresponded to the enriched, specifically bound Nt-TMEM67. Therefore, fractions were collected for further analysis by MS, and Instant Blue gel bands corresponding to the enriched bound Nt-TMEM67 were excised for MS studies (see section next section).

3.3.2.5 Mass Spectrometry (MS)

SDS-PAGE gels stained with Instant Blue had bands between 46 to 58 kDa excised for protein identification by MS. Samples were subjected to tryptic digestion and the peptides identified by MS were matched to a protein sequence database containing all human protein entries (SwissProt database). Potential matches were analysed in the program "Peaks" using a range of statistical parameters to remove poor matches. With reduced stringency search parameters, lower ranking spectrum matches to TMEM67 protein were identified, although there were a number of additional matches to other human proteins (data not shown). These results indicated that a high level of background contaminating protein still remained within the Nt-TMEM67 preparation (see Appendix B.3.2).
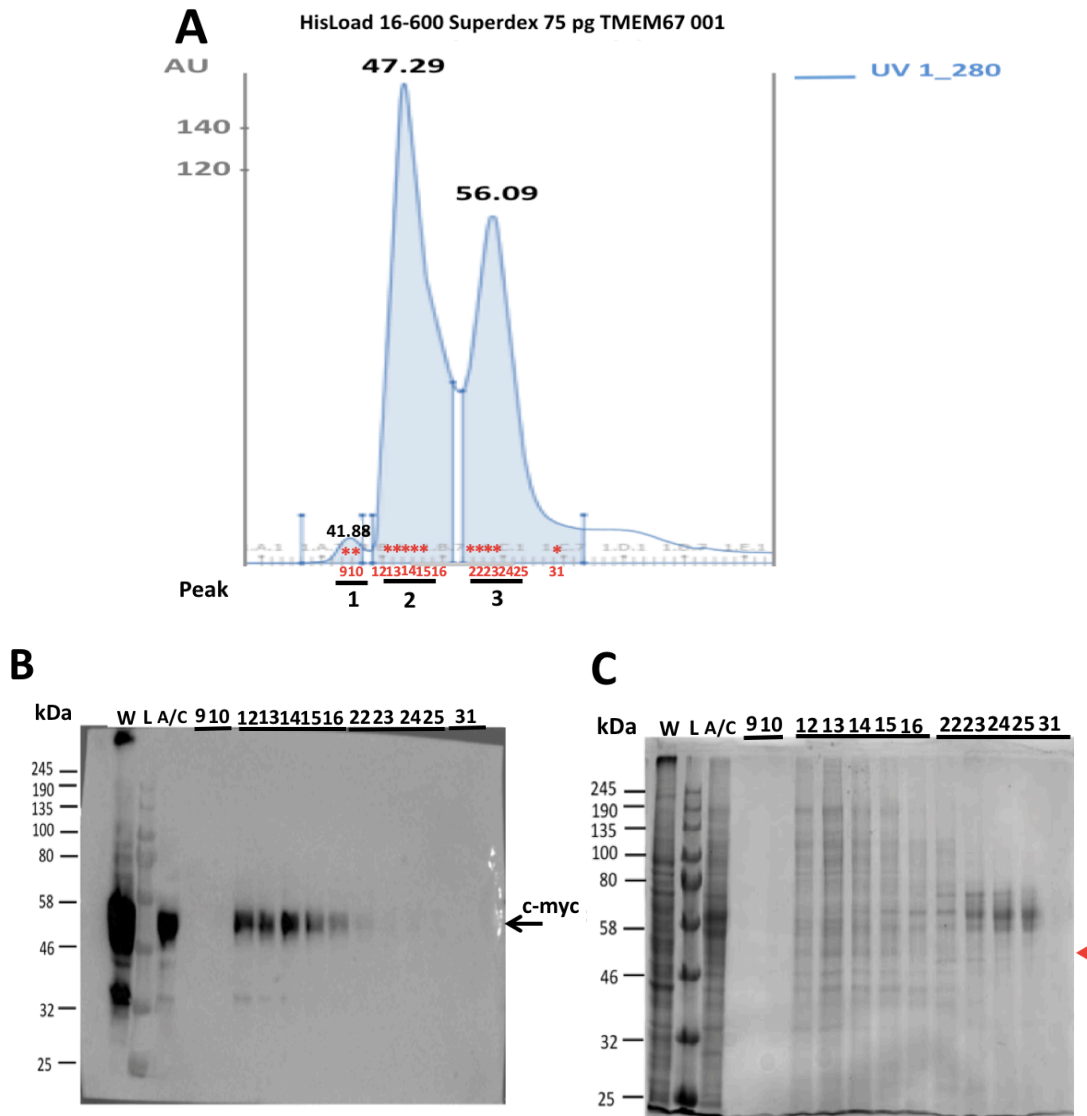
Figure 3. 10: Size exclusion gel filtration purification of pSecTag2A_Nt-TMEM67. (A) HiLoad 16/600 Superdex 75 column purification of Nt-TMEM67 protein. The absorbance was monitored at 280 nm, mAU (ultraviolet absorbance unit). Three elution peaks were observed. **(B)** Selected fractions analysed by SDS-PAGE and western blotting with an anti-c-myc antibody. **(C)** SDS-PAGE followed by Coomassie Blue staining. W: whole cell extract; L: protein ladder; lane A/C indicates input material after the elution of the ion exchange concentrated sample; only peak 2 (fractions 12-16) contained Nt-TMEM67 as confirmed by western blotting. The arrows indicate the relative and predicted positions of the eluted Nt-TMEM67 protein in the gels.

3.4 Discussion

Construction of an expression vector is a basic tool for production of desired proteins. Six transition zone TMEM proteins were selected to study in this project,

comprising the Frizzled-like orphan receptor TMEM67 and the tetraspan-like proteins TMEM216, TMEM138, TMEM237, TMEM17 and TMEM231. The ciliary TMEM proteins were tagged at either the C- or the N- terminus with TAP (streptavidin/FLAG) or FLAG using the "Gateway" cloning system. HEK-293 cells were used to confirm the expression of these constructs and the WB results showed that the generated constructs were successfully expressing the full-length protein (Figure 3.2). Afterward, immunofluorescence methods were performed to confirm whether these selected proteins are ciliary proteins localized at the ciliary Basal body/transition zone; the confocal imaging confirmed the sub-cellular localization of epitope-tagged TMEM to the basal body (Chapter 4).

In addition, Figures 3.3-3.10 illustrate the purification of the extracellular domain of TMEM67, an integral transmembrane protein implicated in ciliary signal transduction pathways. In order to purify the selected protein for functional and structural studies, the first step was to generate an expression system where the protein was secreted by the cell line into the tissue culture medium. The cell line chosen for over-expression was human HEK-293, and the protein was expressed as a secreted protein used Ig K-chain sequence in the pSecTag2 A vector.

To improve yield and reduce background, a variety of purification methods were employed, including affinity, ion exchange and size exclusion gel filtration column purifications. Using these in combination reduced the background and showed significant improvements in purification (Figures 3.7-3.10) compared to preliminary analysis. Notably, protein yields improved after gel filtration purification. The next step was to confirm the identity of the protein by MS analysis.

The yield of the protein was not sufficient for MS identification and unfortunately was also of insufficient yield and purity for crystallization trials. Such studies are critical to obtain x-ray data providing a picture of the tertiary structure of the protein. Optimization of expression, solubilisation and purification were all issues during this project. In conclusion, the expressed and secreted Nt-TMEM67 protein had a predicted size of 50 kDa and the anti-c-myc western blots showed a major band at 50 kDa, but it was not possible to purify enough of this protein for MS analysis. Due to time constraints it was not possible to further

optimize this part of the study and to determine why protein was undetectable by MS analysis.

3.4.1 Further investigations and experimental limitations

One of the aims for this chapter was to purify Nt-TMEM67 for analysis by MS and crystallography. However, as noted above this work could not be satisfactorily completed in the time available. Some of the challenges discussed in this chapter could be fully resolved through the optimal use of cell lines, epitope tags and buffers. One of the current challenges for Nt-TMEM67 and other cysteine-rich proteins is low protein yield because disulphide bridges in extracellular proteins tend to result in protein aggregation (Moghadam et al., 2015). To overcome these expression problems in the future, it will be important to choose the right expression system for each particular transmembrane protein. In this instance, *TMEM67* cDNA cloning into insect cell expression constructs, such as FastBac, followed by protein production using baculovirus expression systems may be the best way forward to ensure sufficient yield and purity for subsequent structural and biochemical studies. As an alternative, a number of proteins have been successfully expressed with a SUMO-tag. It has been reported that a SUMO-tag does not adversely affect protein function and can be used to dramatically improve both solubility and protection from proteolytic degradation, therefore improving protein expression (Malakhov et al., 2004, Butt et al., 2005).

Chapter 4 Biochemical interactions and localization of ciliary TMEM proteins

4.1 Introduction

Several recent large-scale proteomics studies (Boldt et al., 2016, Mick et al., 2015, Gupta et al., 2015) have described many interacting ciliary proteins that are organized into larger multi-subunit complexes, all of which are important for cilia formation and function. Amongst its various functions the transition zone establishes a diffusion barrier between the cilium and the cytoplasm, thus compartmentalizing the cilia from the cell body (see section 1.2.4.4). Genetic and cell biology analyses have shown that the small tetraspanin-like transmembrane proteins (TMEMs) TMEM17, TMEM67, TMEM138, TMEM216, TMEM231, and TMEM237 localize to the transition zone of cilia in *C. elegans*, and most of the mammalian orthologues localize to the transition zone in mammalian ciliated cells (Yee et al., 2015, Li et al., 2016). However, the relationship between function and localization is poorly understood for these ciliary TMEMs (Blacque and Sanders, 2014). In this chapter, I therefore investigated the potential functional relationships between these ciliary TMEMs and other components of three functional modules that localize to the transition zone.

A small evolutionarily conserved ciliary sub-compartment, transition zone plays an essential role in building cilia by acting as a 'gate' to control ciliary composition and function (Goncalves and Pelletier, 2017, Dean et al., 2016). Two conserved and redundant modules, including the so-called NPHP and MKS/JBTS modules, have been characterized by both genetic and biochemical approaches and have been suggested to contribute to a gating function (see section: 1.2.4.4 and 1.3). However, the precise mechanisms underlying their functions remain largely unclear and elusive. The ciliary TMEMs are part of the MKS/JBTS module. The MKS module includes TMEM67 (see section 1.6.3.1) TMEM216 (see section 1.6.3.2), and TMEM231 (see section 1.6.3.3). I also selected the two JBTS proteins TMEM237 (see section 1.6.3.7) and TMEM138 (see section 1.6.3.6). TMEM17, a CEP290-dependent transition zone protein that requires CEP290 and other MKS and NPHP module components for transition zone localisation and functions, was also included because it is a suitable candidate disease gene for ciliopathies (see section 1.6.3.5). These proteins have important

biological functions, and mutations in the genes that encode these proteins, are implicated in the pathogenesis of a wide range of human ciliopathies (see section 1.6).

In order to establish functional relationships between the ciliary TMEMs listed above, their localization to the transition zone was examined and confirmed by their endogenous and exogenous expression in ciliated mIMCD-3 cells using immunofluorescence confocal microscopy (Figures 4.4 and 4.5). A common approach to studying these organelles *in vitro* is to use immunofluorescent-labelled antibodies directed against the ciliary TMEMs. ARL13B and acetylated α-tubulin staining were used as reliable ciliary markers, since they labelled the majority of cilia (Figure 4.3). The basal body markers γ-tubulin and the poly-glutamylated tubulin (clone GT335) were successful in mIMCD-3 cells following methanol fixation (Table 4.1). Poly-glutamylated tubulin also marks the proximal region of the ciliary axoneme. Sources of all primary and secondary antibodies, as well as the optimized dilutions, are listed in Tables 4.1 and 4.2. Subsequently, the protein–protein interaction network of the selected ciliary TMEMs was characterized by co-immunoprecipitation (Figures 4.6-4.9) and tandem affinity purification followed by mass spectrometry (see appendix C; Table C.1) to identify large numbers of potential protein–protein interactions.

The aims of this chapter were to:

- Perform immunofluorescence localization analysis of endogenous and exogenous ciliary TMEMs.
- Functionally characterize the selected ciliary TMEMs through biochemical methods by using co-immunoprecipitation and tandem affinity purification/mass spectrometry analyses.

4.2 Materials and methods

Several analytic techniques described in Chapter 3 as also applicable to this study, including cell culture, immunofluorescence confocal microscopy, western blotting, protein extraction and whole cell lysate preparations. In addition, this chapter focuses on 2 biochemical methods to analyse protein-protein interactions, specifically co-immunoprecipitation and Strep-tag/FLAG tandem affinity purification (SF-TAP) coupled with

mass spectrometry (MS) analysis. In this study, biological replicates describe a repeat of the entire experiment in which each replicate was from the same HEK-293 cell line, but grown, harvested, and processed independently of each other with a different passage number, as described previously (Blainey et al., 2014).

4.2.1 Co-immunoprecipitation

Co-immunoprecipitation is often used for the analysis of interactions of multiple proteins and their functions. In this protocol, unless stated otherwise, all solutions were kept on ice. HEK-293 cells were grown on a 6-well plate or T75 flask (see section 3.2.2.1). Cells were then transfected with constructs (expressing SF-TAP or eYFP-tagged TMEM17, TMTM138, TMEM231, TMEM237 and TMEM67) using the transfection reagent Lipofectamine 2000 (Thermo Fisher Scientific) for 72 hours (see section 3.2.4). Lysates were prepared as described previously (see section 3.2.6.1); cells were extracted using four mild buffer conditions supplemented with protease inhibitors as follows: CHAPS buffer, Nonidet P-40 B (NP40) B buffer, radio-immunoprecipitation assay (RIPA) buffer, and hydrophobic buffer, or unless stated otherwise. Lysates then were pre-cleaned by incubating with 25 µl 50% (v/v) protein A agarose beads for 30 minutes at 4°C. Lysates were then cleared by centrifugation at 500 xg for 5 minutes at 4°C. The supernatant was incubated with rabbit antisera overnight at 4°C on a tube rotator.

25 µl of Protein-A-Agarose (Roche # PROTAA-RO) were washed 3 times with the incubation buffer. Beads were added to the lysates to capture the immunocomplexes and incubated for 3 to 6 hours at 4°C on a tube rotator, followed by washing 3 times in wash buffer. Beads were re-suspended in 30 µl of 2% SDS and incubated for 15 minutes and then spun at high speed (12000 xg) for a further 2 minutes. The supernatant was re- suspended in 2x SDS-PAGE loading buffer and denatured for 5 minutes, at 95°C. Immunoprecipitants were resolved on an SDS gel and transferred to PVDF membrane (Invitrogen #LC2005). The membrane was blocked with 5% (w/v) non-fat dried milk (Marvel) in 1x DPBS with 0.1% (v/v) Tween-20 (DPBS-T). The membrane was then incubated with primary antibody followed by secondary antibody in 5% non-fat dried milk in DPBS-T. The blot was developed with SuperSignal West Femto Maximum substrate (Thermo Fisher Scientific). The molecular weights were determined using ChemoDoc MP Imaging System with Image Lab software

(Bio-Rad). Figure 4.1 shows a schematic diagram of the protocol, outlining the different experimental steps.

4.2.1.1 Buffers used in coimmunoprecipitation methods

4.2.1.1.1 CHAPS buffer

- **Lysis buffer***

TrisCl pH7.6	50 mM
NaCl	150 mM
CHAPS (Sigma #C-5070)	10 mM

- **Incubation buffer***

TrisCl pH8	20 mM
NaCl	30 mM
EDTA	0.5 mM
Glycerol	10% (v/v)

- **Wash buffer***

TrisCl pH8	50 mM
NaCl	150 mM
EDTA	0.5 mM
NP40 (IPEGAL CA-630) (Sigma-Aldrich)	0.1% (v/v)

4.2.1.1.2 NP40 (B) buffer

- **Lysis, incubation, wash buffer, (All -in- One Buffer)***

Tris-HCl pH8	50 mM
KCl	80 mM
Glycerol (Sigma-Aldrich)	10 %
EDTA	10 mM
NP40 (IPEGAL CA-630) (Sigma-Aldrich)	1 % (v/v)
$NaVO_4$	10 mM
NaF	10 mM

4.2.1.1.3 Hydrophobic buffer

- **lysis/incubation buffer***

Tris-HCl pH8	20 mM
NaCl	25 mM
Glycerol (Sigma-Aldrich)	10 % (v/v)
EDTA	2 mM
n-dodecyl-ß-D-maltoside (βDM)	0.05% (w/v)
Ethanol	10 % (v/v)

4.2.1.1.4 RIPA buffer

- **lysis /incubation buffer***

Tris-HCl pH8	10 mM
NaCl	140 mM
Sodium deoxycholate	0.1 %
EDTA	1 mM
SDS	0.1 %
Triton X-100	1 %
PMSF	1 mM

* x100 dilution of "Halt" Protease/Phosphatase Inhibitor Cocktail (Thermo Fisher Scientific #78442) or 1x protease inhibitor cocktail (Cell signaling #5872S) supplemented buffers immediately before use.
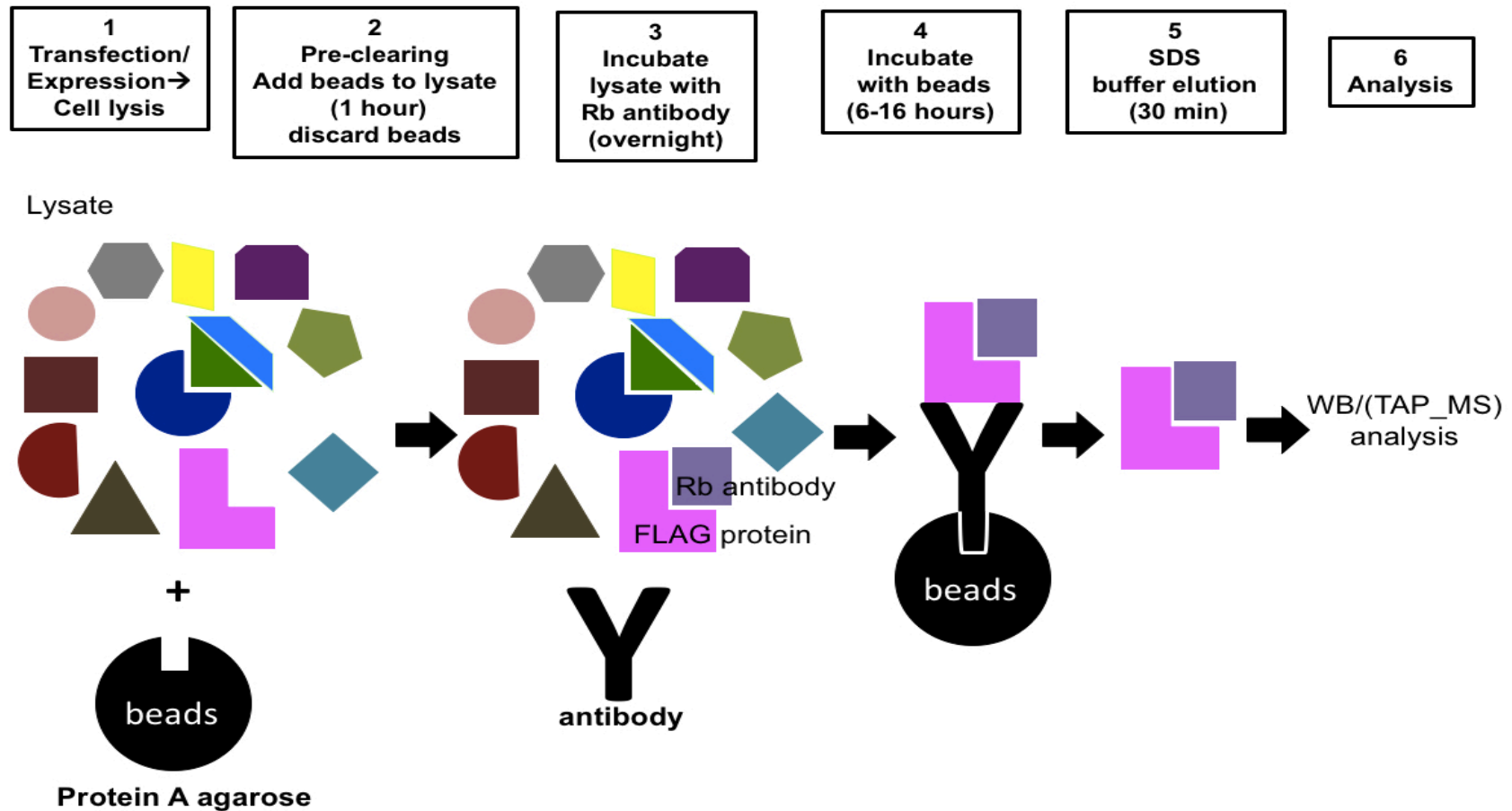
Figure 4. 1: Schematic representation of co-immunoprecipitation protocol. HEK-293 cells were transfected with Nt and Ct-terminal SF-TAP-tagged TMEM and lysed to produce whole cell extracts. These were processed for immunoprecipitations with rabbit polyclonal antibodies and protein A-Sephrose (see section 4.2.1) to isolate co-immunoprecipitated interacting proteins. Proteins were then subsequently identified by LC-MS (see section 4.3.3).

4.2.2 Tandem affinity purification

Tandem Affinity Purification (TAP) is a mass spectrometry (MS)-based approach (Rigaut et al., 1999), one of the most effective affinity purification approaches to identify stable protein-protein interactions (Dedecker et al., 2015). HEK-293 cells containing SF-TAP/FLAG-tagged proteins were generated by transiently transfecting them using Lipofectamine 2000. Subsequently, a TAP assay was performed as described previously (Klymenko et al., 2006).

For a T75 flask, either 100 µl Strep-Tactin Superflow beads (IBA Lifesciences, Goettingen, Germany) or 50 µl FLAG beads, as appropriate, were washed three times with 1 ml of ice-cold TAP wash buffer (see section 4.2.2.1) and once with 1 ml ice-cold 1x DPBS. The buffer was then removed. All the following steps were carried out at 4°C. Transfected cells were extracted under mild buffer conditions using TAP lysis buffer supplemented with protease inhibitors (see section 4.2.2.1).

The Strep-Tactin Superflow beads were added to cell lysate samples in a 1.5 ml centrifuge tube for Strep-tag affinity purification. Binding was performed for 3 hours with end-over-end mixing. The unbound material was discarded following centrifugation of the beads at 5000 *xg* for 5 minutes and the beads were transferred to a new 1.5 ml centrifuge tube. The native complex was eluted by incubation in 200 µl ice-cold D-desthiobiotin elution buffer (IBA Lifesciences Goettingen, Germany) (see section 4.2.2.1) for 15 minutes with end-over-end mixing. Beads were pelleted by centrifugation at 5000 *xg* for 5 minutes and the supernatant was transferred to a new 1.5 ml centrifuge tube. Subsequently, 50µl of washed anti-FLAG M2 affinity gel beads (Sigma Aldrich) were added to the elute and incubated for 3 hours with end-over-end mixing. Beads were pelleted at 5000 *xg* and washed 3 times with 500 µl ice-cold wash buffer (see section 4.2.2.1) and once with 1x DPBS. The bound proteins were eluted with 200 µl ice-cold FLAG peptide elution buffer [200 µg/ml FLAG peptide (Sigma Aldrich #F3290-4MG) in 1x DPBS] for 15 minutes.

The elution was tested by western blotting and followed by protein precipitation as described in Table 4.3. Precipitated proteins were sent for MS to the Medical Proteome Centre Institute for Ophthalmic Research University of Tubingen. The samples were processed by Dr. Karsten Boldt and Nicola Horn. Analysis of MS, the results and the number

of the biological replicates performed for each sample are explained in detail in the results section (4.3.3). Results of the three biological replicates were analysed together.

4.2.2.1 Buffers used in TAP method

4.2.2.1.1 TAP buffer
- **TAP lysis buffer***

Tris-HCl pH8	50 mM
NaCl	125 mM
NP40	1%
Glycerol	5%
$MgCl_2$	1.5 mM
$NaVO_4$	1 mM
NaF	25 mM

- **Elution buffer***

Tris-HCl pH8	100 mM
NaCl	150 mM
D-desthiobiotin (Sigma-Aldrich)	5 mM
EDTA	1 mM

- **Wash buffer***

TBS (10x)	1 ml
Protease/Phosphatase Inhibitor	50 µl
NP40 0.1% (v/v)	12 µl

A tablet/10 ml Roche protease inhibitor

* x100 dilution of "Halt" Protease/Phosphatase Inhibitor Cocktail (Thermo Fisher Scientific #78442) or 1x protease inhibitor cocktail (Cell signaling #5872S) supplemented buffers immediately before use.
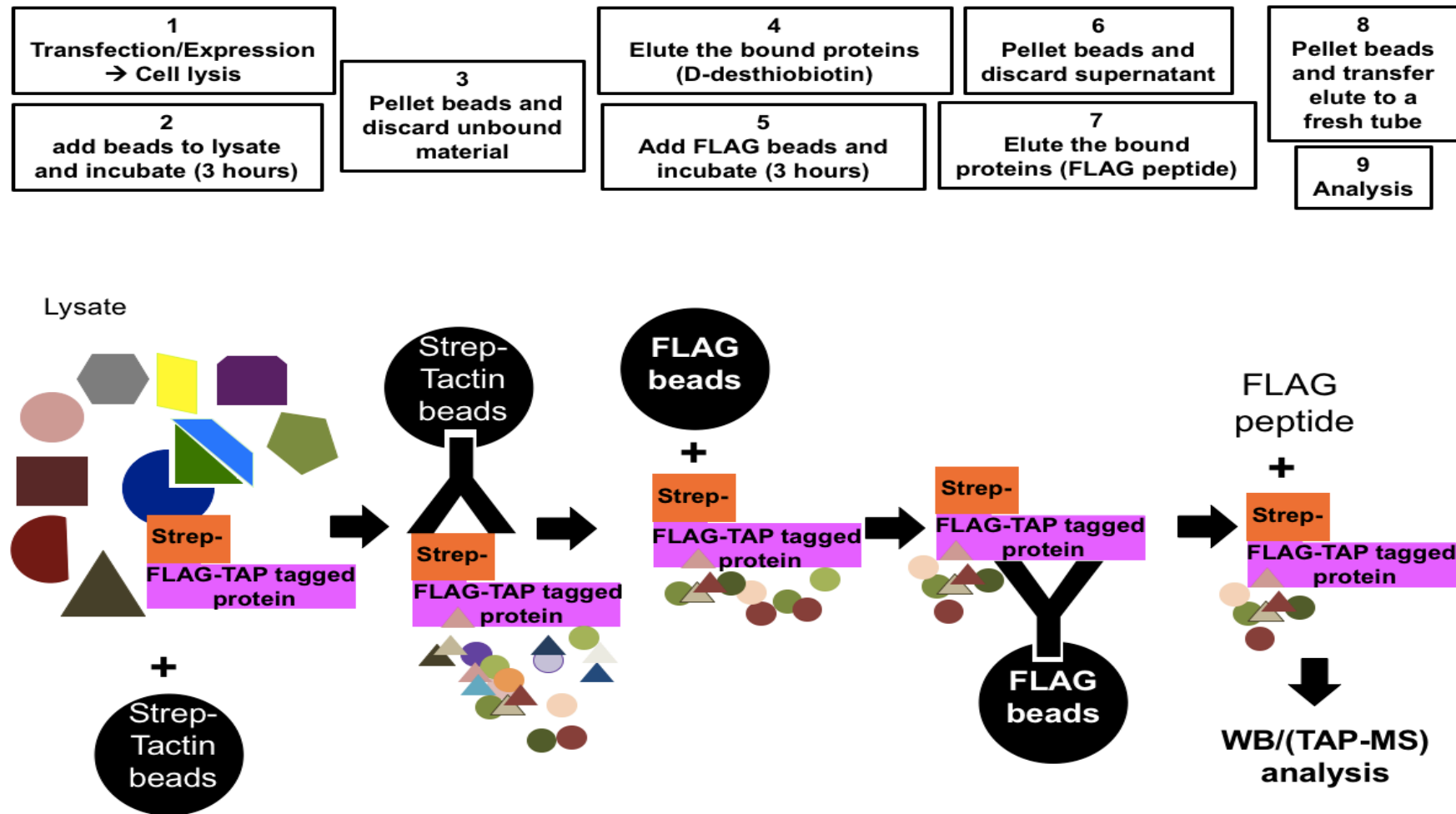
Figure 4. 2: Schematic representation of Streptavidin-II/FLAG TAP workflow for characterizing TMEM complexes. The TAP procedure includes expression, extraction and purification from whole cell extracts of epitope-tagged TMEMs and associated interacting proteins.

4.2.2.2 Methanol/chloroform protein precipitation

The experiment was performed at RT. Four volumes of methanol (Sigma-Aldrich #32213) were mixed vigorously with 1 volume of the protein sample for 60 seconds. Afterwards, 1 volume of chloroform was added, and the mixture was vortexed for 60 seconds. Three volumes of dH_2O were then added to the mixture and vortexing for 60 seconds. The mixture was subsequently centrifuged at 1000 *xg* for 5 minutes. The mixture was in 3 layered phases. The proteins remained at the phase boundary between the upper aqueous methanol layer and the lower chloroform layer. The upper fluid phase was carefully removed and another 4 volumes of methanol were added to wash the precipitate. The mixture was centrifuged at 14000 *xg* for 15 minutes. The supernatant was discarded without disturbing the pellet and the protein pellet was air dried and then stored at - 80°C.

4.2.3 Antibodies used in this chapter

Table 4. 1: List of primary antibodies used for immunofluorescence studies. Table includes the species the antibody was raised in, dilutions of antibodies used in this study, and the antibody supplier. The fixation methods were either 4% (w/v) para-formaldehyde (PFA; Sigma-Aldrich) for cilia markers, or absolute methanol (Sigma-Aldrich #32213) to visualize the basal body markers.

Antigen	Host/Clone species	Dilution (1:x)	Supplier
Acetylated-α-tubulin	Mouse monoclonal (Clone 6-11B-1; Isotype IgG2b)	(1:1000)	Sigma-Aldrich
γ-tubulin	Goat polyclonal	(1:50)	Santa Cruz
FLAG	Mouse monoclonal (Clone M2; Isotype IgG1)	(1:2500)	Sigma-Aldrich #F9291-1MG
ARL13B	Rabbit polyclonal	(1:1000)	Proteintech # 17711-1-AP
Poly-glutamylated tubulin	Mouse monoclonal (Clone GT335; Isotype IgG1κ)	(1:1000)	Enzo Life Science
TMEM231	Rabbit polyclonal	(1:200)	Gift of Dr. Brian Chih
TMEM67 (R24)	Rabbit polyclonal	(1:200)	In-house to Johnson lab
TMEM17	Rabbit polyclonal	(1:200)	Gift of Dr. Brian Chih

Table 4. 2: List of secondary conjugated antibodies and stains used for immunofluorescence study.

Antibody	Species	Dilution (1:x)	Supplier
Alexa Fluor 568- anti Mouse IgG	Goat	(1:500)	Invitrogen #A11004
Alexa Fluor 488- anti Rabbit IgG	Goat	(1:500)	Invitrogen #A11034
DAPI		(1:1000)	Sigma-Aldrich

Table 4. 3: List of antibodies used for co-immunoprecipitation and WB studies.

Antigen	Host/Clone species	Dilution (1:x)	Supplier
FLAG	Mouse monoclonal (Clone M2; Isotype IgG1)	(1:2500)	Sigma-Aldrich #F9291-1MG
TMEM231	Rabbit polyclonal	(1:200)	Gift of Dr. Brian Chih
TMEM67 (R24)	Rabbit polyclonal	(1:200)	In-house to Johnson lab
TMEM17	Rabbit polyclonal	(1:200)	Gift of Dr. Brian Chih
IFT88	Rabbit polyclonal	(1:200)	Proteintech #13967-1-AP
Adenylyl cyclase III (ACIII)	Rabbit polyclonal	(1:200)	Santa Cruz Biotechnology (sc-588)
TMEM237	Rabbit polyclonal	(1:200)	Abcam #633634
TMEM216	Rabbit polyclonal	(1:200)	In-house to Johnson lab
PRPF8	Rabbit polyclonal	(1:200)	Santa Cruz Biotechnology (sc-30207)
TMEM107	Rabbit polyclonal	(1:200)	Gift of Dr. Oliver Blacque
TXNDC15	Rabbit polyclonal	(1:200)	Atlas #HP A015483
Aquaporin2	Rabbit polyclonal	(1:200)	Abcam #ab62628-100

Table 4. 4: List of Secondary conjugated antibodies used for western blotting. HRP: horseradish peroxidase.

Secondary antibody	Conjugate	Dilution (1:x)	Supplier
Goat anti Mouse immunoglobulin	HRP	1:10000	Dako #P0447
Goat anti Rabbit immunoglobulin	HRP	1:10000	Dako #P0448

4.2.4 Validation of ciliary markers

Two ciliated mIMCD-3 cell-lines (see section 3.2.2) were used to determine endogenous and exogenous localization of selected TMEM proteins to the base of cilia or transition zone. One cell-line was stably transfected and expressed the ciliary marker 5HT6 serotonin receptor-RFP. These lines were used to confirm the correct localization of commercial ciliary markers, for acetylated α-tubulin (a marker of the ciliary axoneme) and ARL13B (a marker of the ciliary membrane), to primary cilia (Figure 4.3). The 5HT6-RFP cell line demonstrated variable localization to most but not all cilia.
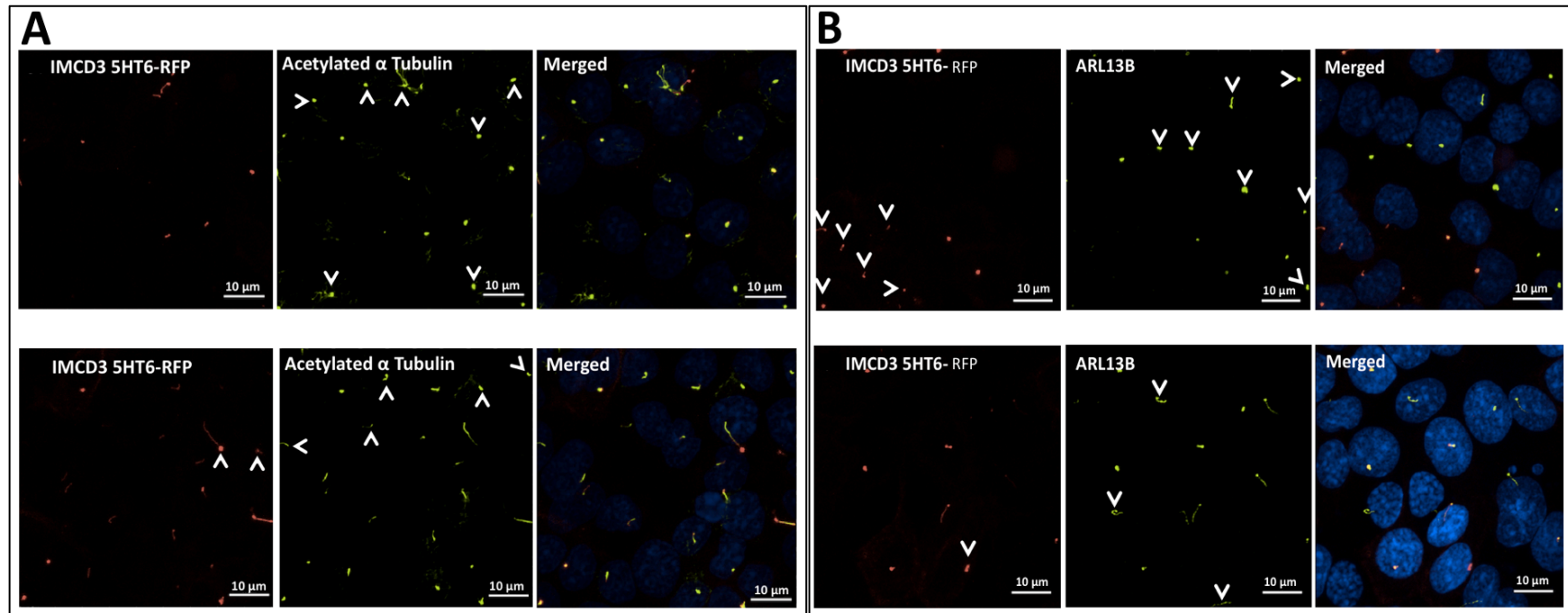
Figure 4. 3: Subcellular localization of acetylated α- tubulin and ARL13B in mIMCD-3 cells stably expressing the ciliary marker 5HT6-RFP. (A) The stably-transfected ciliated mIMCD-3 5HT6-RFP cell-line, marking cilia in red, had co-localization of acetylated α- tubulin (green) with most but not all cilia. Examples of primary cilia localization are indicated by white arrowheads. The left-hand panels show stable transfected mIMCD-3 5HT6-RFP (red). The middle panels showed the location of endogenous marker proteins acetylated α- tubulin (green). In merged images, the DAPI counterstain (blue) revealed the position of nuclei. Merged images showed that acetylated α-tubulin was a robust marker of primary cilia. Scale bars = 10 µm. **(B)** Primary cilia were detected using an antibody against ARL13B (green) on mIMCD-3 cells stably expressing 5HT6-RFP (red), both localizing to the cilium. Nuclei were stained with DAPI (blue). The left-side panels show stable transfected mIMCD-3 5HT6-RFP (red). The middle panels showed the location of endogenous marker proteins ARL13B (green). The presence of primary is indicated by white arrowheads. Merged images showed that ARL13B was a robust marker of primary cilia. Scale bars = 10 µm. All images are confocal maximum-intensity z-projections.

4.3 Results

4.3.1 Characterization of endogenous and epitope-tagged TMEM protein localization using immunofluorescence confocal microscopy

4.3.1.1 Sub-cellular localization of endogenous TMEMs

For the sub-cellular localization of endogenous TMEM17, TMEM67 and TMEM231, mIMCD-3 cells were split and cultured as described in (see section 3.2.2.1) and subjected to serum starvation for a further 72 hours prior to fixation. This was in order to inhibit cell cycle entry and promote ciliation, since cilia are found on most cells in G0 and G1 and to lesser extent in S/G2 (Plotnikova et al., 2009). Ciliated cells were then washed, fixed with absolute methanol and stained as described in (see section 3.2.5.1). Endogenous TMEM17 and TMEM231 (Figure 4.4) were stained with the primary antibodies, anti-rabbit TMEM17 (1:200), anti-rabbit TMEM67 (R24) (1:200), and anti-rabbit TMEM231 (1:200) and with rabbit anti-sera as a negative control (Table 4.1). Immunofluorescence of anti- rabbit secondary fluorophores were incubated (Table 4.2), analysed and visualized using a Nikon A1R laser scanning confocal microscope equipped with 568, 488, and 405 nm lasers using oil immersion objectives (see section 3.2.5.1.1).

Confocal microscopy images were taken using a 100x oil-immersion objective and showing almost exclusive localization of endogenous TMEM17, TMEM67 and TMEM231 to the base of primary cilia. Maximum intensity projections (MIPs) of confocal z-stacks were used to visualize protein sub-cellular localization. Nikon.nd2 files for full z-stacked images were used for co-localization correlation studies with ciliary markers. The result showed that the endogenous TMEM17, TMEM67 and TMEM231 all co-localized with the ciliary marker poly-glutamylated tubulin (GT335), consistent with localization to the ciliary transition zone in the ciliated mIMCD-3 cells (Figure 4.4).
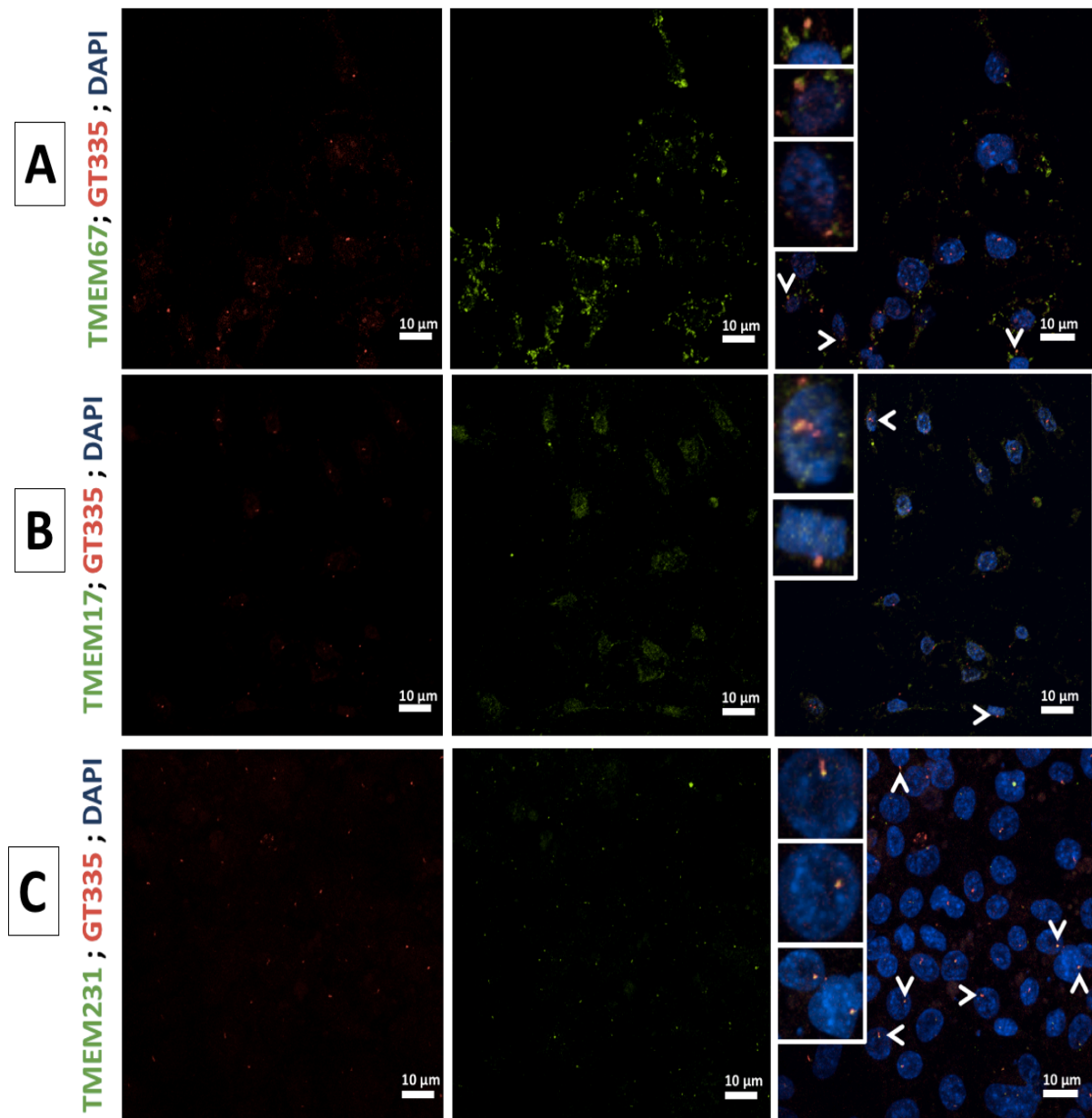
Figure 4. 4: Co-localization of endogenous TMEM 17, TMEM67 and TMEM231. The left-hand panels show mIMCD-3 cells labelled with the endogenous basal body/proximal ciliary marker poly-glutamylated tubulin (GT335; red). The middle panels show the location of endogenous ciliary TMEM67 **(A)**, TMEM17 **(B)**, and TMEM231 **(C)**, labelled with specific rabbit antibodies (green). Merged images are shown on the right with nuclei stained with DAPI (blue) and co-localization of proteins indicated by white arrowheads and shown in magnified insets. Scale bar = 10 µm.

4.3.1.2 Over-expressed N-terminus FLAG-tagged TMEM17 and TMEM67 localize to the ciliary apparatus in ciliated mIMCD-3 cells

For the sub-cellular localization of epitope-tagged TMEM proteins, mIMCD-3 cells were split and cultured as described in (see section 3.2.2.1). Then cells were transfected with N-terminal SF-TAP-tagged TMEM17, N-terminal SF-TAP-tagged TMEM231, and C-terminal tagged TMEM67-SF-TAP constructs and subjected to serum starvation for a further 72 hours prior to fixation (see section 3.2.5.1). Ciliated mIMCD-3 cells were washed and fixed as described (see section 3.2.5.1) with absolute methanol. 5HT6-RFP mIMCD-3 cells were fixed with 4% PFA then permeabilized with 1.0% (v/v) Triton x100 as described in section (3.2.5.1). Nuclei were counterstained with DAPI. In Nt-TAP-TMEM17, Nt-TAP-TMEM231 experiments, cells were incubated with mouse monoclonal anti-FLAG (1:2500) for 1 hour then the fluorescently labelled secondary antibody was added and incubated for 1 hour (see Tables 4.1 and 4.2).

Confocal microscopy images were taken using a 100x objective showing almost exclusive localization of the exogenous TMEMs to the endogenous markers γ-tubulin or 5HT6-RFP labelled cilia. The result showed that exogenous over-expressed TMEM17 co-localized with γ-tubulin, whereas exogenous over-expressed TMEM231 did not (Figure 4.5). In addition, transfection of TMEM67 tagged at the C-terminus with enhanced yellow fluorescent protein (eYFP) (C-eYFP-TMEM67; YFP fluorescence was excited with a λex 514 nm and λem 527 nm band-pass filter) showed that the tagged protein co-localized to the base of cilia marked in mIMCD-3 cells stably-transfected with 5HT6-RFP (Figure 4.5).
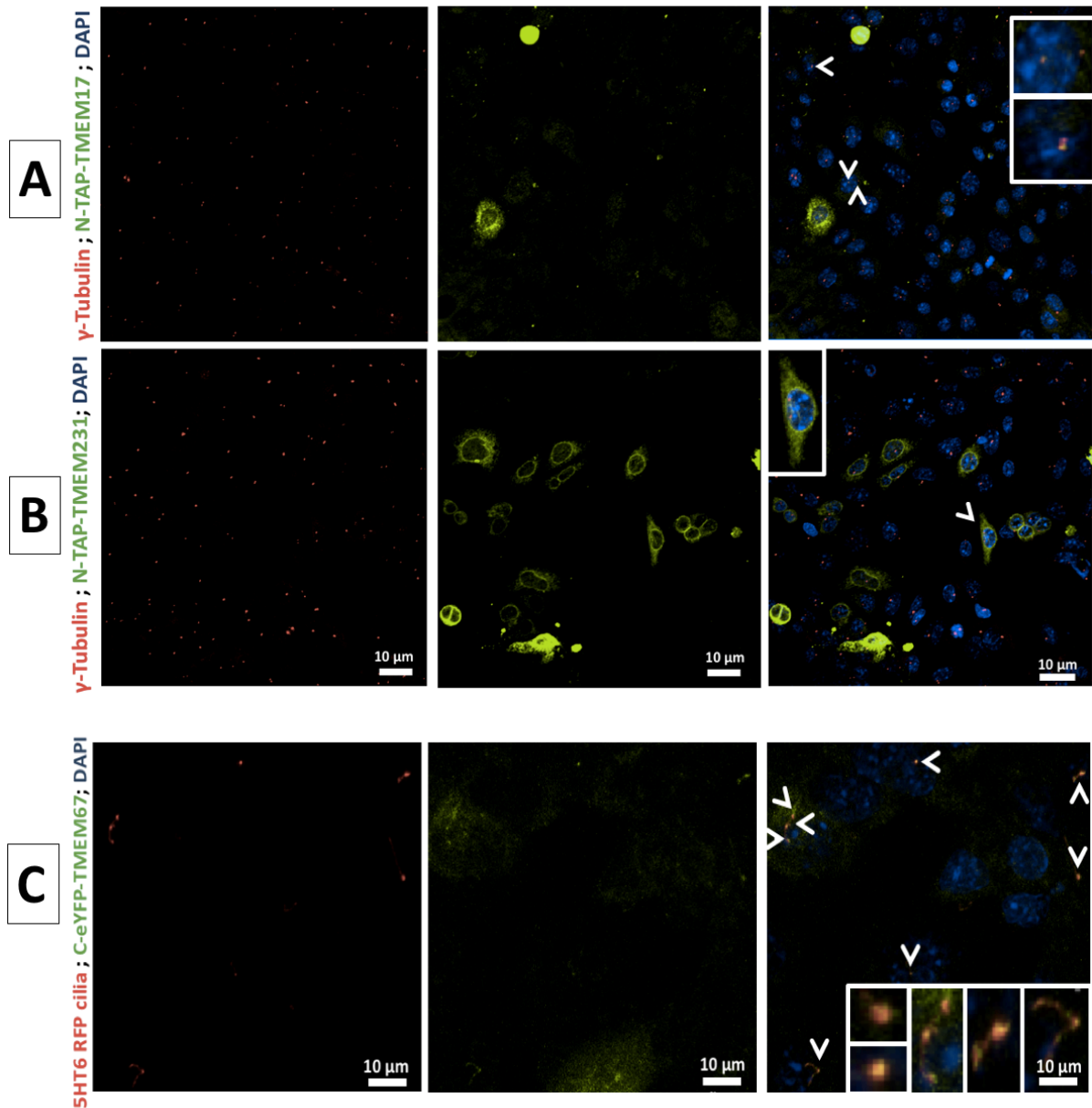
Figure 4. 5: Co-localization of exogenous epitope-tagged TMEM17, TMEM231 and TMEM67 at the base of primary cilia. mIMCD-3 cells were transiently transfected with FLAG-tagged N-TAP-TMEM17 and FLAG-tagged N-TAP-TMEM231 (green) while C-eYFP-TMEM67 was expressed in stable 5HT6 RFP mIMCD-3 cells. Cells were stained with γ-tubulin (red) against the basal body of the primary cilia and DAPI to visualize nuclei (blue). **(A)** Right merged image shows the co-localization of N-TAP-TMEM17 (green) to γ-tubulin (red). **(B)** Right merged image shows TMEM231 co-localization to peripheral cell membrane. **(C)** Right merged image shows C-eYFP-TMEM67 co-localization to cilia marker 5HT6-RFP (red). All images are confocal maximum-intensity z projections (MIPs). Scale bars = 10 μm.

4.3.2 Identifying novel TMEM protein-protein interactions using co-immunoprecipitation technique in HEK-293 cells

The specificity of the interactions between TMEM17, TMEM67, TMEM138 and TMEM237 were examined by co-immunoprecipitation assays (see section 4.2.1). Briefly, SF-TAP or 3xFLAG- tagged TMEM17, TMEM67, TMEM138 and TMEM237 were over-expressed in HEK-293 cells and pulled down or immunoprecipitated from whole cell extracts (WCE). Mock- transfected cells and irrelevant IgG antibodies were used as negative controls. Membrane proteins are difficult to purify since they are often expressed at low levels and they require detergents to become soluble in an aqueous solution (Lin and Guidotti, 2009). Therefore, in this study, a series of different buffers were used to solubilize selected ciliary TMEMs. The buffers contained varying non-ionic detergent concentrations and comprised CHAPS buffer (Sigma #C-5070), NP40 (B) buffer, RIPA buffer and hydrophobic buffer that had reduced ionic strength. The buffers were used to identify proteins that interacted with different affinities with the expressed TMEM proteins. When possible, a positive control was developed which consisted of pull-down of the epitope-tagged TMEM with the cognate antibody against the endogenous protein. Comparison of different lysis buffers indicated that the most efficient extraction of the selected ciliary TMEM proteins was achieved with CHAPS buffer.

4.3.2.1 Co-immunoprecipitation using CHAPS buffer results

Non-ionic detergents, such as CHAPS, solubilize the plasma and intracellular membranes, and break many weak intermolecular bonds (Labeta et al., 1988). CHAPS is ideal for co-immunoprecipitation analysis since it maintains intermolecular interactions following transmembrane and cytosolic protein extraction (see section 4.2.1.1.1) CHAPS buffer. Using this buffer condition, the results showed that TMEM237 pulled down TMEM216, TMEM17 and TMEM67 (Figure 4.6 A, B), and also co-immunoprecipitated with IFT88 (Figure 4.6 C). In addition, TMEM138 interacted with TMEM17 (Figure 4.6 D) and TMEM237, although no interaction was detected between TMEM138 and either TMEM67 or TMEM216 (Figure 4.6 E)

A

Lane	1	2	3	4	5	6
TAP-TMEM237	+	+	+	+	+	+

no Ab | RbαPI | irr. Ab | RbαTMEM67 | RbαTMEM216 | RbαTMEM237

KDa

50 — (WCE)

← TMEM237

IB: Ms anti FLAG
CHAPS buffer

B

Lane	1	2	3	4	5
TAP-TMEM237	+	+	+	+	+

WCE | no Ab | RbαTMEM237 | RbαTMEM216 | RbαTMEM17 | RbαTMEM67

KDa

50 — ← TMEM237 (high exposure)

50 — ← TMEM237 (low exposure)

IB: Ms anti FLAG
CHAPS buffer

C

Lane	1	2
TAP-TMEM237	+	+

Control | RbαIFT88

KDa

50 — ← TMEM237

IB: Ms anti FLAG
CHAPS buffer

D

Lane	1	2	3
TAP-TMEM138	+	+	+

WCE | no Ab | irr. Ab | RbαTMEM17

KDa

20 — ← TMEM138

IB: Ms anti FLAG
CHAPS buffer

E

Lane	1	2	3	4	5	6
TAP-TMEM138	+	+	+	+	+	+

WCE | no Ab | RbαPI | irr. Ab | RbαTMEM67 | RbαTMEM216 | RbαTMEM237

KDa

20 — ← TMEM138

IB: Ms anti FLAG
CHAPS buffer

Figure 4. 6: Co-immunoprecipitation assays of TMEM237 and TMEM138 identify interacting proteins using CHAPS buffer. (A-C) SF-TAP-TMEM237 cell lysates immunoprecipitated with rabbit polyclonal antibodies and western blotted with a mouse anti-FLAG monoclonal antibody against the SF-TAP tag. Molecular weight markers (kDa) are indicated on the left and whole cell extract (WCE) was used as a band positive marker. **(A)** Equal amounts of TMEM237 WCE, extracted using CHAPS buffer, were used in each co-immunoprecipitation experiment (1-6). The following rabbit polyclonal antibodies were used: Lane 1, no antibody; lane 2, pre-immune serum (PI); lane 3, aquaporin 2 irrelevant antibody; lane 4, Rb anti-TMEM67; lane 5, Rb anti-TMEM216; lane 6, Rb anti-TMEM237. Western blotting was performed to detect TMEM237. The result showed that pull-down of TMEM237 validated the experimental technique and TMEM237 co-immunoprecipitated with TMEM216. **(B)** Co-immunoprecipitation assay of TMEM237 with the indicated rabbit antisera using CHAPS buffer. The following polyclonal antibodies were used: Lane 1, no antibody; lane 2, Rb anti-TMEM237; lane 3, Rb anti-TMEM216; lane 4, Rb anti-TMEM17; lane 5, Rb anti-TMEM67. Western blotting was performed to detect TMEM237. The result showed that TMEM237 co-immunoprecipitated with TMEM216, TMEM17, and TMEM67. **(C)** Co-immunoprecipitation assay of TMEM237 with a negative control (un-transfected cells) and the indicated rabbit antisera Rb anti-IFT88 using CHAPS buffer. Western blotting was performed to detect TMEM237. The result showed that TMEM237 co-immunoprecipitated with IFT88. **(D-E)** Equal amounts of SF-TAP-TMEM138 cell lysate were used in immunoprecipitation experiments. **(D)** Polyclonal antibodies used as follows: Lane 1, no antibody; lane 2, aquaporin 2 irrelevant antibody; lane 3, Rb anti-TMEM17. Western blotting was performed to detect TMEM138. The result revealed that TMEM138 interacted with TMEM17. **(E)** Polyclonal antibodies used as follows: Lane 1, no antibody; lane 2, preimmune serum; lane 3, aquaporin 2 irrelevant antibody; lane 4, Rb anti-TMEM67; lane 5 Rb anti-TMEM216; lane 6, Rb anti-TMEM237. Western blotting was performed to detect TMEM138. The result showed that TMEM138 interacted with TMEM237. (TMEM237 **(A-C)**, n = 3; TMEM138 **(D&E)**, n = 2 (biological replicates/CHAPS buffer)).

4.3.2.2 Co-immunoprecipitation using NP40 (B) buffer results

NP40 is a soluble non-ionic detergent that is less harsh than ionic detergents such as SDS. NP40 preserves proteins in their native conformation and minimizes denaturation of antibody binding sites. NP-40 is thought to solubilize the plasma and intracellular membranes and to break weak intermolecular bonds, resulting in an increase of the target antigen concentration within the lysate (DeCaprio and Kohl, 2017). This present protocol was adapted and modified from (Lane, 1999). NP40 (B) buffer was used for cell lysis, incubation and washing as described above (see section 4.2.1.1.2).

The results in (Figure 4.7 A) indicated that TMEM138 co-immunoprecipitated with TMEM67 and IFT88 (n=1, biological replicate). Figure 4.7 B indicated that there was a potential interaction between TMEM216 with TMEM237 and that the anti-TMEM216

antibody immunoprecipitated epitope-tagged TMEM216 (n=1, biological replicate), thus validating the specificity of this antibody. Similarly, in Figure 4.7 C the antibody specificity against TMEM17 was validated. Furthermore, TMEM17 was shown to interact with TMEM216, TMEM67, TMEM237 and IFT88 (n=1, biological replicate).
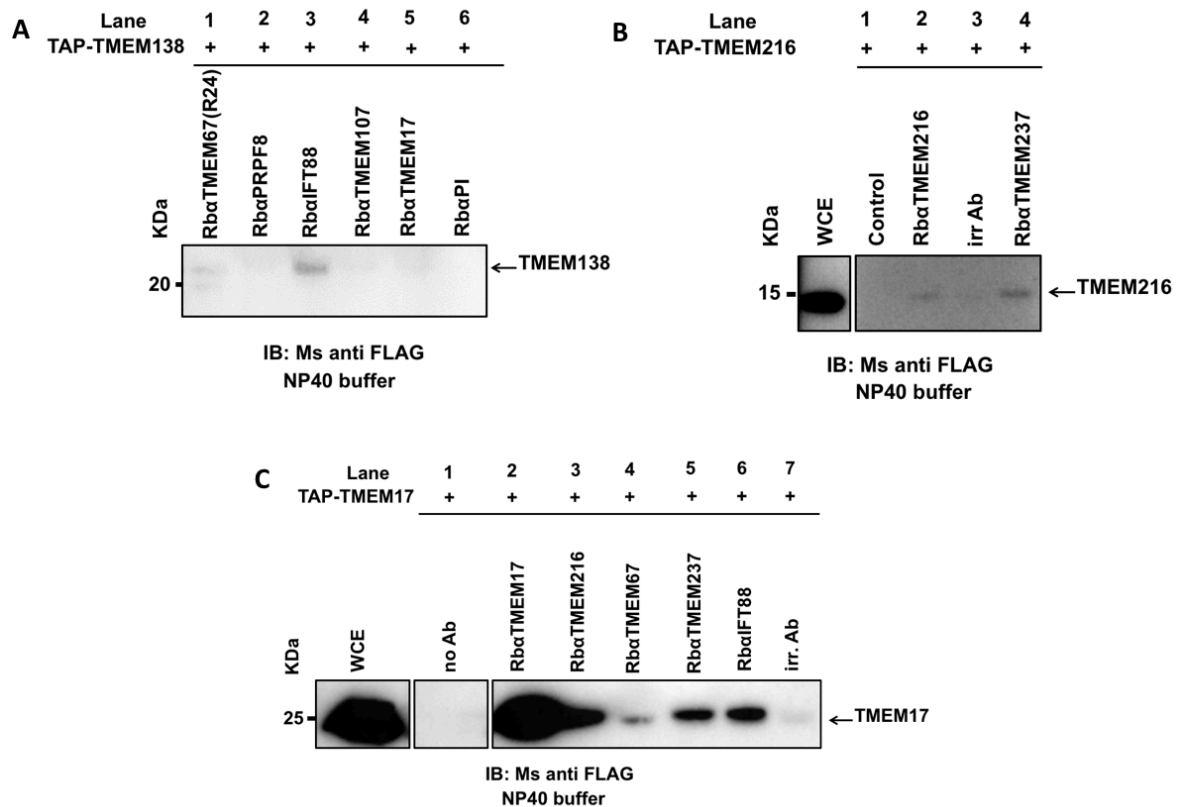
Figure 4. 7: Co-immunoprecipitation assays of TMEM138, TMEM216, and TMEM17 identify selected TMEM proteins as potential interactants using NP40 (B) buffer. (A) SF-TAP-TMEM138 cell lysates were incubated with the indicated rabbit polyclonal antibodies and probed with anti-FLAG antibody against the SF-TAP tag. Molecular weight markers (kDa) are indicated on the left. PI indicates pre-immune negative control. TMEM138 co-immunoprecipitated with TMEM67 and IFT88. **(B)** SF-TAP-TMEM216 cell lysates were incubated with the indicated rabbit polyclonal antibodies and probed with anti-FLAG antibody. Whole cell extract (WCE) was used as a band positive marker. Lane 1 (control) is WCE from un-transfected cells and lane 3 is irrelevant (irr.) antibody. TMEM216 co-immunoprecipitated with TMEM237. **(C)** SF-TAP-TMEM17 cells lysates were incubated with the indicated rabbit polyclonal antibodies and probed with anti-FLAG antibody. Whole cell extract (WCE) was used as a band positive marker and un-transfected cells were a negative control. TMEM17 co-immunoprecipitated with TMEM216, TMEM67, TMEM237 and IFT88. TMEM138 **(A)**, TMEM216 **(B)**, and TMEM17 **(C)** experiments with NP40 (B) buffer are based on only one biological replicate (n=1).

4.3.2.3 Co-immunoprecipitation using a hydrophobic buffer result

To test the specificity of the TMEM17 interactions with other ciliary TMEM proteins, an optimised hydrophobic buffer was used for additional co-immunoprecipitation assays of TMEM17 with the rabbit polyclonal antibodies against TMEM231, TMEM216 and TMEM67 (see section 4.2.1.1.3). The final concentration of components of this buffer were optimized to enhance potential hydrophobic interactions between TMEMs (Valente et al., 2010). Although this buffer enabled anti-TMEM17 to immunoprecipitate epitope-tagged TMEM17 as expected, only low levels of TMEM216 were co-immunoprecipitated (Figure 4.8). Since TMEM17 was shown to interact with TMEM216, TMEM67, TMEM237 and IFT88 in NP40 buffer (Figure 4.7), this suggests that the TMEM17-TMEM216 interaction is strongly hydrophobic. Data represents one biological replicate.
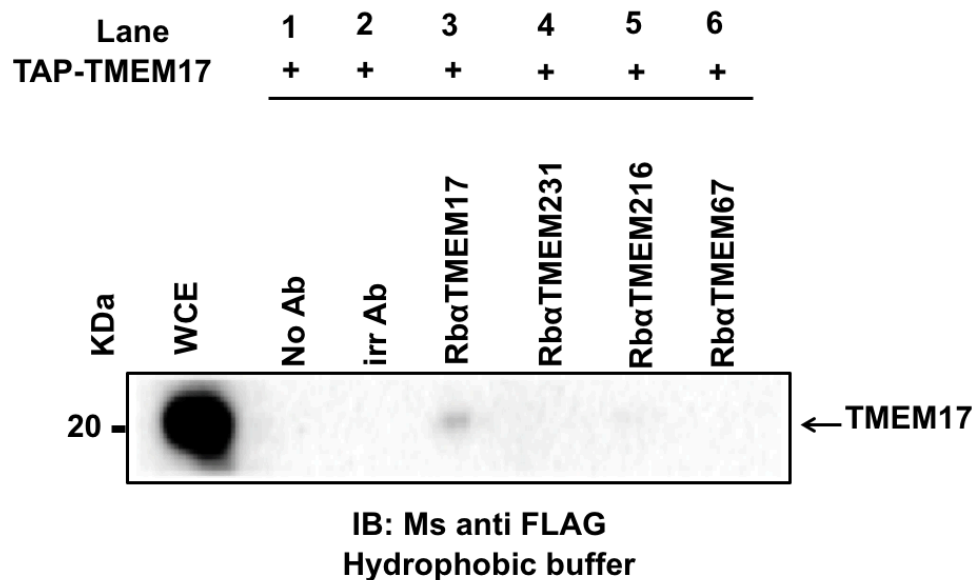
Figure 4. 8: Co-immunoprecipitation identifies TMEM216 as a TMEM17 interacting protein using hydrophobic buffer. SF-TAP-TMEM17 cell lysate was incubated with the indicated rabbit polyclonal antibodies and probed with anti-FLAG antibody against the SF-TAP tag. Molecular weight markers (kDa) are indicated on the left and whole cell extract (WCE) was used as a band positive marker. No Ab (lane 1) indicates no antibody negative control; lane 2 is irrelevant (irr) antibody against aquaporin 2 as a negative control. TMEM216 was weakly co-immunoprecipitated by TMEM17, suggesting a strong hydrophobic interaction between these proteins that is maintained in this buffer (n=1 biological replicate).

4.3.2.4 Co-immunoprecipitation using RIPA buffer results

The standard RIPA buffers contain non-ionic and ionic detergents and are usually used to solubilize nuclear membrane and insoluble proteins while maintaining antibody-antigen binding (Lane, 1999, DeCaprio and Kohl, 2017). The RIPA lysis buffer used in this study is a commercial preparation (see section 4.2.1.1.4). With this buffer condition, co-immunoprecipitation confirmed the interaction between TMEM17 and TMEM67 (n=1, biological replicate) (Figure 4.9) as previously identified using NP40 (B) (Figure 4.7 C).
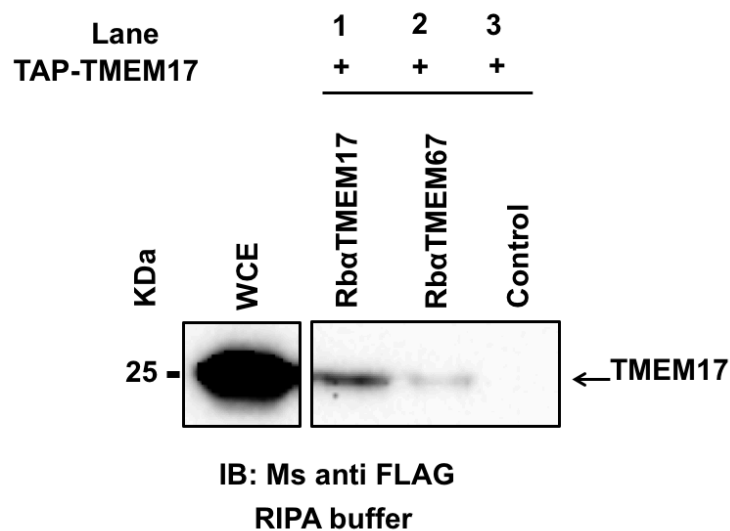
Figure 4. 9: Co-immunoprecipitation identifies TMEM67 as a TMEM17 interacting protein using RIPA buffer. SF-TAP-TMEM17 cell lysate was incubated with the indicated rabbit polyclonal antibodies and probed with anti-FLAG antibody against the SF-TAP tag. Molecular weight markers (kDa) are indicated on the left and whole transfected cell extract (WCE) was used as a band positive marker. Control (lane 3) is WCE from un-transfected cells as a negative control. TMEM17 co-immunoprecipitated TMEM67 compared to the control. Data represent one independent experiment.

4.3.3 Identifying novel TMEM protein-protein interactions using (TAP-MS) technique in HEK-293 cells

A Streptavidin-II/FLAG TAP experiment was performed to identify interacting partners of TMEM17, TMEM138, TMEM231 and TMEM237, as described previously (see section 4.2.2), using TAP-tagged constructs (see section 3.3.1) to pull-down peptides which were then interrogated by MS. The pulled-down peptides were matched to corresponding

proteins. The results were initially filtered on the basis of n ≥ 2 peptides and absence in a negative control dataset of pull-downs of RAF1-CTAP.

Table C.1 in the appendix C shows the results of the Nt-TAP-TMEM17 experiment, identifying a number of pulled-down peptides in four biological replicates. Pull-down of TMEM17 validated the experimental technique. The top hits in Nt-TAP-TMEM17 experiments were pre-mRNA-processing-splicing factor 8 (PRPF8; Q6P2Q9), pre-mRNA-processing factor 6 (PRPF6; O94906) and other background proteins (Table C.1). The latter included chaperone proteins such as heat shock protein HSP 90kDa-beta (P08238) and heat shock 70 kDa protein (P08107), and cytoskeletal proteins that included the major constituent of microtubules tubulin beta chain (P07437), cytoplasmic actin 1 (P60709) and vimentin (P08670) (Table C.1). TMEM17 appeared to have a number of interesting interacting partners, consistent with hypothesized ciliary functions for these proteins that were identified in a whole genome reverse genetics screen (Wheway et al., 2015), including PRPF8, PRPF6, and C21orf2 (Table C.1). Table C.1 shows that purified Nt-TAP-TMEM237 was identified as a pulled-down protein, validating the specificity of the experimental technique and that expression of the bait cognate protein could be detected. In particular, this TAP experiment identified an interaction between TMEM237 and TMEM17 in one biological replicate, which confirmed the previously presented co-immunoprecipitations (Figure 4.6 B; Figure 4.7 C). However, the TAP experiment pulled-down a number of background proteins such as beta-tubulin (P07437). TAP experiments on purified Nt-TAP-TMEM231 also identified the cognate bait protein, also validating the experiment approach. Although this TAP experiment identified several background cytoskeletal proteins shared with other experiments in this series, including beta-tubulin (P07437) and cytoplasmic actin 1 (P60709), there were no significant interactions and unique peptides identified that was only in one biological replicate. Furthermore, Nt-TAP-TMEM138 and Nt-TAP-TMEM216 TAP experiments failed to identify the cognate bait proteins TMEM138 and TMEM216, respectively, indicating these experiments were unreliable (see Table C.1; Appendix C). In addition, an attempt to identify TAP interactions with Ct-TAP-TMEM67 were not successful, most likely because tagging TMEM67 with a bulky C-terminal TAP fusion was incompatible with the solubilisation buffer using in this protocol. The whole cell solubilization protocols for TMEM67 therefore need to be optimised in order to preserve the integrity of TMEM67 protein-protein interactions and complexes.

4.4 Discussion

This project aimed to explore the potential role of TMEM17, TMEM67, TMEM138, TMEM216, TMEM231, and TMEM237 proteins in mammalian kidney cells by addressing the biochemical interactions between ciliary TMEMs in order to determine the potential components of a multi-subunit complexes at the ciliary transition zone region. We first examined the expression and localization of the selected transition zone TMEMs using immunofluorescence microscopy for localizations of endogenous and epitope-tagged (SF-TAP and eYFP) proteins, as well as western blot analyses (see section 3.3.1). Since the over-expressed proteins were confirmed by western blotting and localized to the expected locations in the cilium, I then used co-immunoprecipitation assays to further investigate the possible functional relationships between these proteins.

4.4.1 Co-localization studies

The overexpression of exogenous ciliary proteins can be used to test their possible localization to cilia, particularly in the absence of specific antibody reagents, but this may also cause artefactual localizations. However, this approach is useful to increase the detection limit by using antibodies with high specificity or by tagging the protein of interest with a suitable epitope. Immunofluorescent analysis showed the endogenous co-localization to base of cilia of the ciliary TMEM17, TMEM67, TMEM231 (and TMEM237; data not shown) and the presence of the FLAG and the eYFP tags (Figure 4.5) by antibody staining. For instance, endogenous TMEM17 appeared to co-localize with the basal body marker poly-glutamylated tubulin (GT335) (Figure 4.4), which was reiterated following moderate transient over-expression of SF-TAP-tagged TMEM17 (Figure 4.5). This suggests that over-expression of TMEM17, and possibly other TMEMs, did not disrupt the normal correct localization of the transmembrane protein at the base of primary cilia. In addition, endogenous expression studies confirmed the co-localization of TMEM67 in mIMCD-3 cells with poly-glutamylated tubulin (GT335) at the base of cilia, as has been reported previously in ciliated mIMCD-3 cells (Arts et al. 2007). Surprisingly, the known transition zone ciliopathy protein SF-TAP-TMEM231 did not appear to be localized at a discrete ciliary structure but occurred in perinuclear and cytoplasmic regions (Figure 4.5). Endogenous TMEM231 localization was determined by optimizing the titre (in serial dilution experiments) and

fixation conditions of the anti-TMEM231 antibody in order to reduce non-specific binding and background staining (Figure 4.4). However, unlike endogenous TMEM231, the exogenous over-expressed TMEM231 did not appear to localize to the base of cilia. Although cells with higher expression levels of this protein appeared to have disrupted this expected localization, the loss of ciliary localization even at moderate expression levels could be explained by the interference of the epitope tag at the N-terminus of the protein with correct localization. This could be due to incorrect targeting away from the ciliary membrane at the transition zone or disrupted folding of the tagged protein.

By contrast, confocal micrographs taken 72 hours after co-transfection of TMEM67 tagged at the C-terminus with eYFP (Ct-eYFP-TMEM67) demonstrated that it localized correctly to the expected regions at the base of cilia in mIMCD-3 cells (Figure 4.5), where it colocalised with 5HT6-RFP. Prior to this experiment ciliary-specific antibodies, including against acetylated α-tubulin and ARL13B (Figure 4.3), were used to confirm that 5HT6-RFP was indeed correctly localizing to primary cilia in this stably-transfected mIMCD-3 cell-line. However, not all cilia identified with the endogenous markers also expressed detectable levels of 5HT6-RFP (Figure 4.3), indicating that tagged serotonin receptor is not always correctly localized to cilia.

4.4.2 Biochemical characterization

Co-immunoprecipitation assays have been successfully used to study the direct or indirect interactions of transition zone TMEMs, with results dependent on the type of buffer used in the assay. Buffers of different ionic strength and detergent properties yielded different results. The salt concentration can be increased (up to 500 mM) or decreased (lower than the isotonic physiological concentration of 130 mM), since high salt concentration tends to weaken the binding (Arnold and Linke, 2008) whereas concentrations lower than 130 mM will increase non-specific interactions (Gerace and Moazed, 2014). In this project, I used four different salt concentrations, two of which were lower than 130 mM, comprising: 25 mM NaCl, 80 mM KCl, 140 mM NaCl and 150 mM NaCl for hydrophobic buffer, NP40 (B) buffer, RIPA buffer and CHAPS buffer, respectively.

In this project for co-immunoprecipitation of TMEMs, I used several mild lysis buffers with a non-ionic detergent to reduce the probability of interfering with protein-protein interactions. The majority of protein-protein interactions were shown with CHAPS buffer and NP40 (B) buffer conditions (salt concentrations 150 mM and 80 mM, respectively), whereas hydrophobic buffer only showed a single interaction (between TMEM17 and TMEM216; Figures 4.6-4.8). RIPA buffer contains both non-ionic and ionic detergents (including SDS) and can therefore denature the protein of interest and is more likely to disrupt protein-protein interactions. However, the interaction between TMEM67 and TMEM17 was maintained in RIPA buffer (Figure 4.9), indicating that this is a stronger interaction that is not easily disrupted by detergents. The data suggests a possible new model for the formation of transition zone ciliary complexes, highlighting the importance of the TMEM17-TMEM67 interaction. Epitope-tagged TMEM17, TMEM138, TMEM216 and TMEM237 were used for efficient and specific co-immunoprecipitation experiments, which included the pull-down of the cognate bait protein thereby validating the experimental approach in all cases. Epitope-tagged TMEM231 (data not shown) did not co-immunoprecipitated or pulled down other TMEMs. Finally, an anti-TMEM138 antibody was not available at the time these experiments were performed. In this project, however the A simplified summary of co-immunoprecipitation results is shown in Figure 4.10.
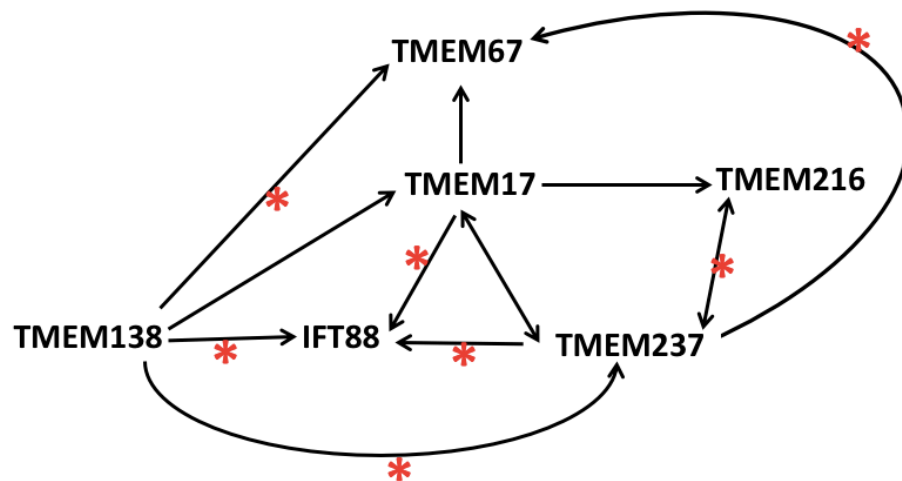
Figure 4. 10: Summary of co-immunoprecipitation results. Double sided arrow represents reciprocal interactions, for example between TMEM17 and TMEM237. Red asterisks indicate novel interactions between ciliary TMEMs and other ciliary proteins.

Novel interaction partners were also identified in this study, which may suggest that selected TMEMs play novel roles together as a complex during signal transduction,

trafficking and maintenance of the primary cilia. The identification of novel interaction partners provides an immediate lead into biological function and possible insights into disease mechanisms. Co-immunoprecipitation assays and TAP-MS studies provided information about complex composition and organization between the selected TMEMs. These studies assumed that two proteins share the same function if they interact with each other or they have related roles and work as a complex. In addition, however, these studies showed that not all selected TMEMs interacted with each other even though they co-localized in the same ciliary sub-compartment; therefore, the results perhaps not do support the former hypothesis, and based on my data not all the TMEMs appear to biochemically interact.

The STRING (http://string-db.org/) database by (Szklarczyk et al., 2015) was used in this study to explore predicted protein interaction networks including direct (physical) and indirect (functional) associations for TMEM138, TMEM17, TMEM216 and TMEM237 and to show global significance of the various pulled-down proteins. The functional partners predicted by STRING are based on co-expression analysis, evolutionary signals across genomes, automatic text-mining of the biomedical literature and orthology-based transfer of evidence across organisms. The STRING analyses (Figure 4.9) provided a summary of potential functional partner proteins that were identified in this project by biochemical assays for *Homo sapiens* TMEM17, TME138, TMEM216 and TMEM237. However, these did not identify a common shared functional pathway.

4.4.2.1 Interactions between SF-TAP TMEM17 and ciliary transition zone TAP-tagged proteins were confirmed by biochemical studies in HEK-293 cells

To further investigate interactions with TMEM17 in protein complexes, systematic proteomic analyses using co-immunoprecipitation and pull-down experiments followed by MS were used to identify interacting proteins. Co-immunoprecipitation analysis showed that SF-TAP-TMEM17 interacted with TMEM216 (n=2, biological replicates), TMEM67 (n=3), TMEM237 (n=1) and IFT88 (n=1) (Figures 4.7; 4.8 C; 4.9). Furthermore, rabbit anti-TMEM17 pulled down epitope-tagged TMEM17 in these co-immunoprecipitation experiments, confirming the specificity of the antibody. TMEM17 interacted with TMEM216, TMEM237 and IFT88 in both NP40 (B) buffer and RIPA buffers, whereas TMEM17 also appeared to only

interact with TMEM216 using hydrophobic buffer (with a low salt concentration) which suggests that the TMEM17-TMEM216 interaction is maintained irrespective of the salt concentration and even in the presence of SDS, a strong ionic detergent. This indicates that a TMEM17 and TMEM216 complex is mediated by strong hydrophobic interactions. TMEM17 interactions with TMEM67 and TMEM216 were summarized in the STRING networks, revealing other interactions with ciliary proteins (figure 4.11 C, D) such as TMEM67, TMEM216 and TMEM237 that are consistent with a previous study (Gupta et al. 2015).

Next, therefore, the possible functional interactions between TMEM17 and the associated proteins were investigated using TAP-MS. The TAP experiments indicated that the cognate TMEM17 bait protein was pulled-down, validating the experimental approach, and that TMEM17 interacted with two pre-mRNA processing factors (PRPF6 and PRPF8), and C21orf2 (Tables C.1) (Figure 4.11). Interestingly, C21orf2, PRPF6 and PRPF8 were all validated hits in a whole genome reverse genetics screen of ciliogenesis modulators (Wheway et al., 2015). C21orf2 was implicated in ciliogenesis (Lai et al., 2011), whereas *PRPF6* and *PRPF8* were found to be key effectors of cell division in the Mitocheck screen (Neumann et al., 2010) and were implicated in the ubiquitin-dependent regulation of the spliceosome. This result suggested that PRPFs affect ciliogenesis through regulation of correct splicing of transcripts encoding α-tubulin, a structural component of the cilium (Song et al., 2010, Pelisch et al., 2013). These results could provide insights into the function of ciliogenesis of the identified proteins and demonstrate their involvement in molecular processes of cilia biology and other related cell biological processes.

A further interesting interaction of TMEM17 was with membrane-associated progesterone receptor component 1 (PGRMC1; Table C.1), although the peptide counts in the TAP pull-downs are low. This result is supported by entries in the neXtProt knowledgebase: https://www.nextprot.org/entry/NX_Q86X19/interactions

https://www.nextprot.org/entry/NX_O15173/interactions, and is consistent with the results of a previous study (Gupta et al. 2015). The neXtProt knowledgebase (https://www.nextprot.org), is an integrated ive resource platform of human proteins annotating their function, subcellular location, expression, interactions and role in diseases (Zahn-Zabal et al., 2020). However, these are preliminary data and the biochemical

interaction between TMEM17 and PGRMC1 will need to be demonstrated through additional experimental work.

In summary, the result of a series of *in vitro* SF-TAP binding and co-immunoprecipitation studies demonstrated robust interactions between TMEM17 and TMEM67 (Figure 4.7; Figure 4.9). Therefore, I suggest that these two transition zone proteins may work together to form a complex that is required for correct structure and function of the primary cilia.

4.4.2.2 Interactions between SF-TAP TMEM237 and ciliary transition zone TAP-tagged proteins were confirmed by biochemical studies in HEK-293 cells

Epitope-tagged TMEM237 had a reciprocal interaction with TMEM216 (Figures 4.6 A, B; 4.7 B) in both CHAPS and NP40 (B) buffers, but also interacted with TMEM17 (Figure 4.8) and TMEM67 (Figure 4.6 B). Systematic TAP/MS to identify protein-protein interactions confirmed reciprocal biochemical interactions between TMEM237 and TMEM17 (Table 4.14). Furthermore, this interaction is identified in the neXtProt knowledgebase and is consistent with a previous study (Gupta et al., 2015). However, TMEM237 interactions with TMEM216 and TMEM67 are novel. These results provide insights into the network of TMEM237, since the proteins may work together as a complex in the transition zone, providing mechanistic insight into to the composition of the MKS module. TMEM237 interactions with TMEM67, TMEM138 and TMEM216 were summarized by STRING networks, but this also revealed other interactions with other important ciliary proteins (Figure 4.11 G, H) such as TMEM67, TMEM216 and TMEM231 that are supported by the Gupta et al. (2015) study. In contrast, TMEM216 interactions with TMEM237 were not supported by Gupta et al. (2015), but did identify interactions with other ciliary proteins (Figure 4.11 E, F) including TMEM67, a self-interaction with TMEM216, RPGRIP1L and CEP290.

In addition, a novel interaction was identified between epitope-tagged TMEM237 and IFT88 (Figure 4.6 C); TMEM138 and TMEM17 co-immunoprecipitation experiments also supported an interaction with IFT88 (Figure 4.7 A, C). This suggests that the three ciliary proteins TMEM237, TMEM17 and IFT88 could interact as a complex, since the TMEM17 and TMEM237 interaction is confirmed by reciprocal biochemical interaction assays. Little is

known about how IFT-B and its component IFT88 mediate ciliary protein trafficking, and how entry into and exit from cilia of IFT particles via the transition zone are regulated (Nakayama and Katoh, 2018). My data suggests that these processes could be mediated, at least in part, through interactions between TMEMs (TMEM237, TMEM17 and TMEM138) and the motor protein IFT88. How the small TMEMs assemble and work together with the motor protein IFT88 to mediate ciliary trafficking or ciliogenesis is unknown. Therefore, the next chapter I examined each one in siRNA knockdown studies in order to gain some preliminary functional insights.

4.4.2.3 Interactions between SF-TAP TMEM138 and ciliary transition zone TAP-tagged proteins were confirmed by biochemical studies in HEK-293 cells

Co-immunoprecipitation assays of TMEM138 using two different buffers, containing either CHAPS or NP40 (B) as described previously (see section: 4.4.1 and 4.4.2), yielded different results in whole cell lysates from mammalian HEK-293 cells. The buffers have different ionic strengths and detergents which were used to crudely assess the specificity and strength of protein-protein interactions between ciliary TMEMs. Co-immunoprecipitation assays showed that epitope-tagged TMEM138 interacted with TMEM17, TMEM237, TMEM67 and IFT88 (Figure 4.10). The assays indicated that TMEM138 interacted with TMEM17 and TMEM237 (see section 4.4.1; Figure 4.6 D, E), an interaction that was maintained in a high ionic strength buffer (CHAPS buffer). In contrast, epitope-tagged TMEM138, co-immunoprecipitated with TMEM67 and IFT88, was maintained in a low ionic strength buffer (NP40 (B) buffer) (see section 4.4.2; Figure 4.7 A). The TMEM138 interactions with TMEM67 and TMEM237 were shown in a STRING network which revealed other interactions with important ciliary proteins (Figure 4.11 A, B) such as TMEM67, TMEM237 and TMEM231.

The interaction between TMEM138 and TMEM17 was identified in previous study (Gupta et al., 2015), whereas the TMEM138 interactions with TMEM237, TMEM67 and IFT88 were not identified in any recent studies. This suggests that these are novel interactions need further investigation. TMEM138 co-immunoprecipitated with TMEM237 and TMEM67, suggesting it is part of the MKS/JTSB protein complex and work as group to support ciliary or transition zone function. In addition, the intraflagellar transport protein

IFT88 is an essential component of primary cilia, shuttling ciliary cargo proteins signals along the axoneme in an anterograde direction and is required for ciliary maintenance (see section 1.2.4.5.1 in Chapter 1). TMEM138 co-immunoprecipitated with IFT88, consistent with the previous results in the above section (4.4.2.2). That is a novel interaction with the motor protein IFT88 suggesting that the indicated TMEMs may play a role in restricting IFT88 to the ciliary axoneme segment. If so, this indicates the trafficking in cilia is highly regulated by involving TMEM138, along with TMEM17 and TMEM237 in ciliary trafficking or ciliogenesis. This findings re uncover unexpected diversity in the mechanisms that traffic and localize TMEMs and IFT88 to cilia both within and across cell types, highlighting the essential contribution of this process to cellular functions. Accordingly, TMEM138, and TMEM237 appear to play a crucial role in trafficking and/or axoneme stabilities as shown in Chapter 5.

4.4.3 Further investigations and experimental limitations

Do biochemical interaction studies that confirm an *in vitro* interaction between TMEM17 and TMEM67 (Figure 4.7 C; Figure 4.9) support the hypothesis that there is a direct or indirect functional relationship between TMEM17 and TMEM67, and a given network can be viewed as potential functional module? In my opinion, further studies focused on the identification of component members of the TMEM17-TMEM67 network would substantiate this complex or module, and will help to understand their specific functions and their role in the pathogenesis of ciliopathies. Therefore, further investigations were carried out in Chapter 5. Importantly, however, at least three biological replicates of TAP and co-immunoprecipitation studies of TMEM67 and TMEM17 should be achieved in order to substantiate the existence of this module.

In addition, in this study, I constructed TMEM231 expression constructs with N-terminal epitope tags and confirmed expression by western blotting and TAP pull-downs. However, notable differential expression was observed and epitope-tagged TMEM231 localized to the cell membrane which is a common artefact following the over-expression of some membrane proteins or fusion with different epitopes. Therefore, the level of expression could be modulated by using a different promoter in the expression construct, or

the composition of residues in epitope-tagged TMEM231 could be altered to ensure better trafficking of TMEM231 to the cilium and normal localization to the transition zone.

Additional co-immunoprecipitation studies of IFT88 should be performed in order to more fully understand its roles in a potential complex with TMEM17, TMEM138 and TMEM237. The introduction of sequence variants that model ciliopathy patient mutations in the expressed TMEMs could provide further insights into mechanisms of molecular pathogenesis in ciliopathies. Finally, in this study, co-immunoprecipitation experiments were performed multiple times for four different buffers in order to standardize the right conditions for each that demonstrate the presence or absence of an interaction. However, one limitation should be noted which is that only one biological replicate was performed for some of the coimmunoprecipitation and TAP-MS experiments (see sections 4.3.2.2, 4.3.2.3, 4.3.2.4, 4.3.3). Unfortunately, time limitations precluded further validation which is significant issue to be addressed in future studies. Therefore, in future studies, three biological replicates should be conducted to fully validate an interaction which would prevent false positive results due to the co-immunoprecipitation of non-specific interacting proteins. The use of proper controls and the ability to perform these experiments in triplicate can allow for the identification of even low-abundance and weak interactors as significate.

Further studies are also needed to confirm the co-immunoprecipitation experiments. The studies on the coimmunoprecipitations have discovered that TMEMs proteins formed a single, monodisperse complex and some novel interactions. Using a high-confidence proteomic network analysis would be beneficial to confirm the results. Future studies should use the proximity-dependent biotin identification (BioID) approach to generate proximity interaction maps for TMEM proteins, which may will confirm existing interactions and identify new interactions, regulators and mechanisms that contribute to the functional modules that are critical for transition zone sub-compartment and cilium biogenesis. I would perform BioID in two conditions, namely non-ciliated cells and serum-starved ciliated cells to observe any differences in the interaction between them which could provide insights into novel regulators of ciliogenesis. The analysis of BioID was used previously in human cells to screen for interactors of most known transition zone modules by (Gupta et al., 2015) (see section 6.2).
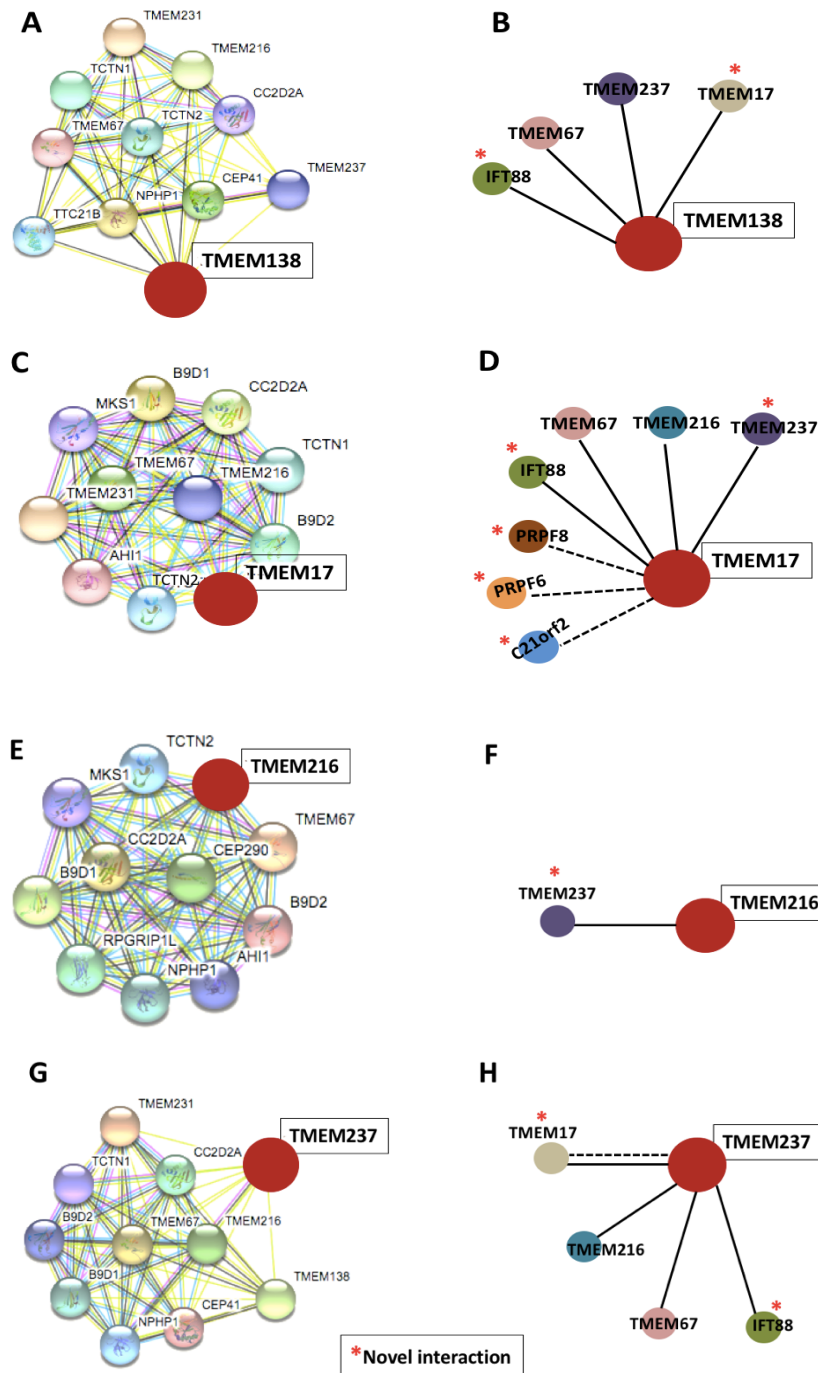
Figure 4. 11: The STRING network view and schematic outlines of data derived from the co-immunoprecipitation and (TAP-MS) studies. Panels **(A)**, **(C)**, **(E)**, and **(G)** show STRING network analysis which indicate connections between the proteins associated with TMEM138, TMEM17, TMEM216, and TMEM237. Panels **(B)**, **(D)**, **(F)**, and **(H)** summarize all of the biochemical interactions described in this chapter. Schematic outlines indicate: solid black lines indicate interactions determined by co-immunoprecipitation assays, dashed lines indicate interactions identified by TAP-MS pulldowns. Red asterisks indicate novel interactions between ciliary TMEMs or ciliary proteins predicted in this project. Note: epitope-tagged TMEM231 did not co-immunoprecipitate or pull-down other TMEMs, and therefore its networks are not shown.

Chapter 5 Functional characterization of putative ciliary genes using siRNA

5.1 Introduction

Many proteins linked to ciliopathies are specifically localized at the ciliary transition zone as mentioned and described in detail in Chapter 1. For instance, mutations in the *TMEM67*, *TMEM216*, *TMEM237* and *TMEM231* genes are known to cause ciliopathies, but the function of these TMEMs is unclear and it is unknown how the mutations in these genes disrupt ciliary structure or function. Recent findings in biomedical and genetic research have suggested that transition zone proteins work as a complex and this concept was confirmed in the biochemical interaction results in the previous Chapter 4. Additionally, (Vieillard et al., 2016) have shown that the MKS module proteins co-localize and together contribute to the construction of the transition zone in several organisms, from *C. elegans* to mammals.

Therefore, for further investigation and to begin to understand the potential function of the selected ciliary TMEMs, small interfering RNAs (siRNAs) were designed against *TMEM17, TMEM138, TMEM231* and *TMEM237* (Table 5.1). Here, I hypothesize that altering the expression of the selected TMEMs causes reduction in primary cilia length or number in association with deregulation of primary cilia sub-compartments including the basal body, transition zone and axoneme in ciliated cells. Figure 5.1 summarizes the possible effects on ciliary sub-compartment organization, cilia morphology and cilia length after knockdown of the selected ciliary TMEM genes. Figure 5.1 illustrates the idea that mild ciliary defects cause a slight reduction in axoneme length and some co-localization between the transition zone and axoneme, whereas more severe defects cause a greater decrease in axoneme length and greater co-localization between the transition zone and axoneme, as well as the transition zone and basal body.

To test this hypothesis, the knockdown experiments were performed to infer synthetic genetic interactions that could predict a structural or organizational function for selected ciliary transition zone components in 3 different sub-compartments of the ciliary apparatus in mIMCD-3. The ciliary apparatus in these cells is 1 to 10 μm in length (Gerhardt et al., 2016) and the separate sub-compartments were visualized separately. γ-tubulin was

used as a marker of the basal body and acetylated α-tubulin was used to mark the ciliary axoneme. Finally, antibodies against *TMEM67*, *RPGRIP1L* and *CEP290* were used to mark the transition zone for each of the ciliary module associated with these proteins.

The experimental approach in this chapter was quantifying co-localization of TMEMs with components of the ciliary apparatus, using imaging data to integrate this into a descriptive genetic interaction network that provided insights into the functional relationships between these ciliary proteins. The efficiency of knockdowns was evaluated by immunoblotting, when suitable antibodies against the target protein were available (Figure 5.9). Significant increases and decreases in the co-localization of ciliary sub-compartments were associated with knockdown of some of the selected genes. In addition, knockdowns caused distinct ciliary phenotypes including changes in numerical incidence (Figure 5.4 C, E). These results suggest that ciliary trafficking and maintenance were disrupted and/or suggest that TMEM knockdowns perturbed ciliary protein-protein localization.
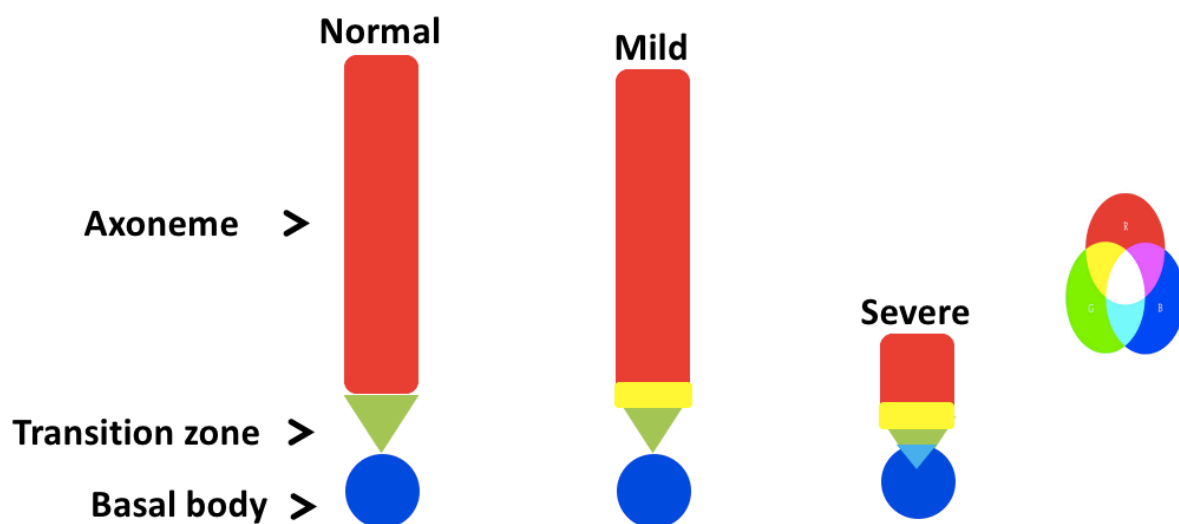
Figure 5. 1: Schematic that summarizes how knockdown of selected ciliary TMEM genes affects the relative positioning of ciliary structural sub-compartments, primary cilia morphology and length. Black arrowheads indicate ciliary axoneme (red), transition zone (green) and basal body (blue). Mild ciliary defects cause a slight decrease in axoneme length and some co-localization between the transition zone and axoneme (yellow). More severe defects cause a greater decrease in axoneme length and greater co-localization between the transition zone and axoneme (yellow), and transition zone and basal body (turquoise).

The overall aim in this chapter was to understand how ciliary TMEMs function in primary cilia and investigate and support the previous results in Chapter 4, specifically by investigating the genetic interactions between selected transition zone ciliary genes:

- Evaluate the knockdown of ciliary TMEM genes by reverse and forward transfection of siRNA and examine the effect on ciliary sub-compartments and phenotypes.
- Quantify co-localization of ciliary sub-compartments (basal body, transition zone and axoneme) after siRNA knockdown.

5.2 Materials and methods

Thermo Scientific Dharmacon was the supplier for "SMARTpool" siRNA reagents. Each gene was targeted by a pool of 4 duplexes per well, including N-TARGETplus individual or "SMARTpool" pooled siRNAs targeting the mouse genes *Tmem17*, *Tmem67*, *Tmem138*, *Tmem216*, *Tmem231* and *Tmem237* (sequences listed in Table 5.1). The medium or low GC non-targeting scrambled siRNA duplexes (Dharmacon) were used as negative controls. Unless otherwise stated, siRNA solutions were made up in 5x siRNA buffer (GE Healthcare Dharmacon #B-002000-UB-100) diluted to 1x with RNase-Free water (GE Healthcare Dharmacon #B-003000-WB-100). siRNAs were re-suspended in 1x siRNA buffer to a stock concentration of 2 µM for a 96-well plate reverence transfection experiments and 20 µM for a 6-well plate forward transfection experiments. Following agitation on a rotary shaker for an hour, aliquots of 2 µM and 20 µM were prepared and stored at -20°C to avoid freeze-thaw degradation. Mouse mIMCD-3 cells were used in this study as a model of ciliated cell line (see section 3.2.2). In this study, technical replicates describe repetitions of the same sample using different fields of view from the same sample well or plate as described previously (Blainey et al., 2014).

Table 5. 1: Sequences of siRNA duplexes used in siRNA analysis.

Target mouse gene	Gene ID	Gene accession	siRNA sequence (5' to 3')
Plk1	18817	NM_011121	CCAACCAAAGUGGAAUAUGA
			GCAAUUACAUGAGUGAGCA
			GCAAGAUCGUGCCUAAGUC
			UCACUCUCCUCAACUAUUU
Ift88	21821	NM_009376	CGGAGAAUGUUGAAUGUUU
			GCUUGGAGCUUAUUACAUU
			CGUCAGCUCUCACUAAUAA
			GUAGCUAGCUGCUUUAGAAA
Rpgrip1l	244585	NM_173431	GGAUCAAGCUAUUCGACUU
			CAGCACAGAUUACGAAACA
			GAAUACUGGUUCCGAUUAA
			CAAUAAAGAUCUAGACCGA
Tmem17	103765	NM_198276	GGUAAGACAAUGCACGGAA
			UAUGCUGAGUGGUGAACGA
			GAUUGAAGCGAUCCGGUUA
			GUAUGGCACUUCAGACGAA
Tmem67	329795	NM_177861	GCAGUAAGUGGACGAGAAA
			CCUUAAAAGAGAAGCGGAA
			UGACUUAACUGCCGAAGGA
Tmem138	72982	NM_016464	GGGUCAUGAACGUGCGAUG
			CCGAAUGGCUCCUGUUAUC
			CAUGCAAGUCCGAAGGUGA
			AGGUUAGCCUGUAGAGAGA
Tmem231	234740	NM_001077416	CGUGCUUGCUGGCGGGUAA
			CCUUCAAAGCACCGAGGGA
			GCUGAAGCUCCGUUCGUGA
			CCAGGGAGAGAUACGGAAA
Tmem237	381259	NM_001044385	UCUCUACUACGGAACGAAA
			UAUCAGUAGCAAUCCGGAA
			AGGCAUGGAUCUUAGUGAA
			CGAUAUUCCACUUAGUCAU
Scrambled negative control	N/A	N/A	UGGUUUACAUGUCGACUAA
			UGGUUUACAUGUUUUCUGA
			UGGUUUACAUGUUGUGUGA
			UGGUUUACAUGUUUUCCUA

* N/A: Not Applicable

5.2.1 siRNA knockdown
5.2.1.1 Cell plating, transfection, fixation, data imaging and analysis of reverse transfection experiments in 96-well culture plates)

The reverse genetics visual screen was performed as described previously (Wheway et al., 2015). A PerkinElmer 96-well plate was used in this study. 2.5 µl/well of 2 µM siRNA was pipetted and placed in the bottom of each well (50 nM siRNA in 100 µl liquid). 17.3 µl Opti-MEM medium was mixed with 0.2 µl/well Lipofectamine RNAiMAX transfection reagent (Invitrogen) and incubated for 5 minutes at RT. The 17.5 µl mixture was then added to the well and incubated for 20 minutes in a NuAire Labgard 437 ES Class II Biosafety Cabinet. During the incubation of the reagent in the plate, a T75 flask Corning® #431464U of 80 % confluent low-passage (P17-25) culture of mIMCD-3 cells were trypsinized and centrifuged as described in (see section 3.2.2.1). The supernatant was aspirated and the cell pellet re-suspended in 10 ml of Opti-MEM reduced serum (Gibco #31985-047), antibiotic-free medium and gently pipetted. The Trypan Blue dye exclusion Countess™ cell counting described in (see section 3.2.2.2) was used to calculate cell concentration and viability.

80 µl mIMCD-3 cells at a density of 10^5 cells per ml in Opti-MEM were seeded per well to a plate. The plate was incubated for 60 minutes in a NuAire Labgard 437 ES Class II Biosafety Cabinet, followed by further incubation in a cell culture incubator (Sanyo MCO 20A/C set at 37°C with 5% CO_2) for 72 hours. Subsequently, transfection medium was detached from the plate by inverting the plate and blotting on clean tissue paper to remove excess liquid. Plates were processed for fixation and immunofluorescence staining as described in (3.2.5.1); however, in this experiment a 96 well plate was used, therefore the number of reagents and solution used to stain, fix and wash the cells were reduced. Briefly, cells were washed 3 times with 100 µl 1x DPBS, using a Star-pet-E 8-channel electronic pipette. 50 µl ice cold absolute methanol was dispensed against the left side of each well and the plate was placed in a freezer at -20 °C for 5 minutes. The plate was inverted and blotted to remove methanol and washed with 50 µl 1x DPBS. For immunofluorescence staining, 100 µl 1% Marvel dried milk/DPBS (w/v) blocking solution was added for each well for an hour. Primary and secondary antibodies are listed in Table 2; antibodies were prepared and diluted in the blocking milk solution and clarified by centrifugation at 12000 *xg* for 5 minutes at RT. 50 µl of the primary antibody solution was added to each well and

incubated for an hour at RT. Cells were washed twice with 100 µl 1x DPBS per well. Secondary antibody solution combined with either DAPI or TOTO3 was added and incubated for 1 hour at RT in the dark. The cells were washed twice with 100 µl 1x DPBS per well and the plate was stored with filtered 100 µl 1x DPBS per well at 4 °C for up to a week before imaging.

5.2.1.1.1 "Operetta" High-Content Imaging system analysis

siRNA reverse transfection was analysed by high content imaging using an Operetta High-Content Imaging system (Perkin-Elmer Inc.) and images were then transferred to "Columbus" Harmony software (Perkin-Elmer Inc.) for further analysis; the visual screen was performed using an amended protocol (Wheway et al., 2015) to meet the scope of the co-localization investigation. Wells were imaged using a 60x air objective lens, detecting 4 colours in 4 separate focal planes to obtain high resolution for each colour channel (at 405 nm, 488 nm, 594 nm and 633 nm). The bottom of each well was sensed automatically by the Operetta infra-red focusing laser and focal planes for each colour channel were calculated relative to this value. Ten fields of view (each 510x675 µm) were imaged per well, with an estimated total of 4000 cells detected and examined per well. In this assay, acetylated α-tubulin (Sigma-Aldrich # 070M4755) was used as a ciliary axoneme marker. C-TMEM67 (In-house to Johnson lab) or CEP290 or RPGRIP1L were used as transition zone markers. γ-tubulin (Santa Cruz # c-20) was used as basal body marker. DAPI (Sigma-Aldrich) was used to determine cell and nuclear boundaries. Primary and secondary antibodies used in this analysis are listed in Table 5.2. siRNA pool targeting mouse *Plk1* was used as a positive transfection control and siRNA pool targeting mouse *Ift88* was used as positive controls for effects on ciliogenesis compared to a negative control, 2 duplicate Dharmacon scrambled non-targeting siRNAs. The data shown in section (5.3.1.1) is from only one biological replicate and 2 technical replicates. Sequences of control siRNA duplexes are given in Table 5.1.

5.2.1.1.2 Image analysis

Appendix D.1 lists and explains the modified PerkinElmer image analysis algorithms that were used in this the study of ciliary sub-compartments axoneme, transition zone, and basal body. The analysis was based on the fluorescent staining comprising the red channel

that visualized the ciliary axoneme marker; green for transition zone markers, and far-red for the basal body (Figure 5.2 A). The analysis quantified the degree of co-localization between green with red, or far red with red, or green with far red, in order to calculate the overlap between sub-compartments. Border objects were excluded and only whole cells were analysed. Nuclei were detected as blue (DAPI) fluorescent regions. Ciliary axonemes labelled with acetylated α- tubulin on whole cells were detected using a modified 'find spots' algorithm, identifying fluorescent spots of area in the 546 nm colour channel as shown in appendix D.1. Transition zones labelled with the TMEM67 C-terminus antibody (R24), on every ciliary axoneme on every cell, were detected using a modified 'find spots' algorithm, identifying green fluorescent spots in the 488 nm colour channel as shown in appendix D.1. Basal bodies labelled with γ-tubulin, on every ciliary axoneme on every cell, were detected using a modified 'find spots' algorithm, identifying far red (DRAQ5) fluorescent spots as shown in appendix D.1. The number of whole cells and percentage of whole cells with a single cilium was calculated.

5.2.1.2 Cell plating, transfection, fixation, data imaging and analysis of forward transfection experiments

Prior to each experiment, a T75 flask Corning® #431464U of 80 % confluent low-passage (P17-25) culture of mIMCD-3 cells were trypsinized and centrifuged as described in (3.2.2.1). The supernatant was aspirated and the cell pellet re-suspended in 10 ml of Opti-MEM reduced serum (Gibco #31985-047), antibiotic-free medium and gently pipetted. 2.5 x 10^5 cells/well were seeded onto sterile glass coverslips in 6-well culture plates while gently swirling as described in (3.2.5.1), using the Trypan Blue dye exclusion method (3.2.2.2) to determine cell concentration and viability. Plates were processed for knockdowns (forward transfection); 5 µl (20 µM) of siRNA were mixed with 196 µl Opti-MEM medium and incubated for 5 minutes at RT. In a separate tube, 5 µl Lipofectamine RNAiMAX transfection reagent was mixed with 196 µl Opti-MEM medium and incubated for 5 minutes at RT. The contents of both tubes were combined and vortexed briefly and incubated for 20 minutes at RT. The mixture was then added drop-wise to the 50% confluent cells on the coverslips. Subsequently the cells were incubated for 72 hours at 37°C, 5% CO_2. Plates were processed for fixation and immunofluorescence staining as described in (3.2.5.1).

5.2.1.2.1 'Volocity x 64' 3D Imaging system analysis

siRNA forward transfection was first imaged by confocal microscopy to generate Nikon.nd2 files for 3D image data. The resulting images are optically sectioned into Z-stacks that can be combined to generate a maximum intensity projection image.(Dunn et al., 2011). All confocal Nikon.nd2 images were obtained with identical gain, offset, and laser power settings. The primary cilia sub-compartments were marked as follows: ciliary axoneme labelled with gold (Alexa Fluor 555) fluorescent spots. Transition zones labelled with C-TMEM67 (R24) or CEP290 or RPGRIP1L, identifying green (Alexa Fluor 488) fluorescent spots. Basal bodies labelled with γ-tubulin, identifying far red (Alexa Fluor 633) fluorescent spots. Second, for the quantitative analysis of the fluorescence, Volocity x64 (PerkinElmer Inc.) software was used to measure the fluorescence intensities of the basal body, transition zone, and axoneme ciliary sub-compartments. For example, fluorescence-density differences were calculated by outlining each ciliary axoneme and obtaining the area of each cilium and the raw integrated densities of the acetylated α-tubulin by using these features in the software. Volocity x64 analysed the 3D image data and transformed the observations of primary cilia staining of the sub-compartments into quantitative results.

The analysis protocol was created by adding pre-configured measurement tasks specifically for quantifying co-localization between cilia stained sub-compartments, and then applying (8-10) 3D images to the software as a batch process. The co-localizations between transition zone and axoneme, transition zone and basal body, and axoneme and basal body were measured separately to generate Pearson's coefficient values. The data was then exported into Microsoft Excel for graphical and statistical analysis. The effect of the knockdown on ciliary phenotype data such as morphology and co-localization of markers was graphed in Microsoft Excel; the statistical significance of pair-wise comparisons was calculated using Student's t test (two-tailed, two sample equal variance). The effect of siRNA knockdown on cilia number was assessed by calculating the percentage of cells with a single cilium and was measured using Fiji software as described in (Appendix D.3), with the statistical significance of this effect assessed by t-test. The effectiveness of siRNA knockdowns was determined by western immunoblotting (Figure 5.9).

5.2.1.2.2 Image analysis

The details of quantitative co-localization image analysis using Volocity x64 are provided in Appendix D.1. The Nikon.nd2 images were analysed by Volocity x64. In any given image slice, fields of view were stitched together. Fluorescence co-localization analysis, using Pearson's correlation coefficient, was used to determine the degree that 2 ciliary sub-compartments associated with the same primary cilia structure after knockdown, compared to the scrambled negative control. Pearson's correlation coefficient described the correlation of the intensity distribution between channels: the values ranged between −1.0 and 1.0, where 0 indicated no significant correlation, −1.0 indicates complete negative correlation and 1 a strong positive correlation (Zinchuk et al., 2007).

5.2.2 Antibodies

Table 5. 2: List of the primary and secondary antibodies with experimental conditions used in the study.

Primary Antibodies	Concentration (1:x)	Supplier	Cat. Number
Rabbit anti C-TMEM67 (R24)	1:200	In-house to Johnson lab	N/A
Rabbit anti RPGRIP1L	1:100	Proteintech	55160-1-AP
Moues anti CEP290	1:500	Gift of Ciaran Morrison	N/A
Rabbit anti IFT88	1:200	Proteintech	13967-1-AP
Moues Acetylated α-tubulin	1:1000	Sigma-Aldrich	070M4755
Goat anti γ-Tubulin	1:50	Santa Cruz	C-20
Secondary Antibodies	**Concentration**	**Supplier**	**Cat. Number**
AlexaFluor594 chicken anti-mouse IgG	1:500	Molecular Probes	A-21201
CF405M donkey anti goat IgG	1:500	Biotium	20398
AlexaFluor488 donkey anti-rabbit IgG	1:500 (forward transfection)	Biotium	A-21206
	1:2000 (reverse transfection)		
AlexaFluor555 donkey anti-mouse IgG	1:500 (forward transfection)	Life technologies	A-31570
	1:2000 (reverse transfection)		
AlexaFluor633 donkey anti-goat IgG	1:500 (forward transfection)	Invitrogen	A-21082
	1:2000 (reverse transfection)		
DAPI (5 mg/ml)	1:500 (forward transfection)	Sigma-Aldrich	MBD0015
	1:2000 (reverse transfection)		
TOTO3 (1 mM)	1:5000	Life Technologies	T3604

5.2.3 siRNA validation

mIMCD-3 cells were cultured and prepared (see section 3.2.2.1) for siRNA transfection in Opti-MEM low-serum transfection medium as described in section (5.2.1.2). 72 hours later, cell lysates were prepared as described in section (3.2.6.1) from *Tmem17*, *Tmem231*, *Tmem237*, *Rpgrip1l* and *Ift88* siRNA-treated cells. Protein samples underwent SDS-PAGE and were transferred onto a PVDF membrane as described in section (3.2.6.3). The transferred protein was probed with specific rabbit polyclonal primary antibodies (Table 5.2) followed by an HRP enzyme-conjugated secondary antibody (Chapter 4; Table 4.4), the data shown in section (5.4) is from only one biological replicate. Band intensities were measured using Image Lab software (Bio-Rad) and the gene silencing effect was evaluated by comparing the relative protein expression of the sample with scrambled negative control.

5.3 Results from forward and reverse TMEM knockdowns
5.3.1 siRNA reverse transfection using "Operetta" high content imaging

5.3.1.1 TMEM67 module

The primary screen identified some significant alterations between transition zone and axoneme co-localizations following knockdowns with siRNAs for *Rpgrip1l*, *Tmem231*, *Ift88* and *Plk1* compared to the scrambled siRNA negative control (Figure 5.2). Two wells were tested for the scrambled siRNA negative control and the positive control for transfection efficiency control (*Plk1*), the positive control for cilia number (*Ift88*) and two experimental samples of each gene of interest in order (Figure 5.2 B). Figure 5.3 shows the calculation of Pearson's coefficient for the co-localization of the axoneme *acetylated α-tubulin* and *TMEM67* transition zone compartments after the knockdown of *Rpgrip1l*, *Tmem231*, *Plk1*, and *Ift88*. The cilia numbers were comparable to siRNA knockdown of *Ift88*, a key regulator of ciliogenesis and a positive control (Pazour et al., 2000, Wheway et al., 2015) (Figure 5.2 C). Furthermore, *Plk1* siRNA knockdown was used as a positive control for effect on cell number and as a measure of the efficiency of transfection, with the result showing fewer cells following knockdown as expected (Figure 5.2 C). In addition, the results identify potential synthetic genetic interactions between *acetylated α-tubulin* and *TMEM67*

after knockdown of both *Tmem231* or *Rpgrip1l*. However, Pearson's coefficients calculated after knockdown of either *Rpgrip1l* or*Tmem231* were close to 0 (Figure 5.3). This indicates a poor co-localization between axoneme and transition zone compared to the *scrambled* siRNA negative control. However, high content imaging only provides an un-deconvoluted epifluorescence microscopy image that does not consider the 3-dimensional structure of the cilia being imaged. This could artificially increase co-localization values. To address this potential analysis artefact, a subsequent confirmation study using confocal microscopy was performed. Three-dimensional images were reconstructed using "Volocity x64" software (PerkinElmer Inc.) in order to generate more accurate co-localization values.

B

siRNA

Scrambled

Plk1

Ift88

Rpgrip1l

Tmem231

Well

Field

C

Negative control
Scrambled

Positive control
Ift88

Transfection control
Pkl1
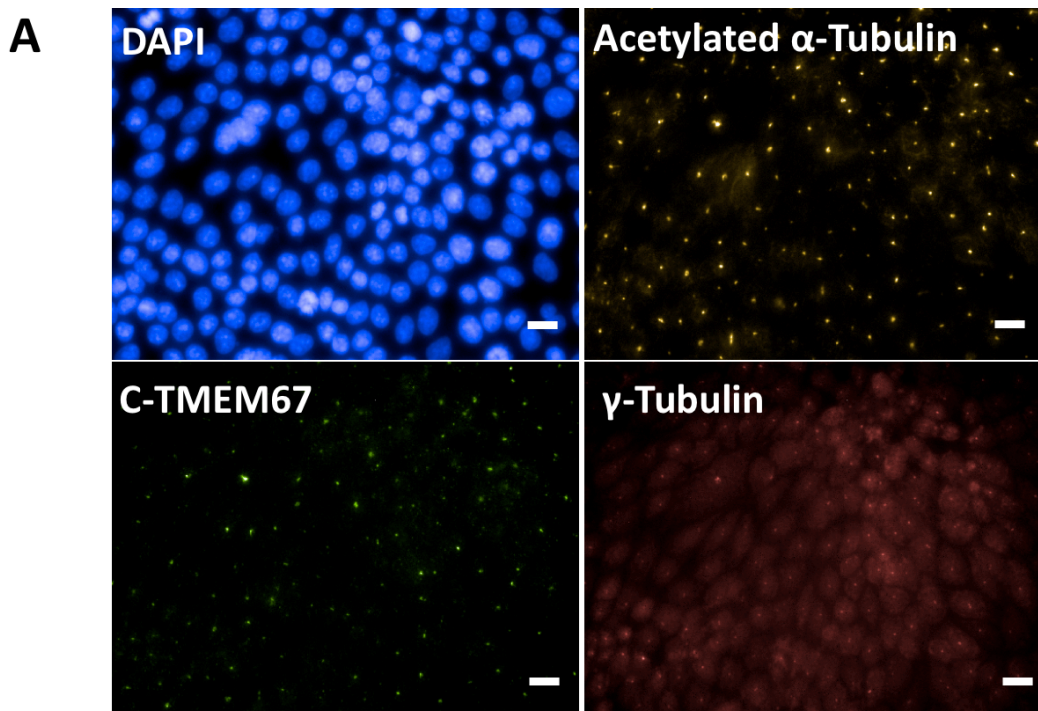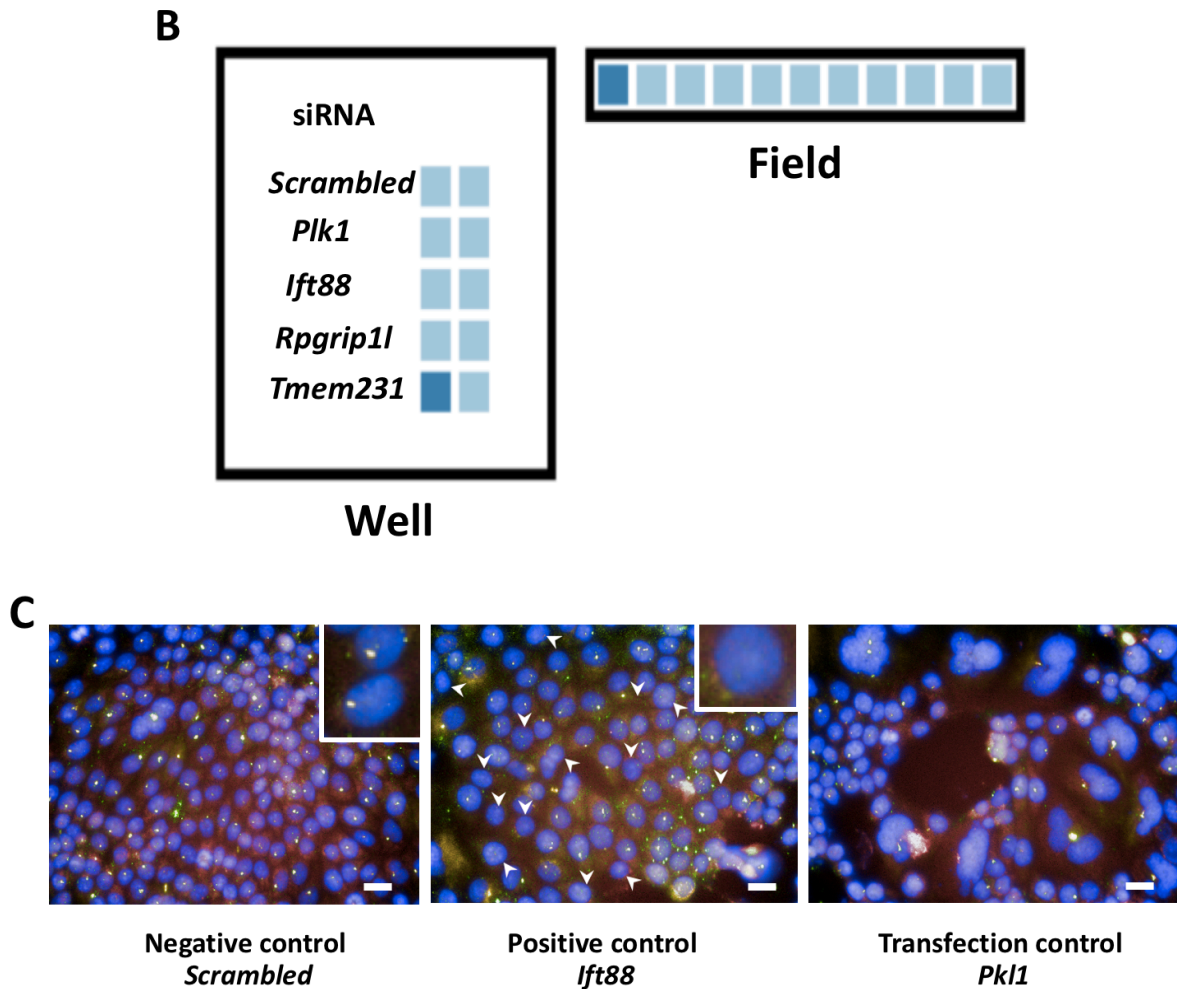
Figure 5. 2: Sample of Columbus images and field of view for Operetta siRNA study in mIMCD-3 cells. (A) Four panels show antibody staining performed in this study. DAPI (blue) stains nuclear boundaries. Acetylated α-tubulin (gold) stains ciliary axoneme. Antibody against the TMEM67 C-terminus (green) stains the transition zone. γ-tubulin (far red) stains the basal body. **(B)** Ten fields of view were imaged per well with an approximate total of 8000 cells detected and analysed per well and two wells were tested for each gene). **(C)** Left panel shows negative control siScrambled. Middle panel shows the positive control for cilia loss si*Ift88* indicates fewer cilia (acetylated α-tubulin, gold) than the negative control siScrambled. Right-hand panel shows transfection efficiency control si*Plk1* with noticeable cell loss compared to *siScrambled* negative control. Scale bar= 20 μm. The data is shown n=1 biological replicate and n=2 technical replicates.
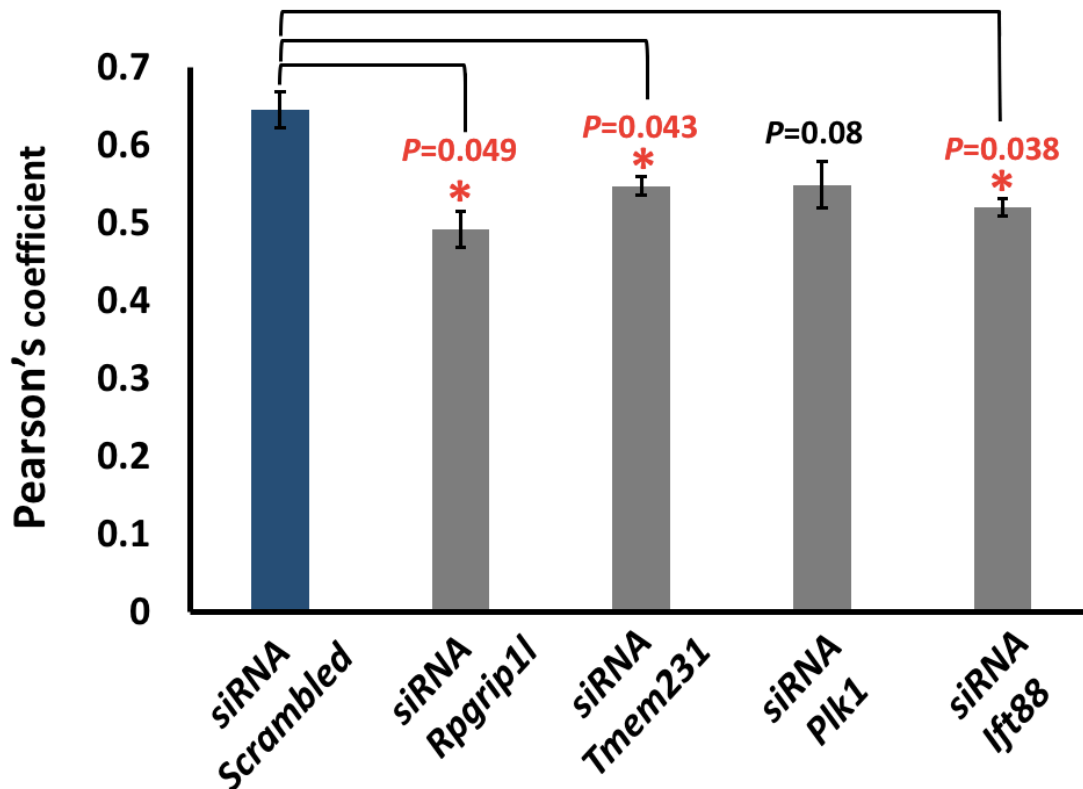
Figure 5. 3: Calculated mean Pearson's coefficient for the co-localization of the axoneme acetylated α-tubulin and TMEM67 transition zone compartments after the knockdown of *Rpgrip1l*, *Tmem231*, *Plk1*, and *Ift88*. The Pearson's coefficients were calculated using data generated using the Operetta/Columbus high-content imaging platform (PerkinElmer). Pearson's coefficients were close to 1 for the scrambled siRNA negative control, indicating a high degree of co-localization between the axoneme and TMEM67. For *Rrpgrip1L*, *Tmem231* and *Ift88* knockdowns, Pearson's coefficients were close to 0, indicating poor or weak co-localization between axoneme and transition zone. Statistical significance of pairwise comparisons are indicated (Student's t-test: *, p<0.05); error bars show standard deviation for 2 technical replicates.

5.3.2 siRNA forward transfection for TMEM Volocity 64x analysis

5.3.2.1 TMEM67 module

Confocal microscopy images were taken with an oil immersion 100x objective on a Nikon A1R instrument, to visualize the localization of basal body, transition zone and ciliary axoneme after knockdown by transfection of siRNA for *Tmem17*, *Tmem67*, *Tmem138*, *Tmem231*, and *Tmem237* into mIMCD-3. Figure 5.4 A shows an example of the immunofluorescence staining performed for the *TMEM67* module. As previously mentioned

in section (5.2.1.2.2), Pearson's coefficients were used to calculate the degree of co-localizations between the sub-compartments with ranges between 1 and zero (1 being perfect co-localisation, and zero indicating absence of co-localization).

Knockdown of *TMEM67* was used as a positive control for Volocity analysis since the transition zone was stained with TMEM67 and the knockdown was performed for one biological replicate to examine any changes in ciliary sub-compartments. The result demonstrated that only transition zone and acetylated α-tubulin sub-compartments had a reduced level of co-localization compared to negative control (Figure 5.4 B; Figure 5.5). Pearson's coefficients were close to 1, indicating a high degree of co-localization between axoneme and TMEM67 for the negative control scrambled siRNA treated cells, whereas Pearson's coefficients were close to 0, indicating absence of co-localization, following *Tmem67* knockdown.

Volocity analysis also indicated that knockdown of *Tmem231* caused 2 structural defects in ciliary sub-compartments localization: *TMEM67* transition zone and both acetylated α-tubulin and γ-tubulin basal body sub-compartments mislocalized and overlapped more compared to the negative control (Figure 5.4 B; Figure 5.5) following knockdown of *Tmem231*. The bar graph (Figure 5.4 B) quantified co-localization between the ciliary sub-compartments following knockdown of *Tmem231*. Pearson's coefficient was 0.15, which indicated that the transition zone overlaps with the axoneme, as well as the transition zone overlapping with the basal body, compared to the scrambled negative control siRNA.

The bar graph (Figure 5.4 D) quantified co-localization between the ciliary sub-compartments following knockdown of Tmem17. First, the Pearson's coefficient for co-localization between the transition zone (marked by TMEM67) and the basal body (marked by γ-tubulin) were close to 0 when compared to negative control. This indicates that these sub-compartments are distinct and separated by a structural gap following Tmem17 knock-down. Second, there was poor co-localization between acetylated α-tubulin and the basal body following Tmem17 knockdown (Pearson's coefficients also close to 0) indicating that these sub-compartments were also more separated compared to the negative control

(Figure 5.4 D; Figure 5.5). This suggests that TMEM17 is an important protein that maintains ciliary structural integrity.

Volocity analysis showed that knockdown of *Tmem138* expression resulted in a defect between the *TMEM67* transition zone and acetylated α-tubulin sub-compartments. The sub-compartments mislocalized and were more detached than in the negative control (Figure 5.4 D; Figure 5.5), indicating gaps between the transition zone and axoneme. In addition, Volocity analysis indicated that knockdown of *Tmem237* expression developed defects in TMEM67 transition zone and the basal body γ-tubulin sub-compartments (Figure 5.4 D; Figure 5.5). Pearson's coefficient was close to 0, which indicated poor co-localization, suggesting a gap between these sub-compartments compared to the scrambled siRNA negative control.

In summary, the Volocity analyses indicated that the knockdown of *Tmem67* (Figure 5.4 B), *Tmem231* (Figure 5.4 B), *Tmem17* (Figure 5.4 D), *Tmem138* (Figure 5.4 D) and *Tmem237* (Figure 5.4 D) had a significant effect on ciliary sub-compartments and disrupted co-localization between them. Also, the knockdown of these genes had an important effect on cilia length or incidence (Figure 5.4 C, E). Consistent with these findings the ciliary sub-compartments were altered, such that significant increases or decreases in TMEM67 co-localization with either acetylated α-tubulin and/or γ-tubulin were observed following knockdowns of TMEM17, *TMEM67, TMEM138, TMEM231* and *TMEM237*.

Consistent with these findings in the TMEM67 module, this raises the question of how TMEM17, TMEM67, TMEM138, TMEM231 and TMEM237 proteins are functionally connected. Moreover, these TMEM proteins had different disrupted network properties and had distinct effects on the localization of the transition zone marker TMEM67. This suggests that the TMEM17, TMEM67, TMEM138, TMEM231 and TMEM237 proteins may mediate transition zone structural organization and that they are arranged into a hierarchical network of interactions. This point is expanded in the Discussion in Chapter 6.
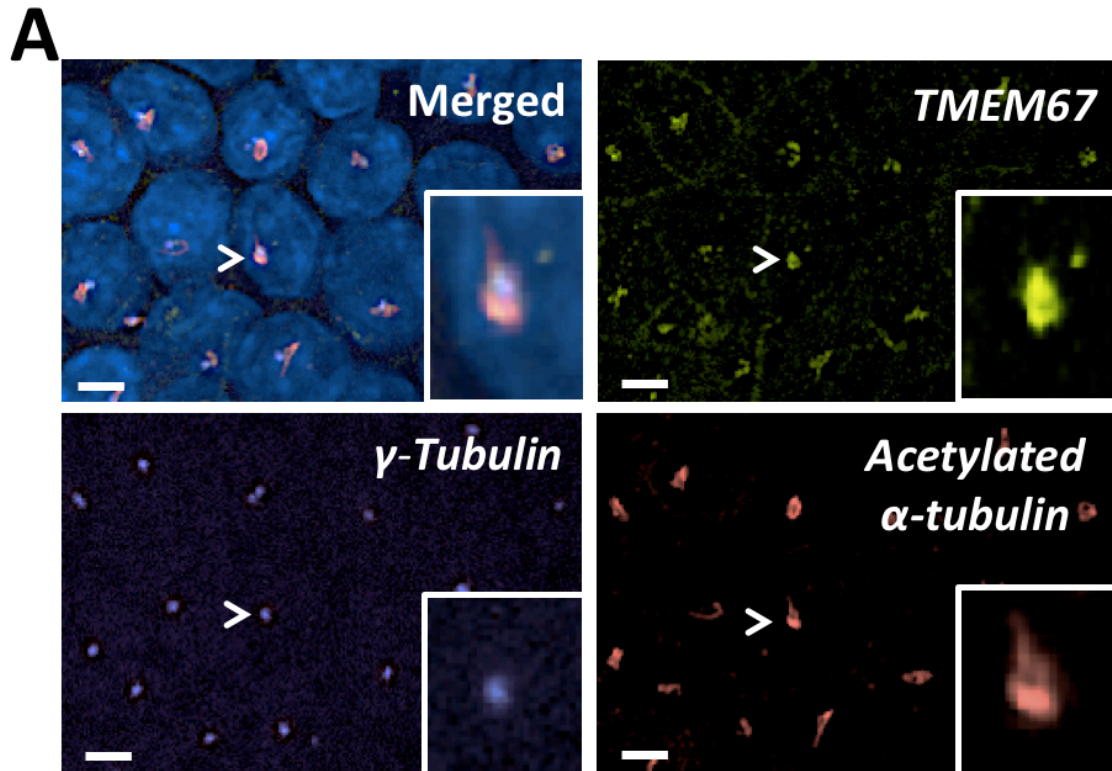
A

Merged

TMEM67

γ-Tubulin

Acetylated α-tubulin

B

Results of Pearson's coefficient calculation of ciliary compartments of (*TMEM67*) Module

| Pearson's coefficient of the colocalization of axoneme and transition zone | Pearson's coefficient of the colocalization of transition zone and basal body | Pearson's coefficient of the colocalization of axoneme and basal body |
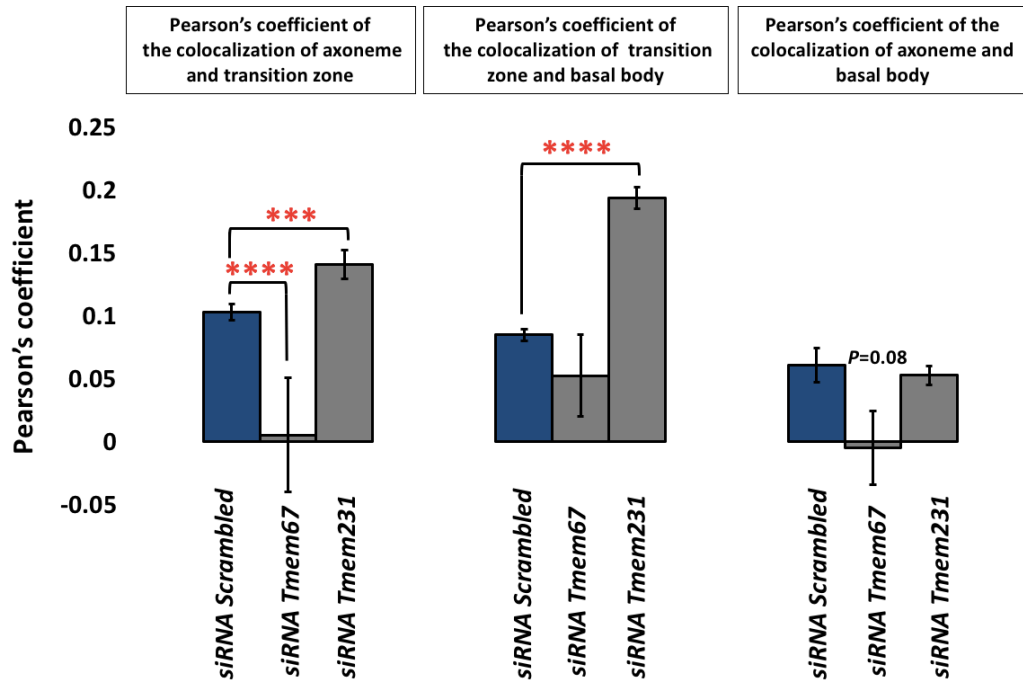
C **Primary cilia incidence**
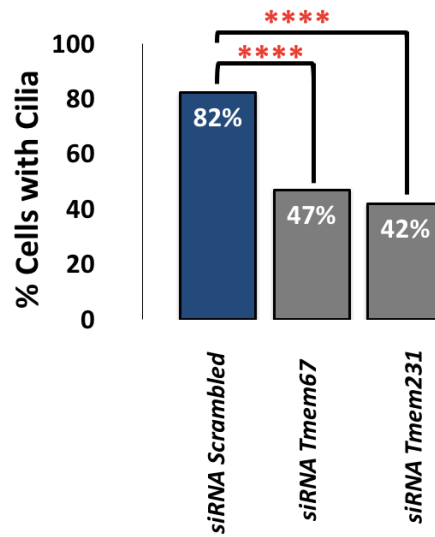
D Results of Pearson's coefficient calculation of ciliary compartments of (*TMEM67*) Module

Pearson's coefficient of the colocalization of axoneme and transition zone	Pearson's coefficient of the colocalization of transition zone and basal body	Pearson's coefficient of the colocalization of axoneme and basal body
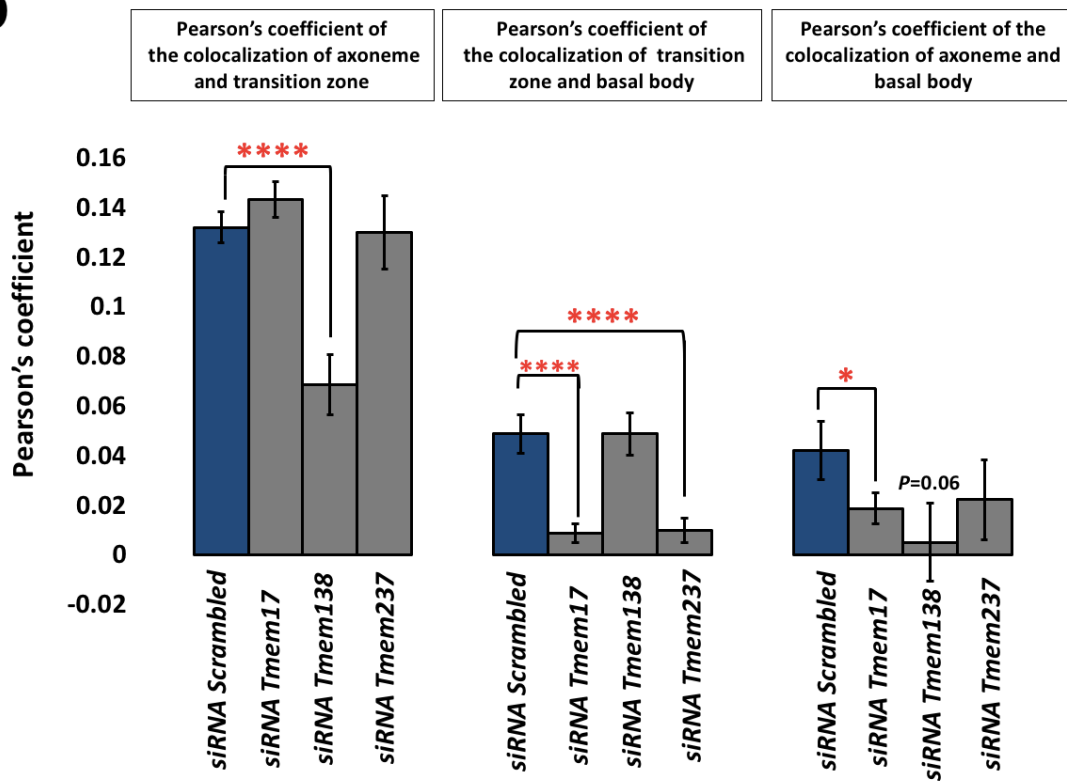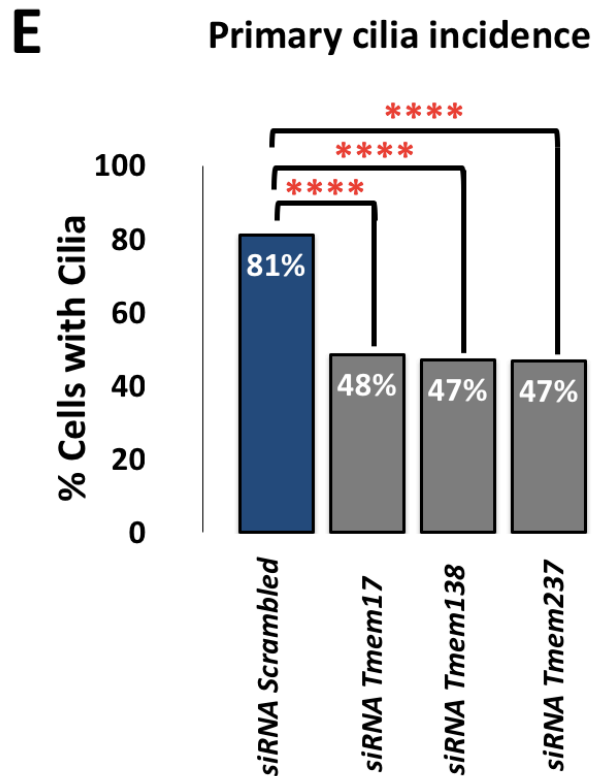
Figure 5. 4: TMEM67 module results: sub-cellular localization of endogenous ciliary sub-compartments in mIMCD-3 cells following siRNA knockdowns. (A) The sub-compartments were triple stained with antibodies against acetylated α-tubulin (red) for the axoneme, TMEM67 (green) at the transition zone and γ-tubulin at the basal body (purple). Cells were counterstained with DAPI (blue). Insets show details of the cilium sub compartments indicated by the arrowhead. Scale bar= 20 μm. **(B)** Calculated mean Pearson's coefficient for the co-localization of the ciliary sub-compartments after the knockdown of *Tmem67* and *Tmem231*.The bar graph quantifies co-localization between the indicated ciliary sub-compartments following knockdown of *Tmem67*, the positive control for this data-set, and *Tmem*231. The Pearson's coefficients were generated using Volocity. Statistical significance of pairwise comparisons are indicated (Student's t-test: *, $p<0.05$, *** $p<0.001$ and **** $p<0.0001$) which indicated by red asterisk; error bars show standard deviation for one biological replicate and 8 technical replicates. **(C)** Quantification of morphological defects in mIMCD-3 cells after knockdown of *Tmem*67 and *Tmem*231. A reduction in cilia incidence after the knockdown of *Tmem67* and *Tmem231* is shown. **(D)** Calculated mean Pearson's coefficient for the co-localization of the ciliary sub-compartments after the knockdown *of Tmem17, Tmem138, Tmem231* and *Tmem*237. Error bars show standard deviation for 2 biological replicates and six technical replicates. **(E)** Quantification of morphological defects in mIMCD-3 cells after knockdown of *Tmem17*, *Tmem138* and *Tmem237*. A reduction in cilia incidence was seen after the knockdown of these genes.
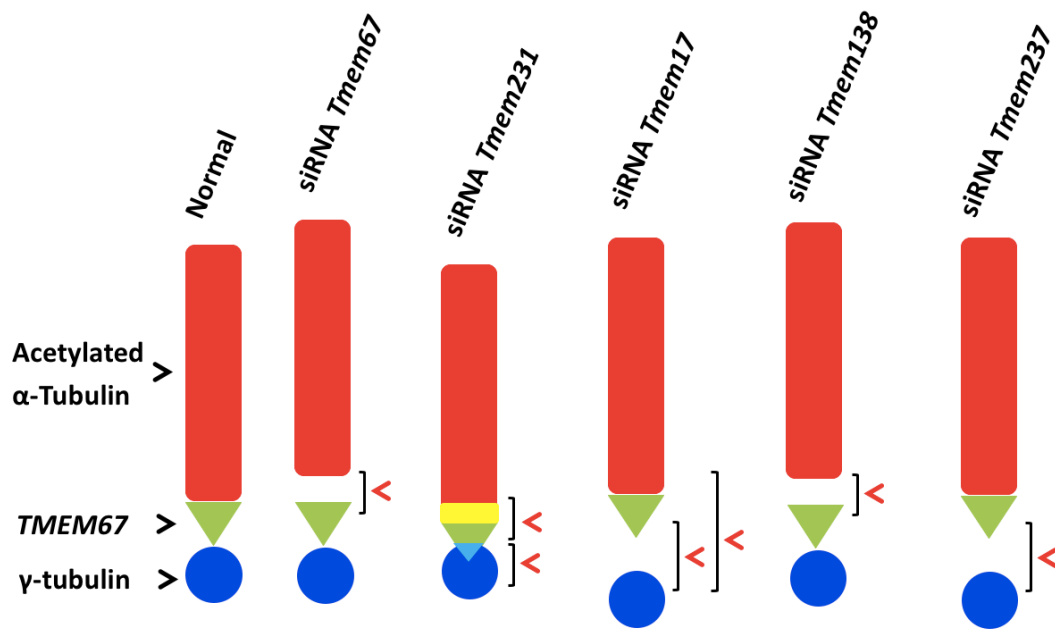
Figure 5. 5: Schematic drawing of primary cilia showing some structural defects after knockdown of *Tmem67*, *Tmem231*, *Tmem17*, *Tmem138* and *Tmem237* in mIMCD-3 cells. Black arrowheads indicate ciliary axoneme (acetylated α-tubulin; red), transition zone (TMEM67; green) and basal body (γ-tubulin; blue). Red arrowheads indicate how gene knockdown affects the relative positioning of ciliary structural sub-compartments. *Tmem67* knockdown caused a decrease in the co-localization between the transition zone marker TMEM67 and acetylated α-tubulin which generated a gap between these sub-compartments. *Tmem231* knockdown caused an increase in the co-localization between the transition zone marker *Tmem67* and acetylated α-tubulin, as well as *Tmem67* and the basal body (marked by γ-tubulin). This increase suggests an overlap between these sub-compartments which is indicated by yellow and turquoise, respectively. *Tmem17* knockdown resulted in a decrease in the co-localization between *Tmem*67 at the transition zone and the basal body marked by γ-tubulin sub-compartments, as well as decreased axoneme (acetylated α-tubulin) and basal body (γ-tubulin) co-localization. *Tmem138* knockdown decreased the association between the transition zone (*Tmem67*) and acetylated α-tubulin. *Tmem237* knockdown resulted in a decrease in the co-localization between TMEM67 and basal body (γ-tubulin).

5.3.2.2 *RPGRIP1L* module

Confocal microscopy images were taken with an oil immersion 100x objective on a Nikon A1R instrument, to visualize the localization of basal body, transition zone and ciliary axoneme after knockdown by transfection of siRNA for *Tmem17*, *Tmem67*, *Tmem138*, *Tmem231* and *Tmem237* into mIMCD-3. Figure 5.6 A displays an example of the immunofluorescence staining for RPGRIP1L. As detailed above (see section 5.2.4.1),

Pearson's coefficients were the method for evaluating co-localization of ciliary sub-compartments.

In this experiment *Tmem17*, *Tmem67*, *Tmem138*, *Tmem231* and *Tmem237* were knocked-down and the relative localization of RPGRIP1L was compared to γ-tubulin at the basal body and acetylated γ-tubulin at the ciliary axoneme. The Volocity analysis results indicated that knockdown of these genes had no significant effect on the co-localization of these sub-compartments (Figure 5.6 B). This suggests that loss of the *Tmem17*, *Tmem67*, *Tmem138*, *Tmem231* and *Tmem237* components has no effect on RPGRIP1L positioning, implying that *RPGRIP1L* is higher in an organizational hierarchy than the TMEM proteins and that it is required for the correct formation of a normal transition zone.
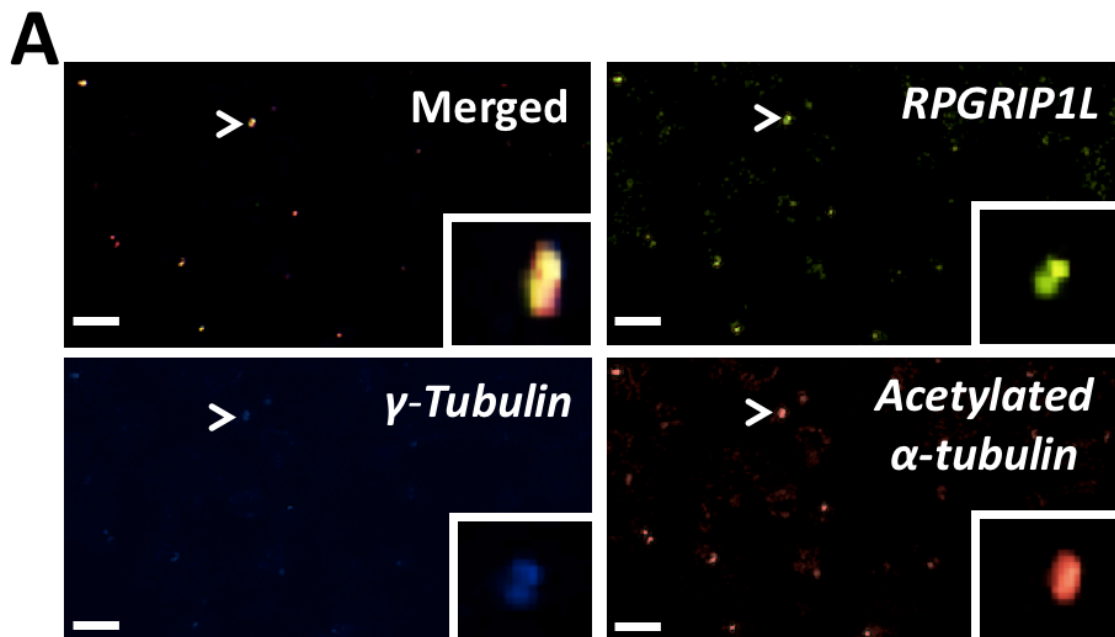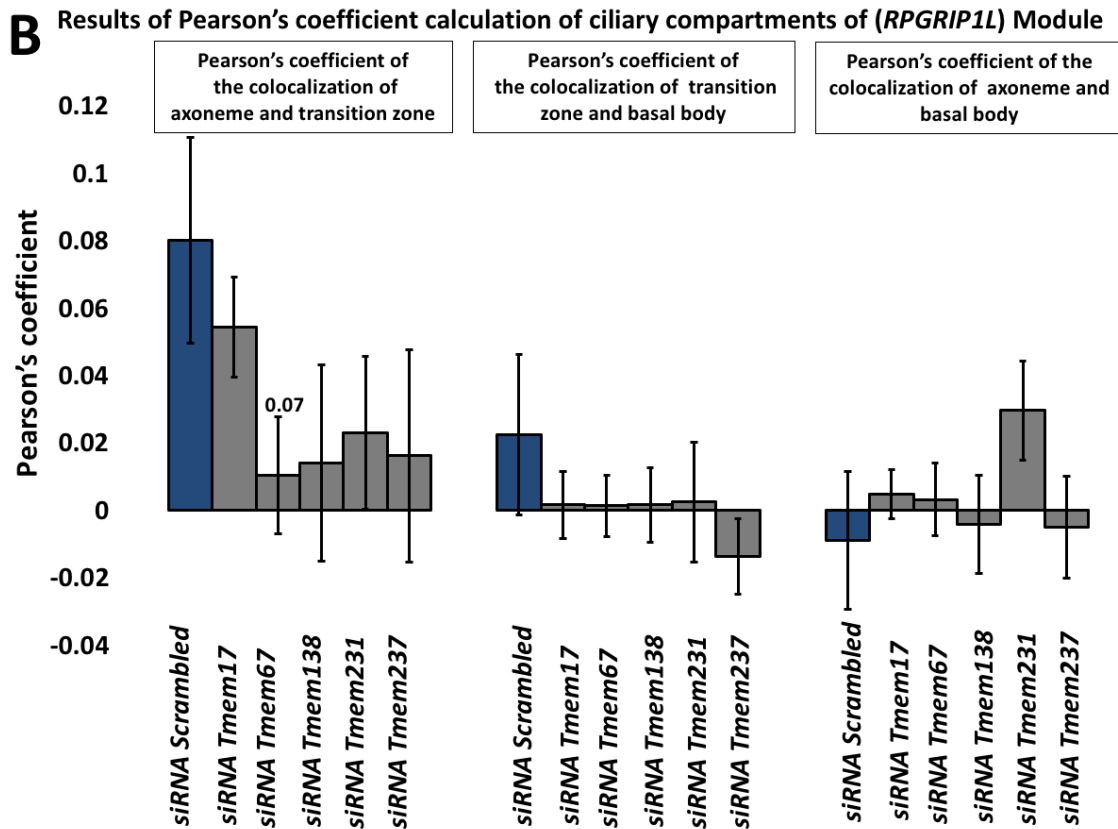
Figure 5. 6: RPGRIP1L module results: sub-cellular localization of endogenous ciliary sub-compartments in mIMCD-3 cells following siRNA knockdowns. (A) The sub-compartments were triple-stained with antibodies against acetylated α-tubulin (red, axoneme), RPGRIP1L (green, transition zone), and γ-tubulin (basal body, blue) as markers. Insets show details of the cilium sub compartments indicated by the arrowhead. Scale bar= 20 μm. **(B)** Calculated mean Pearson's coefficient for the co-localization of the ciliary sub-compartments after the knockdown of *Tmem17, Tmem67, Tmem138, Tmem231* and *Tmem237*. The Pearson's coefficients were generated using Volocity and showed no significant changes in the co-localization between axoneme and transition zone, transition zone and basal body, axoneme and basal body compared to the scrambled siRNA control. Error bars show standard deviation for one biological replicate and three technical replicates.

5.3.2.3 *CEP290* module

Confocal microscopy images were taken with an oil immersion 100x objective on a Nikon A1R instrument, to visualize the localization of basal body, transition zone and ciliary axoneme after knockdown by transfection of siRNA for *Tmem17, Tmem138, Tmem231,* and *Tmem237* into mIMCD-3. The transition zone was visualized by immunofluorescent staining for CEP290 using a mouse monoclonal antibody (the gift of Ciaran Morrison, University of Cork). However, this meant that the monoclonal antibody against acetylated α-tubulin was not used in this series of experiments. Instead IFT88 was used as a ciliary axoneme marker

since it has been recognized to be located both at the ciliary base and tip (Appendix D.4). Figure 5.7 A shows an example of the immunofluorescence staining that was performed in this module. Pearson's coefficients were used as explained in the above sections.

Volocity analysis in this module indicated that knockdown of *Tmem17* expression caused a clear defect in ciliary sub-compartment localization: specifically, the CEP290 transition zone and the γ-tubulin basal body sub-compartments were mis-localized and overlapped to a greater extent than the scrambled non-targeting negative control (Figure 5.7 B; Figure 5.8). The bar graph (Figure 5.7 B) quantifies co-localization between the ciliary sub-compartments following knockdown of *Tmem17*. Volocity analysis also indicated that knockdown of *Tmem138* expression caused 2 mis-localization defects: IFT88 at the axoneme and the CEP290 localized to the transition zone sub-compartments were mis-localized and overlapped to a greater extent than the negative control. In addition, both IFT88 and γ-tubulin at the basal body sub-compartment were mis-localized and overlapped to a greater extent than the negative control (Figure 5.7 B; Figure 5.8). The bar graph (Figure 5.7 B) quantifies the co-localization between the ciliary sub-compartments following knockdown of *Tmem138*.

Volocity analysis following *Tmem231* knockdown indicated the presence of a different mis-localization defect of ciliary sub-compartments. CEP290 and IFT88 were mis-localized but were more separated compared to the negative control (Figure 5.7 B; Figure 5.8). The bar graph (Figure 5.7 B) quantifies co-localization between the ciliary sub-compartments following knockdown of *Tmem231* and suggested that a gap formed between the transition zone and the basal body. A similar mis-localization defect was also observed following *Tmem*237 knockdown, however it appeared to be less significant than *Tmem231* knockdown.

In summary, the results from Volocity analysis indicated that the knockdown of *Tmem17, Tmem138, Tmem231,* and *Tmem237* (Figure 5.7B; Figure 5.8) had a significant effect on primary cilia organization and caused mis-localization between the ciliary basal body, transition zone and axoneme sub-compartments. Remarkably, significant increases or decreases were shown in CEP290 co-localization with either IFT88 and/or γ-tubulin following knockdowns of *Tmem17*, *Tmem138, Tmem231* and *Tmem237*, indicating that their

knockdown (Figure 5.7 B) had a significant effect on ciliary sub-compartments. Significant changes in the co-localization between axoneme and transition zone were also seen when *Tmem138*, *Tmem231* and *Tmem237* were knocked down. Specifically, there were changes in the co-localization between transition zone and basal body when *Tmem17* was knocked-down, and alterations in the co-localization between axoneme and basal body when *Tmem138* was knocked down. These findings suggest that TMEM17 and TMEM138 are both important proteins that maintain ciliary structural integrity by constraining the localization of CEP290.
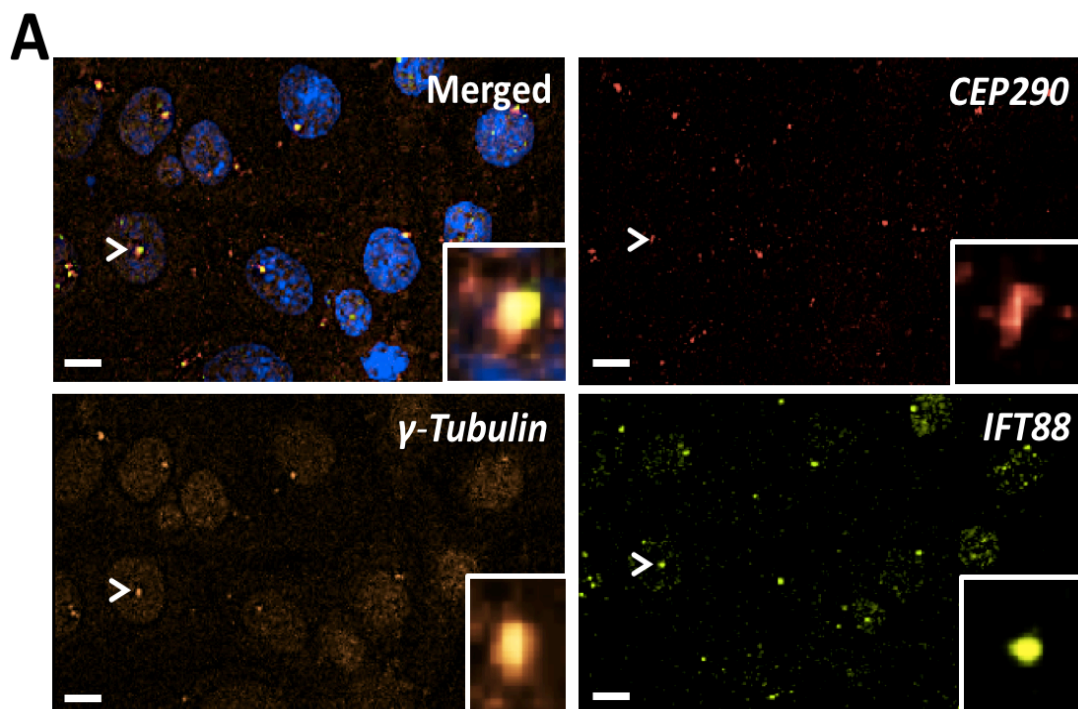
B Results of Pearson's coefficient calculation of ciliary compartments of (*CEP290*) Module
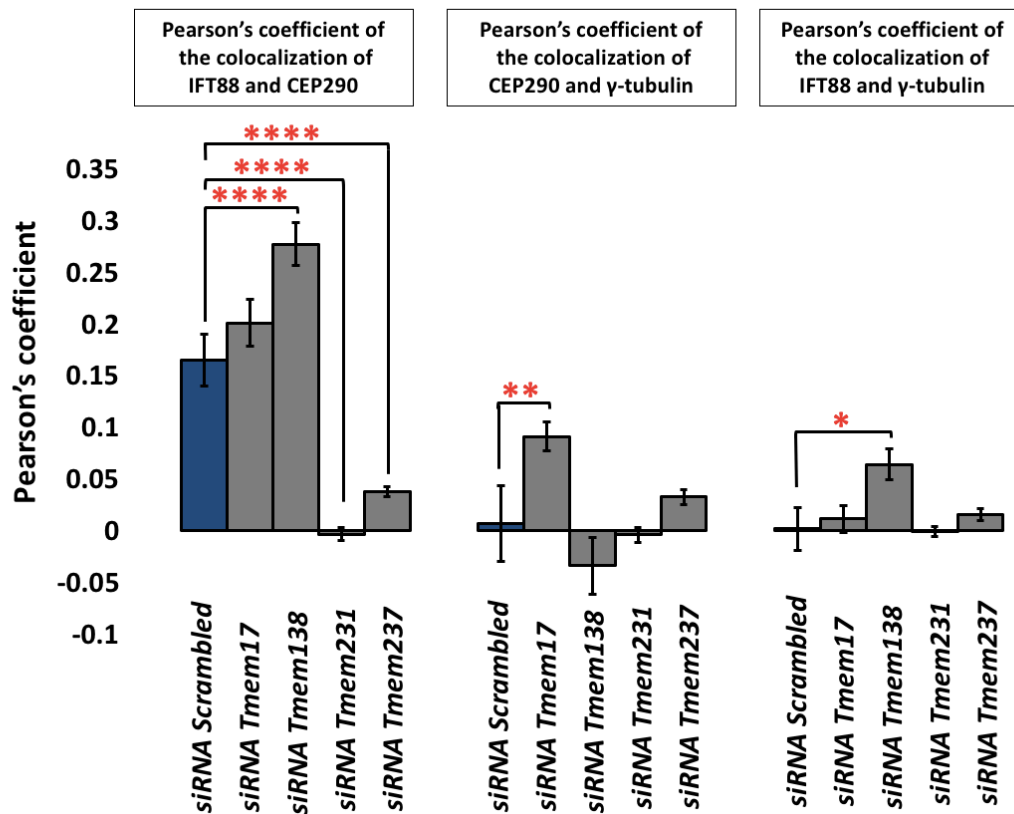
Figure 5. 7: *CEP290* **module results: sub-cellular localization of endogenous ciliary sub-compartments in mIMCD-3 cells following siRNA knockdowns. (A)** The sub-compartments triple stained with antibodies against *IFT88 (*green, axoneme)*, CEP290* (red, transition zone), and γ-tubulin (basal body, far red) markers. Cells were counterstained with DAPI (blue). Insets show details of the cilium sub compartments indicated by the arrowhead. Scale bar = 20 μm. **(B)** Calculated mean Pearson's coefficient for the co-localization of the ciliary sub-compartments after the knockdown of *Tmem17, Tmem138, Tmem231* and *Tmem237* using Volocity. Statistical significance of pairwise comparisons are indicated (Student's t-test: *, *p*<0.05, ** *p*<0.001 and **** *p*<0.0001) which indicated by red asterisk; error bars show standard deviation for one biological replicate and 6 technical replicates. Pearson's coefficients showed significant changes in the co-localization between axoneme and transition zone when cells treated with the knockdowns of *Tmem138, Tmem231*, and *Tmem237*. Pearson's coefficients also showed significant changes in the co-localization between transition zone and basal body when *TMEM17* was knocked down. Pearson's coefficients showed significant changes in the co-localization between axoneme and basal body when *TMEM138* was knocked down. All knock downs were compared to the scrambled siRNA control.
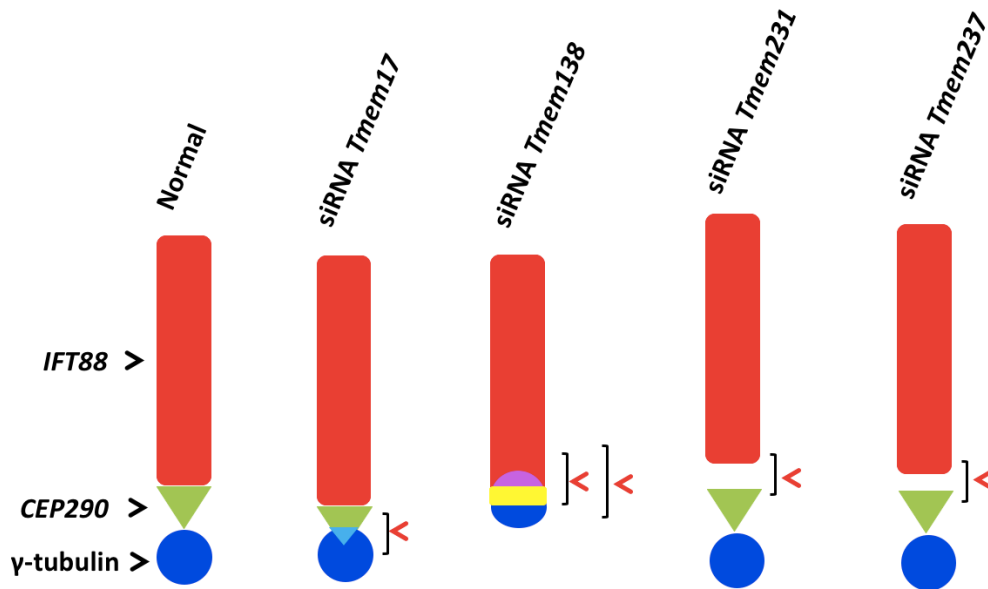
Figure 5. 8: Schematic drawing of primary cilia showing some structural defects after knockdown of *Tmem17*, *Tmem138*, *Tmem231*, and *Tmem237* in mIMCD-3 cells. Black arrowheads indicate ciliary axoneme (visualized by *IFT88*; red), transition zone (*CEP290*; green) and basal body (γ-tubulin; blue). Red arrowheads indicate the effect of knockdown on the relative positioning of ciliary structural sub-compartments. Knockdown of *Tmem17* caused an increase in the co-localization between the transition zone (CEP290) and the basal body (γ-tubulin), indicated by the turquoise overlap. Knockdown of *Tmem138* increased co-localization between the transition zone (CEP290) and the axoneme (IFT88) as well as the basal body (γ-tubulin), indicated by the pink and yellow overlaps, respectively. Knockdown of either *Tmem231* or *Tmem237* resulted in a decrease in the co-localization between transition zone and axoneme sub-compartments, suggesting that gaps may form between these sub-compartments.

5.4 siRNA validation results

siRNA validation experiments were performed as described in (5.2.3). Gene knockdown of *Rpgrip1l*, *Ift88*, *Tmem17*, *Tmem67*, *Tmem231* and *Tmem237* were demonstrated by the analysis of Operetta and Volocity results. However, validation of knockdown efficacy by western blotting was limited to *Rpgrip1l*, *Ift88*, *Tmem17* and *Tmem237* (Figure 5.9) due to the availability of antibodies. Quantitative analysis of the RPGRIP1L, IFT88, TMEM17 and TMEM237 band intensities included normalization for protein loading as determined from the intensity of β-actin bands. Band intensities were quantified using Image Lab software (Bio-Rad). Normalized band intensities for *Rpgrip1l*, *Ift88*, *Tmem17* and *Tmem237* siRNA knockdowns were all <70% of bands in the scrambled non-targeting negative control.

Significant reductions of *Ift88, Tmem237, Rpgrip1l, Tmem17* protein levels were 23%, 35%, 50% and 77%, respectively. The rabbit polyclonal antibodies against IFT88, TMEM237, RPGRIP1L appeared to work well in western blots and gave strong signals at the expected molecular weights of 94 kDa, 45.5, 151 kDa, but for both bands were observed at about 100 kDa that were ablated by the cognate siRNA knockdown. These antibodies were therefore likely to be highly specific against the target protein. The rabbit polyclonal antibody against TMEM17 did not give a strong signal in western blots, although it did produce a band at 23 kDa at the expected size for TMEM17. An antibody against TMEM231 did not produce any specific bands at the correct predicted molecular weight for TMEM231 (data not shown) and analyses with this antibody were not continued.
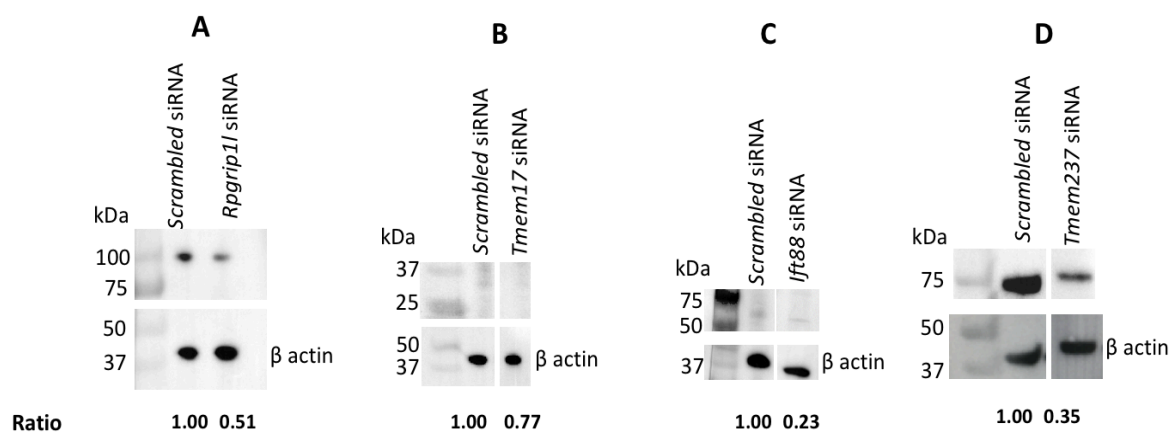
Figure 5. 9: Western blotting showing loss of protein after siRNA knockdown. Western blotting was used to demonstrate the effect of siRNA knockdown of *Rpgrip1l* **(A)**, *Tmem17* **(B)**, *Ift88* **(C)**, and *Tmem237* **(D)** in HEK-293 cells compared to the scrambled non-targeting negative control. β actin was used as a loading control and relative reduction in expression (ratio) was compared to siScrambled knockdown. Molecular weights of proteins: RPGRIP1L (150 kDa); IFT88 (94 kDa); TMEM17 (23 kDa); TMEM237 (45.5 kDa); β actin (45 kDa). Slices from separate parts of the blot were spliced together as shown by a vertical white line on each figure **(B-D)**. The data shown is from only one biological replicate.

5.5 Discussion

One of the central questions in this chapter is what the molecular mechanism is underlying primary ciliary sub-compartment organization and whether ciliary defects arise from disruption in the assemblies or modules of the selected TMEM proteins. Furthermore, do the genetic interactions support the results of biochemical interactions in Chapter 4 that have also been determined in the same ciliated model system?

Increasing evidence has indicated that the transition zone is organized into multiple protein modules with distinct functions, such as the MKS and NPHP modules, which are composed of proteins mutated in the ciliopathies Meckel-Gruber syndrome and nephronophthisis as details in Chapter 1. Therefore, a selection of antibodies raised against transition zone proteins were used in order to understand their genetic interaction within the ciliary transition zone compartment and their association with other primary cilia sub-compartments including the ciliary axoneme and ciliary basal body. The disruption of some of these sub-compartments is thought to underlie a wide spectrum of ciliopathies. To determine whether TMEM17, TMEM67, TMEM138, TMEM231 and TMEM237 are essential regulators of transition zone organisation and function, and whether or not they work as a complex to build primary cilia or do relative functions together, mIMCD-3 cells were transfected either with control non-targeting small interfering (si)RNA or siRNAs against *Tmem17*, *Tmem67*, *Tmem138*, *Tmem231* or *Tmem237*.

In the first instance, high content imaging with an Operetta High-Content Imaging system was used. A series of experiments in the TMEM67 module successfully confirmed that knock-downs had detectable structural effects on ciliary compartments. It also enabled staining and imaging protocols to be optimized (Figure 5.2; Figure 5.3) Following this, 3 dimensional reconstructions were performed from confocal microscopy images and co-localization was analysed with Volocity x64 software. The extent of co-localization between ciliary sub-compartments was quantitated by calculated Pearson's correlation in each image and then deriving statistical outputs as shown in Figures 5.4 B & D; Figure 5.6 B; and Figure 5.7 B. For co-localization studies, special consideration needed to be made to find software that could take advantage of high-quality confocal images at high resolution in order to perform proper co-localization analyses for sub-cellular compartments.

For Volocity x64 analysis, mIMCD-3 cells were used as a standard model ciliated cell-line since it is easy to grow and has a high transfection efficiency. Three separate data-sets or modules were generated and selected for analysis of the ciliary sub-compartments: the *TMEM67* module (using an antibody against the C-terminal region), the RPGRIP1L module and the *CEP290* module. γ-tubulin was selected as a well-established basal body marker that is known to be essential for centriole assembly and structural maintenance (Pearson et al., 2009, Dupuis-Williams et al., 2002, Dutcher et al., 2002). Acetylated α-tubulin antibody was used as well-established axoneme markers in investigations of the *TMEM67* module and *RPGRIP1L* module, whilst *IFT88* was used for the *CEP290* module as an axoneme marker because of the limitations of available antibodies and its localization validated to the cilia by immunofluorescence staining (Figure D.3 in the appendix D). Using siRNA, we examined a group of 6 TMEM proteins, 5 of which are mutated as causes of ciliopathies. The efficiency of each siRNA was tested, firstly, by confirming that they all decreased cilia incidence and, secondly, by performing western blotting for those that had antibodies available for the cognate proteins.

Although 3D reconstruction in Volocity allowed co-localization volumes to be determined for protein localizations, this image analysis did not allow the reliable measurement of cilia length. However, the knockdown of all ciliary TMEMs tested in this chapter caused a significant decrease in cilia incidence. Since cilium length is a key determinant of normal cilium structure and function, cilium length was also measured in order to validate positive and negative modulators because length increase or decrease is a highly specific indicator for normal or abnormal ciliary structure. However, the morphology of primary cilia in mIMCD-3 cells was challenging to measure in single z-slices or in maximum intensity projections. In both instances, the true length of cilia was likely to be under-estimated since they project vertically from the apical cell surface in the mIMCD-3 cell line. For this reason, co-localization measurements were performed on 3D reconstructions from confocal z-stacks (in the Nikon.nd2 file format) using Volocity software.

Our experiments identify some novel roles for the selected TMEM proteins in transition zone structural stability and ciliogenesis. This chapter therefore extends our understanding of how molecular components within the cilium associate in structural

compartments within the cilium. Further discussion of the data-sets for each transition zone modules is presented below.

5.5.1 *TMEM67* module

The data presented here implicate TMEM67 as an indispensable regulator of ciliary transmembrane expansion and compartmentalization of signalling receptors, with potential involvement in ciliopathies and other human diseases as has been reported previously. (Barker et al., 2014) identified a core group of 6 proteins that have critical conserved functions including TMEM67, CCD2A, B9D1, B9D2, AHI1 and a single TCTN family member. The 6 proteins are associated in MKS and JBST syndromes which highlights their importance for cilia function. The knockdown of *Tmem67* was investigated and subsequently used as a positive control in this study. In a separate experimental series, *Tmem67* knock-down was used as a positive control in order to confirm that robust data was generated in the mIMCD-3 model system. *siRNA Tmem67* caused considerable changes in the localization of ciliary sub-compartments, including transition zone, basal body and ciliary axoneme (Figure 4 B). siRNA *Tmem67* causes defective localization of primary ciliary sub-compartments which results in a disruption in the expected pattern of ciliary marker staining, suggesting a possible structural dissociation between the axoneme and the transition zone (Figure 5.5).

As an additional positive control to demonstrate efficacy of knockdown, siRNA against *TMEM67* caused a significant decrease in cilia incidence (Figure 5.4 B). Therefore, this data showed that loss of mammalian TMEM67, which localizes to the ciliary transition zone, resulted in defective ciliogenesis and significant disturbances and disorganization of ciliary compartments. Also, the result showed that *siRNATmem67* caused a loss of primary cilia. Our results show that inhibition of TMEM proteins affects the correct localization of *TMEM67* in the proper ciliary structural compartment at the transition zone (Figures 5.4-5.8). Specifically, it was found that the knockdown of *Tmem17*, *Tmem138, Tmem237* and *TMEM231* caused defective organization of ciliary sub-compartments in this module indicating that these proteins control or have functional roles in maintaining the structure or stability of the ciliary axoneme, transition zone and basal body sub-compartments. Furthermore, cilia incidence decreased after the knockdown of *Tmem17*, *Tmem138,*

Tmem237 and *Tmem231*, suggesting that loss of function of these proteins could be essential for triggering the destabilization of structure of the primary cilium.

As noted in Chapter 4, there appears to be a strong biochemical interaction between *TMEM67* and *TMEM17*. TMEM17 was identified as an interactor with TMEM67 by coimmunoprecipitation in multiple experiments over a variety of conditions. Although TMEM17 was considerably less abundant in TAP purification than other unrelated ciliary proteins, it may still participate in TMEM complex function (Chapter 4). Supporting a functional relationship between TMEM67 and TMEM17, the siRNA results confirmed that the knockdown of *Tmem17* mis-localized *Tmem67* at the transition zone *vs* basal body and the axoneme *vs* basal body sub-compartments. Therefore, both biochemical and genetic interactions demonstrate that TMEM67 and TMEM17 form a functional complex required to organise ciliary sub-compartments. In contrast, *Tmem138* knockdown in mIMCD-3 cells did not appear to affect similar compartments to *Tmem17*. However, the knockdown of *Tmem138* affected the relative positioning of the transition zone and ciliary axoneme in the *TMEM67* module which may indicate that TMEM138 is working within the TMEM67 complex at the transition zone.

In addition, Chapter 4 showed that TMEM138 biochemically interacted with TMEM67, suggesting that these proteins also form a complex that facilitates transition zone formation and composition. In contrast to other TMEMs, *TMEM231* knockdown appeared to have a significant and consistent effect on increasing co-localization of TMEM67 between the transition zone vs axoneme, as well as the transition zone vs basal body compartments. This suggests that the loss of *Tmem231* increases the spread of TMEM67 in the transition zone across greater proportions of the basal body and axoneme. One conclusion from this result is that TMEM231 is higher in the organizational hierarchy than TMEM67, suggesting a specific role for TMEM231 in ciliogenesis within this module.

5.5.1.1 Loss of TMEM17 arrests ciliogenesis and disrupts ciliary structure at the stage of transition zone assembly

TMEM67 is a ciliary receptor that localizes to the transition zone and ciliary membrane. TMEM67 is a key regulator of ciliary structure and function that is essential for ciliogenesis and regulating ciliary membrane composition (Leightner et al., 2013). Like

TMEM67, TMEM17 is a ciliary TMEM protein required for ciliogenesis (Li et al., 2016). Analysis of pixel co-localization using Pearson's coefficient showed that *Tmem17* knock-down had the most significant effect on the localization of the basal body relative to both the transition zone and axoneme in comparison to the scrambled control (Figure 5.4 D). In addition, cilia number was reduced (Figure 5.4 E). The knockdown of *Tmem17* reduced the localization of TMEM67 at the transition zone with the basal body marker (γ-tubulin), suggesting that TMEM17 is required for correct TMEM67 localization. Furthermore, there also appeared to be reduced co-localization between the axoneme and basal body when *Tmem17* was knocked down suggesting a possible transition zone structural defect (Figure 5.4 D). The identification of genetic interactions and functional similarities between *TMEM67* and *TMEM17* suggests that *TMEM17* is required by *TMEM67* to organize the structure and function of the primary cilia. TMEM67 and TMEM17, in fact, have been recognized as a distinct group of proteins that interact with TMEM237 and tectonic proteins (TCTNs) at the transition zone (Goncalves and Pelletier, 2017). However, this work did not investigate if there were functional interactions between these proteins at the cellular level.

5.5.1.2 TMEM138 is required for proper formation and function of primary cilia

A further investigation was carried out into the effect of TMEM138 inhibition to see whether knockdown of *Tmem138* induced co-localization changes in cilia compartments. Mutations in *Tmem138* cause a human ciliopathy, Joubert syndrome, suggesting that TMEM138 is required for ciliogenesis. Knockdown of *Tmem138* caused a significant disturbance to co-localization between the ciliary axoneme and transition zone sub-compartments (Figures 5.4 D & 5.5) in addition to a significant decrease in cilia incidence (Figure 5.4 E). This implies that loss of *TMEM138* severely impaired the ability of the mIMCD-3 cells to produce a normal transition zone/microtubule axoneme ciliary structure. In contrast, loss of *Tmem138* did not significantly affect the transition zone *vs* basal body and axoneme *vs* basal body compartments but did result in a slight change in axoneme *vs* basal body co-localization at the base of many cilia compared to the more uniform ciliary distribution in control cells. Therefore, transition zone organization was disrupted when cells were treated with siRNA against *Tmem138*, which was significantly different from that found in controls in only one compartment. This result indicates a close genetic interaction

between *TMEM138* and *TMEM67* since these proteins are related and required for ciliogenesis. However, little is known about the mechanistic relationship between these proteins during ciliogenesis.

5.5.1.3 Loss of TMEM237 causes ciliogenesis defects in mammalian mIMCD-3 cells

Mutation in *TMEM237* causes Joubert syndrome type 14. This component of the transition zone in primary cilia is required for ciliogenesis and involved in regulating Wnt signalling pathways (Oh and Katsanis, 2013). Knockdown of *Tmem237* in mIMCD-3 cells also had a significant effect on ciliary compartments, specifically co-localization between the transition zone *vs* basal body (Figure 5.4 D). The observed significant decrease in co-localization implied disruption of *Tmem237* expression produced structural defects consistent with ciliary dysfunction (Figure 5.4 D). In addition, *Tmem237* knockdown caused a significant decrease in cilia incidence (Figure 5.4 E). These observations suggest that loss of TMEM237 arrested ciliogenesis at the stage of transition zone assembly. These data define a role for TMEM237 in regulating the basal body and transition zone sub- compartments and in the correct formation of primary cilia in mIMCD-3 cells.

5.5.1.4 Knockdown of TMEM231 expression causes structural defects in ciliary compartments

In contrast to the above findings, analyses of genetic interactions in mIMCD-3 cells indicated that disruption of *TMEM231* significantly increased the relative co-localizations of ciliary compartments, meaning that ciliary compartments were more overlapped than in the negative control. Changes in basal body *vs* transition zone and axoneme *vs* transition zone compartments were observed following *Tmem231* knockdown (Figure 5.4 D), causing increased transition zone co-localization with both the basal body and axoneme compartments. This indicated that knockdown of *Tmem231* facilitated ciliary basal body, transition zone and axoneme organization suggesting that TMEM231 has a fundamental role in determining ciliary compartments and ciliary organization.

5.5.2 *RPGRIP1L* module

RPGRIP1L localises to the transition zone and is implicated in ciliopathies (Watnick and Germino, 2003). For instance, Delous et al. (2007) showed that mutations in RPGRIP1L cause the complex multiorgan syndromes of cerebello-oculo-renal syndrome (CORS) and MKS. They showed that foetuses with MKS and in *Rpgrip1l$^{-/-}$* mice had a complete loss of RPGRIP1L function with neural tube defects and embryonic lethality. RPGRIP1L is suggested to form the linker protein between two ciliary modules, the small NPHP complex and the large MKS complex (Barker et al., 2014). To determine whether RPGRIP1L and associated ciliary components are important for cilia function and correct organisation, knockdown of selected ciliary TMEMs was performed. Our data show that knockdowns of all the selected TMEMs, that we assumed play roles in cilia formation to regulate the stability of the ciliary axoneme during maintenance and resorption of cilia, did not disrupt the localization of RPGRIP1L. A possible explanation is that RPGRIP1L functions as a cilium-specific scaffold that regulates cilium stability and is not affected by the presence or absence of the TMEMs. *C. elegans* localization dependency data has indicated that the relative position of RPGRIP1L in the organizational hierarchy is at the top of the model of the MKS module (Lambacher et al., 2016) and therefore RPGRIP1L localisation is unaffected because of its position. Such an explanation suggests that RPGRIP1L may retain the ability to stabilize the co-localisation of TMEMs at the transition zone. To conclude, this module showed that RPGRIP1L remained tethered at the cilia base and was not disrupted by knockdown of selected TMEMs (Figure 5.6 B) and ensured that ciliary axoneme and basal body were maintained and stabilized as separate compartments.

5.5.3 *CEP290* module

CEP290 is an appropriate candidate marker for the transition zone because it is implicated it in Y-link formation and localised to the region between the microtubule doublets and the ciliary membrane (Craige et al., 2010). Mutations in *CEP290* are responsible for about 50% of JBTS but they are rarely detected in LCA, SLS, MKS, BBS and OFD (Waters and Beales, 2011)(Chapter 1). These mutations, including nonsense, splice-site or frameshift usually cause loss of protein function and are interpreted as null alleles (Coppieters et al., 2010). CEP290 interacts with a number of proteins within a complex

(Figure 1.4 B). According to (Murga-Zamalloa et al., 2010) the CEP290 complex includes retinitis pigmentosa GTPase regulator (RPGR), NPHP6 and NPHP8/RPGRIP1L. Hypomorphic mutations in NPHP6 and NPHP8/RPGRIP1L disrupt their association with proteins within this complex, such as RPGR, which may explain the phenotypic heterogeneity that is associated with *CEP290* mutation (Murga-Zamalloa et al., 2010, Chang et al., 2006) (Murga-Zamalloa et al., 2009). Previous localization data has suggested distinct roles for CEP290 compared to other MKS/NPHP proteins at the transition zone (Schouteden et al., 2015). This study indicated that *CEP290* serves as a core component of the central cylinder and acts as an inner scaffold for transition zone assembly, whereas MKS/NPHP proteins function in the assembly of peripheral Y-links in *C. elegans* (Li et al., 2016).

We therefore chose *CEP290* as a third transition zone marker, distinct to TMEM67 and RPGRIP1L, for further analysis. In addition, IFT is required for ciliary localization of proteins and signalling pathways to produce normal mature cilia (Chih et al., 2011). IFT88 was selected to serve as an axoneme marker, since IFT is a dynamic process that is required for protein trafficking up and down ciliary microtubules. In this data-set endogenous IFT88 strongly labelled the base of primary cilia. The genetic interactions between TMEMs and CEP290 were then examined. In mIMCD-3 cells, we confirmed the localization of CEP290 to the basal body and transition zone of cilia (Figure 5.7 A), as reported in previous studies (Yang et al., 2015). Mis-localisation of *CEP290* was caused by the knockdown of *Tmem17* and *Tmem138*, suggesting that these proteins are involved in regulating the stability of axoneme and transition zone sub-compartments in this module. For example, *siRNA* against *Tmem138* increased the co-localization between CEP290 and IFT88 as well as the co-localization between IFT88 and γ-tubulin which resulted in disruption of ciliary sub-compartments (Figure 5.7 B; Figure 5.8). Distinct from *TMEM138*, *TMEM17* knock-down increased the co-localization between CEP290 and the γ-tubulin basal body compartment (Figure 5.7 B; Figure 5.8). Our data suggests that in this module *TMEM17* and *TMEM138* have a role in regulating ciliogenesis and their depletion results in defective cilia. Furthermore, although knockdown of *Tmem237* inhibited the formation of cilia and resulted in defects in the TMEM67 module, knockdown of the same gene in the CEP290 module did not have an effect. This suggests that TMEM237 plays a different role in transition zone interaction networks in these 2 modules (Figure 5.7 B; Figure 5.8).

To conclude, knockdown of some of the selected TMEM genes in *TMEM67* and *CEP290* modules completely disrupted transition zone organization. In addition, TMEM proteins in the *RPGRIP1L* module were only mildly perturbed, since RPGRIP1L appears to be a master regulator of transition zone organization and is at the top of the organizational hierarchy. It will be interesting to try to detect other known ciliary transition zone in the primary cilium and determine how they are regulated during the process of knockdowns with the selected TMEMs. Such studies may benefit from higher resolution techniques such as fluorescence resonance energy transfer or electron microscopy to identify close associations between specific proteins and effects on ciliary ultrastructure.

5.5.3.1 Knockdown of TMEM17, TMEM231, TMEM237 and TMEM138 expression causes structural defects in ciliary sub-compartments in the CEP290 module

In this experiment *TMEM17*, *TMEM138*, *TMEM231* and *TMEM237* were knocked-down and the relative localization of CEP290 at the transition zone was compared to γ-tubulin at the basal body and IFT88 at the ciliary axoneme. In a similar result to that seen for TMEM67 co-localizations (Figure 5.4 B), *TMEM17* knockdown had the most significant effect on the co-localization of the basal body and the transition zone marked by CEP290 (Figure 5.7 B; Figure 5.8). As expected, there was very little co-localization between IFT88 and the basal body. However, knockdown of all *TMEMs* other than *Tmem17* caused significantly increased co- localization between IFT88 and CEP290 (*Tmem138* knockdown), or significantly decreased co-localization between IFT88 and CEP290 (*Tmem231* and *Tmem237* knockdowns). This contrasts with the observation that knockdown of *Tmem231* and *Tmem237* gave no obvious ciliary phenotype defect when RPGRIP1L was examined (Figure 5.6 B). To conclude, the IFT88 and CEP290 modules did not match the effect on co-localization seen in either the *TMEM67* module or the *RPGRIP1L* module. Knockdown of *Tmem17* has a very significant effect on co-localization of CEP290 by moving its position at the transition zone towards and overlapping with γ-tubulin, while no evidence of ciliary phenotype defects in IFT88 and CEP290, and IFT88 and γ-tubulin, compartments were seen (Figure 5.7 B; Figure 5.8). Furthermore, knockdown of *Tmem138* significantly disturbed the localization of CEP290 in IFT88 vs CEP290 and IFT88 vs basal body compartments, which suggests that TMEM138 dislocates CEP290 localization and moves CEP290 toward IFT88 or

γ-tubulin (Figure 5.7 B; Figure 5.8). Moreover, knockdown of *Tmem231* reduced the localization of CEP290 with IFT88 which generated a substantial gap between them, with no major effect on other compartments (Figure 5.7 B; Figure 5.8). Finally, similarly to Tmem231, the effect seen for *Tmem237* knockdown suggested that it has an important influence on co-localization of CEP290 in only the IFT88 vs CEP290 compartment (Figure 5.7 B; Figure 5.8).

5.5.4 Future investigations and experimental limitations

Previous quantitative co-localization studies have lacked a unified approach for interpretation of results (Zinchuk et al., 2013). To address this issue, in this work the degree of co-localization was described using subjective qualifiers between 1.0 and -1.0 to convey information. Co-localization was described using custom terminology, such as close to 1, or 0 to indicate TMEM protein overlap or complete separation with sub-cellular compartments. This establishes a simple, consistent and objective set of variables. RPE1 cell-line is widely used for studies of ciliogenesis and ciliary function. This is an alternative model system to mIMCD-3 cells which would facilitate co-localization studies using confocal microscopy to provide insights into the arrangement and organization of the ciliary apparatus. This would considerably aid efforts to elucidate the mechanisms of ciliary assembly, maintenance and function affected by these genes by providing a different model system in which to confirm my initial findings. Furthermore, whilst 3D imaging by using confocal microscopy techniques provides high quality and interpretable data, a higher resolution for specific protein localisation is required for better analysis of ciliary organisation. A super-resolution microscopy technique, such as direct Stochastic Optical Reconstruction Microscopy (dSTORM) or stimulated emission depletion (STED) microscopy would provide this in future work.

One major limitation of the siRNA validation studies was the availability of suitable antibodies for western blot or immunofluorescence analysis. Consequently, it was not possible to validate all siRNA knockdown experiments. An alternative technique such as qPCR could be used to validate the effects of siRNA-based gene silencing on target gene expression. Also, it would be useful to identify and include positive controls for the siRNA validation by western blotting, such as si*Mks1*, a positive control for a ciliogenesis defects

(Wheway et al. 2015). This study also has potential limitations when I performed only one biological replicate in TMEM67 module for *Tmem67* and *Tmem231* experiments and in the entire RPGRIP1L module and CEP290 module experiments. To verify the dynamic nature of the siRNA, 2-3 independent and complementary biological replicates should perform since a higher number of robust biological replicates will increase the power of the analysis and result in quality research. Therefore, at least three biological replicates should be performed and averaged for each gene in the CEP290 and *RPGRIP1L* modules to generate more robust datasets and strengthen the conclusions of this work.

Finally, generating *TMEM* mutants should be considered. Although TMEM-based siRNA knockdown is a quick method to inhibit the function of selected TMEMs, models containing genomic mutants, in particular modelling know pathogenic mutations identified from ciliopathy patients, would be useful to confirm the effects of complete loss of function of these proteins. To generate TMEM mutants, the CRISPR-Cas9 methodology could be utilized to create indels (insertions-deletions) or knock-ins of missense mutations in specific TMEM genes.

Chapter 6 Final Discussion

6.1 Summary of aims and key findings

Ciliopathies comprise an ever-expanding group of heterogeneous inherited developmental disorders with variable phenotypes that result in the abnormal formation or function of cilia (see section 1.6). Cilia are essential organelles because they perform significant cellular functions. They regulate biological processes such as cellular homeostasis and provide a discrete compartment to harbour components of key developmental signalling pathways. The proteins encoded by ciliopathy disease genes mainly localize to the anchoring structure of the ciliary axoneme, known as the basal body, or to an adjacent sub-compartment known as the transition-zone comprising the first 0.2 to 0.5 μm of the proximal ciliary axoneme (see section: 1.2.4.1 and 1.2.4.3). Recent studies have highlighted the importance of the transition-zone as the key regulator of cilium composition and signalling by the establishment of diffusion barriers that restrict both cytosolic protein entry in a size-dependent manner, and the lateral exchange of proteins between ciliary and non-ciliary membranes.

The characterization of these proteins and the multi-subunit complexes in which they interact provides insights into their potential roles in ciliary organization and function. This is a significant and topical area of study that may explain the pathogenic mechanisms that underlie ciliopathies and renal cystic disease. Therefore, this project aimed to examine the role of the transition-zone by characterizing the biochemical and genetic functions of the TMEM proteins found there using biochemical, genetic, and cell biology techniques. The overall aim of this project was to understand, identify and characterise TMEM functions involved in ciliogenesis and human ciliopathies. For this study, the ciliary transition zone proteins TMEM17, TMEM67, TMEM138, TMEM216, TMEM231 and TMEM237 were selected in order to better understand the molecular architecture and function of this specialized proximal region of the primary cilium. To accomplish this aim, I had 3 main objectives:

Objective 1: Screening for mutations in *TMEM218* and *TMEM17* as novel causes of MKS

To begin to address this question, I sequenced coding exons in *TMEM17* and *TMEM218* for patients and families who had been diagnosed with MKS but were mutation negative in the known MKS disease genes at the time of the study. In summary, the results were as follows:

- There were no novel biallelic variants identified that could be interpreted as pathogenic mutations in *TMEM17* and *TMEM218.*
- Screening identified two novel heterozygous missense variants in *TMEM17* comprising: c.76G>A:p.(Gly26Ser) and c.64T>A:(p.Ser22Thr). The screening also identified several known variants in *TMEM17* including: c.59G>C (p.Ser20Thr), c.54G>A (p.Val18=), c.12G>A (p.Pro4=), c.216A>G (p.Leu72=), c.24C>T (p.Arg8=), c.264C>T (p.Thr88=).
- There were no variants identified in *TMEM218* in those samples that could be interpreted as pathogenic.

Objective 2: To perform functional characterization of TMEMs using established biochemical and cell biology techniques, identifying new interacting ciliary proteins and complexes.

The investigations of TMEM17, TMMEM67, TMEM138, TMEM216, TMEM231 and TMEM237 in transition zone function and maintenance provided insights into their roles during embryonic development and the molecular basis of ciliopathies. Over-expression of epitope-tagged and TAP-tagged selected ciliary TMEMs allowed the identification of protein-protein interactions within the ciliary transition zone using systematic proteomic analyses to investigate indirect and reciprocal interactions between TMEMs. This delineated a hierarchical network of biochemical interactions between the TMEMs as follows:

- Immunofluorescence confocal microscopy confirmed the sub-cellular localization of endogenous and epitope-tagged TMEMs to the transition zone.
- Novel biochemical interactions of ciliary TMEMs comprise: interactions of TMEM17 with IFT88 and a reciprocal interaction with TMEM237, as well as verification of known interactions with TMEM67 and TMEM216 and TMEM231; interactions of TMEM237 with TMEM67 and IFT88, a reciprocal interaction with TMEM216, as well as verification of a known interaction with TMEM17; interactions of TMEM138 with TMEM67, TMEM237 and IFT88, as well as verification of a known interaction with TMEM17.

- Systematic proteomic analyses using TAP identified the following indirect interactions and reciprocal interactions: interaction of TMEM17 with PRPF8, PRPF6 and C21orf2; interaction of TMEM237 with TMEM17.

A second aspect of Objective 2 was to clone and express the N-terminal domain of TMEM67 (Nt-TMEM67) in order to produce protein for X-ray crystallography trials and for production of an "Affimer" artificial non-antibody binding protein. The overall objective of this work was to use structural biology methods to identify potential ligands of the orphan receptor TMEM67 and to determine the role of missense variants and mutations in the Nt-TMEM67 domain. Unfortunately, the yield of purified Nt-TMEM67 was not sufficient for MS identification and crystallization trials.

Objective 3: To perform RNA interference-based studies to characterize genetic and potential functional interactions between ciliary TMEMs and to quantify their relative co-localizations at the basal body, in the transition zone and in the axoneme.

- Confirmed that knock-down of *TMEM17*, *TMEM67*, *TMEM138*, *TMEM231* and *TMEM237* caused significant reductions in cilia incidence.
- Knock-down of *TMEM17*, *TMEM138*, *TMEM231* and *TMEM237* significantly mis-localized TMEM67. These results indicate that TMEMs are potential mediators that may link TMEM17, TMEM138, TMEM231, and TMEM237 with TMEM67 in common molecular pathways, suggesting potentially new interactions and localization-based functions; it may there are both physical and genetic interactions between TMEMs and the TMEM67 that may link in common molecular pathways such as Wnt signalling.
- Knock-down of the selected TMEMs did not have any significant effect on the co-localization of RPGRIP1L with ciliary sub-compartments. This means that RPGRIP1L is the sole protein responsible for TMEMs recruitment to cilia. In addition, it implying that *RPGRIP1L* is higher in an organizational hierarchy than the TMEMs and RPGRIP1L has critical functionality at the transition zone beyond being a mediator of ciliogenesis, possibly it functions as a cilium-specific scaffold that regulates cilium stability and is not affected by the presence or absence of the TMEMs.
- Knock-down of *Tmem17*, *Tmem138*, *Tmem231* and *Tmem237* significantly mis-localized *CEP290*, implying that these TMEMs are responsible for CEP290 recruitment to the transition zone of cilia involved in regulating the stability of axoneme and transition zone sub-compartments in this module. All of which work as a mediator of primary cilia formation and may reveal new compartment-specific biological functions or/and these observations suggest that CEP290's role may be ciliogenesis pathway-specific. In addition, the transition zone proteins TMEMs are required for primary cilium formation and mediate the correct organization of the

IFT88 and CEP290 modules. Such modules (*CEP290*) and (*TMEM67*), work togather as ciliary gatekeeper modules, anticipated functions in mIMCD-3 are by facilitating entry into the out of cilia at the transition zone by blocking unauthorized entry of proteins or preventing diffusion of those proteins into ciliary membrane.

These results raise questions of whether these biochemical and/or genetic interactions are limited to the mIMCD-3 kidney epithelial cell-line. Furthermore, why would the loss of a single transmembrane protein have such a profound consequence on different ciliary sub-compartments? Do TMEM17, TMEM 138, TMEM216, TMEM231 and TMEM237 act as a co- receptor for TMEM67, previously described as a possible Frizzled-like receptor for Wnt5a (Abdelhamed et al., 2015). If so, what is the molecular basis of these interactions? A novel interaction between TMEM components of the ciliary transition zone and an IFT-B component, IFT88, was also identified here. Previous studies have only suggested an interaction with IFT-A components (Scheidel and Blacque, 2018), strengthening the link between transition zone and IFT activities.

The overall conclusion of this work is that the TMEM17, TMEM67, TMEM216, TMEM138, TMEM231 and TMEM237 proteins are necessary for the proper functions of primary cilia but have specialized, discrete functions. In particular, multiple approaches demonstrated that TMEM17 is a robust interaction partner of TMEM67. In addition, IFT-B mediates ciliary protein trafficking through interactions between its component IFT88 and possibly 3 TMEMs that include TMEM17, TMEM138 and TMEM237. These provide new insights into the organization of the ciliary transition zone and the disease mechanisms of human ciliopathies.

6.2 How do the key findings complement those from other studies?

The most recent research on ciliopathies has shifted towards a focus on ciliary transition zone proteins since many of these components are mutated as a cause of ciliopathies (see section 6.1) (Ishikawa and Marshall, 2011). Hence, in this project selected ciliary transition zone genes that are implicated in defects in signal transduction pathways, and the maintenance and formation of cilia, were studied. Figure 6.1 reviews the biochemical and genetic interactions of ciliary proteins within ciliary sub-compartments, focusing on those documented to occur in the transition zone from previous studies and comparing these with the results of the current study. It should be noted that not all of the

proteins represented in Figure 6.1 are exclusively located in the transition zone, but may also be found at the basal body. The following provides an overview of previous research studies.

Sang et al. (2011) provided an initial basis for choosing the protein-protein interactions and functional modules of most relevance for the current study; Sang et al. (2011) investigated 3 ciliated model cell-lines comprising NIH 3T3 fibroblasts, mIMCD-3 kidney epithelial cells and human retinal pigment epithelial (RPE) cells using a tandem affinity G-LAP-Flp purification strategy followed by MS identification of protein species. The authors used disease proteins NPHP1, NPHP2/Inversin, NPHP3, NPHP4, NPHP5/IQCB1, NPHP6/CEP290, NPHP8/RPGRIP1L, AHI1/Jouberin and MKS1 for the identification of interacting proteins but did not included TMEMs in their study. They demonstrated that *RPGRIP1L* localised at the ciliary transition zone and interacted with NPHP1 and NPHP4, an interaction confirmed by a subsequent study (Williams et al., 2011). This study described 2 separate functional modules in *C. elegans*. The MKS/MKSR module contained MKS1, MKSR1/B9D1, MKSR2/B9D2, MKS3/TMEM67 and MKS6/CC2D2A, whereas the NPHP module contained NPHP1 and NPHP4 (Williams et al., 2011). Their analyses revealed that RPGRIP1L was functionally linked to both modules.

Garcia-Gonzalo et al. (2011) also used standard ciliated model cell-lines to identify genetic and biochemical analyses. This study identified mutations in *TCTN1*, encoding the transmembrane protein Tectonic-1, that localized to the ciliary transition zone and interacted with CC2D2A, MKS1, B9D1, Tectonic-2/TCTN2, Tectonic-3/TCTN3, CEP290, TMEM67 and TMEM216. Furthermore, Tectonic-1 was required for transition zone localization of MKS1 and TMEM67. Interestingly, CEP290 was identified as a Tectonic-1 interactor by MS analysis and chromatography, but not by coimmunoprecipitation assay, whereas TMEM67 and TMEM216 coimmunoprecipitated with Tectonic-1 but were not detected by MS analysis. Therefore, the authors proposed that CEP290, TMEM67 and *TMEM216* serve as sub-stoichiometric or peripheral components of the Tectonic complex.

In a parallel study, Huang et al. (2011) identified *TMEM237* as a ciliopathy gene using next generation DNA sequencing. They found mutations in *TMEM237* as a cause of JBTS type 14. The model systems used in this study comprised mIMCD-3 ciliated cells, *C. elegans*,

and *Danio rerio* (zebrafish) to investigate the biochemical and genetic interactions of *TMEM237* and other ciliary proteins. First, Huang et al. (2011) confirmed the localization of TMEM237 to the transition zone and demonstrated that TMEM237 functionally interacted with TMEM216, B9D1, B9D2 and NPHP4 at the transition zone in *C. elegans*. Second, this study indicated that TMEM237 required RPGRIP1L for localization to the transition zone in both the mIMCD-3 cell and *C. elegans* models. Third, in *Rpgrip1l* zebrafish mutants, both TMEM237 and TMEM216 failed to localize to the transition zone. Based on these findings, Huang et al. (2011) suggested that RPGRIP1L has a structural role in mediating the scaffolding or bridging between interacting ciliary proteins. The authors speculated that TMEM237, TMEM216, TMEM67 and possibly other TMEMs form a receptor-coreceptor complex at the transition zone that may help in mediating signaling pathways.

Chih et al. (2011) focused on the characterization of the complex of B9 domain-containing proteins using RNAi screening, proteomics, cell biological and mouse genetics approaches. Chih and colleagues identified B9D1-interacting proteins using TAP/MS assays which included B9D2, TCTN1, TCTN2, MKS1, AHI1, CC2D2A, TMEM231, TMEM17 and KCTD10. In addition, they carried out gel filtration chromatography on lysates of mIMCD-3 and embryos at 13.5 days of gestation and identified that TMEM231, TMEM17, MKS1, CC2D2A, AHI and TCTN1 were in a high molecular weight complex. Furthermore, siRNA assays indicated that all of the members of the B9D1 complex co-localized with TMEM231, and that siRNA knockdowns of B9d1, Tmem17 and Cc2d2a disrupted Tmem231 localization to the transition zone.

In a subsequent study, Gupta et al. (2015) generated a protein interaction map of the human centrosome-cilium interface using *in vivo* proximity-dependent biotinylation (BioID) in ciliated hTERT-RPE1 cells. The MS identification of bait interactions showed that TMEM17 interacted with TMEM237, which is consistent with the TAP interaction data presented in the current study using mIMCD-3 cells (Figure 6.1 J). Gupta et al., (2015) showed that transition zone baits in ciliated and non-ciliated cells comprised of membrane-associated TMEM17, TMEM67, TMEM216 and TMEM237. These results are also consistent with the co-immunoprecipitation and TAP interactions presented here, which demonstrated that TMEM237 interacted with TMEM17, TMEM216 and TMEM67 (Figure 6.1 J); TMEM216

interacted with TMEM237 (see Figure 6.1 H); TMEM67 interacted with TMEM17 (see Figure 6.1 F); and TMEM17 interacted with TMEM67, TMEM216 and TMEM237 (see Figure 6.1 D). The TMEM67 and TMEM237 interactions are therefore consistent with the hierarchy of interactions within the transition zone reported in previous studies (Garcia-Gonzalo et al., 2011, Williams et al., 2011).

In a parallel proteomics study, Yang et al. (2015) reconstructed a molecular map of important proteins in the transition zone, the transition fibers and the basal body by STED super-resolution microscopy. (Yang et al., 2015) selected and imaged components known to be associated with the 3 major multiprotein complexes of the transition zone sub-compartment including CEP290, RPGRIP1L, MKS1, TMEM67 and TCTN2. They found that TMEM67 and TCTN2 localized at the same axial level as RPGRIP1L and MKS1 and they suggested that these proteins may interact directly with each other because of this. Yang and colleagues also suggested that these proteins may serve regulatory roles for tissue-specific ciliogenesis, suggesting that mutation in *TCTN2* affects ciliogenesis in a tissue-dependent manner whereas mutation in *TMEM67* has slightly different ciliogenic defects, *TMEM67* mutations are milder than those in *TCTN2* (Garcia-Gonzalo et al., 2011), because mouse *Tctn2* mutant embryos lacked nodal cilia, while cilia in neural tubes were almost absent, morphologically defective or failed to elongate axonemes. In contrast, in the mouse *Tmem67* mutant embryonic kidneys developed cysts and kidney tubules displayed few, morphologically defective cilia. This study also showed that CEP290 localised at a different axial level, appearing to bridge the basal body and other transition zone proteins. Hence, they determined there are at least 2 layers of proteins at the transition zone: one containing RPGRIP1L and MKS1, and the other comprising CEP290. TMEM67 and TCTN2 localised at the ciliary membrane, corresponding to the ciliary necklace, at the same axial level as RPGRIP1L and MKS1. In summary, mapping the localizations of RPGRIP1L and CEP290 provided insights into the potential tethering and anchoring functions of these important ciliary proteins.

Lambacher et al. (2016) focused on *TMEM107* as a novel transition zone protein and investigated its function. First, they identified mutations in *TMEM107* as a cause of OFD and JBTS in patients. Second, studies in *C. elegans* revealed that *TMEM107* controlled ciliary

composition by demonstrating that *TMEM107* genetically interacted with NPHP4. Lambacher et al. (2016) speculated that this interaction could regulate cilium formation and assembly of ciliary membrane with the Y-shaped linkers. Also, they predicted the position of TMEM107 at an intermediate level within a hierarchical organization, suggesting the existence of a new module at the transition zone containing only TMEM107 that is intermediate between 2 layers. The top layer is a module containing TMEM17, TMEM237, TMEM67, MKS1 and CC2D2A. The lower layers included TMEM216, B9D1, B9D2 and TMEM231, with RPGRIP1L at the root of the hierarchy. This study expanded the MKS module and provided insights into transition zone subdomain architecture in worms (summarized in Figure 6.1).

Li et al. (2016) provided fundamental insights into the assembly pathway of the ciliary transition zone and identified 2 genes, *TMEM218* and *TMEM80*, as novel MKS module components in *C. elegans.* Additionally, they also identified *TMEM138* and *CDKL1-4* as components of a CEP290-associated module. Moreover, they confirmed the connection of *TMEM17* to human ciliopathies when they showed that a private mutation in *TMEM17* was a probable cause of OFD type 6. In addition, Li et al. (2016) also identified possible private mutations for *TMEM138* and *TMEM231*. In this study, CEP290 was considered to be the core of its own NPHP5-6 network, but was part of an MKS module as described by Garcia-Gonzalo et al. (2011). Li et al. (2016) suggested the existence of an RPGRIP1L- and CEP290-dependent assembly pathway for building a functional transition zone. Finally, they drew a proposed module for the transition zone based on their findings and some major direct and indirect connections between different modules or proteins (summarized in Figure 6.1). In particular, Li et al. (2016) showed in *C. elegans* that TMEM218 interacted with NPHP4 but not TMEM216, and its localization at the transition zone depended on RPGRIP1L and MKS module proteins including TMEM216. They indicated that TMEM218 required CEP290 for assembly at the transition zone, and both CDKL1 and TMEM138 required CEP290 for their transition zone localisation although their function is independent of either the MKS or NPHP modules. Moreover, they showed that the newly identified transition zone component TMEM80 required TCTN1, TCTN2, and CC2D2A for its correct localisation.

The current project is a continuation of these studies by providing a systematic analysis and collation of localization data, genetic analyses through siRNA knockdowns and biochemical interaction patterns (through co-immunoprecipitations and TAP assays), revealing a map of transition zone protein interactions (summarized in Figure 6.1). This network involves many known ciliopathy proteins and reveals notable novel interactions. In this project, TMEM17 was the transition zone protein that had most interactions, in comparison to TMEM67, TMEM138, TMEM216, TMEM231 and TMEM237. This result is consistent with the previous study of Gupta et al. (2015) which showed that *TMEM17* had the most transition zone protein interactors from a broad selection of ciliopathy proteins (ranked by decreasing numbers of baits as: MKS1, B9D2, RPGRIP1L, TCTN1, RPGRIP1, DYNIT1, TCTN2,TMEM67, RPGR, LCA5, NEK8, NPHP4 and AHI1).

6.3 Biochemical and genetic interactions of TMEM proteins in the ciliary transition zone and implications for ciliary sub-compartment organization

The general aim of the project was to examine in greater detail the ciliary interactions among multiple proteins within the ciliary transition zone. In the first instance, N-TAP (streptavidin-FLAG)-tagged ciliary transition zone proteins were successfully generated, including TMEM17, TMEM138, TMEM216, TMEM231 and TMEM237, as well as C-TAP (streptavidin-FLAG)- and eYFP-tagged TMEM67. Co-immunoprecipitation experiments were then performed to investigate if the selected ciliary transition zone TMEMs formed a biochemical network required for proper cilia formation and function. TAP-tagged TMEMs were exogenously over-expressed in HEK-293 cells and were pulled-down with specific antibodies. In addition, to assess the nature of the ciliary organisation defects following depletion of specific TMEMs, specific analyses for siRNA knock-down assays were developed. Disruption of ciliary organization and localization of marker proteins following knock-downs was quantified by Volocity 64x analyses.

To illustrate both approaches, TMEM67 and TMEM17 localization to the ciliary transition zone was confirmed (Figure 4.4 B; Figure 4.5 A) and results from co-immunoprecipitations (Figures 4.7 C; 4.9) confirmed an interaction between TMEM67 and TMEM17. Furthermore, siRNA knockdown was used to delineate the interactions with the

TMEM67 module, at both the genetic and biochemical levels. This is important because *TMEM67* mutations are associated with a number of ciliopathies, including MKS3, and TMEM67 is a key player in the Wnt signalling pathway and could act as a component of selective permeability at the transition zone (Leightner et al., 2013). TMEM17, a newly identified protein, was described as a cilium-associated protein (Li et al., 2016) and a homozygous missense private mutation in a single family has been described as causative for Oral-Facial-Digital syndrome type 6 (OFD6) (Li et al., 2016) (see section 1.6.3.5; Figure 1.10).

In this thesis, comparison of ciliary organization between a specific siRNA knockdown and a scrambled siRNA negative control revealed re-organization and changes in localization of the ciliary axoneme marked by acetylated α-tubulin and the basal body. A decreased association of the ciliary transition zone with the basal body following knockdown of *TMEM17* was noted (Figure 5.4 D). Possible interpretations of this result may be that the transition zone and axoneme move away from their correct positions, in order to maintain the new structure, which allows this compartment to be functional and to be connected to the axoneme and basal body. This is an unexpected and novel result that emphasizes the importance of TMEM17 in organizing the ciliary transition zone in mIMCD-3. Furthermore, these results indicate that TMEM17 is required for the correct localization of TMEM67 at the ciliary transition zone. By contrast, in *C. elegans*, (Lambacher et al., 2016) indicated that in the MKS module, TMEM17 is not required for the localization of other transition zone proteins. Two possible explanations for the difference in TMEM17 function in the mammalian compared to the nematode transition zone are the molecular assembly hierarchies. The differences in biochemical and genetic interactions for the MKS modules are likely due to differences in cilia structure and assembly in mammals and *C. elegans*. Some *C. elegans* and mammalian ciliary genes are highly conserved (for example, TMEM67 and the B9 domain proteins), but there are many that are not (for example, CEP290). This may be because *C. elegans* does not have SHH or Wnt signalling and therefore may have a reduced need for defined ciliary sub-compartments.

In the TMEM67 module, the effect of *TMEM138* depletion was also studied. This indicated that the ciliary transition zone protein TMEM138 is necessary for the structural

organization of primary cilia compartments. Co-immunoprecipitation results revealed that TMEM138 interacted with TMEM67, TMEM17, IFT88 and TMEM237 using buffers with different ionic strength and different detergents (CHAPS and NP40; Figure 4.6 D E; Figure 4.7 A). In addition, disordered organization and localization of the transition zone and axoneme was observed following *TMEM138* knockdown (Figure 5.4 D), suggesting that the transition zone-axoneme compartments move away from each other and form a gap (Figure 5.5). This implies that TMEM138 is an essential ciliary protein required for proper localization of ciliary compartments.

With regard to the functional roles of TMEM216, it appears to cooperate with TMEM237 and TMEM67 in maintaining normal ciliary functions (Huang et al., 2011). In addition, TMEM216 serves as a possible co-receptor that regulates the RhoA pathway (Valente et al., 2010) and mediates the cytoskeletal rearrangements needed for basal body docking during ciliogenesis (Valente et al., 2010). Co-immunoprecipitation assays confirmed a reciprocal interaction: TMEM216 interacted biochemically with TMEM237 (Figure 4.6 A, B; Figure 4.7 B). TMEM237 is required for ciliogenesis in mammalian cells, zebrafish and *C. elegans*. Mutations in *TMEM237* causes failure of cilia formation and deregulation of both canonical and noncanonical/PCP Wnt signalling pathways (Huang et al., 2011). Co-immunoprecipitations demonstrated that TMEM237 interacted with TMEM216 in a reciprocal co-immunoprecipitation (Figure 4.6 A, B; Figure 4.7), which extended the previous observations of (Huang et al., 2011) that TMEM237 interacted functionally with TMEM216 at the transition zone in mIMCD-3 cells. In addition, and consistent with a previous study (Youn and Han, 2018), the co-immunoprecipitation results indicated that *TMEM237* genetically interacted with the *TMEM67* module, and its knockdown resulted in a stronger defective phenotype at the transition zone/basal body compartment (Figure 5.4 D; Figure 5.5). These results support a possible function of TMEM237 and other transition zone proteins in basal body anchoring and in establishing a ciliary gate during ciliogenesis.

In the *TMEM67* module, I also examined the possible roles of the ciliary transition zone protein, TMEM231. This is mutated as a cause of JBTS type 20 and MKS type 11 (Youn and Han, 2018). I observed significant and striking phenotypes across the *TMEM67* module following *TMEM231* depletion, resulting in disruptions to the organization of the transition

zone and basal body, as well as their positioning relative to the ciliary axoneme. These results emphasize the importance of TMEM231 in organizing these ciliary compartments, suggesting that it prevents aberrant extension of the transition zone in order to maintain connection to the axoneme and basal body (Figure 5.4 B; Figure 5.5).

RPGRIP1L plays a central role in anchoring other MKS and NPHP proteins (Williams et al., 2011) and mutations in this gene are causative of a range of ciliopathies. Previous studies have shown that RPGRIP1L localises at the base of primary cilia and describe it to be either a basal body protein (Arts et al., 2007, Delous et al., 2007, Vierkotten et al., 2007) or a transition zone protein. Gerhardt et al. (2015) observed that RPGRIP1L localised at the transition zone during G_0 and at both centrosomes during mitosis in mouse embryonic fibroblasts (MEFs), suggesting that its localization is dependent on the cell cycle but not providing detail into the molecular mechanism that could regulate this intriguing switch in localization and potential function. In support of this observation, Gerhardt et al. (2015) also described the surprising biochemical interaction of mouse RPGRIP1L with PSMD2, a component of the proteasomal 19S subunit. They suggested that RPGRIP1L could regulate the activity of a ciliary-specific proteasome, presumably associated with RPGRIP1L localization at the centrosome rather than the transition zone, that could regulate cilia-mediated signalling. Izawa et al. (2015) suggested that the key mechanism in controlling ciliogenesis by RPGRIP1L in the Gerhardt et al. (2015) study was ubiquitination/de-ubiquitination of key ciliogenesis proteins at the ciliary base including the ubiquitin E3 ligases Von Hippel-Lindau tumor suppressor (pVHL) and mindbomb E3 ubiquitin protein ligase 1 (MIB1) (Thoma et al., 2007, Huang et al., 2009a). Correct proteasomal function is essential for proper development and function of multiple organs (Rubinsztein, 2006, Breusing et al., 2009, Wang and Robbins, 2014). Gerhardt et al. (2015) suggested that the disruption of protein degradation could also result in ciliopathies, but the mechanistic details of this process remain unclear.

Data in this thesis indicated that RPGRIP1L localized to the transition zone as expected, but after *TMEM17, TMEM231, TMEM237* and *TMEM67* depletions there was no disruption of localizations of other sub-compartments including the transition zone (Figure 5.6). This suggests that RPGRIP1L is higher in an organizational hierarchy than the TMEM

proteins and that it is required for the correct formation of a normal transition zone, as suggested in previous studies (Yang et al., 2015).

Basal bodies are believed to associate with membrane compartments in the early stages of cilia formation and to initiate axonemal growth (Goggolidou et al., 2014). Some studies suggest that CEP290 localizes to the basal body/centriole and centriolar satellites and that CEP290 could mediate basal body organization as well as regulation of ciliogenesis (May-Simera and Kelley, 2012, Murga-Zamalloa et al., 2011). Mutations in *CEP290* cause nephronophthisis (Sayer et al., 2006) and a broad range of other ciliopathies including JBTS, BBS, LCA, SLS and MKS (Valente et al., 2006, Baala et al., 2007, Perrault et al., 2007) which affect distinct functions at the transition zone and centriolar satellites (Kobayashi et al., 2014, Klinger et al., 2014). On the other hand, a previous study (Craige et al., 2010) and a more recent study Yang et al. (2015) indicate that CEP290 organizes a discrete module in the transition zone by tethering ciliary membranes to axonemal microtubules. CEP290 was therefore potential candidate protein for further investigation in this project. IFT88 has been used as an axoneme marker in a previous study (Yang et al., 2015) and was used for this purpose in work here where ciliary marker choice for immunofluorescence microscopy was limited. My aim for studying IFT88 and CEP290 was to gain insights into how selected TMEMs affected CEP290 and IFT88 localization, and whether transition zone TMEMs affect the potential function of an IFT-B component (see section 1.2.4.5.1). Furthermore, a recent study on IFT-A components Scheidel and Blacque (2018) identified functional interactions between ciliopathy-associated IFT-A and transition zone MKS modules. They showed that the localization of TMEM216, TMEM67 and RPGRIP1L in the MKS module was disrupted, for example in *ift-121/139* and *ift-43/139* double mutant worms and *ift-43/139* and *ift-121/139* double mutants, respectively. In contrast, CEP290 localization was unaffected in mutants, even in the *ift-43/121/139* triple mutant. Furthermore, this study showed that IFT140 regulated the transition zone restriction of MKS module components and exclusion of periciliary membrane proteins, and that IFT-43/121/139 control their entry and removal. These findings demonstrate that the IFT-A complex regulates ciliogenesis and the transition zone gating system.

The siRNA studies in this thesis suggest that TMEM17, TMEM138, TMEM231 and TMEM237 all have significant roles in cilia formation in both the TMEM*67 and CEP290* modules. For example, TMEM17 is required for CEP290 localization in primary cilia: siRNA depletion of *Tmem17* caused CEP290 mis-localization at the base of primary cilia in this module, resulting in aberrant co-localizations between the axoneme and basal body compartments (Figure 5.7 B; Figure 5.8). *Tmem138* knockdown resulted in defects in localization of IFT88 vs CEP290, as well as IFT88 vs basal body, causing aberrant co-localizations and gaps between these compartments (Figure 5.7 B; Figure 5.8). These results reveal an important function of TMEM138 in cilia biology in this cellular model. Similarly, knockdown of *Tmem231* and *Tmem237* mislocalized cilia sub-compartments (Figure 5.7 B; Figure 5.8). Therefore, the transition zone proteins TMEM231 and TMEM237 are required for primary cilium formation and mediate the correct organization of the IFT88 and CEP290 modules. Co-immunoprecipitation studies also demonstrated a novel interaction between some of the transition zone proteins (TMEM17, TMEM138 and TMEM237) and the IFT-B component IFT88 (Figure 4.6 C; 4.7 A, C). This suggests that these protein work as a complex and warrants further study in order to understand the functional purpose of this complex on, for example, transition zone gating.

The siRNA results also suggested that TMEM ciliary components within these modules mediate partially separate ciliary functions: inactivating one selected component from an MKS module such as TMEM17 appears to be sufficient to fully disrupt another component, such as TMEM67 in the same module, and may be sufficient to fully disrupt the whole module.

Overall, this project provides a better understanding of functional roles and interactions of ciliary TMEMs, providing further mechanistic understanding of the ciliopathy disease state. This may inform the design of future therapeutic interventions. The fact is that defining the mechanism of disease is a first step towards therapy. I demonstrated that TMEMs mutations using siRNA-based genetics experiments lead to the disruption of the cilia sub-compartments in ciliated kidney cells (mIMCD-3), thereby gaining potential insights into pathomechanisms of cystic kidney disease or ciliopathy disease progression. Specifically, the mis-localization of Tmem67 or Cep290, but not Rpgrip1l*,* when ciliary TMEMs are

ablated by RNAi provides insights into the hierarchy of transition zone proteins and may allow the best ciliary proteins to be more effectively prioritized during the development of a new targeted therapies.

The coimmunoprecipitation and TAP-MS experiments have identified roles for unexpected interactions between ciliary transition zone proteins and, for example, splicing factors. The identification of new disease gene functions, and its interactions or complexes that related to the ciliary transition zone, may enable the future rational design of preventative treatments or new therapeutic interventions for cystic kidney disease which would have a major impact on the quality of life for patients and their relatives. For example, by understanding how the ciliary transition zone and associated ciliopathy proteins regulate ciliary sub-compartments and structure, this thesis work could lead to the design of small molecules that can advantageously increase or decrease permeability at the ciliary base, and thereby improve some of the progressive post-natal ciliopathy pathologies. Also, since the disrupted localizations of ciliary compartments resulted from the absence of transition zone proteins, they could, in principle, be corrected by gene replacement. For example, the restoration of a specific ciliary sub-compartments may be sufficient as an appropriate therapeutic target that leads to the prevention of progression of renal disease.

In summary, the novel biochemical and genetic interactions between ciliary components that have been identified in this thesis, will enable us to better understand the pathogenesis and relationship between cilia and cystic diseases. This may contribute to new therapeutic strategies, since at the present time hemodialysis and renal replacement therapy remain the only effective treatments for end-stage kidney disease.

6.3.1 Future plan

The data in section (4.4.2.1) supports biochemical and genetic interactions between TMEM237, TMEM17 and TMEM138 and IFT88, linking transition zone components with the IFT-B complex. This is an interesting and unexpected observation, and in further investigations I would assess the following hypothesis: do transition zone TMEMs affect ciliary trafficking by IFT88 (and the IFT-B complex)? I would plan for a systematic mapping of TMEMs interaction network in living cells using BioID. The map would provide new insights or confirm the functional role of these TMEMs and IFT88 in cilia and disease. Also, I would

combine that with a CRISPR-Cas9 knock-out screen in which each TMEM gene tested in this thesis was targeted by different guide RNAs to order to ablate every gene. I would then use a high-content imaging approach, similar to the design of the siRNA experiments in Chapter 5, in order to gain new insights into ciliary functions and better understand the molecular mechanisms underlying ciliopathies. Finally, $Cep290^{-/-}$ and $Tmem67^{-/-}$ mouse models, would be required to determine fully the *in vivo* effects of TMEM genes ablation and functional module disruption in physiologically-relevant kidney tissue.

6.4 Biochemical and genetic interactions between ciliary transition zone transmembrane proteins identify a TMEM17-TMEM67 functional module in mammalian cells

Further research is required to gain insights into the biological functions of these ciliary genes that are mutated as a cause of ciliopathies. It was investigated here how ciliopathy-associated genes interact to support ciliogenesis, and the effect of gene knock-down on ciliary organization was examined. Firstly, *TMEM17* mutation screening was performed in a cohort of 36 patients with MKS that were negative for mutations in other known MKS genes. I confirmed that these individuals did not have sequence variants in *TMEM17* that could be interpreted as pathogenic. Secondly, the biochemical interaction between TMEM67 and TMEM17 was confirmed using a series of co-immunoprecipitations with FLAG-tagged constructs (Figure 4.7 C; Figure 4.9). The biochemical interaction was further supported by evidence for a genetic interaction between *TMEM17* and *TMEM67* using siRNA knockdowns (Figure 5.4 D).

One possible explanation is that the interaction between *TMEM17* and *TMEM67* at the transition zone is required to regulate ciliary complexes in response to cilia formation. Since knock-down of *Tmem17* resulted in mis-localization of ciliary compartments, this suggests that the interaction with TMEM17 blocks the cues for correct localization of TMEM67 to the ciliary transition zone. A second interpretation, not mutually exclusive to this first, is that TMEM67 is a receptor that involved in non-canonical Wnt signalling (Abdelhamed et al., 2015). I speculate that TMEM17 may work as co-receptor for TMEM67, and may function to coordinate signalling pathways with TMEM67. A third explanation is

that disruption or loss of TMEM17 changes the conformation and available binding sites of transition zone ciliary components in such a way as to prevent or block the interaction of TMEM17 with TMEM67. This would restrict the binding of TMEM17 with TMEM67, creating only a small pool of TMEM17-bound TMEM67. For instance, some variants in the predicted transmembrane helices of TMEM17 might alter hydrophobic interactions with TMEM67 in the ciliary membrane that may contribute to disruption of cilia signalling pathways such as Wnt signal transduction as a cause of ciliopathy phenotypes.
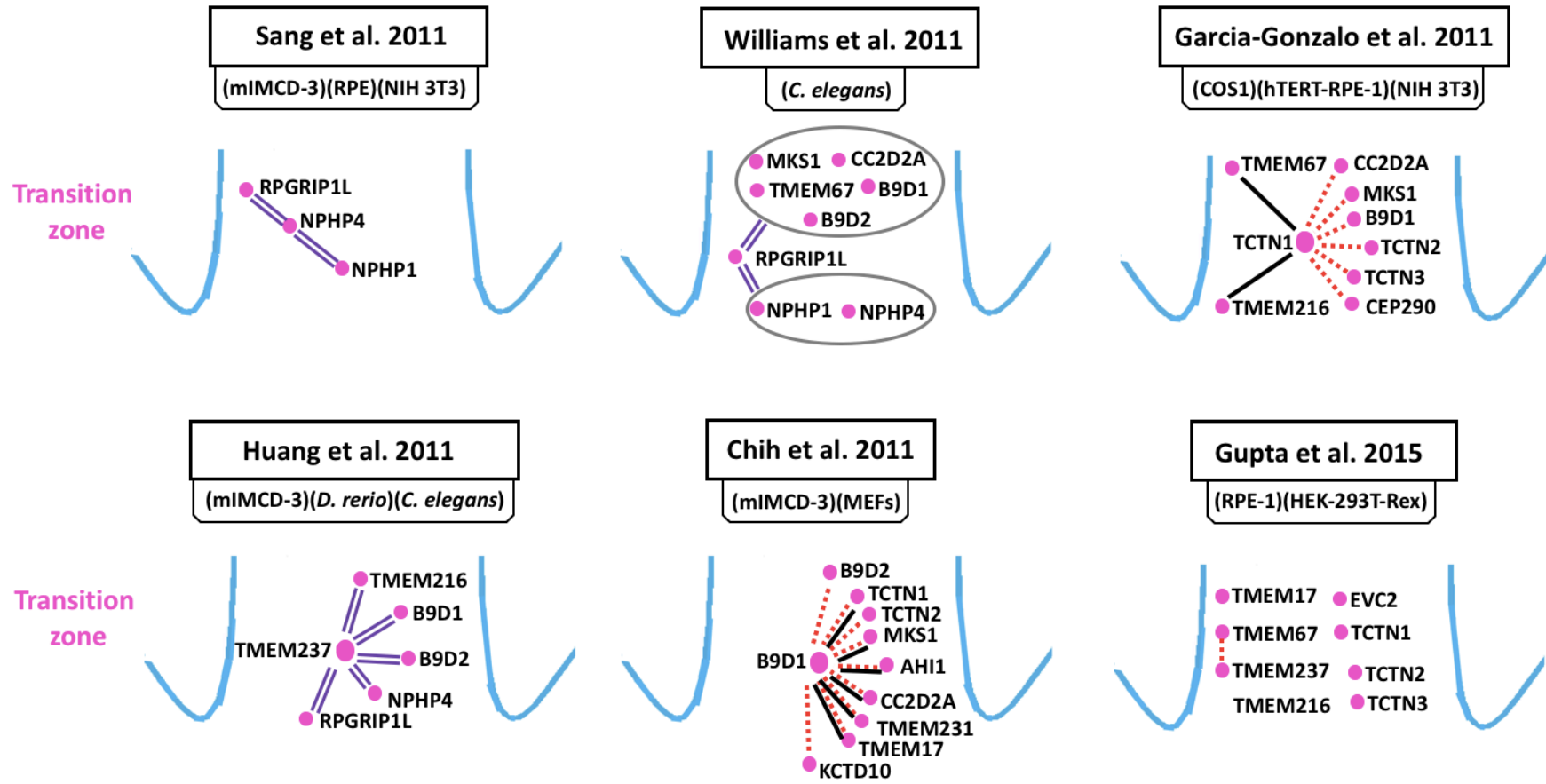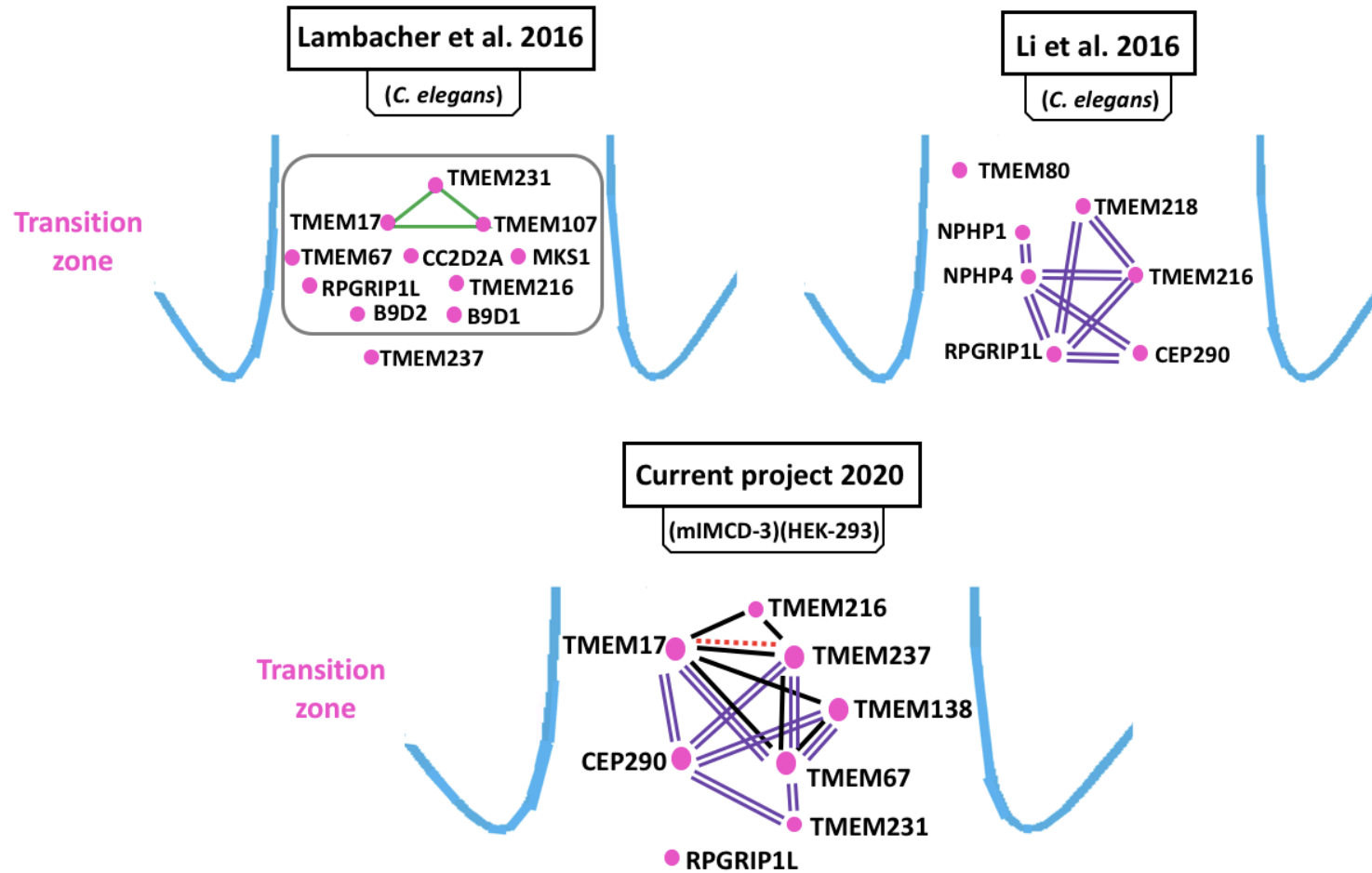
Figure 6. 1: Schematic of biochemical and genetic interaction networks for ciliary transition zone proteins based on previous studies and this thesis. The published study and model systems used to generate these data are shown above each representation of the ciliary transition zone. Each transition zone schematic indicates of the composition of the identified ciliary proteins and their interaction networks in this sub-compartment. Pink dot indicates transition zone ciliary components identified by different studies; a double violet line indicates a genetic interaction; a black line indicates a biochemical interaction identified by co-immunoprecipitation assay; a dashed line indicates a biochemical interaction identified by a TAP/MS assay; a grey oval indicates two grouped modules. For the Lambacher et al. (2016) study, the grey box indicates co-evolution relationships between MKS components using differential Dollo parsimony and the green triangle indicates a phylogenetically-conserved role for *C. elegans* TMEM107 in organising an MKS submodule with TMEM231 and TMEM17. Published studies are: Sang et al. 2011, Garcia- Gonzalo et al. 2011, Williams et al. 2011, Huang et al. 2011; Chih et al. 2011, Gupta et al. 2015, Lambacher et al. 2016 and Li et al. 2016. Findings from the current project (2020) are summarized in the lowest schematic.

6.5 Final remarks

As highlighted throughout this project, this research aimed to understand and identify the relationship between many of the disease-related ciliary transition zone genes that are mutated in this group of ciliopathies. This project has developed an approach to combining complementary methods of functional genomics with proteomics in order to gain new insights into the function of the ciliary transition zone sub-compartment. This approach has demonstrated that TMEM67, RPGRIP1L and CEP290 are essential for assembly of cilia compartments in mouse ciliated mIMCD-3 cells. They also interact, at genetic and biochemical levels, with other proteins in the transition zone including IFT88, TMEM17, TMEM231, TMEM138 and TMEM237. These studies suggest that the selected ciliary proteins work together as a complex or a series of potentially interlocking complexes.

Individually, each of these proteins is located within MKS/JBTS complexes that transduce Sonic Hedgehog and probably other ciliary-related signalling events. The specificity in localization and function of these proteins indicate that they are fundamental to mediating these processes. However, there is little insight into the mechanistic detail of these processes and there must be significant effort invested into system biology approaches (for example, affinity proteomic and reverse-genetics screens, super-resolution microscopy/(STORM) and cellular cryoEM approaches) to understand the relevance of transition zone proteins for ciliogenesis and the pathomechanisms of ciliopathies. For

example, in the future if "Affimer" artificial binding reagents were generated for TMEM67 or other selected TMEMs, these could be used as direct replacements for antibodies. Affimers, because of their smaller size, are useful for super resolution microscopy studies of intracellular signalling and the interactions of extracellular receptors, as well as the overall organization and localization of ciliary transition zone proteins. As an example of this approach, Shi et al. (2017) indicated that NPHP1, TMEM231, and RPGRIP1L form nested rings comprised of nine- fold doublets using super-resolution microscopy.

In a further recent advance using cryoelectron tomography (cryoET), SunSun et al. (2019) determined the architecture of primary cilia on epithelial kidney cells (the LLC-PK1 and mIMCD-3 cell-lines). Surprisingly, this data demonstrated that the architecture of primary cilia differed extensively from the commonly acknowledged 9+0 paradigm (Sun et al., 2019). It seems likely that 3D structural studies and mapping the organization of the ciliary transition zone will reveal further surprises and provide new exciting insights into the functional roles of TMEMs in cilia formation and maintenance.

Appendix A

A.1 Ethical Approval

The Leeds Teaching Hospitals NHS
NHS Trust

Ref: Amanda Burd

29/04/2011

Research & Development

Leeds Teaching Hospitals NHS Trust
34 Hyde Terrace
Leeds
LS2 9LN

Dr Colin A. Johnson

Section of Ophthalmology and Neurosciences,
Wellcome Trust Brenner Bui
Leeds Institute of Molecular Medicine,
St. James's University Hospital
LS9 7TF

Tel: 0113 392 2878
Fax: 0113 392 6397

r&d@leedsth.nhs.uk
www.leedsth.nhs.uk

Dear Dr Johnson

Re: NHS Permission at LTHT for: Molecular genetic investigations of autosomal recessive conditions
LTHT R&D Number: CG11/9764 (53788/WY)
REC: 11/H1310/1

I confirm that *NHS Permission for research* has been granted for this project at The Leeds Teaching Hospitals NHS Trust (LTHT). NHS Permission is granted based on the information provided in the documents listed below. All amendments (including changes to the research team) must be submitted in accordance with guidance in IRAS. Any change to the status of the project must be notified to the R&D Department.

Permission is granted on the understanding that the study is conducted in accordance with the *Research Governance Framework for Health and Social Care*, ICH GCP (if applicable) and NHS Trust policies and procedures available at http://www.leedsth.nhs.uk/sites/research_and_development/.

This permission is granted only on the understanding that you comply with the requirements of the *Framework* as listed in the attached sheet "Conditions of Approval".

If you have any queries about this approval please do not hesitate to contact the R&D Department on telephone 0113 392 2878.

Indemnity Arrangements

Chairman Mike Collier CBE   Chief Executive Maggie Boyle

The Leeds Teaching Hospitals incorporating:
Chapel Allerton Hospital   Leeds Dental Institute   Seacroft Hospital
St James's University Hospital   The General Infirmary at Leeds   Wharfedale Hospital

The Leeds Teaching Hospitals NHS Trust participates in the NHS risk pooling scheme administered by the NHS Litigation Authority 'Clinical Negligence Scheme for NHS Trusts' for: (i) medical professional and/or medical malpractice liability; and (ii) general liability. NHS Indemnity for negligent harm is extended to researchers with an employment contract (substantive or honorary) with the Trust. The Trust only accepts liability for research activity that has been managerially approved by the R&D Department.

The Trust therefore accepts liability for the above research project and extends indemnity for negligent harm to cover you as investigator and the researchers listed on the Site Specific Information form. Should there be any changes to the research team please ensure that you inform the R&D Department and that s/he obtains an appropriate contract, or letter of access, with the Trust if required.

Yours sincerely

Dr D R Norfolk
Associate Director of R&D

Approved documents
The documents reviewed and approved are listed as follows

Document	Version	Date of document
NHS R&D Form	3.1	02/03/2011
SSI Form	3.1	08/03/2011
Directorate Approval		08/03/2011
Radiology Approval		N/A
Pharmacy Approval		N/A
Protocol	1.0	14/12/2010
REC Letter confirming favourable opinion		18/02/2011
Evidence of Insurance		Not dated
Patient information sheet (REC Approved) Parent	2.0	08/02/2011
Patient information sheet (REC Approved) 8/younger URDU	1.0	14/12/2010
Patient information sheet (REC Approved) Parent URDU	1.0	14/12/2010
Patient information sheet (REC Approved) 12-15 yrs	2.0	08/02/2011
PIS (REC Approved) Adult relatives/young Person	2.0	08/02/2011
PIS (REC Approved) Children aged 8 or younger	1.0	14/12/2010
PIS (REC Approved) Children aged 8 – 12 years	1.0	14/12/2010
Informed Consent (REC Approved) Assent older children	1.0	14/12/2010
Letter of Invitation to participants (REC Approved)	1.0	14/12/2010

Conditions of NHS Permission for Research:

- Permission from your Directorate must be obtained before starting the study.

- Favourable Opinion of the appropriate Research Ethics Committee, where necessary, must be obtained before starting the study.

- Arrangements must be made to ensure that all members of the research team, where applicable, have employment contracts with the Trust (either full or honorary).

- Agreements must be in place with appropriate support departments regarding the services required to undertake the project and arrangements must be in place to recompense them for the costs of their services.

- Arrangements must be in place for the management of financial and other resources provided for the study, including intellectual property arising from the work.

- Priority should be given at all times to the dignity, rights, safety and well being of participants in the study

- Healthcare staff should be suitably informed about the research their patients are taking part in and information specifically relevant to their care arising from the study should be communicated promptly.

- Each member of the research team must be qualified by education, training and experience to discharge his/her role in the study. Students and new researchers must have adequate supervision, support and training.

- The research must follow the protocol approved by the relevant research ethics committee. Any proposed amendments to or deviations from the protocol must be submitted for review by the Research Ethics Committee, the research sponsor, regulatory authority and any other appropriate body. The R&D Department should be informed where the amendment has resource implications within the Directorate and the Directorate research lead/clinical director notified.

- Adverse Events in clinical trials of investigational medicinal products must be reported in accordance with the Medicines for Human Use (Clinical Trials) Regulations 2004.

- Complete and return Study Status Reports, when requested, to the R&D Department within 28 days of receipt as requested. (NB Failure to comply to such request with the requirement will lead to suspension of NHS Permission.)

- Procedures should be in place to ensure collection of high quality, accurate data and the integrity and confidentiality of data during processing and storage.

- Arrangements must be made for the appropriate archiving of data when the research has finished. Records must normally be kept for 15 years.

- All data and documentation associated with the study must be available for audit at the request of the appropriate auditing authority. Projects are randomly selected for audit by the R&D Department. You will be informed by letter if your study is selected.

- Findings from the study should be disseminated promptly and fed back as agreed to research participants.

- Findings from the study should be exposed to critical review through accepted scientific and professional channels.

- All members of the research team must ensure that the process of informed consent adheres to the standards GCP outlined in the UK Clinical Trials Regulations. Investigators are directed to the R&D website for further information and training availability.

- Where applicable, this NHS Permission includes aspects of the study previously covered by the NRES Site Specific Assessment (SSA) process.

Commercially Sponsored Trials

If the study is commercially sponsored, NHS Permission is given subject to provision of the following documents.

- Clinical Trials Agreement - agreed and signed off by the R&D Department (on behalf of the Leeds Teaching Hospitals NHS Trust) and the Sponsor. Investigators do not have the authority to sign contract on behalf of the Trust.

- Indemnity agreement, if not included in the Clinical Trials Agreement- (standard ABPI no fault arrangements apply) signed by the R&D Department and the Sponsor

It is essential that all the responsibilities set out in the Research Governance Framework, including those outlined above are fulfilled. The Trust reserves the right to withdraw NHS Permission where the above criteria are not being met. The Trust will not accept liability for any activity where NHS Permission has not been granted.

Carbon Copy: (PI) Dr Eamonn Sheridan

NHS

National Research Ethics Service

South Yorkshire Research Ethics Committee
Millside
Mill Pond Lane
Meanwood
Leeds
LS6 4RA

Telephone: 0113 305 0128

18 February 2011

Prof Colin A Johnson
Professor of Medical & Molecular Genetics
Section of Ophthalmology and Neuroscience
Leeds Inst of Molecular Medicine
St James University Hospital
Leeds LS9 7TF

Dear Prof Johnson

Study Title:	**Molecular genetic investigations of autosomal recessive conditions**
REC reference number:	**11/H1310/1**

Thank you for your letter of 8th February 2011, responding to the Committee's request for further information on the above research and submitting revised documentation.

The further information has been considered on behalf of the Committee by the Chair.

Confirmation of ethical opinion

On behalf of the Committee, I am pleased to confirm a favourable ethical opinion for the above research on the basis described in the application form, protocol and supporting documentation as revised, subject to the conditions specified below.

Ethical review of research sites

The favourable opinion applies to all NHS sites taking part in the study, subject to management permission being obtained from the NHS/HSC R&D office prior to the start of the study (see "Conditions of the favourable opinion" below).

Conditions of the favourable opinion

The favourable opinion is subject to the following conditions being met prior to the start of the study.

Management permission or approval must be obtained from each host organisation prior to the start of the study at the site concerned.

For NHS research sites only, management permission for research ("R&D approval") should be obtained from the relevant care organisation(s) in accordance with NHS research governance arrangements. Guidance on applying for NHS permission for research is available in the Integrated Research Application System or at http://www.rdforum.nhs.uk.

This Research Ethics Committee is an advisory committee to the Yorkshire and The Humber Strategic Health Authority
The National Research Ethics Service (NRES) represents the NRES Directorate within
the National Patient Safety Agency and Research Ethics Committees in England

Where the only involvement of the NHS organisation is as a Participant Identification Centre (PIC), management permission for research is not required but the R&D office should be notified of the study and agree to the organisation's involvement. Guidance on procedures for PICs is available in IRAS. Further advice should be sought from the R&D office where necessary.

Sponsors are not required to notify the Committee of approvals from host organisations.

It is the responsibility of the sponsor to ensure that all the conditions are complied with before the start of the study or its initiation at a particular site (as applicable).

Approved documents

The final list of documents reviewed and approved by the Committee is as follows:

Document	Version	Date
Investigator CV	1	14 December 2010
Covering Letter		08 February 2011
Letter from Sponsor		
REC application		14 December 2010
Response to Request for Further Information		
Participant Information Sheet: for children, aged 8 years or younger (Mirpuri Urdu translation)	1	14 December 2010
Evidence of insurance or indemnity		
Participant Information Sheet: Children aged 12 - 15 years	2	08 February 2011
Letter of invitation to participant	1	14 December 2010
Participant Information Sheet: for parents (Mirpuri Urdu translation)	1	14 December 2010
Participant Information Sheet: Relatives that are adults or young persons	2	08 February 2011
Participant Information Sheet: for children aged 8 year or younger	1	14 December 2010
Participant Information Sheet: Parents	2	08 February 2011
Participant Information Sheet: for children aged 8-12 years	1	14 December 2010
Participant Consent Form: Assent form for older children	1	14 December 2010
Protocol	1	14 December 2010

Statement of compliance

The Committee is constituted in accordance with the Governance Arrangements for Research Ethics Committees (July 2001) and complies fully with the Standard Operating Procedures for Research Ethics Committees in the UK.

After ethical review

Now that you have completed the application process please visit the National Research Ethics Service website > After Review

You are invited to give your view of the service that you have received from the National Research Ethics Service and the application procedure. If you wish to make your views known please use the feedback form available on the website.

The attached document *"After ethical review – guidance for researchers"* gives detailed guidance on reporting requirements for studies with a favourable opinion, including:

- Notifying substantial amendments
- Adding new sites and investigators
- Progress and safety reports
- Notifying the end of the study

The NRES website also provides guidance on these topics, which is updated in the light of changes in reporting requirements or procedures.

We would also like to inform you that we consult regularly with stakeholders to improve our service. If you would like to join our Reference Group please email referencegroup@nres.npsa.nhs.uk.

| 11/H1310/1 | Please quote this number on all correspondence |

With the Committee's best wishes for the success of this project

Yours sincerely

Ms Jo Abbott
Chair

Email: Sinead.audsley@leedspft.nhs.uk

Enclosures: "After ethical review – guidance for researchers"

Copy to: Mrs Rachel E de Souza, University of Leeds
                Mrs Anne Gowing, Leeds Teaching Hospitals NHS Trust

A.2 Primer sequences

Primer sequences used in this chapter. Primer sequences were checked using a BLAST tool (http://blast.ncbi.nlm.nih.gov/Blast) to ensure specific binding and avoidance of SNPs. Primers covered the open reading frames including the protein-coding exons for *TMEM17* (NM_198276.3) and *TMEM218 (NM_001258241.2)*. Primers were ordered from Sigma-Aldrich.

Primer	Sequence 5'-3'
TMEM17 exon1 Fw	GGAACCACGGAGCCTCG
TMEM17 exon1 Rv	TAGGTACGGGCAAATTCTGG
TMEM17 exon2-3 Fw	AAAATTTGGTGTTTTACTGAGCC
TMEM17 exon2-3 Rv	CTGTGCTCTTTCTGCCACAC
TMEM17 exon4 Fw	TTGGAATCACTCACAGAGCC
TMEM17 exon4 Rv	AACACTTGCTTTGTCCCTTTTC

Primer	Sequence 5'-3'
TMEM218 exon6 Fw	TAAGGGACTCTGGGACTGGA
TMEM218 exon6 Rv	TGTTTAGTGAGCATCAGCGA
TMEM218 exon7 Fw	GGAAGAGACTGTCCAGACCTAA
TMEM218 exon7 Rv	GACGGATGTGCAGACCAA
TMEM218 exon8 Fw	CCCACTCATCATGGAGTTCA
TMEM218 exon8 Rv	TAGTGCCTTCCTGCTCATCA

A.3 Examples of high and poor-quality Sanger sequences

Example 1: A high quality sequence with accurate base-called (Raw data were collected on an electronic .zip folder (see supplement 1).
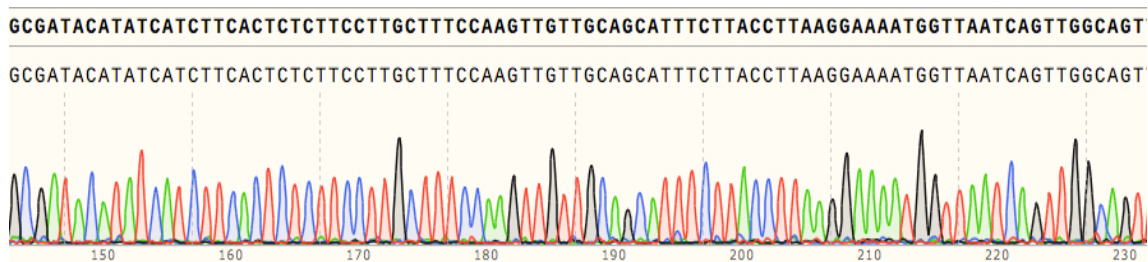
Example 2: Poor quality sequence, for which samples were excluded or re-sequenced (Raw data were collected on an electronic .zip folder (see supplement 1).
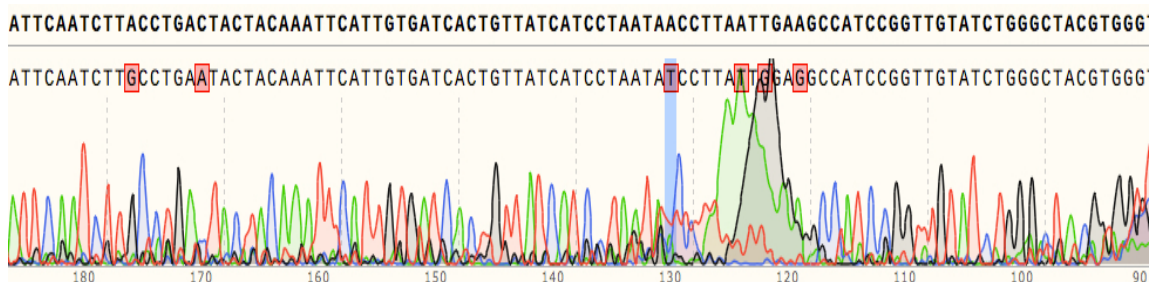
Appendix B

B.1 Examples of the expression vectors generated in this study using TAP_GW331.
Representation of the N-terminal TAP TMEM138, TMEM216, and TMEM237 constructs, respectively. The TMEM genes are shown in pink. Restriction enzyme sites are shown by grey lines. Images adapted from SnapGene (http://www.snapgene.com).

B.1.1: N-TAP_GW331/TMEM138
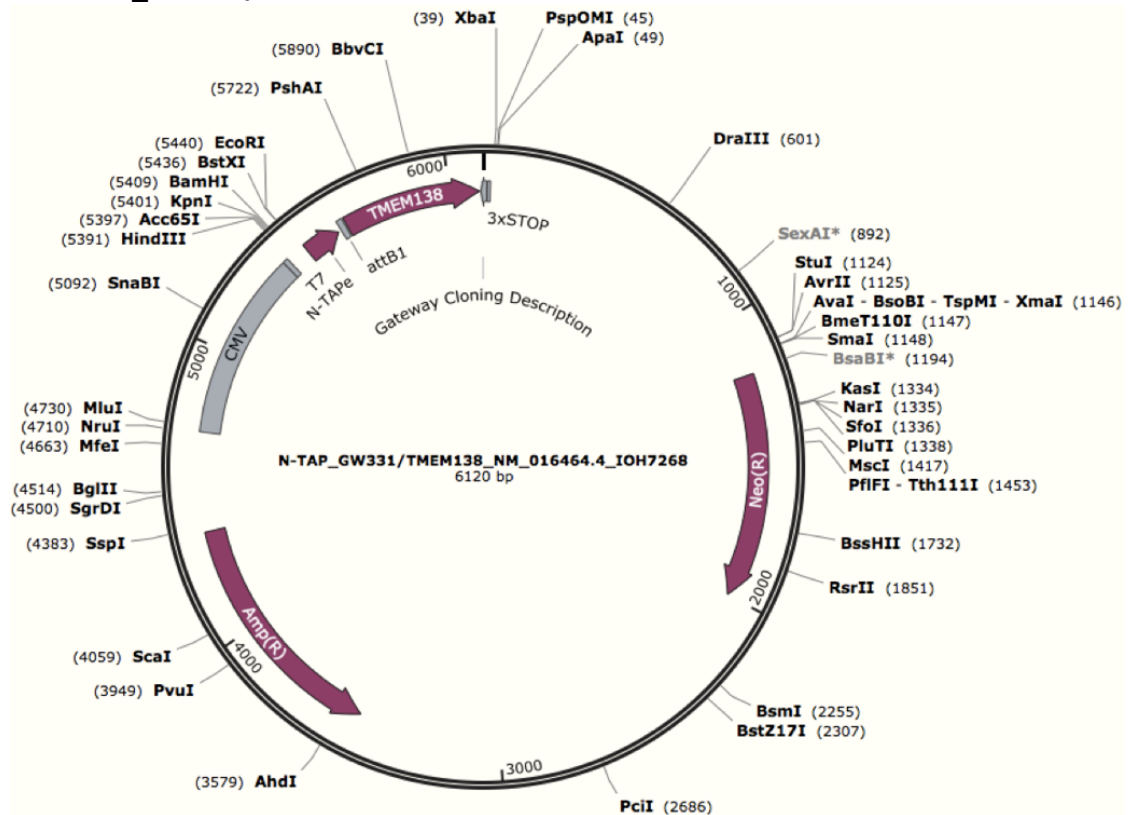
B.1.2: N-TAP_GW331/TMEM216
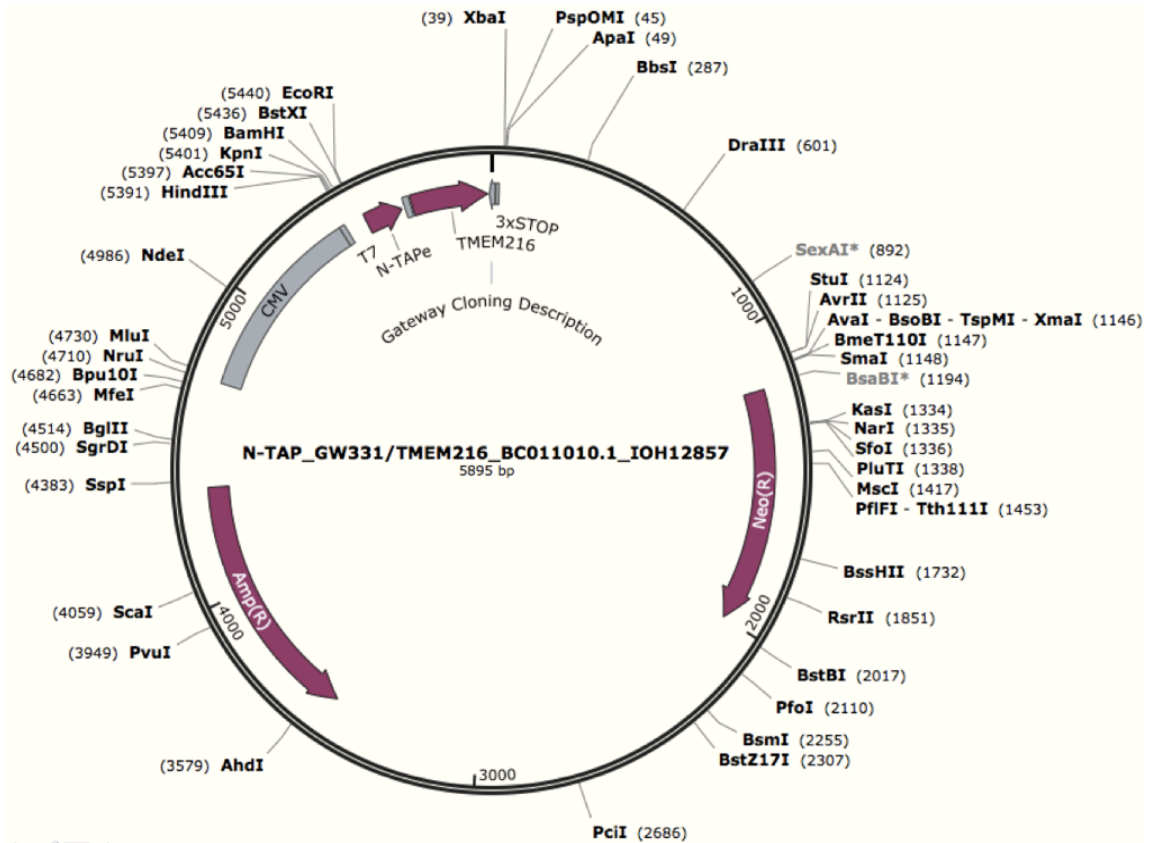
B.1.3: N-TAP_GW331/TMEM237

B.2 Sequencing Primers

List of forward (Fw) and reverse (Rv) universal primer sequences used in this study.

Name	Primer sequence
T7	TAA-TAC-GAC-TCA-CTA-TAG-GG
SP6	ATT-TAG-GTG-ACA-CTA-TAG
M13 Fw	TGT-AAA-ACG-ACG-GCC-AGT
M13 Rv	CAG-GAA-ACA-GCT-ATG-ACC
BGH	TAG-AAG-GCA-CAG-TCG-AGG

B.3 MS results

B.3.1: protein list from experiment 1. (Raw data were collected on an electronic .zip folder (see supplement 2).

Protein Group	Protein ID	Accession	-10lgP	Coverage (%)	#Peptides	#Unique	PTM	Avg. Mass	Description
1	257	sp|P02769|ALBU_BOVIN	211.63	46	28	17	Y	69294	Serum albumin OS=Bos taurus GN=ALB PE=1 SV=4
4	258	sp|P14639|ALBU_SHEEP	166.89	18	11	1	Y	69188	Serum albumin OS=Ovis aries GN=ALB PE=2 SV=1
2	2446	sp|P12763|FETUA_BOVIN	156.02	42	12	12	Y	38419	Alpha-2-HS-glycoprotein OS=Bos taurus GN=AHSG PE=1 SV=2
3	2370	sp|Q29443|TRFE_BOVIN	146.25	14	7	6	Y	77753	Serotransferrin OS=Bos taurus GN=TF PE=2 SV=1
8	276	sp|A6YF56|ALBU_MESAU	64.55	4	2	0	Y	68226	Serum albumin OS=Mesocricetus auratus GN=ALB PE=1 SV=1
6	4108	sp|Q3SZR3|A1AG_BOVIN	63.19	11	2	2	N	23182	Alpha-1-acid glycoprotein OS=Bos taurus GN=ORM1 PE=2 SV=1
7	287	sp|P02770|ALBU_RAT	61.88	2	1	0	Y	68731	Serum albumin OS=Rattus norvegicus GN=Alb PE=1 SV=2
5	4107	sp|Q9DBD0|ICA_MOUSE	58.00	2	1	0	Y	76766	Inhibitor of carbonic anhydrase OS=Mus musculus GN=Ica PE=1 SV=1
9	168	sp|P00761|TRYP_PIG	33.67	0	0	0	N	24409	Trypsin OS=Sus scrofa PE=1 SV=1
10	2387	sp|P34955|A1AT_BOVIN	27.54	0	0	0	N	46104	Alpha-1-antiproteinase OS=Bos taurus GN=SERPINA1 PE=1 SV=1
10	2386	sp|P12725|A1AT_SHEEP	27.54	0	0	0	N	45985	Alpha-1-antiproteinase OS=Ovis aries PE=1 SV=1
11	2761	sp|Q58D62|FETUB_BOVIN	24.72	0	0	0	N	42663	Fetuin-B OS=Bos taurus GN=FETUB PE=2 SV=1
14	4111	sp|P00974|BPT1_BOVIN	21.78	0	0	0	N	10903	Pancreatic trypsin inhibitor OS=Bos taurus PE=1 SV=2
23	6899	sp|Q96553-2|C1TC_DROME	20.85	0	0	0	N	99627	Isoform A of C-1-tetrahydrofolate synthase, cytoplasmic OS=Drosophila melanogaster GN=pug
15	6885	sp|P43304|GPDM_HUMAN	20.22	0	0	0	N	80853	Glycerol-3-phosphate dehydrogenase, mitochondrial OS=Homo sapiens GN=GPD2 PE=1 SV=3

total 15 proteins

B.3.2: Table 1: MS results following affinity purification of Nt-TMNEM67. Only proteins that were identified in experiments 1 and 2 are listed. (Raw data were collected on an electronic .zip folder (see supplement 2).

Protein ID description	Accession number	MW	#Peptides (experiment 1)	#Peptides (experiment 2)
Nucleobindin-1 OS=Homo sapiens GN=NUCB1 PE=1 SV=4	Q02818	53879	17	11
Pyruvate kinase PKM OS=Homo sapiens GN=PKM PE=1 SV=4	P14618	57937	9	16
Heterogeneous nuclear ribonucleoprotein L OS=Homo sapiens GN=HNRNPL PE=1 SV=2	P14866	64133	4	6
Elongation factor 2 OS=Homo sapiens GN=EEF2 PE=1 SV=4	P13639	95338	2	6

Appendix C

Table C.1: Proteins associated with peptides pulled-down in a TAP experiment, identified by mass spectrometry, including Nt-TAP-TMEM17 constructs biological replicates (rep.) n=4, Nt-TAP-TMEM138 (n=2), Nt-TAP-TMEM216 (n=1), Nt-TAP-TMEM231 (n=1), and Nt-TAP-TMEM237 (n=1). A table to show the full mass-spectrometry results demonstrating the pulled down proteins and number of peptides associated. Some cilia related proteins interactions are highlighted in green. (Raw data were collected on an electronic .zip folder (see supplement 2).

Protein ID description	Accession number	MW	TMEM17				TMEM67	TMEM138		TMEM216	TMEM231	TMEM237
			#Peptides (rep. 1)	#Peptides (rep. 2)	#Peptides (rep.3)	#Peptides (rep. 4)	#Peptides (rep.1)	#Peptides (rep.1)	#Peptides (rep. 2)	#Peptides (rep.1)	#Peptides (rep.1)	#Peptides (rep.1)
Tubulin beta chain OS=Homo sapiens GN=TUBB PE=1 SV=2	P07437	50 kDa	2	17	14	0	0	15	0	0	8	2
Actin, cytoplasmic 1 OS=Homo sapiens GN=ACTB PE=1 SV=1	P60709	42 kDa	4	5	16	0	0	8	0	0	2	0
78 kDa glucose-regulated protein OS=Homo sapiens GN=HSPA5 PE=1 SV=2	P11021	72 kDa	0	2	11	0	0	5	0	0	0	2
Tubulin alpha-1B chain OS=Homo sapiens GN=TUBA1B PE=1 SV=1	P68363	50 kDa	0	15	12	11	0	9	0	0	5	0
Elongation factor 1-alpha 1 OS=Homo sapiens GN=EEF1A1 PE=1 SV=1	P68104	50 kDa	2	5	11	0	0	10	0	0	2	2
Heat shock 70 kDa protein 1A/1B OS=Homo sapiens GN=HSPA1A PE=1 SV=5	P08107	70 kDa	2	2	13	15	0	8	0	0	2	0
Transmembrane protein 17 OS=Homo sapiens GN=TMEM17 PE=2 SV=2	**Q86X19**	**23 kDa**	**4**	**4**	**3**	**3**	**0**	**0**	**0**	**0**	**0**	**2**
Polyubiquitin-B OS=Homo sapiens GN=UBB PE=1 SV=1	P0CG47	26 kDa	2	2	2	2	0	3	0	0	0	0
Haptoglobin OS=Homo sapiens GN=HP PE=1 SV=1	P00738	45 kDa	2	0	0	0	0	0	2	2	2	2
GTP-binding nuclear protein Ran OS=Homo sapiens GN=RAN PE=1 SV=3	P62826	24 kDa	3	0	3	0	0	0	0	0	0	0
Sodium/potassium-transporting ATPase subunit alpha-1 OS=Homo sapiens GN=ATP1A1 PE=1 SV=1	P05023	113 kDa	2	0	3	2	0	0	0	0	0	0
40S ribosomal protein S18 OS=Homo sapiens GN=RPS18 PE=1 SV=3	P62269	18 kDa	2	2	2	3	0	0	0	0	0	0
transport protein Sec61 subunit alpha isoform 1 OS=Homo sapiens GN=SEC61A1 PE=1 SV=2	P61619	52 kDa	3	0	0	2	0	0	0	0	0	0
Collagen alpha-1(I) chain OS=Homo sapiens GN=COL1A1 PE=1 SV=5	P02452	139 kDa	2	0	0	0	0	0	0	2	0	0
Histone H2B type 1-J OS=Homo sapiens GN=HIST1H2BJ PE=1 SV=3	P06899	14 kDa	0	6	4	0	0	7	0	0	0	0
Heterogeneous nuclear ribonucleoprotein U OS=Homo sapiens GN=HNRNPU PE=1 SV=6	Q00839	91 kDa	0	8	4	0	0	6	0	0	0	0
ATP synthase subunit alpha, mitochondrial OS=Homo sapiens GN=ATP5A1 PE=1 SV=1	P25705	60 kDa	0	3	16	0	0	0	0	0	0	0
Histone H4 OS=Homo sapiens GN=HIST1H4A PE=1 SV=2	P62805	11 kDa	0	6	2	7	0	7	0	0	0	0
Heat shock cognate 71 kDa protein OS=Homo sapiens GN=HSPA8 PE=1 SV=1	P11142	71 kDa	0	5	14	0	0	6	0	0	0	0

Protein	Accession	Mass									
Pre-mRNA-processing-splicing factor 8 OS=Homo sapiens GN=PRPF8 PE=1 SV=2	**Q6P2Q9**	**274 kDa**	**0**	**58**	**2**	**7**	**0**	**0**	**0**	**0**	**0**	**0**
Poly [ADP-ribose] polymerase 1 OS=Homo sapiens GN=PARP1 PE=1 SV=4	P09874	113 kDa	0	7	3	3	0	11	0	0	0	0
Histone H1.2 OS=Homo sapiens GN=HIST1H1C PE=1 SV=2	P16403	21 kDa	0	6	2	0	0	9	0	0	0	0
Histone H2A.Z OS=Homo sapiens GN=H2AFZ PE=1 SV=2	P0C0S5	14 kDa	0	3	2	4	0	3	0	0	0	0
Histone H3.1 OS=Homo sapiens GN=HIST1H3A PE=1 SV=2	P68431 (+3)	15 kDa	0	3	2	0	0	3	0	0	0	0
Nucleophosmin OS=Homo sapiens GN=NPM1 PE=1 SV=2	P06748	33 kDa	0	7	5	4	0	6	0	0	0	0
Polyubiquitin-B OS=Homo sapiens GN=UBB PE=1 SV=1	P0CG47 (+3)	26 kDa	0	2	0	2	0	0	0	0	0	0
Heterogeneous nuclear ribonucleoproteins C1/C2 OS=Homo sapiens GN=HNRNPC PE=1 SV=4	P07910	34 kDa	0	4	0	4	0	2	0	0	0	0
Heterogeneous nuclear ribonucleoprotein M OS=Homo sapiens GN=HNRNPM PE=1 SV=3	P52272	78 kDa	0	2	6	6	0	0	0	0	0	0
40S ribosomal protein S4, X isoform OS=Homo sapiens GN=RPS4X PE=1 SV=2	P62701	30 kDa	0	5	0	3	0	4	0	0	0	0
Lamina-associated polypeptide 2, isoforms beta/gamma OS=Homo sapiens GN=TMPO PE=1 SV=2	P42167	51 kDa	0	2	3	0	0	0	0	0	0	0
Histone H2B type 1-K OS=Homo sapiens GN=HIST1H2BK PE=1 SV=3	O60814(+7)	14 kDa	0	2	2	0	0	2	0	0	0	0
Tubulin beta-4B chain OS=Homo sapiens GN=TUBB4B PE=1 SV=1	P68371	50 kDa	0	2	3	0	0	2	0	0	0	0
Ig kappa chain V-I region Lay OS=Homo sapiens PE=1 SV=1	P01605	12 kDa	0	2	0	0	0	0	0	2	0	0
Reticulocalbin-2 OS=Homo sapiens GN=RCN2 PE=1 SV=1	Q14257	37 kDa	0	2	0	0	0	0	0	0	0	0
60S ribosomal protein L4 OS=Homo sapiens GN=RPL4 PE=1 SV=5	P36578	48 kDa	0	3	0	0	0	0	0	0	0	0
RuvB-like 1 OS=Homo sapiens GN=RUVBL1 PE=1 SV=1	Q9Y265	50 kDa	0	2	5	3	0	0	0	0	0	0
60S ribosomal protein L7 OS=Homo sapiens GN=RPL7 PE=1 SV=1	P18124	29 kDa	0	3	2	2	0	0	0	0	0	0
40S ribosomal protein S2 OS=Homo sapiens GN=RPS2 PE=1 SV=2	P15880	31 kDa	0	2	0	3	0	0	0	0	0	0
CAD protein OS=Homo sapiens GN=CAD PE=1 SV=3	P27708	243 kDa	0	6	0	0	0	0	0	0	0	0
40S ribosomal protein S8 OS=Homo sapiens GN=RPS8 PE=1 SV=2	P62241	24 kDa	0	2	2	0	0	2	0	0	0	0
Histone H1.0 OS=Homo sapiens GN=H1F0 PE=1 SV=3	P07305	21 kDa	0	2	0	0	0	3	0	0	0	0
60S ribosomal protein L8 OS=Homo sapiens GN=RPL8 PE=1 SV=2	P62917	28 kDa	0	2	3	2	0	0	0	0	0	0
60S ribosomal protein L3 OS=Homo sapiens GN=RPL3 PE=1 SV=2	P39023	46 kDa	0	2	0	0	0	2	0	0	0	0
ATP-dependent RNA helicase A OS=Homo sapiens GN=DHX9 PE=1 SV=4	Q08211	141 kDa	0	2	0	5	0	0	0	0	0	0

Protein	Accession	Mass									
40S ribosomal protein S3a OS=Homo sapiens GN=RPS3A PE=1 SV=2	P61247	30 kDa	0	2	0	2	0	0	0	0	0	0
60S ribosomal protein L15 OS=Homo sapiens GN=RPL15 PE=1 SV=2	P61313	24 kDa	0	2	0	2	0	0	0	0	0	0
60S ribosomal protein L23 OS=Homo sapiens GN=RPL23 PE=1 SV=1	P62829	15 kDa	0	2	2	0	0	0	0	0	0	0
Transcription factor A, mitochondrial OS=Homo sapiens GN=TFAM PE=1 SV=1	Q00059	29 kDa	0	2	0	0	0	2	0	0	0	0
Serine/arginine-rich splicing factor 7 OS=Homo sapiens GN=SRSF7 PE=1 SV=1	Q16629	27 kDa	0	2	0	0	0	0	0	0	0	0
E3 ubiquitin-protein ligase TRIM21 OS=Homo sapiens GN=TRIM21 PE=1 SV=1	P19474	54 kDa	0	5	0	0	0	0	0	0	0	0
60S ribosomal protein L18 OS=Homo sapiens GN=RPL18 PE=1 SV=2	Q07020	22 kDa	0	2	0	0	0	0	0	0	0	0
60S ribosomal protein L19 OS=Homo sapiens GN=RPL19 PE=1 SV=1	P84098	23 kDa	0	2	0	0	0	0	0	0	0	0
Multiple PDZ domain protein OS=Homo sapiens GN=MPDZ PE=1 SV=2	O75970	222 kDa	0	2	0	0	0	0	0	0	0	0
60S ribosomal protein L10 OS=Homo sapiens GN=RPL10 PE=1 SV=4	P27635	25 kDa	0	2	0	4	0	0	0	0	0	0
Ig kappa chain V-II region RPMI 6410 OS=Homo sapiens PE=4 SV=1	P06310	15 kDa	0	0	0	0	0	0	0	0	2	2
Glyceraldehyde-3-phosphate dehydrogenase OS=Homo sapiens GN=GAPDH PE=1 SV=3	P04406	36 kDa	0	0	0	0	0	8	0	0	3	0
Calnexin OS=Homo sapiens GN=CANX PE=1 SV=2	P27824	68 kDa	0	0	4	3	0	0	0	0	5	0
Transmembrane protein 231 OS=Homo sapiens GN=TMEM231 PE=1 SV=1	**Q9H6L2**	**36 kDa**	**0**	**0**	**0**	**0**	**0**	**0**	**0**	**0**	**10**	**0**
Iron-responsive element-binding protein 2 OS=Homo sapiens GN=IREB2 PE=1 SV=3	P48200	105 kDa	0	0	0	0	0	0	0	0	2	0
Ig kappa chain V-I region Lay OS=Homo sapiens PE=1 SV=1	P01605	12 kDa	0	0	0	0	0	0	0	0	2	2
Transmembrane protein 237 OS=Homo sapiens GN=TMEM237 PE=1 SV=2	**Q96Q45**	**46 kDa**	**0**	**0**	**0**	**0**	**0**	**0**	**0**	**0**	**0**	**9**
Hemopexin OS=Homo sapiens GN=HPX PE=1 SV=2	P02790	52 kDa	0	0	0	0	0	0	2	0	0	2
Filaggrin-2 OS=Homo sapiens GN=FLG2 PE=1 SV=1	Q5D862	248 kDa	0	0	0	0	0	6	0	0	0	2
Ceruloplasmin OS=Homo sapiens GN=CP PE=1 SV=1	P00450	122 kDa	0	0	0	0	0	0	0	0	0	0
60 kDa heat shock protein, mitochondrial OS=Homo sapiens GN=HSPD1 PE=1 SV=2	P10809	61 kDa	0	0	4	10	0	28	0	0	0	0
Heat shock protein HSP 90-beta OS=Homo sapiens GN=HSP90AB1 PE=1 SV=4	P08238	83 kDa	0	0	18	0	0	10	0	0	0	0
Stress-70 protein, mitochondrial OS=Homo sapiens GN=HSPA9 PE=1 SV=2	P38646	74 kDa	0	0	18	0	0	0	0	0	0	0
Calnexin OS=Homo sapiens GN=CANX PE=1 SV=2	P27824	68 kDa	0	0	6	4	0	0	0	0	0	0
Vimentin OS=Homo sapiens GN=VIM PE=1 SV=4	P08670	54 kDa	0	0	17	6	0	3	0	0	0	0
Elongation factor 2 OS=Homo sapiens GN=EEF2 PE=1 SV=4	P13639	95 kDa	0	0	14	5	0	0	0	0	0	0

Protein	Accession	MW										
Alpha-enolase OS=Homo sapiens GN=ENO1 PE=1 SV=2	P06733	47 kDa	0	0	13	4	0	0	0	0	0	0
Heterogeneous nuclear ribonucleoprotein A1 OS=Homo sapiens GN=HNRNPA1 PE=1 SV=5	P09651	39 kDa	0	0	7	2	0	10	0	0	0	0
Splicing factor, proline- and glutamine-rich OS=Homo sapiens GN=SFPQ PE=1 SV=2	P23246	76 kDa	0	0	5	3	0	0	0	0	0	0
Transketolase OS=Homo sapiens GN=TKT PE=1 SV=3	P29401	68 kDa	0	0	3	0	0	0	0	0	0	0
Pyruvate kinase PKM OS=Homo sapiens GN=PKM PE=1 SV=4	P14618	58 kDa	0	0	14	2	0	8	0	0	0	0
Endoplasmin OS=Homo sapiens GN=HSP90B1 PE=1 SV=1	P14625	92 kDa	0	0	8	4	0	0	0	0	0	0
14-3-3 protein epsilon OS=Homo sapiens GN=YWHAE PE=1 SV=1	P62258	29 kDa	0	0	12	0	0	6	0	0	0	0
Plasminogen activator inhibitor 1 RNA-binding protein OS=Homo sapiens GN=SERBP1 PE=1 SV=2	Q8NC51	45 kDa	0	0	4	0	0	0	0	0	0	0
Elongation factor Tu, mitochondrial OS=Homo sapiens GN=TUFM PE=1 SV=2	P49411	50 kDa	0	0	3	4	0	3	0	0	0	0
Heterogeneous nuclear ribonucleoprotein H OS=Homo sapiens GN=HNRNPH1 PE=1 SV=4	P31943	49 kDa	0	0	7	5	0	3	0	0	0	0
Nucleolin OS=Homo sapiens GN=NCL PE=1 SV=3	P19338	77 kDa	0	0	8	6	0	12	0	0	0	0
Heterogeneous nuclear ribonucleoproteins A2/B1 OS=Homo sapiens GN=HNRNPA2B1 PE=1 SV=2	P22626	37 kDa	0	0	4	3	0	9	0	0	0	0
Protein disulfide-isomerase A3 OS=Homo sapiens GN=PDIA3 PE=1 SV=4	P30101	57 kDa	0	0	4	3	0	0	0	0	0	0
T-complex protein 1 subunit beta OS=Homo sapiens GN=CCT2 PE=1 SV=4	P78371	57 kDa	0	0	3	0	0	0	0	0	0	0
Pre-mRNA-processing factor 6 OS=Homo sapiens GN=PRPF6 PE=1 SV=1	**O94906**	**107 kDa**	**0**	**0**	**21**	**50**	**0**	**0**	**0**	**0**	**0**	**0**
High mobility group protein B1 OS=Homo sapiens GN=HMGB1 PE=1 SV=3	P09429	25 kDa	0	0	5	0	0	0	0	0	0	0
Prelamin-A/C OS=Homo sapiens GN=LMNA PE=1 SV=1	P02545	74 kDa	0	0	2	0	0	3	0	0	0	0
C-1-tetrahydrofolate synthase, cytoplasmic OS=Homo sapiens GN=MTHFD1 PE=1 SV=3	P11586	102 kDa	0	0	6	3	0	3	0	0	0	0
T-complex protein 1 subunit theta OS=Homo sapiens GN=CCT8 PE=1 SV=4	P50990	60 kDa	0	0	4	3	0	0	0	0	0	0
Tyrosine--tRNA ligase, cytoplasmic OS=Homo sapiens GN=YARS PE=1 SV=4	P54577	59 kDa	0	0	2	0	0	2	0	0	0	0
Transcription intermediary factor 1-beta OS=Homo sapiens GN=TRIM28 PE=1 SV=5	Q13263	89 kDa	0	0	3	0	0	0	0	0	0	0
Peptidyl-prolyl cis-trans isomerase A OS=Homo sapiens GN=PPIA PE=1 SV=2	P62937	18 kDa	0	0	6	3	0	0	0	0	0	0
Heat shock protein HSP 90-alpha OS=Homo sapiens GN=HSP90AA1 PE=1 SV=5	P07900	85 kDa	0	0	9	0	0	5	0	0	0	0
Glutamate dehydrogenase 1, mitochondrial OS=Homo sapiens GN=GLUD1 PE=1 SV=2	P00367	61 kDa	0	0	2	0	0	0	0	0	0	0
Fructose-bisphosphate aldolase A OS=Homo sapiens GN=ALDOA PE=1 SV=2	P04075	39 kDa	0	0	10	0	0	3	0	0	0	0
40S ribosomal protein S3 OS=Homo sapiens GN=RPS3 PE=1 SV=2	P23396	27 kDa	0	0	3	0	0	5	0	0	0	0
Nucleoside diphosphate kinase B OS=Homo sapiens GN=NME2 PE=1 SV=1	P22392	17 kDa	0	0	3	0	0	0	0	0	0	0

Protein	Accession	MW	1	2	3	4	5	6	7	8	9	10
T-complex protein 1 subunit gamma OS=Homo sapiens GN=CCT3 PE=1 SV=4	P49368	61 kDa	0	0	2	2	0	0	0	0	0	0
Transitional endoplasmic reticulum ATPase OS=Homo sapiens GN=VCP PE=1 SV=4	P55072	89 kDa	0	0	12	0	0	2	0	0	0	0
T-complex protein 1 subunit epsilon OS=Homo sapiens GN=CCT5 PE=1 SV=1	P48643	60 kDa	0	0	2	0	0	0	0	0	0	0
ADP/ATP translocase 2 OS=Homo sapiens GN=SLC25A5 PE=1 SV=7	P05141	33 kDa	0	0	5	8	0	3	0	0	0	0
T-complex protein 1 subunit delta OS=Homo sapiens GN=CCT4 PE=1 SV=4	P50991	58 kDa	0	0	3	2	0	0	0	0	0	0
Triosephosphate isomerase OS=Homo sapiens GN=TPI1 PE=1 SV=3	P60174	31 kDa	0	0	8	2	0	2	0	0	0	0
Creatine kinase B-type OS=Homo sapiens GN=CKB PE=1 SV=1	P12277	43 kDa	0	0	6	0	0	2	0	0	0	0
Peroxiredoxin-1 OS=Homo sapiens GN=PRDX1 PE=1 SV=1	Q06830	22 kDa	0	0	8	5	0	2	0	0	0	0
Exportin-2 OS=Homo sapiens GN=CSE1L PE=1 SV=3	P55060	110 kDa	0	0	3	4	0	0	0	0	0	0
Peroxiredoxin-2 OS=Homo sapiens GN=PRDX2 PE=1 SV=5	P32119	22 kDa	0	0	5	0	0	2	0	0	0	0
T-complex protein 1 subunit zeta OS=Homo sapiens GN=CCT6A PE=1 SV=3	P40227	58 kDa	0	0	5	0	0	0	0	0	0	0
ATP-dependent RNA helicase DDX1 OS=Homo sapiens GN=DDX1 PE=1 SV=2	Q92499	82 kDa	0	0	2	0	0	0	0	0	0	0
Prothymosin alpha OS=Homo sapiens GN=PTMA PE=1 SV=2	P06454	12 kDa	0	0	2	2	0	0	0	0	0	0
Ubiquitin-like modifier-activating enzyme 1 OS=Homo sapiens GN=UBA1 PE=1 SV=3	P22314	118 kDa	0	0	4	0	0	2	0	0	0	0
Malate dehydrogenase, mitochondrial OS=Homo sapiens GN=MDH2 PE=1 SV=3	P40926	36 kDa	0	0	5	0	0	0	0	0	0	0
Elongation factor 1-gamma OS=Homo sapiens GN=EEF1G PE=1 SV=3	P26641	50 kDa	0	0	8	2	0	0	0	0	0	0
Protein SET OS=Homo sapiens GN=SET PE=1 SV=3	Q01105	33 kDa	0	0	4	2	0	4	0	0	0	0
Phosphoglycerate kinase 1 OS=Homo sapiens GN=PGK1 PE=1 SV=3	P00558	45 kDa	0	0	6	0	0	0	0	0	0	0
Heterogeneous nuclear ribonucleoprotein K OS=Homo sapiens GN=HNRNPK PE=1 SV=1	P61978	51 kDa	0	0	9	4	0	2	0	0	0	0
Annexin A5 OS=Homo sapiens GN=ANXA5 PE=1 SV=2	P08758	36 kDa	0	0	3	0	0	7	0	0	0	0
D-3-phosphoglycerate dehydrogenase OS=Homo sapiens GN=PHGDH PE=1 SV=4	O43175	57 kDa	0	0	5	4	0	0	0	0	0	0
Carbonic anhydrase 2 OS=Homo sapiens GN=CA2 PE=1 SV=2	P00918	29 kDa	0	0	5	0	0	0	0	0	0	0
40S ribosomal protein SA OS=Homo sapiens GN=RPSA PE=1 SV=4	P08865	33 kDa	0	0	3	2	0	0	0	0	0	0
Complement component 1 Q subcomponent-binding protein, mitochondrial OS=Homo sapiens GN=C1QBP PE=1 SV=1	Q07021	31 kDa	0	0	3	3	0	0	0	0	0	0
Apoptosis-inducing factor 1, mitochondrial OS=Homo sapiens GN=AIFM1 PE=1 SV=1	O95831	67 kDa	0	0	3	0	0	0	0	0	0	0
RNA-binding protein FUS OS=Homo sapiens GN=FUS PE=1 SV=1	P35637	53 kDa	0	0	3	3	0	0	0	0	0	0
14-3-3 protein zeta/delta OS=Homo sapiens GN=YWHAZ PE=1 SV=1	P63104	28 kDa	0	0	3	0	0	3	0	0	0	0

Poly(rC)-binding protein 1 OS=Homo sapiens GN=PCBP1 PE=1 SV=2	Q15365	37 kDa	0	0	5	5	0	0	0	0	0	0
Proliferation-associated protein 2G4 OS=Homo sapiens GN=PA2G4 PE=1 SV=3	Q9UQ80	44 kDa	0	0	2	0	0	0	0	0	0	0
40S ribosomal protein S10 OS=Homo sapiens GN=RPS10 PE=1 SV=1	P46783	19 kDa	0	0	2	0	0	2	0	0	0	0
Profilin-1 OS=Homo sapiens GN=PFN1 PE=1 SV=2	P07737	15 kDa	0	0	4	3	0	0	0	0	0	0
L-lactate dehydrogenase B chain OS=Homo sapiens GN=LDHB PE=1 SV=2	P07195	37 kDa	0	0	7	7	0	0	0	0	0	0
Protein-L-isoaspartate(D-aspartate) O-methyltransferase OS=Homo sapiens GN=PCMT1 PE=1 SV=4	P22061	25 kDa	0	0	6	6	0	0	0	0	0	0
Peroxiredoxin-6 OS=Homo sapiens GN=PRDX6 PE=1 SV=3	P30041	25 kDa	0	0	6	0	0	0	0	0	0	0
Transgelin-2 OS=Homo sapiens GN=TAGLN2 PE=1 SV=3	P37802	22 kDa	0	0	3	2	0	0	0	0	0	0
L-lactate dehydrogenase A chain OS=Homo sapiens GN=LDHA PE=1 SV=2	P00338	37 kDa	0	0	4	2	0	0	0	0	0	0
Guanine nucleotide-binding protein subunit beta-2-like 1 OS=Homo sapiens GN=GNB2L1 PE=1 SV=3	P63244	35 kDa	0	0	3	0	0	2	0	0	0	0
Lamin-B1 OS=Homo sapiens GN=LMNB1 PE=1 SV=2	P20700	66 kDa	0	0	2	2	0	0	0	0	0	0
Thioredoxin-dependent peroxide reductase, mitochondrial OS=Homo sapiens GN=PRDX3 PE=1 SV=3	P30048	28 kDa	0	0	3	0	0	0	0	0	0	0
U1 small nuclear ribonucleoprotein 70 kDa OS=Homo sapiens GN=SNRNP70 PE=1 SV=2	P08621	52 kDa	0	0	2	0	0	0	0	0	0	0
Spliceosome RNA helicase DDX39B OS=Homo sapiens GN=DDX39B PE=1 SV=1	Q13838	49 kDa	0	0	2	0	0	0	0	0	0	0
14-3-3 protein beta/alpha OS=Homo sapiens GN=YWHAB PE=1 SV=3	P31946	28 kDa	0	0	2	0	0	0	0	0	0	0
Elongation factor 1-beta OS=Homo sapiens GN=EEF1B2 PE=1 SV=3	P24534	25 kDa	0	0	3	0	0	0	0	0	0	0
Protein arginine N-methyltransferase 5 OS=Homo sapiens GN=PRMT5 PE=1 SV=4	O14744	73 kDa	0	0	4	3	0	0	0	0	0	0
60S ribosomal protein L13 OS=Homo sapiens GN=RPL13 PE=1 SV=4	P26373	24 kDa	0	0	2	0	0	2	0	0	0	0
10 kDa heat shock protein, mitochondrial OS=Homo sapiens GN=HSPE1 PE=1 SV=2	P61604	11 kDa	0	0	2	4	0	0	0	0	0	0
Thioredoxin OS=Homo sapiens GN=TXN PE=1 SV=3	P10599	12 kDa	0	0	2	0	0	0	0	0	0	0
Cofilin-1 OS=Homo sapiens GN=CFL1 PE=1 SV=3	P23528	19 kDa	0	0	3	3	0	0	0	0	0	0
40S ribosomal protein S28 OS=Homo sapiens GN=RPS28 PE=1 SV=1	P62857	8 kDa	0	0	2	0	0	0	0	0	0	0
Y-box-binding protein 3 OS=Homo sapiens GN=YBX3 PE=1 SV=4	P16989	40 kDa	0	0	2	0	0	0	0	0	0	0
Ras-related protein Rab-1A OS=Homo sapiens GN=RAB1A PE=1 SV=3	P62820	23 kDa	0	0	4	0	0	0	0	0	0	0
Glutathione S-transferase P OS=Homo sapiens GN=GSTP1 PE=1 SV=2	P09211	23 kDa	0	0	4	0	0	0	0	0	0	0
Nucleoside diphosphate kinase A OS=Homo sapiens GN=NME1 PE=1 SV=1	P15531	17 kDa	0	0	2	0	0	0	0	0	0	0
Protein C21orf2 OS=Homo sapiens GN=C21orf2 PE=1 SV=1	**O43822**	**28 kDa**	**0**	**0**	**6**	**9**	**0**	**0**	**0**	**0**	**0**	**0**

Protein	Accession	MW										
Protein deglycase DJ-1 OS=Homo sapiens GN=PARK7 PE=1 SV=2	Q99497	20 kDa	0	0	4	0	0	0	0	0	0	0
40S ribosomal protein S11 OS=Homo sapiens GN=RPS11 PE=1 SV=3	P62280	18 kDa	0	0	2	3	0	0	0	0	0	0
Serine/arginine-rich splicing factor 2 OS=Homo sapiens GN=SRSF2 PE=1 SV=4	Q01130	25 kDa	0	0	2	0	0	0	0	0	0	0
Hypoxanthine-guanine phosphoribosyltransferase OS=Homo sapiens GN=HPRT1 PE=1 SV=2	P00492	25 kDa	0	0	2	0	0	0	0	0	0	0
Heterogeneous nuclear ribonucleoprotein D0 OS=Homo sapiens GN=HNRNPD PE=1 SV=1	Q14103	38 kDa	0	0	2	0	0	0	0	0	0	0
Phosphatidylethanolamine-binding protein 1 OS=Homo sapiens GN=PEBP1 PE=1 SV=3	P30086	21 kDa	0	0	3	0	0	0	0	0	0	0
Hydroxyacylglutathione hydrolase, mitochondrial OS=Homo sapiens GN=HAGH PE=1 SV=2	Q16775	34 kDa	0	0	3	0	0	0	0	0	0	0
Phosphoglycerate mutase 1 OS=Homo sapiens GN=PGAM1 PE=1 SV=2	P18669	29 kDa	0	0	2	0	0	0	0	0	0	0
Tropomyosin alpha-4 chain OS=Homo sapiens GN=TPM4 PE=1 SV=3	P67936	29 kDa	0	0	2	0	0	3	0	0	0	0
Nascent polypeptide-associated complex subunit alpha, muscle-specific form OS=Homo sapiens GN=NACA PE=1 SV=1	E9PAV3	205 kDa	0	0	2	0	0	0	0	0	0	0
Adenosylhomocysteinase OS=Homo sapiens GN=AHCY PE=1 SV=4	P23526	48 kDa	0	0	2	0	0	0	0	0	0	0
60S acidic ribosomal protein P2 OS=Homo sapiens GN=RPLP2 PE=1 SV=1	P05387	12 kDa	0	0	3	2	0	0	0	0	0	0
Eukaryotic initiation factor 4A-II OS=Homo sapiens GN=EIF4A2 PE=1 SV=2	Q14240	46 kDa	0	0	3	0	0	0	0	0	0	0
Zyxin OS=Homo sapiens GN=ZYX PE=1 SV=1	Q15942	61 kDa	0	0	2	0	0	0	0	0	0	0
40S ribosomal protein S14 OS=Homo sapiens GN=RPS14 PE=1 SV=3	P62263	16 kDa	0	0	2	3	0	0	0	0	0	0
Phosphoserine aminotransferase OS=Homo sapiens GN=PSAT1 PE=1 SV=2	Q9Y617	40 kDa	0	0	2	0	0	0	0	0	0	0
60S ribosomal protein L12 OS=Homo sapiens GN=RPL12 PE=1 SV=1	P30050	18 kDa	0	0	2	0	0	0	0	0	0	0
14-3-3 protein gamma OS=Homo sapiens GN=YWHAG PE=1 SV=2	P61981	28 kDa	0	0	2	0	0	0	0	0	0	0
Small nuclear ribonucleoprotein Sm D2 OS=Homo sapiens GN=SNRPD2 PE=1 SV=1	P62316	14 kDa	0	0	2	0	0	0	0	0	0	0
Ran-specific GTPase-activating protein OS=Homo sapiens GN=RANBP1 PE=1 SV=1	P43487	23 kDa	0	0	2	0	0	0	0	0	0	0
Fatty acid synthase OS=Homo sapiens GN=FASN PE=1 SV=3	P49327	273 kDa	0	0	4	0	0	0	0	0	0	0
60S ribosomal protein L22 OS=Homo sapiens GN=RPL22 PE=1 SV=2	P35268	15 kDa	0	0	2	0	0	2	0	0	0	0
14-3-3 protein eta OS=Homo sapiens GN=YWHAH PE=1 SV=4	Q04917	28 kDa	0	0	3	0	0	0	0	0	0	0
Myristoylated alanine-rich C-kinase substrate OS=Homo sapiens GN=MARCKS PE=1 SV=4	P29966	32 kDa	0	0	2	2	0	0	0	0	0	0
BUB3-interacting and GLEBS motif-containing protein ZNF207 OS=Homo sapiens GN=ZNF207 PE=1 SV=1	O43670	51 kDa	0	0	2	0	0	0	0	0	0	0
ATP synthase subunit d, mitochondrial OS=Homo sapiens GN=ATP5H PE=1 SV=3	O75947	18 kDa	0	0	2	0	0	0	0	0	0	0
GrpE protein homolog 1, mitochondrial OS=Homo sapiens GN=GRPEL1 PE=1 SV=2	Q9HAV7	24 kDa	0	0	2	6	0	0	0	0	0	0

Protein	Accession	MW										
Nuclear autoantigenic sperm protein OS=Homo sapiens GN=NASP PE=1 SV=2	P49321	85 kDa	0	0	2	0	0	0	0	0	0	0
Proteasome subunit alpha type-5 OS=Homo sapiens GN=PSMA5 PE=1 SV=3	P28066	26 kDa	0	0	2	0	0	0	0	0	0	0
Non-POU domain-containing octamer-binding protein OS=Homo sapiens GN=NONO PE=1 SV=4	Q15233	54 kDa	0	0	0		0	2	0	0	0	0
Annexin A2 OS=Homo sapiens GN=ANXA2 PE=1 SV=2	P07355	39 kDa	0	0	0	0	0	15	0	0	0	0
Polypyrimidine tract-binding protein 1 OS=Homo sapiens GN=PTBP1 PE=1 SV=1	P26599	57 kDa	0	0	0	0	0	3	0	0	0	0
Annexin A1 OS=Homo sapiens GN=ANXA1 PE=1 SV=2	P04083	39 kDa	0	0	0	0	0	2	0	0	0	0
Heterogeneous nuclear ribonucleoprotein M OS=Homo sapiens GN=HNRNPM PE=1 SV=3	P52272	78 kDa	0	0	0	0	0	8	0	0	0	0
40S ribosomal protein S19 OS=Homo sapiens GN=RPS19 PE=1 SV=2	P39019	16 kDa	0	0	0	2	0	2	0	0	0	0
Protein S100-A7 OS=Homo sapiens GN=S100A7 PE=1 SV=4	P31151	11 kDa	0	0	0	0	0	6	0	0	0	0
40S ribosomal protein S7 OS=Homo sapiens GN=RPS7 PE=1 SV=1	P62081	22 kDa	0	0	0	0	0	4	0	0	0	0
Protein S100-A9 OS=Homo sapiens GN=S100A9 PE=1 SV=1	P06702	13 kDa	0	0	0	0	0	7	0	0	0	0
Filaggrin OS=Homo sapiens GN=FLG PE=1 SV=3	P20930	435 kDa	0	0	0	0	0	4	0	0	0	0
Heterogeneous nuclear ribonucleoprotein H3 OS=Homo sapiens GN=HNRNPH3 PE=1 SV=2	P31942	37 kDa	0	0	0	0	0	3	0	0	0	0
Involucrin OS=Homo sapiens GN=IVL PE=1 SV=2	P07476	68 kDa	0	0	0	0	0	2	0	0	0	0
Calmodulin-like protein 5 OS=Homo sapiens GN=CALML5 PE=1 SV=2	Q9NZT1	16 kDa	0	0	0	0	0	4	0	0	0	0
Cystatin-A OS=Homo sapiens GN=CSTA PE=1 SV=1	P01040	11 kDa	0	0	0	0	0	6	0	0	0	0
Calmodulin OS=Homo sapiens GN=CALM1 PE=1 SV=2	P62158	17 kDa	0	0	0	2	0	2	0	0	0	0
40S ribosomal protein S16 OS=Homo sapiens GN=RPS16 PE=1 SV=2	P62249	16 kDa	0	0	0	2	0	2	0	0	0	0
Serpin B3 OS=Homo sapiens GN=SERPINB3 PE=1 SV=2	P29508	45 kDa	0	0	0	0	0	9	0	0	0	0
Caspase-14 OS=Homo sapiens GN=CASP14 PE=1 SV=2	P31944	28 kDa	0	0	0	0	0	6	0	0	0	0
Protein S100-A8 OS=Homo sapiens GN=S100A8 PE=1 SV=1	P05109	11 kDa	0	0	0	0	0	6	0	0	0	0
Cathepsin D OS=Homo sapiens GN=CTSD PE=1 SV=1	P07339	45 kDa	0	0	0	0	0	4	0	0	0	0
Heterogeneous nuclear ribonucleoprotein A3 OS=Homo sapiens GN=HNRNPA3 PE=1 SV=2	P51991	40 kDa	0	0	0	0	0	2	0	0	0	0
Neuroblast differentiation-associated protein AHNAK OS=Homo sapiens GN=AHNAK PE=1 SV=2	Q09666	629 kDa	0	0	0	0	0	2	0	0	0	0
Flap endonuclease 1 OS=Homo sapiens GN=FEN1 PE=1 SV=1	P39748	43 kDa	0	0	0	0	0	3	0	0	0	0
Heat shock protein beta-1 OS=Homo sapiens GN=HSPB1 PE=1 SV=2	P04792	23 kDa	0	0	0	0	0	4	0	0	0	0
Myosin-9 OS=Homo sapiens GN=MYH9 PE=1 SV=4	P35579	227 kDa	0	0	0	0	0	7	0	0	0	0

Protein	Accession	kDa										
Zinc-alpha-2-glycoprotein OS=Homo sapiens GN=AZGP1 PE=1 SV=2	P25311	34 kDa	0	0	0	0	0	3	0	0	0	0
40S ribosomal protein S15a OS=Homo sapiens GN=RPS15A PE=1 SV=2	P62244	15 kDa	0	0	0	0	0	2	0	0	0	0
Galectin-7 OS=Homo sapiens GN=LGALS7 PE=1 SV=2	P47929	15 kDa	0	0	0	0	0	4	0	0	0	0
Non-histone chromosomal protein HMG-14 OS=Homo sapiens GN=HMGN1 PE=1 SV=3	P05114	11 kDa	0	0	0	0	0	3	0	0	0	0
14-3-3 protein sigma OS=Homo sapiens GN=SFN PE=1 SV=1	P31947	28 kDa	0	0	0	0	0	3	0	0	0	0
Protein-glutamine gamma-glutamyltransferase K OS=Homo sapiens GN=TGM1 PE=1 SV=4	P22735	90 kDa	0	0	0	0	0	2	0	0	0	0
Glutamine synthetase OS=Homo sapiens GN=GLUL PE=1 SV=4	P15104	42 kDa	0	0	0	0	0	2	0	0	0	0
Fatty acid-binding protein, epidermal OS=Homo sapiens GN=FABP5 PE=1 SV=3	Q01469	15 kDa	0	0	0	0	0	3	0	0	0	0
Protein S100-A14 OS=Homo sapiens GN=S100A14 PE=1 SV=1	Q9HCY8	12 kDa	0	0	0	0	0	3	0	0	0	0
Ig kappa chain C region OS=Homo sapiens GN=IGKC PE=1 SV=1	P01834	12 kDa	0	0	0	0	0	2	0	0	0	0
Protein S100-A6 OS=Homo sapiens GN=S100A6 PE=1 SV=1	P06703	10 kDa	0	0	0	0	0	2	0	0	0	0
Proteasome subunit alpha type-4 OS=Homo sapiens GN=PSMA4 PE=1 SV=1	P25789	29 kDa	0	0	0	0	0	2	0	0	0	0
Ig gamma-1 chain C region OS=Homo sapiens GN=IGHG1 PE=1 SV=1	P01857	36 kDa	0	0	0	0	0	2	0	0	0	0
Cornifin-B OS=Homo sapiens GN=SPRR1B PE=1 SV=2	P22528 (+1)	10 kDa	0	0	0	0	0	2	0	0	0	0
ATP synthase subunit beta, mitochondrial OS=Homo sapiens GN=ATP5B PE=1 SV=3	P06576	57 kDa	0	0	0	8	0	0	0	0	0	0
RuvB-like 2 OS=Homo sapiens GN=RUVBL2 PE=1 SV=3	Q9Y230	51 kDa	0	0	0	6	0	0	0	0	0	0
Exportin-1 OS=Homo sapiens GN=XPO1 PE=1 SV=1	O14980	123 kDa	0	0	0	4	0	0	0	0	0	0
Probable ATP-dependent RNA helicase DDX17 OS=Homo sapiens GN=DDX17 PE=1 SV=2	Q92841	80 kDa	0	0	0	3	0	0	0	0	0	0
116 kDa U5 small nuclear ribonucleoprotein component OS=Homo sapiens GN=EFTUD2 PE=1 SV=1	Q15029	109 kDa	0	0	0	3	0	0	0	0	0	0
T-complex protein 1 subunit alpha OS=Homo sapiens GN=TCP1 PE=1 SV=1	P17987	60 kDa	0	0	0	3	0	0	0	0	0	0
Tubulin beta-2B chain OS=Homo sapiens GN=TUBB2B PE=1 SV=1	Q9BVA1	50 kDa	0	0	0	3	0	0	0	0	0	0
Peptidyl-prolyl cis-trans isomerase B OS=Homo sapiens GN=PPIB PE=1 SV=2	P23284	24 kDa	0	0	0	3	0	0	0	0	0	0
Histone H2B type 1-L OS=Homo sapiens GN=HIST1H2BL PE=1 SV=3	Q99880 (+8)	14 kDa	0	0	0	3	0	0	0	0	0	0
U5 small nuclear ribonucleoprotein 200 kDa helicase OS=Homo sapiens GN=SNRNP200 PE=1 SV=2	O75643	245 kDa	0	0	0	3	0	0	0	0	0	0
Histone H1.4 OS=Homo sapiens GN=HIST1H1E PE=1 SV=2	P10412	22 kDa	0	0	0	3	0	0	0	0	0	0
Inosine-5'-monophosphate dehydrogenase 2 OS=Homo sapiens GN=IMPDH2 PE=1 SV=2	P12268	56 kDa	0	0	0	3	0	0	0	0	0	0
ATP-dependent RNA helicase DDX39A OS=Homo sapiens GN=DDX39A PE=1 SV=2	O00148 (+1)	49 kDa	0	0	0	3	0	0	0	0	0	0

Protein	Accession	Mass									
Methylosome protein 50 OS=Homo sapiens GN=WDR77 PE=1 SV=1	Q9BQA1	37 kDa	0	0	0	3	0	0	0	0	0	0
Dystonin OS=Homo sapiens GN=DST PE=1 SV=4	Q03001	861 kDa	0	0	0	3	0	0	0	0	0	0
Calreticulin OS=Homo sapiens GN=CALR PE=1 SV=1	P27797	48 kDa	0	0	0	3	0	0	0	0	0	0
Voltage-dependent anion-selective channel protein 2 OS=Homo sapiens GN=VDAC2 PE=1 SV=2	P45880	32 kDa	0	0	0	2	0	0	0	0	0	0
Serpin H1 OS=Homo sapiens GN=SERPINH1 PE=1 SV=2	P50454	46 kDa	0	0	0	2	0	0	0	0	0	0
Ig kappa chain V-II region Cum OS=Homo sapiens PE=1 SV=1	P01614 (+3)	13 kDa	0	0	0	2	0	0	0	0	0	0
Acidic leucine-rich nuclear phosphoprotein 32 family member A OS=Homo sapiens GN=ANP32A PE=1 SV=1	P39687	29 kDa	0	0	0	2	0	0	0	0	0	0
ATP synthase subunit delta, mitochondrial OS=Homo sapiens GN=ATP5D PE=1 SV=2	P30049	17 kDa	0	0	0	2	0	0	0	0	0	0
40S ribosomal protein S13 OS=Homo sapiens GN=RPS13 PE=1 SV=2	P62277	17 kDa	0	0	0	2	0	0	0	0	0	0
Membrane-associated progesterone receptor component 1 OS=Homo sapiens GN=PGRMC1 PE=1 SV=3	O00264	22 kDa	0	0	0	2	0	0	0	0	0	0
Putative pre-mRNA-splicing factor ATP-dependent RNA helicase DHX15 OS=Homo sapiens GN=DHX15 PE=1 SV=2	O43143	91 kDa	0	0	0	2	0	0	0	0	0	0
Histone-binding protein RBBP4 OS=Homo sapiens GN=RBBP4 PE=1 SV=3	Q09028 (+1)	48 kDa	0	0	0	2	0	0	0	0	0	0
Matrin-3 OS=Homo sapiens GN=MATR3 PE=1 SV=2	P43243	95 kDa	0	0	0	2	0	0	0	0	0	0
Putative RNA-binding protein Luc7-like 2 OS=Homo sapiens GN=LUC7L2 PE=1 SV=2	Q9Y383	47 kDa	0	0	0	2	0	0	0	0	0	0
Eukaryotic initiation factor 4A-I OS=Homo sapiens GN=EIF4A1 PE=1 SV=1	P60842 (+1)	46 kDa	0	0	0	2	0	0	0	0	0	0
ELAV-like protein 1 OS=Homo sapiens GN=ELAVL1 PE=1 SV=2	Q15717	36 kDa	0	0	0	2	0	0	0	0	0	0
Rootletin OS=Homo sapiens GN=CROCC PE=1 SV=1	Q5TZA2	229 kDa	0	0	0	2	0	0	0	0	0	0
60S ribosomal protein L9 OS=Homo sapiens GN=RPL9 PE=1 SV=1	P32969	22 kDa	0	0	0	2	0	0	0	0	0	0
MARCKS-related protein OS=Homo sapiens GN=MARCKSL1 PE=1 SV=2	P49006	20 kDa	0	0	0	2	0	0	0	0	0	0
Cyclin-dependent kinase 1 OS=Homo sapiens GN=CDK1 PE=1 SV=3	P06493	34 kDa	0	0	0	2	0	0	0	0	0	0
40S ribosomal protein S9 OS=Homo sapiens GN=RPS9 PE=1 SV=3	P46781	23 kDa	0	0	0	2	0	0	0	0	0	0
Serine/arginine-rich splicing factor 3 OS=Homo sapiens GN=SRSF3 PE=1 SV=1	P84103	19 kDa	0	0	0	2	0	0	0	0	0	0
Histone H3.3 OS=Homo sapiens GN=H3F3A PE=1 SV=2	P84243	15 kDa	0	0	0	2	0	0	0	0	0	0
FACT complex subunit SSRP1 OS=Homo sapiens GN=SSRP1 PE=1 SV=1	Q08945	81 kDa	0	0	0	2	0	0	0	0	0	0
Solute carrier family 45 member 4 OS=Homo sapiens GN=SLC45A4 PE=1 SV=2	Q5BKX6	84 kDa	0	0	0	2	0	0	0	0	0	0
Alpha-2-HS-glycoprotein OS=Homo sapiens GN=AHSG PE=1 SV=1	P02765	39 kDa	0	0	0	2	0	0	0	0	0	0
60S ribosomal protein L13a OS=Homo sapiens GN=RPL13A PE=1 SV=2	P40429	24 kDa	0	0	0	2	0	0	0	0	0	0

Mitogen-activated protein kinase kinase kinase 2 OS=Homo sapiens GN=MAP3K2 PE=1 SV=2	Q9Y2U5	70 kDa	0	0	0	2	0	0	0	0	0	0
Zinc finger Ran-binding domain-containing protein 2 OS=Homo sapiens GN=ZRANB2 PE=1 SV=2	O95218	37 kDa	0	0	0	2	0	0	0	0	0	0
DNA-dependent protein kinase catalytic subunit OS=Homo sapiens GN=PRKDC PE=1 SV=3	P78527	469 kDa	0	0	0	2	0	0	0	0	0	0
Single-stranded DNA-binding protein, mitochondrial OS=Homo sapiens GN=SSBP1 PE=1 SV=1	Q04837	17 kDa	0	0	0	2	0	0	0	0	0	0

Appendix D

D.1 Cilia compartments axoneme, transition zone, and basal body recognition protocol:

(Nuclei – DAPI; Cilia axoneme – Alexa Fluor 546; Transition zone – Alexa Fluor 488; Basal body – DRAQ5).

D.1.1 Example: Analysis sequence cilia axoneme and transition zone co-localization Red and Green.

1. Input image
    1. Stack Processing: Individual Planes
    2. Flatfield Correction: None
2. Find nuclei
    1. Channel: DAPI
    2. ROI: None
    3. Method: B   Output Population: Nuclei
        i. Common threshold: 0
        ii. Area: >50 µm^2
        iii. Split factor: 7
        iv. Individual threshold: 0.4
        v. Contrast: >0.1
3. Find cytoplasm
    1. Channel: DRAQ5
    2. Nuclei: Nuclei
    3. Method: B
        i. Common Threshold: 0.1
        ii. Individual Threshold: 0.1
4. Calculate Image
    1. Method: By Formula   Output Image: R
        i. Formula: 1.0*A
        ii. Channel A: Alexa 546
        iii. Negative Values: Set to Zero
        iv. Undefined Values: Set to Local Average
5. Calculate Image (2)
    1. Method: By Formula   Output Image: G
        i. Formula: 1.0*A
        ii. Channel A: Alexa 488
        iii. Negative Values: Set to Zero
        iv. Undefined Values: Set to Local Average
6. Calculate Image (3)
    1. Method: By Formula   Output Image: RG
        i. Formula: A*B
        ii. Channel A: R
        iii. Channel B: G
        iv. Negative Values: Set to Zero
        v. Undefined Values: Set to Local Average

7. Calculate Image (4)
    1. Method: By Formula   Output Image: R^2
        i. Formula: A*A
        ii. Channel A: R
        iii. Negative Values: Set to Zero
        iv. Undefined Values: Set to Local Average
8. Calculate Image (5)
    1. Method: By Formula   Output Image: G^2
        i. Formula: A*A
        ii. Channel A: G
        iii. Negative Values: Set to Zero
        iv. Undefined Values: Set to Local Average
9. Find spots
    1. Channel: Alexa 546
    2. ROI: Nuclei
    3. Method: A   Output Population: Cilia
        i. Relative Spot Intensity: >0.035
        ii. Splitting Coefficient: 0 Calculate Spot Properties
10. Select Population
    1. Population: Cilia
    2. Method: Filter by Property   Output Population: Cilia
        i. Spot Area [px^2]: >=45   Selected
11. Calculate Intensity Properties
    1. Channel: RG
    2. Population: Cilia Selected
    3. Region: Spot
    4. Method: Standard Sum   Output Properties: RGi merge
12. Calculate Intensity Properties (2)
    1. Channel: R
    2. Population: Cilia Selected
    3. Region: Spot
    4. Method: Standard Mean Sum   Output Properties: Ri
13. Calculate Intensity Properties (3)
    1. Channel: G
    2. Population: Cilia Selected
    3. Region: Spot
    4. Method: Standard Mean Sum   Output Properties: Gi
14. Calculate Intensity Properties (4)
    1. Channel: R^2
    2. Population: Cilia Selected
    3. Region: Spot
    4. Method: Standard Sum   Output Properties: R^2i
15. Calculate Intensity Properties (5)
    1. Channel: G^2
    2. Population: Cilia Selected
    3. Region: Spot
    4. Method: Standard Sum   Output Properties: G^2i
16. Calculate Properties
    1. Population: Cilia Selected
    2. Method: By Formula   Output Properties: Pearson Up

        i.   Formula: M - (G*s) - (R*h) + (C*R*G)
       ii.   Variable C: Spot Area [px^2]
     iii.   Variable G: Gi Mean
     iv.   Variable H: Gi Sum
      v.   Variable M: RGi Merge Sum
     vi.   Variable R: Ri Mean
    vii.   Variable S: Ri Sum

17. Calculate Properties (2)
    1. Population: Cilia Selected
    2. Method: By Formula   Output Properties: Pearsons Down
        i. Formula: (q-(2*R*s)+(C*R*R)) *(f-(2*G*h) + (C*G*G))
        ii. Variable C: Spot Area [px^2]
        iii. Variable F: G^2i Sum
        iv. Variable G: Gi Mean
        v. Variable H: Gi Sum
        vi. Variable Q: R^2i Sum
        vii. Variable R: Ri Mean
        viii. Variable S: Ri Sum

18. Calculate Properties (3)
    1. Population: Cilia Selected
    2. Method: By Formula   Output Properties: Pearsons Coefficient
        i. Formula: A/sqrt(B)
        ii. Variable A: Pearsons Up
        iii. Variable B: Pearsons Down

19. Define Results
    1. Method: List of Outputs
    2. Population: Cilia
        i. Apply to All:
        ii. Relative Spot Intensity:
        iii. Corrected Spot Intensity:
        iv. Uncorrected Spot Peak Intensity:
        v. Spot Contrast:
        vi. Spot Background Intensity:
        vii. Spot Area [px^2]:
        viii. Region Intensity:
        ix. Spot To Region Intensity:
        x. Cilia Selected:
    3. Population: Nuclei
        i. Number of Objects
        ii. Apply to All:
        iii. Relative Spot Intensity:
        iv. Number of Spots:
        v. Number of Spots per Area of Cell:
    4. Population: Cilia Selected
        i. Number of Objects
        ii. Apply to All:
        iii. Relative Spot Intensity:
        iv. Corrected Spot Intensity:
        v. Uncorrected Spot Peak Intensity:
        vi. Spot Contrast:

        vii.   Spot Background Intensity:

        viii.   SpotArea[px^2]:

        ix.   Region Intensity:

        x.   Spot To Region Intensity:

        xi.   RGi merge Sum:

        xii.   Ri Mean:

        xiii.   Ri Sum:

        xiv.   Gi Mean:

        xv.   Gi Sum:

        xvi.   R^2i Sum:

        xvii.   G^2i Sum:

        xviii. Pearson Up:

        xix.   Pearson Down:

        xx.   Pearson Coefficient:

        xxi.   Mean+StdDev

5. Population: Cilia: None
6. Population: Nuclei: None
7. Population: Cilia Selected: ALL

D.1.2 Example: Analysis sequence transition zone and Basal body co-localization Green and Far-red for TMEM67 experiment

1. Input image
    1. Stack Processing: Individual Planes
    2. Flatfield Correction: None
2. Find nuclei
    1. Channel: DAPI
    2. ROI: None
    3. Method: B   Output Population: Nuclei
        i.   Common threshold: 0
        ii.   Area: >50 μm^2
        iii. Split factor: 7
        iv. Individual threshold: 0.4
        v.   Contrast: >0.1
3. Find cytoplasm
    1. Channel: DRAQ5
    2. Nuclei: Nuclei
    3. Method: B
        i.   Common Threshold: 0.1
        ii.   Individual Threshold: 0.1
4. Calculate Image
    1. Method: By Formula   Output Image: R
        i.   Formula: 1.0*A
        ii.   Channel A: DRAQ5
        iii. Negative Values: Set to Zero
        iv. Undefined Values: Set to Local Average
5. Calculate Image (2)
    1. Method: By Formula   Output Image: G
        i.   Formula: 1.0*A

ii. Channel A: Alexa 488
iii. Negative Values: Set to Zero
iv. Undefined Values: Set to Local Average

6. Calculate Image (3)
    1. Method: By Formula   Output Image: RG
        i. Formula: A*B
        ii. Channel A: R
        iii. Channel B: G
        iv. Negative Values: Set to Zero
        v. Undefined Values: Set to Local Average

7. Calculate Image (4)
    1. Method: By Formula   Output Image: R^2
        i. Formula: A*A
        ii. Channel A: R
        iii. Negative Values: Set to Zero
        iv. Undefined Values: Set to Local Average

8. Calculate Image (5)
    1. Method: By Formula   Output Image: G^2
        i. Formula: A*A
        ii. Channel A: G
        iii. Negative Values: Set to Zero
        iv. Undefined Values: Set to Local Average

9. Find spots
    1. Channel: DRAQ5
    2. ROI: Nuclei
    3. Method: A   Output Population: γ-Tubulin
        i. Relative Spot Intensity: >0.03
        ii. Splitting Coefficient: 1 Calculate Spot Properties

10. Select Population
    1. Population: γ-Tubulin
    2. Method: Filter by Property   Output Population: γ-Tubulin
        i. Spot Area [px^2]: >=25   Selected

11. Calculate Intensity Properties
    1. Channel: RG
    2. Population: γ-Tubulin Selected
    3. Region: Spot
    4. Method: Standard Sum   Output Properties: RGi merge

12. Calculate Intensity Properties (2)
    1. Channel: R
    2. Population: γ-Tubulin Selected
    3. Region: Spot
    4. Method: Standard Mean Sum   Output Properties: Ri

13. Calculate Intensity Properties (3)
    1. Channel: G
    2. Population: γ-Tubulin Selected
    3. Region: Spot
    4. Method: Standard Mean Sum   Output Properties: Gi

14. Calculate Intensity Properties (4)
    1. Channel: R^2
    2. Population: γ-Tubulin Selected

3. Region: Spot
4. Method: Standard Sum   Output Properties: R^2i

15. Calculate Intensity Properties (5)
    1. Channel: G^2
    2. Population: <mark>γ-Tubulin</mark> Selected
    3. Region: Spot
    4. Method: Standard Sum   Output Properties: G^2i

16. Calculate Properties
    1. Population: <mark>γ-Tubulin</mark> Selected
    2. Method: By Formula   Output Properties: Pearson Up
        i. Formula: M - (G*s) - (R*h) + (C*R*G)
        ii. Variable C: Spot Area [px^2]
        iii. Variable G: Gi Mean
        iv. Variable H: Gi Sum
        v. Variable M: RGi merge Sum
        vi. Variable R: Ri Mean
        vii. Variable S: Ri Sum

17. Calculate Properties (2)
    1. Population: <mark>γ-Tubulin</mark> Selected
    2. Method: By Formula   Output Properties: Pearsons Down
        i. Formula: (q-(2*R*s) + (C*R*R)) *(f-(2*G*h) + (C*G*G))
        ii. Variable C: Spot Area [px^2]
        iii. Variable F: G^2i Sum
        iv. Variable G: Gi Mean
        v. Variable H: Gi Sum
        vi. Variable Q: R^2i Sum
        vii. Variable R: Ri Mean
        viii. Variable S: Ri Sum

18. Calculate Properties (3)
    1. Population: <mark>γ-Tubulin</mark> Selected
    2. Method: By Formula   Output Properties: Pearsons Coefficient
        i. Formula: A/sqrt(B)
        ii. Variable A: Pearsons Up
        iii. Variable B: Pearsons Down

19. Define Results
    1. Method: List of Outputs
    2. Population: <mark>γ-Tubulin</mark>
        i. Apply to All:
        ii. Relative Spot Intensity:
        iii. Corrected Spot Intensity:
        iv. Uncorrected Spot Peak Intensity:
        v. Spot Contrast:
        vi. Spot Background Intensity:
        vii. Spot Area [px^2]:
        viii. Region Intensity:
        ix. Spot To Region Intensity:
        x. <mark>γ-Tubulin</mark> Selected:
    3. Population: Nuclei
        i. Number of Objects
        ii. Apply to All:

       iii.   Total Spot Area:
       iv.   Relative Spot Intensity:
       v.   Number of Spots:
       vi.   Number of Spots per Area of Cell:

4. Population: γ-Tubulin Selected
   i.   Number of Objects
   ii.   Apply to All:
   iii.   Relative Spot Intensity:
   iv.   Corrected Spot Intensity:
   v.   Uncorrected Spot Peak Intensity:
   vi.   Spot Contrast:
   vii.   Spot Background Intensity:
   viii.   Spot Area [px^2]:
   ix.   Region Intensity:
   x.   Spot To Region Intensity:
   xi.   RGi merge Sum:
   xii.   Ri Mean:
   xiii.   Ri Sum:
   xiv.   Gi Mean:
   xv.   Gi Sum:
   xvi.   R^2i Sum:
   xvii.   G^2i Sum:
   xviii.   Pearson Up:
   xix.   Pearson Down:
   xx.   Pearson Coefficient:
   xxi.   Mean+StdDev

5. Population: Cilia: None
   i.   Population: Nuclei: None
   ii.   Population: γ-Tubulin Selected: ALL

D.2 Steps of quantitative co-localization analysis using Volocity 64x:

1. Image acquisition

1.1 Open an image and select two channels to be analysed. The two channels have different colours, easy to visualize.

1.2 Select the object, name the population, and select colour

1.3 Click measure t select the features of the population

1.4 Choose intensity and volume measurements

1.5 Drag and drop a second task to select a second object and follow the above steps

1.6 Remove Noise from objects

1.7 Calculate object co-localization: according to manufacturing-based definition of this calculation described as the detection of signal at the same voxel location in each of two channels. The two channels are made up of images of two different fluorochromes taken from the same sample area.

2. Background correction

2.1 Set thresholds

2.2 Enter the required values manually into the Threshold Maximum and Minimum boxes for each channel or drag the slider controls on the scatter plot

2.3 Select Automatic Thresholding from the Co-localization menu to generate thresholds automatically.

3. Coefficients calculations

3.1 Pearson's correlation coefficient calculates the intensity values over a determined threshold in both channels.

3.2 Interpreting obtained results correlation of the intensity distribution between channels

Exemplar workflow for siRNA scrambled control data

Select all images→ 1. measurements (Finding)→Find objects→ Focus on one channel, transition zone (FITC)→Measure (make the following measurement: Intensity and volume measurement)→ Setting→minimum object size (0.3 µm^3)→ Exclude object by size (>7 µm^3)→ 2. Find second objects→ Focus on one channel, axoneme (TexasRed)→Measure (make the following measurement: Intensity and volume measurement)→ Setting→minimum object size (0.2 µm^3)→ Exclude object by size (>9 µm^3)→ 3.Calculate object co-localization: Inpat [Channel 1 FITC ;Channel 2 TexasRed] (Choose two channels 'two compartments' ex transition zone and axoneme)→ Measurement 'Auto-threshold '→ Display →FITC focus final→ Pearson's correlation→Save setting→Save protocol→run→ File→Export data→ Excel analysis (TMP downloaded text).* Repeat same steps for the remaining compartments ex transition zone and basal body and axoneme and basal body).

D.3 Cilia/cells counting methods after volocity measurement:

I used Fiji software to count cells and cilia instead of volocity 64x, as follows

• Image → Colour → Split Channels → Select Cilia Channel →Maximum Intensity Z-projection **(**Image/Stacks/ Z Project / ✔ Max Intensity**)** → Analysis → 3D Objects Counter **(**Threshold (Filter)/ ✔objects/ ✔ Statistics/ ✔Summary**)**

1. Example of objects counter setting (cilia selection) as follows
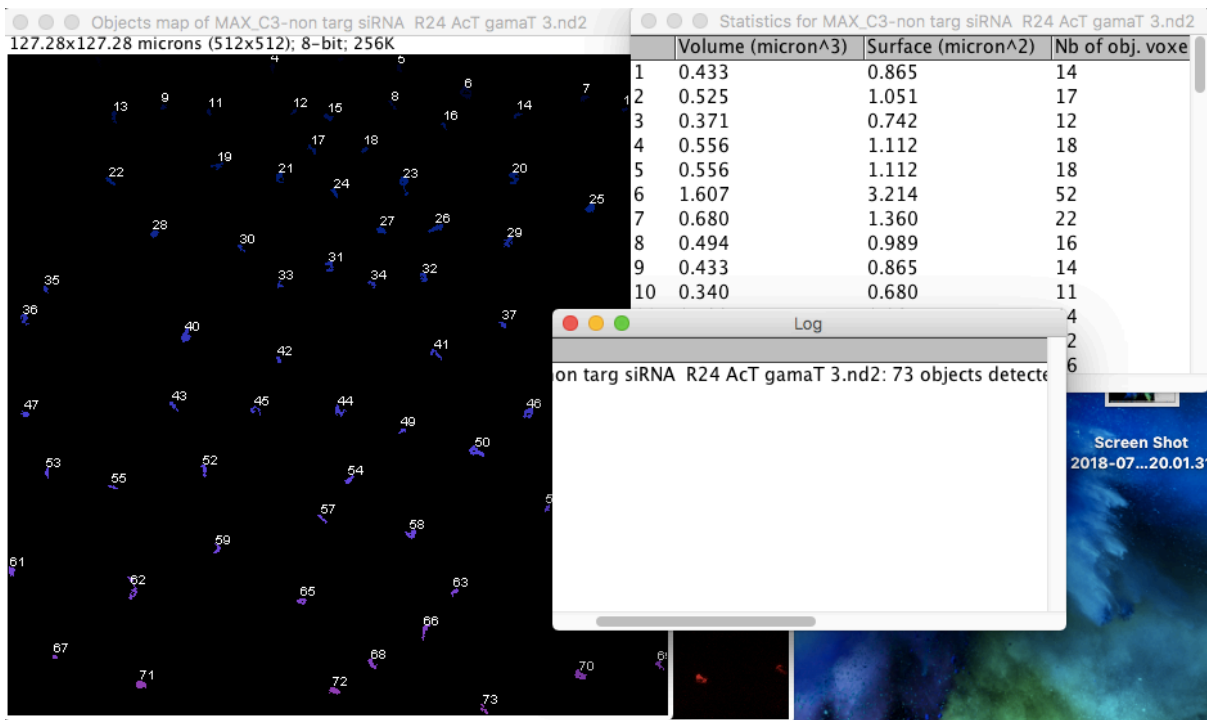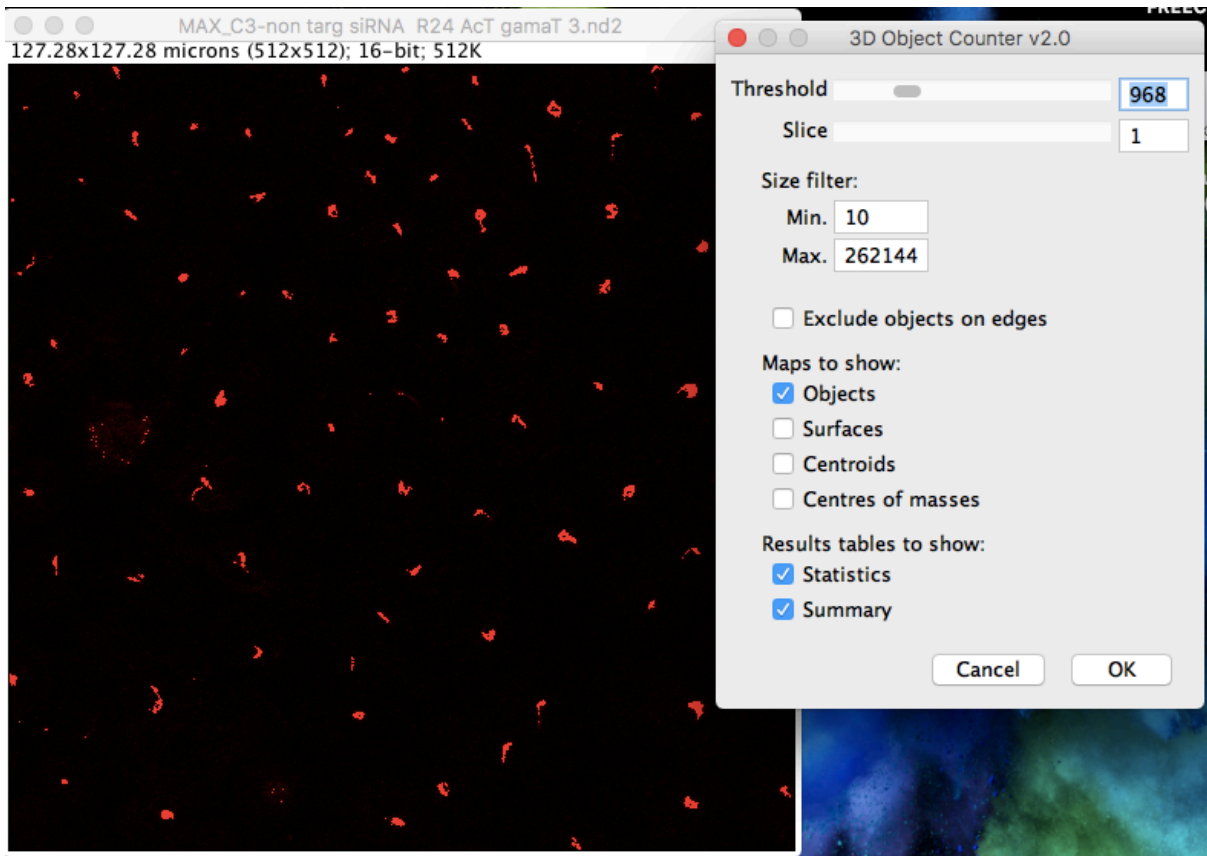
2. Example of objects counter setting (cell selection) as follow

Objects map of MAX_C1-P26 IMCD3 080317 SCRsiRNA R24 AAct Yt f...
63.64x63.64 microns (512x512); 8-bit; 256K

Log

17 SCRsiRNA R24 AAct Yt farred and DAPI2.nd2: 25 objec
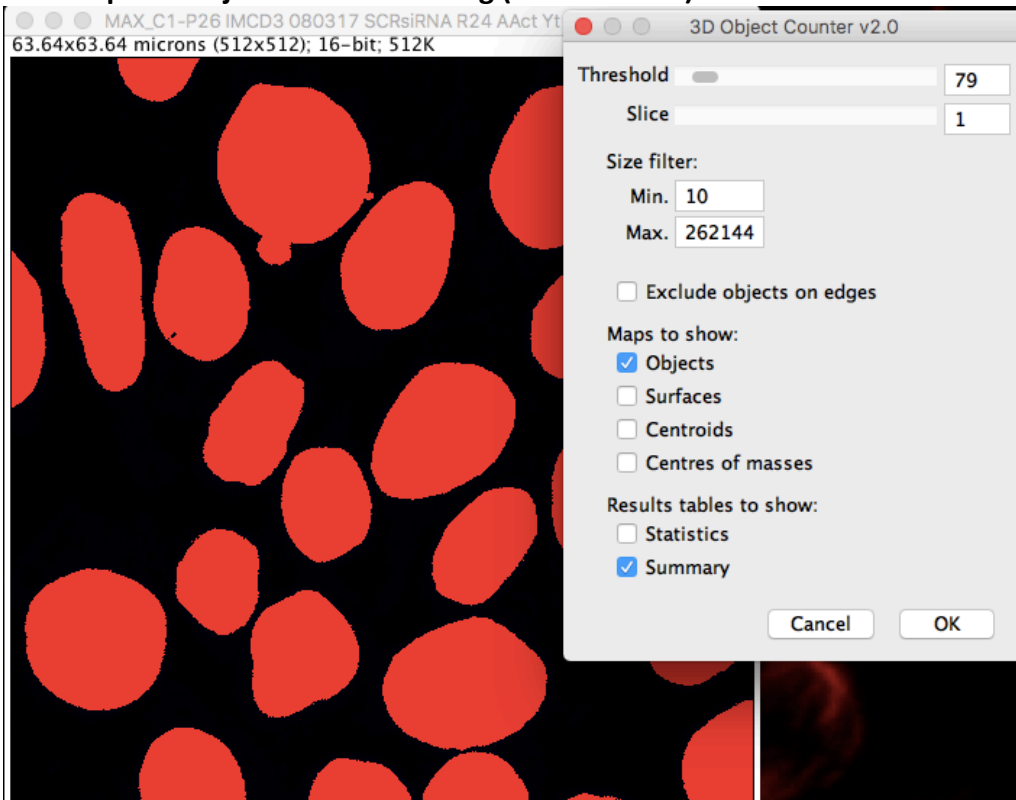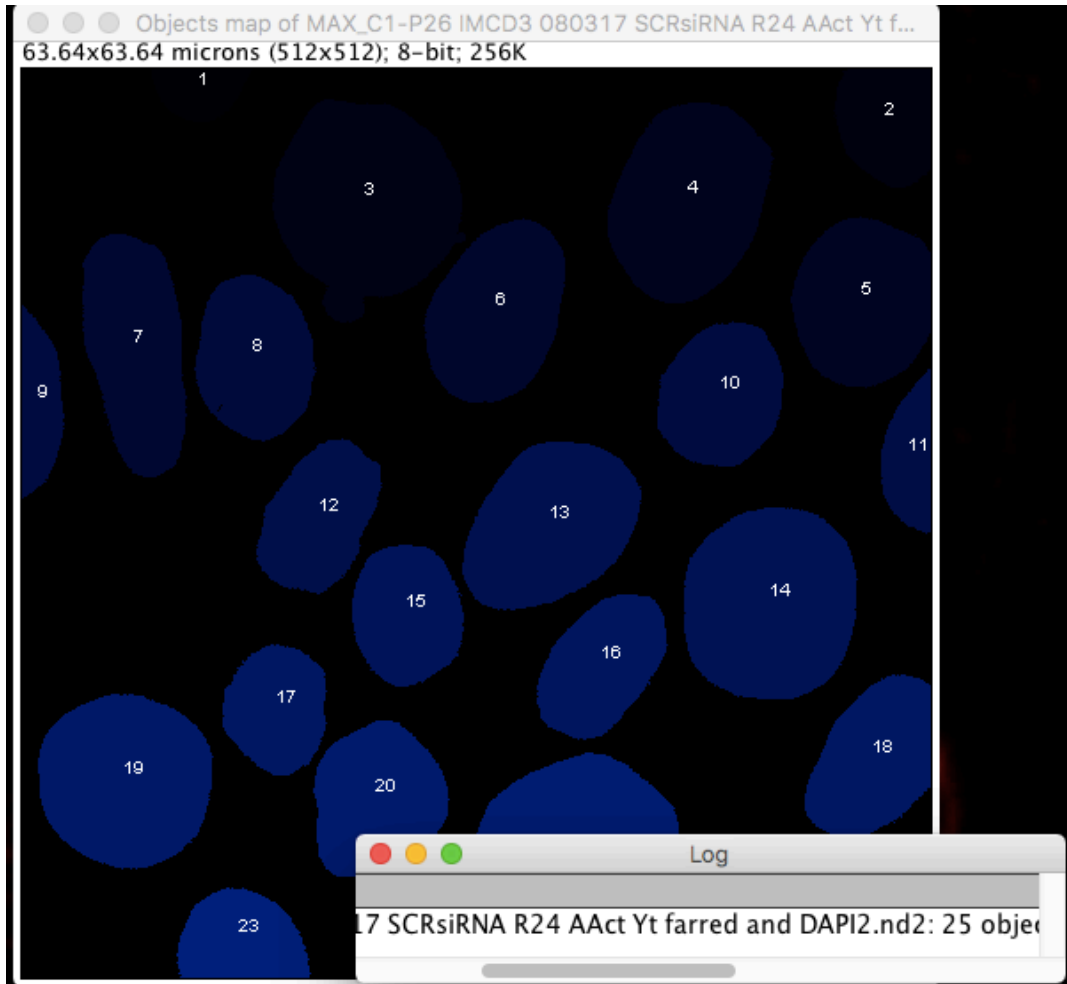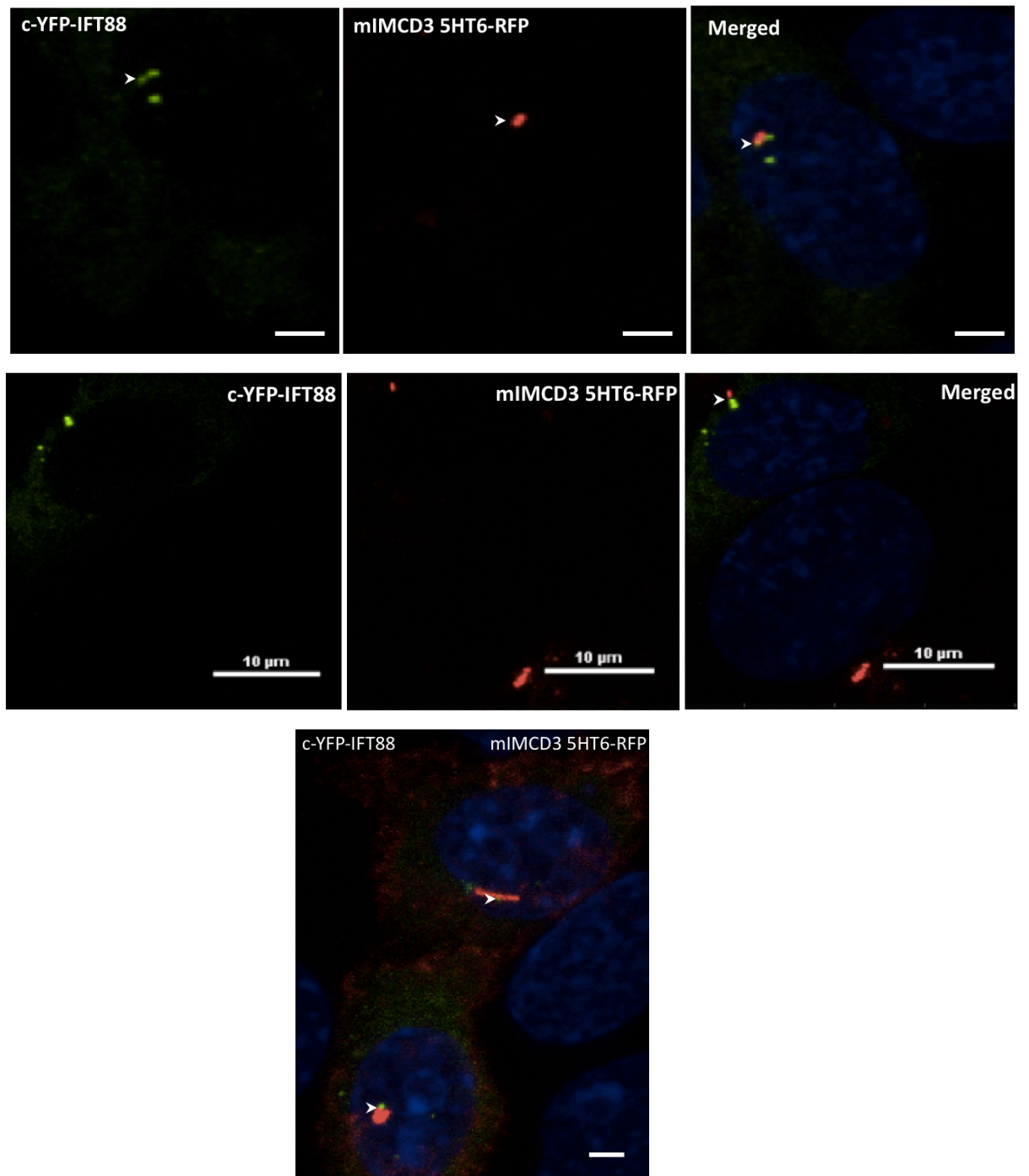
D.4: Validation of subcellular localization of IFT88 in mIMCD-3 cells stably expressing the ciliary marker 5HT6-RFP prior to using IFT88 as an axoneme marker. The use of IFT88 was to test co-localization in cilia with other ciliary-specific antibodies in order to define the organization of the CEP290 module. Merged images below show the stably-transfected ciliated mIMCD-3 5HT6-RFP cell-line, marking cilia in red, had co-localization of c-YFP-IFT88 (green) In merged images, the DAPI counterstain (blue) revealed the position of nuclei. Scale bars = 10 μm. YFP-IFT88 does appear to co-localize with cilia.

List of commercial suppliers

ATCC LGC, Queens Road, Teddington, Middlesex TW11 0LY, UK atcc@lgcstandards.com https://www.lgcstandards-atcc.org/en/Guides/Guides.aspx	**Bio-Rad DC^{TM}Laboratories Ltd** The Junction, Station Road, Watford, Hertfordshire, WD17 1ET, UK Contact_NorthEurope@bio-rad.com https://www.bio-rad.com
Cell Signaling Technology, Inc. 3 Trask Lane Danvers, MA 01923 orders@cellsignal.com https://www.cellsignal.com	**Roche** Roche Diagnostics Limited, Charles Avenue, Burgess Hill, West Sussex, RH15 9RY, UK burgesshill.communicationsteam@roche.com https://www.roche.co.uk
Sigma-Aldrich Company Ltd. The Old Brickyard, New Rd, Gillingham, Dorset, SP8 4XT ukcustomerrelations@merckgroup.com https://www.sigmaaldrich.com/united-kingdom.html	**Agilent Dako** 5301 Stevens Creek Blvd Santa Clara, CA 95051 United States contact_us@agilent.com https://www.agilent.com
Thermo Fisher Scientific Life Technologies Ltd 3 Fountain Drive Inchinnan Business Park Paisley PA4 9RF, UK ukorders.lifesci@thermofisher.com https://www.thermofisher.com/uk/en/home.html	**GE Healthcare** GE Healthcare Life Sciences Amersham Place Little Chalfont Buckinghamshire HP7 9NA UK https://www.gelifesciences.com/en/gb

Reference

ABDELHAMED, Z. A., NATARAJAN, S., WHEWAY, G., INGLEHEARN, C. F., TOOMES, C., JOHNSON, C. A. & JAGGER, D. J. 2015. The Meckel-Gruber syndrome protein TMEM67 controls basal body positioning and epithelial branching morphogenesis in mice via the non-canonical Wnt pathway. *Dis Model Mech,* 8**,** 527-41.

ABDULLAH, N. L., QUEK, S. C., SETO, K. Y. & TEO, L. L. 2015. Clinics in diagnostic imaging (160). Levocardia with abdominal situs inversus. *Singapore Med J,* 56**,** 198-201; quiz 202.

ABOU ALAIWI, W. A., LO, S. T. & NAULI, S. M. 2009. Primary cilia: highly sophisticated biological sensors. *Sensors (Basel),* 9**,** 7003-20.

AFZELIUS, B. A. 1976. A human syndrome caused by immotile cilia. *Science,* 193**,** 317-9.

ANDERSON, C. T., CASTILLO, A. B., BRUGMANN, S. A., HELMS, J. A., JACOBS, C. R. & STEARNS, T. 2008. Primary cilia: cellular sensors for the skeleton. *Anat Rec (Hoboken),* 291**,** 1074-8.

ANDREU-CERVERA, A., ANSELME, I., KARAM, A., LACLEF, C., CATALA, M. & SCHNEIDER-MAUNOURY, S. 2019. The Ciliopathy Gene Ftm/Rpgrip1l Controls Mouse Forebrain Patterning via Region-Specific Modulation of Hedgehog/Gli Signaling. *J Neurosci,* 39**,** 2398-2415.

ANGERS, S., THORPE, C. J., BIECHELE, T. L., GOLDENBERG, S. J., ZHENG, N., MACCOSS, M. J. & MOON, R. T. 2006. The KLHL12-Cullin-3 ubiquitin ligase negatively regulates the Wnt-beta-catenin pathway by targeting Dishevelled for degradation. *Nat Cell Biol,* 8**,** 348-57.

ARJUMAND, W. & SULTANA, S. 2012. Role of VHL gene mutation in human renal cell carcinoma. *Tumour Biol,* 33**,** 9-16.

ARNOLD, T. & LINKE, D. 2008. The use of detergents to purify membrane proteins. *Curr Protoc Protein Sci,* Chapter 4**,** Unit 4 8 1-4 8 30.

ARQUINT, C., SONNEN, K. F., STIERHOF, Y. D. & NIGG, E. A. 2012. Cell-cycle-regulated expression of STIL controls centriole number in human cells. *J Cell Sci,* 125**,** 1342-52.

ARTS, H. H., BONGERS, E. M., MANS, D. A., VAN BEERSUM, S. E., OUD, M. M., BOLAT, E., SPRUIJT, L., CORNELISSEN, E. A., SCHUURS-HOEIJMAKERS, J. H., DE LEEUW, N., CORMIER-DAIRE, V., BRUNNER, H. G., KNOERS, N. V. & ROEPMAN, R. 2011. C14ORF179 encoding IFT43 is mutated in Sensenbrenner syndrome. *J Med Genet,* 48**,** 390-5.

ARTS, H. H., DOHERTY, D., VAN BEERSUM, S. E., PARISI, M. A., LETTEBOER, S. J., GORDEN, N. T., PETERS, T. A., MARKER, T., VOESENEK, K., KARTONO, A., OZYUREK, H., FARIN, F. M., KROES, H. Y., WOLFRUM, U., BRUNNER, H. G., CREMERS, F. P., GLASS, I. A., KNOERS, N. V. & ROEPMAN, R. 2007. Mutations in the gene encoding the basal body protein RPGRIP1L, a nephrocystin-4 interactor, cause Joubert syndrome. *Nat Genet,* 39**,** 882-8.

ARTS, H. H. & KNOERS, N. V. 2013. Current insights into renal ciliopathies: what can genetics teach us? *Pediatr Nephrol,* 28**,** 863-74.

AVASTHI, P. & MARSHALL, W. F. 2012. Stages of ciliogenesis and regulation of ciliary length. *Differentiation,* 83**,** S30-42.

AVASTHI, P., MASER, R. L. & TRAN, P. V. 2017. Primary Cilia in Cystic Kidney Disease. *Results Probl Cell Differ,* 60**,** 281-321.

BAALA, L., ROMANO, S., KHADDOUR, R., SAUNIER, S., SMITH, U. M., AUDOLLENT, S., OZILOU, C., FAIVRE, L., LAURENT, N., FOLIGUET, B., MUNNICH, A., LYONNET, S., SALOMON, R., ENCHA-RAZAVI, F., GUBLER, M. C., BODDAERT, N., DE LONLAY, P., JOHNSON, C. A., VEKEMANS, M., ANTIGNAC, C. & ATTIE-BITACH, T. 2007. The Meckel-Gruber syndrome gene, MKS3, is mutated in Joubert syndrome. *Am J Hum Genet,* 80**,** 186-94.

BADANO, J. L., LEITCH, C. C., ANSLEY, S. J., MAY-SIMERA, H., LAWSON, S., LEWIS, R. A., BEALES, P. L., DIETZ, H. C., FISHER, S. & KATSANIS, N. 2006. Dissection of epistasis in oligogenic Bardet-Biedl syndrome. *Nature,* 439**,** 326-30.

BAKER, K. & BEALES, P. L. 2009. Making sense of cilia in disease: the human ciliopathies. *Am J Med Genet C Semin Med Genet,* 151C**,** 281-95.

BALESTRA, F. R., STRNAD, P., FLUCKIGER, I. & GONCZY, P. 2013. Discovering regulators of centriole biogenesis through siRNA-based functional genomics in human cells. *Dev Cell,* 25**,** 555-71.

BANGS, F. & ANDERSON, K. V. 2017. Primary Cilia and Mammalian Hedgehog Signaling. *Cold Spring Harb Perspect Biol,* 9.

BARBELANNE, M., SONG, J., AHMADZAI, M. & TSANG, W. Y. 2013. Pathogenic NPHP5 mutations impair protein interaction with Cep290, a prerequisite for ciliogenesis. *Hum Mol Genet,* 22**,** 2482-94.

BARENZ, F., MAYILO, D. & GRUSS, O. J. 2011. Centriolar satellites: busy orbits around the centrosome. *Eur J Cell Biol,* 90**,** 983-9.

BARISIC, I., BOBAN, L., LOANE, M., GARNE, E., WELLESLEY, D., CALZOLARI, E., DOLK, H., ADDOR, M. C., BERGMAN, J. E., BRAZ, P., DRAPER, E. S., HAEUSLER, M., KHOSHNOOD, B., KLUNGSOYR, K., PIERINI, A., QUEISSER-LUFT, A., RANKIN, J., RISSMANN, A. & VERELLEN-DUMOULIN, C. 2015. Meckel-Gruber Syndrome: a population-based study on prevalence, prenatal diagnosis, clinical features, and survival in Europe. *Eur J Hum Genet,* 23**,** 746-52.

BARKER, A. R., RENZAGLIA, K. S., FRY, K. & DAWE, H. R. 2014. Bioinformatic analysis of ciliary transition zone proteins reveals insights into the evolution of ciliopathy networks. *BMC Genomics,* 15**,** 531.

BASTEN, S. G., WILLEKERS, S., VERMAAT, J. S., SLAATS, G. G., VOEST, E. E., VAN DIEST, P. J. & GILES, R. H. 2013. Reduced cilia frequencies in human renal cell carcinomas versus neighboring parenchymal tissue. *Cilia,* 2**,** 2.

BEACHY, P. A., KARHADKAR, S. S. & BERMAN, D. M. 2004. Tissue repair and stem cell renewal in carcinogenesis. *Nature,* 432**,** 324-31.

BEALES, P. & JACKSON, P. K. 2012. Cilia - the prodigal organelle. *Cilia,* 1**,** 1.

BEN-SALEM, S., AL-SHAMSI, A. M., GLEESON, J. G., ALI, B. R. & AL-GAZALI, L. 2014. Mutation spectrum of Joubert syndrome and related disorders among Arabs. *Hum Genome Var,* 1**,** 14020.

BERBARI, N. F., O'CONNOR, A. K., HAYCRAFT, C. J. & YODER, B. K. 2009. The primary cilium as a complex signaling center. *Curr Biol,* 19**,** R526-35.

BERNABE-RUBIO, M. & ALONSO, M. A. 2017. Routes and machinery of primary cilium biogenesis. *Cell Mol Life Sci,* 74**,** 4077-4095.

BESSCHETNOVA, T. Y., KOLPAKOVA-HART, E., GUAN, Y., ZHOU, J., OLSEN, B. R. & SHAH, J. V. 2010. Identification of signaling pathways regulating primary cilium length and flow-mediated adaptation. *Curr Biol,* 20**,** 182-7.

BETLEJA, E. & COLE, D. G. 2010. Ciliary trafficking: CEP290 guards a gated community. *Curr Biol,* 20**,** R928-31.

BISGROVE, B. W. & YOST, H. J. 2006. The roles of cilia in developmental disorders and disease. *Development,* 133**,** 4131-43.

BLACHON, S., CAI, X., ROBERTS, K. A., YANG, K., POLYANOVSKY, A., CHURCH, A. & AVIDOR-REISS, T. 2009. A proximal centriole-like structure is present in Drosophila spermatids and can serve as a model to study centriole duplication. *Genetics,* 182**,** 133-44.

BLACQUE, O. E. & SANDERS, A. A. 2014. Compartments within a compartment: what C. elegans can tell us about ciliary subdomain composition, biogenesis, function, and disease. *Organogenesis,* 10**,** 126-37.

BLAINEY, P., KRZYWINSKI, M. & ALTMAN, N. 2014. Points of significance: replication. *Nat Methods,* 11**,** 879-80.

BLOODGOOD, R. A. 2010. Sensory reception is an attribute of both primary cilia and motile cilia. *J Cell Sci,* 123**,** 505-9.

BOEHLKE, C., BASHKUROV, M., BUESCHER, A., KRICK, T., JOHN, A. K., NITSCHKE, R., WALZ, G. & KUEHN, E. W. 2010. Differential role of Rab proteins in ciliary trafficking: Rab23 regulates smoothened levels. *J Cell Sci,* 123**,** 1460-7.

BOLDT, K., VAN REEUWIJK, J., LU, Q., KOUTROUMPAS, K., NGUYEN, T. M., TEXIER, Y., VAN BEERSUM, S. E., HORN, N., WILLER, J. R., MANS, D. A., DOUGHERTY, G., LAMERS, I. J., COENE, K. L., ARTS, H. H., BETTS, M. J., BEYER, T., BOLAT, E., GLOECKNER, C. J., HAIDARI, K., HETTERSCHIJT, L., IACONIS, D., JENKINS, D., KLOSE, F., KNAPP, B., LATOUR, B., LETTEBOER, S. J., MARCELIS, C. L., MITIC, D., MORLEO, M., OUD, M. M., RIEMERSMA, M., RIX, S., TERHAL, P. A., TOEDT, G., VAN DAM, T. J., DE VRIEZE, E., WISSINGER, Y., WU, K. M., APIC, G., BEALES, P. L., BLACQUE, O. E., GIBSON, T. J., HUYNEN, M. A., KATSANIS, N., KREMER, H., OMRAN, H., VAN WIJK, E., WOLFRUM, U., KEPES, F., DAVIS, E. E., FRANCO, B., GILES, R. H., UEFFING, M., RUSSELL, R. B., ROEPMAN, R. & GROUP, U. K. R. D. 2016. An organelle-specific protein landscape identifies novel diseases and molecular mechanisms. *Nat Commun,* 7**,** 11491.

BRAIMAN, A. & PRIEL, Z. 2008. Efficient mucociliary transport relies on efficient regulation of ciliary beating. *Respir Physiol Neurobiol,* 163**,** 202-7.

BRANCATI, F., DALLAPICCOLA, B. & VALENTE, E. M. 2010. Joubert Syndrome and related disorders. *Orphanet J Rare Dis,* 5**,** 20.

BRANCATI, F., IANNICELLI, M., TRAVAGLINI, L., MAZZOTTA, A., BERTINI, E., BOLTSHAUSER, E., D'ARRIGO, S., EMMA, F., FAZZI, E., GALLIZZI, R., GENTILE, M., LONCAREVIC, D., MEJASKI-BOSNJAK, V., PANTALEONI, C., RIGOLI, L., SALPIETRO, C. D., SIGNORINI, S., STRINGINI, G. R., VERLOES, A., ZABLOKA, D., DALLAPICCOLA, B., GLEESON, J. G., VALENTE, E. M. & INTERNATIONAL, J. S. G. 2009. MKS3/TMEM67 mutations are a major cause of COACH Syndrome, a Joubert Syndrome related disorder with liver involvement. *Hum Mutat,* 30**,** E432-42.

BREUSING, N., ARNDT, J., VOSS, P., BRESGEN, N., WISWEDEL, I., GARDEMANN, A., SIEMS, W. & GRUNE, T. 2009. Inverse correlation of protein oxidation and proteasome activity in liver and lung. *Mech Ageing Dev,* 130**,** 748-53.

BROEKHUIS, J. R., RADEMAKERS, S., BURGHOORN, J. & JANSEN, G. 2013. SQL-1, homologue of the Golgi protein GMAP210, modulates intraflagellar transport in C. elegans. *J Cell Sci,* 126, **1785-95.**

BUTT, T. R., EDAVETTAL, S. C., HALL, J. P. & MATTERN, M. R. 2005. SUMO fusion technology for difficult-to-express proteins. *Protein Expr Purif,* 43**,** 1-9.

CANTAGREL, V., SILHAVY, J. L., BIELAS, S. L., SWISTUN, D., MARSH, S. E., BERTRAND, J. Y., AUDOLLENT, S., ATTIE-BITACH, T., HOLDEN, K. R., DOBYNS, W. B., TRAVER, D., AL-GAZALI, L., ALI, B. R., LINDNER, T. H., CASPARY, T., OTTO, E. A., HILDEBRANDT, F., GLASS, I. A., LOGAN, C. V., JOHNSON, C. A., BENNETT, C., BRANCATI, F., INTERNATIONAL JOUBERT SYNDROME RELATED DISORDERS STUDY, G., VALENTE, E. M., WOODS, C. G. & GLEESON, J. G. 2008. Mutations in the cilia gene ARL13B lead to the classical form of Joubert syndrome. *Am J Hum Genet,* 83**,** 170-9.

CARDENAS-RODRIGUEZ, M. & BADANO, J. L. 2009. Ciliary biology: understanding the cellular and genetic basis of human ciliopathies. *Am J Med Genet C Semin Med Genet,* 151C**,** 263-80.

CHANG, B., KHANNA, H., HAWES, N., JIMENO, D., HE, S., LILLO, C., PARAPURAM, S. K., CHENG, H., SCOTT, A., HURD, R. E., SAYER, J. A., OTTO, E. A., ATTANASIO, M., O'TOOLE, J. F., JIN, G., SHOU, C., HILDEBRANDT, F., WILLIAMS, D. S., HECKENLIVELY, J. R. & SWAROOP, A. 2006. In-frame deletion in a novel centrosomal/ciliary protein CEP290/NPHP6 perturbs its interaction with RPGR and results in early-onset retinal degeneration in the rd16 mouse. *Hum Mol Genet,* 15**,** 1847-57.

CHEN, M. H., WILSON, C. W., LI, Y. J., LAW, K. K., LU, C. S., GACAYAN, R., ZHANG, X., HUI, C. C. & CHUANG, P. T. 2009. Cilium-independent regulation of Gli protein function by Sufu in Hedgehog signaling is evolutionarily conserved. *Genes Dev,* 23**,** 1910-28.

CHHIN, B., NEGRE, D., MERROT, O., PHAM, J., TOURNEUR, Y., RESSNIKOFF, D., JASPERS, M., JORISSEN, M., COSSET, F. L. & BOUVAGNET, P. 2009. Ciliary beating recovery in deficient human airway epithelial cells after lentivirus ex vivo gene therapy. *PLoS Genet,* 5**,** e1000422.

CHIH, B., LIU, P., CHINN, Y., CHALOUNI, C., KOMUVES, L. G., HASS, P. E., SANDOVAL, W. & PETERSON, A. S. 2011. A ciliopathy complex at the transition zone protects the cilia as a privileged membrane domain. *Nat Cell Biol,* 14**,** 61-72.

CHILVERS, M. A. & O'CALLAGHAN, C. 2000. Local mucociliary defence mechanisms. *Paediatr Respir Rev,* 1**,** 27-34.

COLELLA, P., RONZITTI, G. & MINGOZZI, F. 2018. Emerging Issues in AAV-Mediated In Vivo Gene Therapy. *Mol Ther Methods Clin Dev,* 8**,** 87-104.

COLLIN, R. W., DEN HOLLANDER, A. I., VAN DER VELDE-VISSER, S. D., BENNICELLI, J., BENNETT, J. & CREMERS, F. P. 2012. Antisense Oligonucleotide (AON)-based Therapy for Leber Congenital Amaurosis Caused by a Frequent Mutation in CEP290. *Mol Ther Nucleic Acids,* 1**,** e14.

CONDUIT, S. E., DYSON, J. M. & MITCHELL, C. A. 2012. Inositol polyphosphate 5-phosphatases; new players in the regulation of cilia and ciliopathies. *FEBS Lett,* 586**,** 2846-57.

CONSUGAR, M. B., KUBLY, V. J., LAGER, D. J., HOMMERDING, C. J., WONG, W. C., BAKKER, E., GATTONE, V. H., 2ND, TORRES, V. E., BREUNING, M. H. & HARRIS, P. C. 2007. Molecular diagnostics of Meckel-Gruber syndrome highlights phenotypic differences between MKS1 and MKS3. *Hum Genet,* 121**,** 591-9.

COPPIETERS, F., LEFEVER, S., LEROY, B. P. & DE BAERE, E. 2010. CEP290, a gene with many faces: mutation overview and presentation of CEP290base. *Hum Mutat,* 31**,** 1097-108.

CORBIT, K. C., SHYER, A. E., DOWDLE, W. E., GAULDEN, J., SINGLA, V., CHEN, M. H., CHUANG, P. T. & REITER, J. F. 2008. Kif3a constrains beta-catenin-dependent Wnt signalling through dual ciliary and non-ciliary mechanisms. *Nat Cell Biol,* 10**,** 70-6.

CRAIGE, B., TSAO, C. C., DIENER, D. R., HOU, Y., LECHTRECK, K. F., ROSENBAUM, J. L. & WITMAN, G. B. 2010. CEP290 tethers flagellar transition zone microtubules to the membrane and regulates flagellar protein content. *J Cell Biol,* 190**,** 927-40.

CZARNECKI, P. G. & SHAH, J. V. 2012. The ciliary transition zone: from morphology and molecules to medicine. *Trends Cell Biol,* 22**,** 201-10.

DAMMERMANN, A. & MERDES, A. 2002. Assembly of centrosomal proteins and microtubule organization depends on PCM-1. *J Cell Biol,* 159**,** 255-66.

DAWE, H. R., ADAMS, M., WHEWAY, G., SZYMANSKA, K., LOGAN, C. V., NOEGEL, A. A., GULL, K. & JOHNSON, C. A. 2009. Nesprin-2 interacts with meckelin and mediates ciliogenesis via remodelling of the actin cytoskeleton. *J Cell Sci,* 122**,** 2716-26.

DAWE, H. R., SMITH, U. M., CULLINANE, A. R., GERRELLI, D., COX, P., BADANO, J. L., BLAIR-REID, S., SRIRAM, N., KATSANIS, N., ATTIE-BITACH, T., AFFORD, S. C., COPP, A. J., KELLY, D. A., GULL, K. & JOHNSON, C. A. 2007. The Meckel-Gruber Syndrome proteins MKS1 and meckelin interact and are required for primary cilium formation. *Hum Mol Genet,* 16**,** 173-86.

DEAN, S., MOREIRA-LEITE, F., VARGA, V. & GULL, K. 2016. Cilium transition zone proteome reveals compartmentalization and differential dynamics of ciliopathy complexes. *Proc Natl Acad Sci U S A,* 113**,** E5135-43.

DECAPRIO, J. & KOHL, T. O. 2017. Detergent Lysis of Tissue Culture Cells for Immunoprecipitation. *Cold Spring Harb Protoc,* 2017**,** pdb prot098558.

DEDECKER, M., VAN LEENE, J. & DE JAEGER, G. 2015. Unravelling plant molecular machineries through affinity purification coupled to mass spectrometry. *Curr Opin Plant Biol,* 24**,** 1-9.

DELAINE-SMITH, R. M., SITTICHOKECHAIWUT, A. & REILLY, G. C. 2014. Primary cilia respond to fluid shear stress and mediate flow-induced calcium deposition in osteoblasts. *FASEB J,* 28**,** 430-9.

DELOUS, M., BAALA, L., SALOMON, R., LACLEF, C., VIERKOTTEN, J., TORY, K., GOLZIO, C., LACOSTE, T., BESSE, L., OZILOU, C., MOUTKINE, I., HELLMAN, N. E., ANSELME, I., SILBERMANN, F., VESQUE, C., GERHARDT, C., RATTENBERRY, E., WOLF, M. T., GUBLER, M. C., MARTINOVIC, J., ENCHA-RAZAVI, F., BODDAERT, N., GONZALES, M., MACHER, M. A., NIVET, H., CHAMPION, G., BERTHELEME, J. P., NIAUDET, P., MCDONALD, F., HILDEBRANDT, F., JOHNSON, C. A., VEKEMANS, M., ANTIGNAC, C., RUTHER, U., SCHNEIDER-MAUNOURY, S., ATTIE-BITACH, T. & SAUNIER, S. 2007. The ciliary gene RPGRIP1L is mutated in cerebello-oculo-renal syndrome (Joubert syndrome type B) and Meckel syndrome. *Nat Genet,* 39**,** 875-81.

DENU, R. A., SASS, M. M., JOHNSON, J. M., POTTS, G. K., CHOUDHARY, A., COON, J. J. & BURKARD, M. E. 2019. Polo-like kinase 4 maintains centriolar satellite integrity by phosphorylation of centrosomal protein 131 (CEP131). *J Biol Chem,* 294**,** 6531-6549.

DOBELL, C. 1932. *Antony van Leeuwenhoek and his 'Little Animals'* New York, Brace and Co.

DOOLEY, S. J., MCDOUGALD, D. S., FISHER, K. J., BENNICELLI, J. L., MITCHELL, L. G. & BENNETT, J. 2018. Spliceosome-Mediated Pre-mRNA trans-Splicing Can Repair CEP290 mRNA. *Mol Ther Nucleic Acids,* 12**,** 294-308.

DUMMER, A., POELMA, C., DERUITER, M. C., GOUMANS, M. J. & HIERCK, B. P. 2016. Measuring the primary cilium length: improved method for unbiased high-throughput analysis. *Cilia,* 5**,** 7.

DUNN, K. W., KAMOCKA, M. M. & MCDONALD, J. H. 2011. A practical guide to evaluating colocalization in biological microscopy. *Am J Physiol Cell Physiol,* 300**,** C723-42.

DUPUIS-WILLIAMS, P., FLEURY-AUBUSSON, A., DE LOUBRESSE, N. G., GEOFFROY, H., VAYSSIE, L., GALVANI, A., ESPIGAT, A. & ROSSIER, J. 2002. Functional role of epsilon-tubulin in the assembly of the centriolar microtubule scaffold. *J Cell Biol,* 158**,** 1183-93.

DUTCHER, S. K., MORRISSETTE, N. S., PREBLE, A. M., RACKLEY, C. & STANGA, J. 2002. Epsilon-tubulin is an essential component of the centriole. *Mol Biol Cell,* 13**,** 3859-69.

DZHINDZHEV, N. S., TZOLOVSKY, G., LIPINSZKI, Z., SCHNEIDER, S., LATTAO, R., FU, J., DEBSKI, J., DADLEZ, M. & GLOVER, D. M. 2014. Plk4 phosphorylates Ana2 to trigger Sas6 recruitment and procentriole formation. *Curr Biol,* 24**,** 2526-32.

EDVARDSON, S., SHAAG, A., ZENVIRT, S., ERLICH, Y., HANNON, G. J., SHANSKE, A. L., GOMORI, J. M., EKSTEIN, J. & ELPELEG, O. 2010. Joubert syndrome 2 (JBTS2) in Ashkenazi Jews is associated with a TMEM216 mutation. *Am J Hum Genet,* 86**,** 93-7.

EGEBERG, D. L., LETHAN, M., MANGUSO, R., SCHNEIDER, L., AWAN, A., JORGENSEN, T. S., BYSKOV, A. G., PEDERSEN, L. B. & CHRISTENSEN, S. T. 2012. Primary cilia and aberrant cell signaling in epithelial ovarian cancer. *Cilia,* 1**,** 15.

EGGENSCHWILER, J. T. & ANDERSON, K. V. 2007. Cilia and developmental signaling. *Annu Rev Cell Dev Biol,* 23**,** 345-73.

ELEY, L., YATES, L. M. & GOODSHIP, J. A. 2005. Cilia and disease. *Curr Opin Genet Dev,* 15**,** 308-14.

ESTEBAN, M. A., HARTEN, S. K., TRAN, M. G. & MAXWELL, P. H. 2006. Formation of primary cilia in the renal epithelium is regulated by the von Hippel-Lindau tumor suppressor protein. *J Am Soc Nephrol,* 17**,** 1801-6.

EZRATTY, E. J., STOKES, N., CHAI, S., SHAH, A. S., WILLIAMS, S. E. & FUCHS, E. 2011. A role for the primary cilium in Notch signaling and epidermal differentiation during skin development. *Cell,* 145**,** 1129-41.

FALK, N., LOSL, M., SCHRODER, N. & GIESSL, A. 2015. Specialized Cilia in Mammalian Sensory Systems. *Cells,* 4**,** 500-19.

FARNUM, C. E. & WILSMAN, N. J. 2011. Axonemal positioning and orientation in three-dimensional space for primary cilia: what is known, what is assumed, and what needs clarification. *Dev Dyn,* 240**,** 2405-31.

FERLAND, R. J., EYAID, W., COLLURA, R. V., TULLY, L. D., HILL, R. S., AL-NOURI, D., AL-RUMAYYAN, A., TOPCU, M., GASCON, G., BODELL, A., SHUGART, Y. Y., RUVOLO, M. & WALSH, C. A. 2004. Abnormal cerebellar development and axonal decussation due to mutations in AHI1 in Joubert syndrome. *Nat Genet,* 36**,** 1008-13.

FLEMING, L. R., DOHERTY, D. A., PARISI, M. A., GLASS, I. A., BRYANT, J., FISCHER, R., TURKBEY, B., CHOYKE, P., DARYANANI, K., VEMULAPALLI, M., MULLIKIN, J. C., MALICDAN, M. C., VILBOUX, T., SAYER, J. A., GAHL, W. A. & GUNAY-AYGUN, M. 2017.

Prospective Evaluation of Kidney Disease in Joubert Syndrome. *Clin J Am Soc Nephrol,* 12**,** 1962-1973.

FOLLIT, J. A., LI, L., VUCICA, Y. & PAZOUR, G. J. 2010. The cytoplasmic tail of fibrocystin contains a ciliary targeting sequence. *J Cell Biol,* 188**,** 21-8.

FOLLIT, J. A., XU, F., KEADY, B. T. & PAZOUR, G. J. 2009. Characterization of mouse IFT complex B. *Cell Motil Cytoskeleton,* 66**,** 457-68.

FORSYTHE, E. & BEALES, P. L. 2013. Bardet-Biedl syndrome. *Eur J Hum Genet,* 21**,** 8-13.

FRANCIS, S. S., SFAKIANOS, J., LO, B. & MELLMAN, I. 2011. A hierarchy of signals regulates entry of membrane proteins into the ciliary membrane domain in epithelial cells. *J Cell Biol,* 193**,** 219-33.

FRETZAYAS, A. & MOUSTAKI, M. 2016. Clinical spectrum of primary ciliary dyskinesia in childhood. *World J Clin Pediatr,* 5**,** 57-62.

FU, W., WANG, L., KIM, S., LI, J. & DYNLACHT, B. D. 2016. Role for the IFT-A Complex in Selective Transport to the Primary Cilium. *Cell Rep,* 17**,** 1505-1517.

GARANTO, A., CHUNG, D. C., DUIJKERS, L., CORRAL-SERRANO, J. C., MESSCHAERT, M., XIAO, R., BENNETT, J., VANDENBERGHE, L. H. & COLLIN, R. W. 2016. In vitro and in vivo rescue of aberrant splicing in CEP290-associated LCA by antisense oligonucleotide delivery. *Hum Mol Genet,* 25**,** 2552-2563.

GARCIA-GONZALO, F. R., CORBIT, K. C., SIREROL-PIQUER, M. S., RAMASWAMI, G., OTTO, E. A., NORIEGA, T. R., SEOL, A. D., ROBINSON, J. F., BENNETT, C. L., JOSIFOVA, D. J., GARCIA-VERDUGO, J. M., KATSANIS, N., HILDEBRANDT, F. & REITER, J. F. 2011. A transition zone complex regulates mammalian ciliogenesis and ciliary membrane composition. *Nat Genet,* 43**,** 776-84.

GARCIA-GONZALO, F. R. & REITER, J. F. 2012. Scoring a backstage pass: mechanisms of ciliogenesis and ciliary access. *J Cell Biol,* 197**,** 697-709.

GARCIA-GONZALO, F. R. & REITER, J. F. 2017. Open Sesame: How Transition Fibers and the Transition Zone Control Ciliary Composition. *Cold Spring Harb Perspect Biol,* 9.

GERACE, E. & MOAZED, D. 2014. Coimmunoprecipitation of proteins from yeast. *Methods Enzymol,* 541**,** 13-26.

GERARD, X., PERRAULT, I., HANEIN, S., SILVA, E., BIGOT, K., DEFOORT-DELHEMMES, S., RIO, M., MUNNICH, A., SCHERMAN, D., KAPLAN, J., KICHLER, A. & ROZET, J. M. 2012. AON-mediated Exon Skipping Restores Ciliation in Fibroblasts Harboring the Common Leber Congenital Amaurosis CEP290 Mutation. *Mol Ther Nucleic Acids,* 1**,** e29.

GERDES, J. M., DAVIS, E. E. & KATSANIS, N. 2009. The vertebrate primary cilium in development, homeostasis, and disease. *Cell,* 137**,** 32-45.

GERHARDT, C., LEU, T., LIER, J. M. & RUTHER, U. 2016. The cilia-regulated proteasome and its role in the development of ciliopathies and cancer. *Cilia,* 5**,** 14.

GERHARDT, C., LIER, J. M., BURMUHL, S., STRUCHTRUP, A., DEUTSCHMANN, K., VETTER, M., LEU, T., REEG, S., GRUNE, T. & RUTHER, U. 2015. The transition zone protein Rpgrip1l regulates proteasomal activity at the primary cilium. *J Cell Biol,* 210**,** 115-33.

GHEBER, L., PRIEL, Z., AFLALO, C. & SHOSHAN-BARMATZ, V. 1995. Extracellular ATP binding proteins as potential receptors in mucociliary epithelium: characterization using [32P]3'-O-(4-benzoyl)benzoyl ATP, a photoaffinity label. *J Membr Biol,* 147**,** 83-93.

GHOLKAR, A. A., SENESE, S., LO, Y. C., CAPRI, J., DEARDORFF, W. J., DHARMARAJAN, H., CONTRERAS, E., HODARA, E., WHITELEGGE, J. P., JACKSON, P. K. & TORRES, J. Z.

2015. Tctex1d2 associates with short-rib polydactyly syndrome proteins and is required for ciliogenesis. *Cell Cycle,* 14**,** 1116-25.

GHOSSOUB, R., HU, Q., FAILLER, M., ROUYEZ, M. C., SPITZBARTH, B., MOSTOWY, S., WOLFRUM, U., SAUNIER, S., COSSART, P., JAMESNELSON, W. & BENMERAH, A. 2013. Septins 2, 7 and 9 and MAP4 colocalize along the axoneme in the primary cilium and control ciliary length. *J Cell Sci,* 126**,** 2583-94.

GILISSEN, C., ARTS, H. H., HOISCHEN, A., SPRUIJT, L., MANS, D. A., ARTS, P., VAN LIER, B., STEEHOUWER, M., VAN REEUWIJK, J., KANT, S. G., ROEPMAN, R., KNOERS, N. V., VELTMAN, J. A. & BRUNNER, H. G. 2010. Exome sequencing identifies WDR35 variants involved in Sensenbrenner syndrome. *Am J Hum Genet,* 87**,** 418-23.

GOETZ, S. C. & ANDERSON, K. V. 2010. The primary cilium: a signalling centre during vertebrate development. *Nat Rev Genet,* 11**,** 331-44.

GOGGOLIDOU, P., HADJIRIN, N. F., BAK, A., PAPAKRIVOPOULOU, E., HILTON, H., NORRIS, D. P. & DEAN, C. H. 2014. Atmin mediates kidney morphogenesis by modulating Wnt signaling. *Hum Mol Genet,* 23**,** 5303-16.

GOGGOLIDOU, P. & WILSON, P. D. 2016. Novel biomarkers in kidney disease: roles for cilia, Wnt signalling and ATMIN in polycystic kidney disease. *Biochem Soc Trans,* 44**,** 1745-1751.

GOMEZ-ORTE, E., SAENZ-NARCISO, B., MORENO, S. & CABELLO, J. 2013. Multiple functions of the noncanonical Wnt pathway. *Trends Genet,* 29**,** 545-53.

GONCALVES, J. & PELLETIER, L. 2017. The Ciliary Transition Zone: Finding the Pieces and Assembling the Gate. *Mol Cells,* 40**,** 243-253.

GRADILONE, S. A., PISARELLO, M. J. L. & LARUSSO, N. F. 2017. Primary Cilia in Tumor Biology: The Primary Cilium as a Therapeutic Target in Cholangiocarcinoma. *Curr Drug Targets,* 18**,** 958-963.

GRADILONE, S. A., RADTKE, B. N., BOGERT, P. S., HUANG, B. Q., GAJDOS, G. B. & LARUSSO, N. F. 2013. HDAC6 inhibition restores ciliary expression and decreases tumor growth. *Cancer Res,* 73**,** 2259-70.

GROOPMAN, E. E., RASOULY, H. M. & GHARAVI, A. G. 2018. Genomic medicine for kidney disease. *Nat Rev Nephrol,* 14**,** 83-104.

GUICHARD, P., HAMEL, V., LE GUENNEC, M., BANTERLE, N., IACOVACHE, I., NEMCIKOVA, V., FLUCKIGER, I., GOLDIE, K. N., STAHLBERG, H., LEVY, D., ZUBER, B. & GONCZY, P. 2017. Cell-free reconstitution reveals centriole cartwheel assembly mechanisms. *Nat Commun,* 8**,** 14813.

GUPTA, G. D., COYAUD, E., GONCALVES, J., MOJARAD, B. A., LIU, Y., WU, Q., GHEIRATMAND, L., COMARTIN, D., TKACH, J. M., CHEUNG, S. W., BASHKUROV, M., HASEGAN, M., KNIGHT, J. D., LIN, Z. Y., SCHUELER, M., HILDEBRANDT, F., MOFFAT, J., GINGRAS, A. C., RAUGHT, B. & PELLETIER, L. 2015. A Dynamic Protein Interaction Landscape of the Human Centrosome-Cilium Interface. *Cell,* 163**,** 1484-99.

H. LODISH, A. B., P. MATSUDAIRA, C. A. KAISER, M. KRIEGER, M. P. SCOTT, S. L. ZIPURSKY, J. DARNELL 2007. *Molecular Cell Biology,* New York, Freeman and Company.

HABAS, R. & HE, X. 2007. Cell signaling: moving to a Wnt-Rap. *Curr Biol,* 17**,** R474-7.

HABBIG, S., BARTRAM, M. P., MULLER, R. U., SCHWARZ, R., ANDRIOPOULOS, N., CHEN, S., SAGMULLER, J. G., HOEHNE, M., BURST, V., LIEBAU, M. C., REINHARDT, H. C., BENZING, T. & SCHERMER, B. 2011. NPHP4, a cilia-associated protein, negatively regulates the Hippo pathway. *J Cell Biol,* 193**,** 633-42.

HARTILL, V., SZYMANSKA, K., SHARIF, S. M., WHEWAY, G. & JOHNSON, C. A. 2017. Meckel-Gruber Syndrome: An Update on Diagnosis, Clinical Management, and Research Advances. *Front Pediatr,* 5**,** 244.

HAYCRAFT, C. J., BANIZS, B., AYDIN-SON, Y., ZHANG, Q., MICHAUD, E. J. & YODER, B. K. 2005. Gli2 and Gli3 localize to cilia and require the intraflagellar transport protein polaris for processing and function. *PLoS Genet,* 1**,** e53.

HE, M., AGBU, S. & ANDERSON, K. V. 2017. Microtubule Motors Drive Hedgehog Signaling in Primary Cilia. *Trends Cell Biol,* 27**,** 110-125.

HE, X., SEMENOV, M., TAMAI, K. & ZENG, X. 2004. LDL receptor-related proteins 5 and 6 in Wnt/beta-catenin signaling: arrows point the way. *Development,* 131**,** 1663-77.

HIGH, F. A. & EPSTEIN, J. A. 2008. The multifaceted role of Notch in cardiac development and disease. *Nat Rev Genet,* 9**,** 49-61.

HILDEBRANDT, F., ATTANASIO, M. & OTTO, E. 2009. Nephronophthisis: disease mechanisms of a ciliopathy. *J Am Soc Nephrol,* 20**,** 23-35.

HILDEBRANDT, F. & ZHOU, W. 2007. Nephronophthisis-associated ciliopathies. *J Am Soc Nephrol,* 18**,** 1855-71.

HIRANO, T., KATOH, Y. & NAKAYAMA, K. 2017. Intraflagellar transport-A complex mediates ciliary entry and retrograde trafficking of ciliary G protein-coupled receptors. *Mol Biol Cell,* 28**,** 429-439.

HIROKAWA, N., TANAKA, Y., OKADA, Y. & TAKEDA, S. 2006. Nodal flow and the generation of left-right asymmetry. *Cell,* 125**,** 33-45.

HIROTA, Y., MEUNIER, A., HUANG, S., SHIMOZAWA, T., YAMADA, O., KIDA, Y. S., INOUE, M., ITO, T., KATO, H., SAKAGUCHI, M., SUNABORI, T., NAKAYA, M. A., NONAKA, S., OGURA, T., HIGUCHI, H., OKANO, H., SPASSKY, N. & SAWAMOTO, K. 2010. Planar polarity of multiciliated ependymal cells involves the anterior migration of basal bodies regulated by non-muscle myosin II. *Development,* 137**,** 3037-46.

HOLLANDER, D. A., SARFARAZI, M., STOILOV, I., WOOD, I. S., FREDRICK, D. R. & ALVARADO, J. A. 2006. Genotype and phenotype correlations in congenital glaucoma: CYP1B1 mutations, goniodysgenesis, and clinical characteristics. *Am J Ophthalmol,* 142**,** 993-1004.

HOPP, K., HEYER, C. M., HOMMERDING, C. J., HENKE, S. A., SUNDSBAK, J. L., PATEL, S., PATEL, P., CONSUGAR, M. B., CZARNECKI, P. G., GLIEM, T. J., TORRES, V. E., ROSSETTI, S. & HARRIS, P. C. 2011. B9D1 is revealed as a novel Meckel syndrome (MKS) gene by targeted exon-enriched next-generation sequencing and deletion analysis. *Hum Mol Genet,* 20**,** 2524-34.

HOSSAIN, T., KAPPELMAN, M. D., PEREZ-ATAYDE, A. R., YOUNG, G. J., HUTTNER, K. M. & CHRISTOU, H. 2003. Primary ciliary dyskinesia as a cause of neonatal respiratory distress: implications for the neonatologist. *J Perinatol,* 23**,** 684-7.

HSIAO, Y. C., TUZ, K. & FERLAND, R. J. 2012. Trafficking in and to the primary cilium. *Cilia,* 1**,** 4.

HU, Q., MILENKOVIC, L., JIN, H., SCOTT, M. P., NACHURY, M. V., SPILIOTIS, E. T. & NELSON, W. J. 2010. A septin diffusion barrier at the base of the primary cilium maintains ciliary membrane protein distribution. *Science,* 329**,** 436-9.

HU, Q. & NELSON, W. J. 2011. Ciliary diffusion barrier: the gatekeeper for the primary cilium compartment. *Cytoskeleton (Hoboken),* 68**,** 313-24.

HUA, K. & FERLAND, R. J. 2018. Primary Cilia Reconsidered in the Context of Ciliopathies: Extraciliary and Ciliary Functions of Cilia Proteins Converge on a Polarity theme? *Bioessays,* 40**,** e1700132.

HUANG, K., DIENER, D. R. & ROSENBAUM, J. L. 2009a. The ubiquitin conjugation system is involved in the disassembly of cilia and flagella. *J Cell Biol,* 186**,** 601-13.

HUANG, L., SZYMANSKA, K., JENSEN, V. L., JANECKE, A. R., INNES, A. M., DAVIS, E. E., FROSK, P., LI, C., WILLER, J. R., CHODIRKER, B. N., GREENBERG, C. R., MCLEOD, D. R., BERNIER, F. P., CHUDLEY, A. E., MULLER, T., SHBOUL, M., LOGAN, C. V., LOUCKS, C. M., BEAULIEU, C. L., BOWIE, R. V., BELL, S. M., ADKINS, J., ZUNIGA, F. I., ROSS, K. D., WANG, J., BAN, M. R., BECKER, C., NURNBERG, P., DOUGLAS, S., CRAFT, C. M., AKIMENKO, M. A., HEGELE, R. A., OBER, C., UTERMANN, G., BOLZ, H. J., BULMAN, D. E., KATSANIS, N., BLACQUE, O. E., DOHERTY, D., PARBOOSINGH, J. S., LEROUX, M. R., JOHNSON, C. A. & BOYCOTT, K. M. 2011. TMEM237 is mutated in individuals with a Joubert syndrome related disorder and expands the role of the TMEM family at the ciliary transition zone. *Am J Hum Genet,* 89**,** 713-30.

HUANG, S., HIROTA, Y. & SAWAMOTO, K. 2009b. Various facets of vertebrate cilia: motility, signaling, and role in adult neurogenesis. *Proc Jpn Acad Ser B Phys Biol Sci,* 85**,** 324-36.

HUANGFU, D. & ANDERSON, K. V. 2005. Cilia and Hedgehog responsiveness in the mouse. *Proc Natl Acad Sci U S A,* 102**,** 11325-30.

HUANGFU, D., LIU, A., RAKEMAN, A. S., MURCIA, N. S., NISWANDER, L. & ANDERSON, K. V. 2003. Hedgehog signalling in the mouse requires intraflagellar transport proteins. *Nature,* 426**,** 83-7.

HUMKE, E. W., DORN, K. V., MILENKOVIC, L., SCOTT, M. P. & ROHATGI, R. 2010. The output of Hedgehog signaling is controlled by the dynamic association between Suppressor of Fused and the Gli proteins. *Genes Dev,* 24**,** 670-82.

IANNICELLI, M., BRANCATI, F., MOUGOU-ZERELLI, S., MAZZOTTA, A., THOMAS, S., ELKHARTOUFI, N., TRAVAGLINI, L., GOMES, C., ARDISSINO, G. L., BERTINI, E., BOLTSHAUSER, E., CASTORINA, P., D'ARRIGO, S., FISCHETTO, R., LEROY, B., LOGET, P., BONNIERE, M., STARCK, L., TANTAU, J., GENTILIN, B., MAJORE, S., SWISTUN, D., FLORI, E., LALATTA, F., PANTALEONI, C., PENZIEN, J., GRAMMATICO, P., INTERNATIONAL, J. S. G., DALLAPICCOLA, B., GLEESON, J. G., ATTIE-BITACH, T. & VALENTE, E. M. 2010. Novel TMEM67 mutations and genotype-phenotype correlates in meckelin-related ciliopathies. *Hum Mutat,* 31**,** E1319-31.

INGHAM, P. W., TAYLOR, A. M. & NAKANO, Y. 1991. Role of the Drosophila patched gene in positional signalling. *Nature,* 353**,** 184-7.

ISHIKAWA, H. & MARSHALL, W. F. 2011. Ciliogenesis: building the cell's antenna. *Nat Rev Mol Cell Biol,* 12**,** 222-34.

IZAWA, I., GOTO, H., KASAHARA, K. & INAGAKI, M. 2015. Current topics of functional links between primary cilia and cell cycle. *Cilia,* 4**,** 12.

JAFFE, A. B. & HALL, A. 2005. Rho GTPases: biochemistry and biology. *Annu Rev Cell Dev Biol,* 21**,** 247-69.

JAMES, M. T., HEMMELGARN, B. R. & TONELLI, M. 2010. Early recognition and prevention of chronic kidney disease. *Lancet,* 375**,** 1296-309.

JENSEN, V. L., LI, C., BOWIE, R. V., CLARKE, L., MOHAN, S., BLACQUE, O. E. & LEROUX, M. R. 2015. Formation of the transition zone by Mks5/Rpgrip1L establishes a ciliary zone of

exclusion (CIZE) that compartmentalises ciliary signalling proteins and controls PIP2 ciliary abundance. *EMBO J,* 34**,** 2537-56.

JIANG, J. & HUI, C. C. 2008. Hedgehog signaling in development and cancer. *Dev Cell,* 15**,** 801-12.

JONES, C., ROPER, V. C., FOUCHER, I., QIAN, D., BANIZS, B., PETIT, C., YODER, B. K. & CHEN, P. 2008. Ciliary proteins link basal body polarization to planar cell polarity regulation. *Nat Genet,* 40**,** 69-77.

JOUBERT, M., EISENRING, J. J. & ANDERMANN, F. 1968. Familial dysgenesis of the vermis: a syndrome of hyperventilation, abnormal eye movements and retardation. *Neurology,* 18**,** 302-3.

KALDERON, D. 2002. Similarities between the Hedgehog and Wnt signaling pathways. *Trends Cell Biol,* 12**,** 523-31.

KARNER, C. M., CHIRUMAMILLA, R., AOKI, S., IGARASHI, P., WALLINGFORD, J. B. & CARROLL, T. J. 2009. Wnt9b signaling regulates planar cell polarity and kidney tubule morphogenesis. *Nat Genet,* 41**,** 793-9.

KE, Y. N. & YANG, W. X. 2014. Primary cilium: an elaborate structure that blocks cell division? *Gene,* 547**,** 175-85.

KEELING, J., TSIOKAS, L. & MASKEY, D. 2016. Cellular Mechanisms of Ciliary Length Control. *Cells,* 5.

KHAN, S. A., MUHAMMAD, N., KHAN, M. A., KAMAL, A., REHMAN, Z. U. & KHAN, S. 2016. Genetics of human Bardet-Biedl syndrome, an updates. *Clin Genet,* 90**,** 3-15.

KHEIR, A. E., IMAM, A., OMER, I. M., HASSAN, I. M., ELAMIN, S. A., AWADALLA, E. A., GADALLA, M. H. & HAMDOON, T. A. 2012. Meckel-Gruber syndrome: A rare and lethal anomaly. *Sudan J Paediatr,* 12**,** 93-6.

KILANDER, M. B. C., WANG, C. H., CHANG, C. H., NESTOR, J. E., HEROLD, K., TSAI, J. W., NESTOR, M. W. & LIN, Y. C. 2018. A rare human CEP290 variant disrupts the molecular integrity of the primary cilium and impairs Sonic Hedgehog machinery. *Sci Rep,* 8**,** 17335.

KIM, J., KRISHNASWAMI, S. R. & GLEESON, J. G. 2008. CEP290 interacts with the centriolar satellite component PCM-1 and is required for Rab8 localization to the primary cilium. *Hum Mol Genet,* 17**,** 3796-805.

KIM, K., LEE, K. & RHEE, K. 2012. CEP90 is required for the assembly and centrosomal accumulation of centriolar satellites, which is essential for primary cilia formation. *PLoS One,* 7**,** e48196.

KIM, M., KIM, M., LEE, M. S., KIM, C. H. & LIM, D. S. 2014. The MST1/2-SAV1 complex of the Hippo pathway promotes ciliogenesis. *Nat Commun,* 5**,** 5370.

KIM, M., KIM, T., JOHNSON, R. L. & LIM, D. S. 2015. Transcriptional co-repressor function of the hippo pathway transducers YAP and TAZ. *Cell Rep,* 11**,** 270-82.

KIM, S. & TSIOKAS, L. 2011. Cilia and cell cycle re-entry: more than a coincidence. *Cell Cycle,* 10**,** 2683-90.

KIM, Y. J., KIM, S., JUNG, Y., JUNG, E., KWON, H. J. & KIM, J. 2018. Eupatilin rescues ciliary transition zone defects to ameliorate ciliopathy-related phenotypes. *J Clin Invest,* 128**,** 3642-3648.

KINZEL, D., BOLDT, K., DAVIS, E. E., BURTSCHER, I., TRUMBACH, D., DIPLAS, B., ATTIE-BITACH, T., WURST, W., KATSANIS, N., UEFFING, M. & LICKERT, H. 2010. Pitchfork regulates primary cilia disassembly and left-right asymmetry. *Dev Cell,* 19**,** 66-77.

KITAGAWA, D., VAKONAKIS, I., OLIERIC, N., HILBERT, M., KELLER, D., OLIERIC, V., BORTFELD, M., ERAT, M. C., FLUCKIGER, I., GONCZY, P. & STEINMETZ, M. O. 2011. Structural basis of the 9-fold symmetry of centrioles. *Cell,* 144**,** 364-75.

KLINGER, M., WANG, W., KUHNS, S., BARENZ, F., DRAGER-MEURER, S., PEREIRA, G. & GRUSS, O. J. 2014. The novel centriolar satellite protein SSX2IP targets Cep290 to the ciliary transition zone. *Mol Biol Cell,* 25**,** 495-507.

KLYMENKO, T., PAPP, B., FISCHLE, W., KOCHER, T., SCHELDER, M., FRITSCH, C., WILD, B., WILM, M. & MULLER, J. 2006. A Polycomb group protein complex with sequence-specific DNA-binding and selective methyl-lysine-binding activities. *Genes Dev,* 20**,** 1110-22.

KNODLER, A., FENG, S., ZHANG, J., ZHANG, X., DAS, A., PERANEN, J. & GUO, W. 2010. Coordination of Rab8 and Rab11 in primary ciliogenesis. *Proc Natl Acad Sci U S A,* 107**,** 6346-51.

KOBAYASHI, T. & DYNLACHT, B. D. 2011. Regulating the transition from centriole to basal body. *J Cell Biol,* 193**,** 435-44.

KOBAYASHI, T., KIM, S., LIN, Y. C., INOUE, T. & DYNLACHT, B. D. 2014. The CP110-interacting proteins Talpid3 and Cep290 play overlapping and distinct roles in cilia assembly. *J Cell Biol,* 204**,** 215-29.

KODANI, A., YU, T. W., JOHNSON, J. R., JAYARAMAN, D., JOHNSON, T. L., AL-GAZALI, L., SZTRIHA, L., PARTLOW, J. N., KIM, H., KRUP, A. L., DAMMERMANN, A., KROGAN, N. J., WALSH, C. A. & REITER, J. F. 2015. Centriolar satellites assemble centrosomal microcephaly proteins to recruit CDK2 and promote centriole duplication. *Elife,* 4.

KOHN, A. D. & MOON, R. T. 2005. Wnt and calcium signaling: beta-catenin-independent pathways. *Cell Calcium,* 38**,** 439-46.

KOMIYA, Y. & HABAS, R. 2008. Wnt signal transduction pathways. *Organogenesis,* 4**,** 68-75.

KONG, J. H., YANG, L., DESSAUD, E., CHUANG, K., MOORE, D. M., ROHATGI, R., BRISCOE, J. & NOVITCH, B. G. 2015. Notch activity modulates the responsiveness of neural progenitors to sonic hedgehog signaling. *Dev Cell,* 33**,** 373-87.

KONIG, J. C., TITIENI, A., KONRAD, M. & CONSORTIUM, N. 2018. Network for Early Onset Cystic Kidney Diseases-A Comprehensive Multidisciplinary Approach to Hereditary Cystic Kidney Diseases in Childhood. *Front Pediatr,* 6**,** 24.

KREBS, L. T., IWAI, N., NONAKA, S., WELSH, I. C., LAN, Y., JIANG, R., SAIJOH, Y., O'BRIEN, T. P., HAMADA, H. & GRIDLEY, T. 2003. Notch signaling regulates left-right asymmetry determination by inducing Nodal expression. *Genes Dev,* 17**,** 1207-12.

KUBO, A., SASAKI, H., YUBA-KUBO, A., TSUKITA, S. & SHIINA, N. 1999. Centriolar satellites: molecular characterization, ATP-dependent movement toward centrioles and possible involvement in ciliogenesis. *J Cell Biol,* 147**,** 969-80.

KUNIMOTO, K., BAYLY, R. D., VLADAR, E. K., VONDERFECHT, T., GALLAGHER, A. R. & AXELROD, J. D. 2017. Disruption of Core Planar Cell Polarity Signaling Regulates Renal Tubule Morphogenesis but Is Not Cystogenic. *Curr Biol,* 27**,** 3120-3131 e4.

KYTTALA, M., TALLILA, J., SALONEN, R., KOPRA, O., KOHLSCHMIDT, N., PAAVOLA-SAKKI, P., PELTONEN, L. & KESTILA, M. 2006. MKS1, encoding a component of the flagellar apparatus basal body proteome, is mutated in Meckel syndrome. *Nat Genet,* 38**,** 155-7.

LABETA, M. O., FERNANDEZ, N. & FESTENSTEIN, H. 1988. Solubilisation effect of Nonidet P-40, triton X-100 and CHAPS in the detection of MHC-like glycoproteins. *J Immunol Methods,* 112**,** 133-8.

LAI, C. K., GUPTA, N., WEN, X., RANGELL, L., CHIH, B., PETERSON, A. S., BAZAN, J. F., LI, L. & SCALES, S. J. 2011. Functional characterization of putative cilia genes by high-content analysis. *Mol Biol Cell,* 22**,** 1104-19.

LAMBACHER, N. J., BRUEL, A. L., VAN DAM, T. J., SZYMANSKA, K., SLAATS, G. G., KUHNS, S., MCMANUS, G. J., KENNEDY, J. E., GAFF, K., WU, K. M., VAN DER LEE, R., BURGLEN, L., DOUMMAR, D., RIVIERE, J. B., FAIVRE, L., ATTIE-BITACH, T., SAUNIER, S., CURD, A., PECKHAM, M., GILES, R. H., JOHNSON, C. A., HUYNEN, M. A., THAUVIN-ROBINET, C. & BLACQUE, O. E. 2016. TMEM107 recruits ciliopathy proteins to subdomains of the ciliary transition zone and causes Joubert syndrome. *Nat Cell Biol,* 18**,** 122-31.

LANCASTER, M. A., SCHROTH, J. & GLEESON, J. G. 2011. Subcellular spatial regulation of canonical Wnt signalling at the primary cilium. *Nat Cell Biol,* 13**,** 700-7.

LANE, E. H. A. D. 1999. *Using antibodies,* NY, USA, Cold Spring Harbor Laboratory Press.

LANE, N. 2015. The unseen world: reflections on Leeuwenhoek (1677) 'Concerning little animals'. *Philos Trans R Soc Lond B Biol Sci,* 370.

LEE, J. H., SILHAVY, J. L., LEE, J. E., AL-GAZALI, L., THOMAS, S., DAVIS, E. E., BIELAS, S. L., HILL, K. J., IANNICELLI, M., BRANCATI, F., GABRIEL, S. B., RUSS, C., LOGAN, C. V., SHARIF, S. M., BENNETT, C. P., ABE, M., HILDEBRANDT, F., DIPLAS, B. H., ATTIE-BITACH, T., KATSANIS, N., RAJAB, A., KOUL, R., SZTRIHA, L., WATERS, E. R., FERRO-NOVICK, S., WOODS, C. G., JOHNSON, C. A., VALENTE, E. M., ZAKI, M. S. & GLEESON, J. G. 2012. Evolutionarily assembled cis-regulatory module at a human ciliopathy locus. *Science,* 335**,** 966-9.

LEE, S. Y., JANG, C. & LEE, K. A. 2014. Polo-like kinases (plks), a key regulator of cell cycle and new potential target for cancer therapy. *Dev Reprod,* 18**,** 65-71.

LEHMAN, J. M., MICHAUD, E. J., SCHOEB, T. R., AYDIN-SON, Y., MILLER, M. & YODER, B. K. 2008. The Oak Ridge Polycystic Kidney mouse: modeling ciliopathies of mice and men. *Dev Dyn,* 237**,** 1960-71.

LEIGH, M. W., PITTMAN, J. E., CARSON, J. L., FERKOL, T. W., DELL, S. D., DAVIS, S. D., KNOWLES, M. R. & ZARIWALA, M. A. 2009. Clinical and genetic aspects of primary ciliary dyskinesia/Kartagener syndrome. *Genet Med,* 11**,** 473-87.

LEIGHTNER, A. C., HOMMERDING, C. J., PENG, Y., SALISBURY, J. L., GAINULLIN, V. G., CZARNECKI, P. G., SUSSMAN, C. R. & HARRIS, P. C. 2013. The Meckel syndrome protein meckelin (TMEM67) is a key regulator of cilia function but is not required for tissue planar polarity. *Hum Mol Genet,* 22**,** 2024-40.

LEITCH, C. C., ZAGHLOUL, N. A., DAVIS, E. E., STOETZEL, C., DIAZ-FONT, A., RIX, S., ALFADHEL, M., LEWIS, R. A., EYAID, W., BANIN, E., DOLLFUS, H., BEALES, P. L., BADANO, J. L. & KATSANIS, N. 2008. Hypomorphic mutations in syndromic encephalocele genes are associated with Bardet-Biedl syndrome. *Nat Genet,* 40, 443-8.

LEMAIRE, M. & PAREKH, R. S. 2017. A Perspective on Inherited Kidney Disease: Lessons for Practicing Nephrologists. *Clin J Am Soc Nephrol,* 12**,** 1914-1916.

LI, A., SAITO, M., CHUANG, J. Z., TSENG, Y. Y., DEDESMA, C., TOMIZAWA, K., KAITSUKA, T. & SUNG, C. H. 2011. Ciliary transition zone activation of phosphorylated Tctex-1 controls ciliary resorption, S-phase entry and fate of neural progenitors. *Nat Cell Biol,* 13**,** 402-11.

LI, C., JENSEN, V. L., PARK, K., KENNEDY, J., GARCIA-GONZALO, F. R., ROMANI, M., DE MORI, R., BRUEL, A. L., GAILLARD, D., DORAY, B., LOPEZ, E., RIVIERE, J. B., FAIVRE, L., THAUVIN-ROBINET, C., REITER, J. F., BLACQUE, O. E., VALENTE, E. M. & LEROUX, M. R. 2016. MKS5 and CEP290 Dependent Assembly Pathway of the Ciliary Transition Zone. *PLoS Biol,* 14**,** e1002416.

LIEM, K. F., JR., ASHE, A., HE, M., SATIR, P., MORAN, J., BEIER, D., WICKING, C. & ANDERSON, K. V. 2012. The IFT-A complex regulates Shh signaling through cilia structure and membrane protein trafficking. *J Cell Biol,* 197**,** 789-800.

LIN, H., GUO, S. & DUTCHER, S. K. 2018. RPGRIP1L helps to establish the ciliary gate for entry of proteins. *J Cell Sci,* 131.

LIN, J. S. & LAI, E. M. 2017. Protein-Protein Interactions: Co-Immunoprecipitation. *Methods Mol Biol,* 1615**,** 211-219.

LIN, S. H. & GUIDOTTI, G. 2009. Purification of membrane proteins. *Methods Enzymol,* 463**,** 619-29.

LIN, Y. C., CHANG, C. W., HSU, W. B., TANG, C. J., LIN, Y. N., CHOU, E. J., WU, C. T. & TANG, T. K. 2013. Human microcephaly protein CEP135 binds to hSAS-6 and CPAP, and is required for centriole assembly. *EMBO J,* 32**,** 1141-54.

LISTE-CALLEJA, L., LECINA, M., LOPEZ-REPULLO, J., ALBIOL, J., SOLA, C. & CAIRO, J. J. 2015. Lactate and glucose concomitant consumption as a self-regulated pH detoxification mechanism in HEK293 cell cultures. *Appl Microbiol Biotechnol,* 99**,** 9951-60.

LIU, A., WANG, B. & NISWANDER, L. A. 2005. Mouse intraflagellar transport proteins regulate both the activator and repressor functions of Gli transcription factors. *Development,* 132**,** 3103-11.

LIU, Y. P., TSAI, I. C., MORLEO, M., OH, E. C., LEITCH, C. C., MASSA, F., LEE, B. H., PARKER, D. S., FINLEY, D., ZAGHLOUL, N. A., FRANCO, B. & KATSANIS, N. 2014. Ciliopathy proteins regulate paracrine signaling by modulating proteasomal degradation of mediators. *J Clin Invest,* 124**,** 2059-70.

LOLKEMA, M. P., MANS, D. A., SNIJCKERS, C. M., VAN NOORT, M., VAN BEEST, M., VOEST, E. E. & GILES, R. H. 2007. The von Hippel-Lindau tumour suppressor interacts with microtubules through kinesin-2. *FEBS Lett,* 581**,** 4571-6.

LOPES, C. A., PROSSER, S. L., ROMIO, L., HIRST, R. A., O'CALLAGHAN, C., WOOLF, A. S. & FRY, A. M. 2011. Centriolar satellites are assembly points for proteins implicated in human ciliopathies, including oral-facial-digital syndrome 1. *J Cell Sci,* 124**,** 600-12.

LOPES, S. S., LOURENCO, R., PACHECO, L., MORENO, N., KREILING, J. & SAUDE, L. 2010. Notch signalling regulates left-right asymmetry through ciliary length control. *Development,* 137**,** 3625-32.

LOUIE, C. M., CARIDI, G., LOPES, V. S., BRANCATI, F., KISPERT, A., LANCASTER, M. A., SCHLOSSMAN, A. M., OTTO, E. A., LEITGES, M., GRONE, H. J., LOPEZ, I., GUDISEVA, H. V., O'TOOLE, J. F., VALLESPIN, E., AYYAGARI, R., AYUSO, C., CREMERS, F. P., DEN HOLLANDER, A. I., KOENEKOOP, R. K., DALLAPICCOLA, B., GHIGGERI, G. M., HILDEBRANDT, F., VALENTE, E. M., WILLIAMS, D. S. & GLEESON, J. G. 2010. AHI1 is required for photoreceptor outer segment development and is a modifier for retinal degeneration in nephronophthisis. *Nat Genet,* 42**,** 175-80.

LU, Q., INSINNA, C., OTT, C., STAUFFER, J., PINTADO, P. A., RAHAJENG, J., BAXA, U., WALIA, V., CUENCA, A., HWANG, Y. S., DAAR, I. O., LOPES, S., LIPPINCOTT-SCHWARTZ, J., JACKSON, P. K., CAPLAN, S. & WESTLAKE, C. J. 2015. Early steps in primary cilium

assembly require EHD1/EHD3-dependent ciliary vesicle formation. *Nat Cell Biol,* 17**,** 531.

MACDONALD, B. T. & HE, X. 2012. Frizzled and LRP5/6 receptors for Wnt/beta-catenin signaling. *Cold Spring Harb Perspect Biol,* 4.

MACDONALD, B. T., TAMAI, K. & HE, X. 2009. Wnt/beta-catenin signaling: components, mechanisms, and diseases. *Dev Cell,* 17**,** 9-26.

MAHJOUB, M. R. & STEARNS, T. 2012. Supernumerary centrosomes nucleate extra cilia and compromise primary cilium signaling. *Curr Biol,* 22**,** 1628-34.

MAHUZIER, A., GAUDE, H. M., GRAMPA, V., ANSELME, I., SILBERMANN, F., LEROUX-BERGER, M., DELACOUR, D., EZAN, J., MONTCOUQUIOL, M., SAUNIER, S., SCHNEIDER-MAUNOURY, S. & VESQUE, C. 2012. Dishevelled stabilization by the ciliopathy protein Rpgrip1l is essential for planar cell polarity. *J Cell Biol,* 198**,** 927-40.

MALAKHOV, M. P., MATTERN, M. R., MALAKHOVA, O. A., DRINKER, M., WEEKS, S. D. & BUTT, T. R. 2004. SUMO fusions and SUMO-specific protease for efficient expression and purification of proteins. *J Struct Funct Genomics,* 5**,** 75-86.

MALICKI, J. J. & JOHNSON, C. A. 2017. The Cilium: Cellular Antenna and Central Processing Unit. *Trends Cell Biol,* 27**,** 126-140.

MANS, D. A., LOLKEMA, M. P., VAN BEEST, M., DAENEN, L. G., VOEST, E. E. & GILES, R. H. 2008. Mobility of the von Hippel-Lindau tumour suppressor protein is regulated by kinesin-2. *Exp Cell Res,* 314**,** 1229-36.

MARQUES, S. R., RAMAKRISHNAN, C., CARZANIGA, R., BLAGBOROUGH, A. M., DELVES, M. J., TALMAN, A. M. & SINDEN, R. E. 2015. An essential role of the basal body protein SAS-6 in Plasmodium male gamete development and malaria transmission. *Cell Microbiol,* 17**,** 191-206.

MARSHALL, W. F. 2008. Basal bodies platforms for building cilia. *Curr Top Dev Biol,* 85**,** 1-22.

MAY-SIMERA, H. L. & KELLEY, M. W. 2012. Cilia, Wnt signaling, and the cytoskeleton. *Cilia,* 1**,** 7.

MCINTYRE, J. C., DAVIS, E. E., JOINER, A., WILLIAMS, C. L., TSAI, I. C., JENKINS, P. M., MCEWEN, D. P., ZHANG, L., ESCOBADO, J., THOMAS, S., SZYMANSKA, K., JOHNSON, C. A., BEALES, P. L., GREEN, E. D., MULLIKIN, J. C., PROGRAM, N. C. S., SABO, A., MUZNY, D. M., GIBBS, R. A., ATTIE-BITACH, T., YODER, B. K., REED, R. R., KATSANIS, N. & MARTENS, J. R. 2012. Gene therapy rescues cilia defects and restores olfactory function in a mammalian ciliopathy model. *Nat Med,* 18**,** 1423-8.

MCINTYRE, J. C., WILLIAMS, C. L. & MARTENS, J. R. 2013. Smelling the roses and seeing the light: gene therapy for ciliopathies. *Trends Biotechnol,* 31**,** 355-63.

MICK, D. U., RODRIGUES, R. B., LEIB, R. D., ADAMS, C. M., CHIEN, A. S., GYGI, S. P. & NACHURY, M. V. 2015. Proteomics of Primary Cilia by Proximity Labeling. *Dev Cell,* 35**,** 497-512.

MITCHELL, B., STUBBS, J. L., HUISMAN, F., TABOREK, P., YU, C. & KINTNER, C. 2009. The PCP pathway instructs the planar orientation of ciliated cells in the Xenopus larval skin. *Curr Biol,* 19**,** 924-9.

MITCHISON, H. M. & VALENTE, E. M. 2017. Motile and non-motile cilia in human pathology: from function to phenotypes. *J Pathol,* 241**,** 294-309.

MIYOSHI, K., KASAHARA, K., MURAKAMI, S., TAKESHIMA, M., KUMAMOTO, N., SATO, A., MIYAZAKI, I., MATSUZAKI, S., SASAOKA, T., KATAYAMA, T. & ASANUMA, M. 2014.

Lack of dopaminergic inputs elongates the primary cilia of striatal neurons. *PLoS One,* 9, e97918.

MOGHADAM, M., GANJI, A., VARASTEH, A., FALAK, R. & SANKIAN, M. 2015. Refolding process of cysteine-rich proteins:Chitinase as a model. *Rep Biochem Mol Biol,* 4, 19-24.

MOLLA-HERMAN, A., GHOSSOUB, R., BLISNICK, T., MEUNIER, A., SERRES, C., SILBERMANN, F., EMMERSON, C., ROMEO, K., BOURDONCLE, P., SCHMITT, A., SAUNIER, S., SPASSKY, N., BASTIN, P. & BENMERAH, A. 2010. The ciliary pocket: an endocytic membrane domain at the base of primary and motile cilia. *J Cell Sci,* 123, 1785-95.

MOOSA, S., OBREGON, M. G., ALTMULLER, J., THIELE, H., NURNBERG, P., FANO, V. & WOLLNIK, B. 2016. Novel IFT122 mutations in three Argentinian patients with cranioectodermal dysplasia: Expanding the mutational spectrum. *Am J Med Genet A,* 170A, 1295-301.

MOSER, J. J., FRITZLER, M. J. & RATTNER, J. B. 2014. Ultrastructural characterization of primary cilia in pathologically characterized human glioblastoma multiforme (GBM) tumors. *BMC Clin Pathol,* 14, 40.

MOYER, T. C., CLUTARIO, K. M., LAMBRUS, B. G., DAGGUBATI, V. & HOLLAND, A. J. 2015. Binding of STIL to Plk4 activates kinase activity to promote centriole assembly. *J Cell Biol,* 209, 863-78.

MUKHOPADHYAY, S., BADGANDI, H. B., HWANG, S. H., SOMATILAKA, B., SHIMADA, I. S. & PAL, K. 2017. Trafficking to the primary cilium membrane. *Mol Biol Cell,* 28, 233-239.

MUKHOPADHYAY, S., WEN, X., CHIH, B., NELSON, C. D., LANE, W. S., SCALES, S. J. & JACKSON, P. K. 2010. TULP3 bridges the IFT-A complex and membrane phosphoinositides to promote trafficking of G protein-coupled receptors into primary cilia. *Genes Dev,* 24, 2180-93.

MÜLLER, O. F. 1786. *Animalcula infusoria; fluvia tilia et marina, que detexit, systematice descripsit et ad vivum delineari curavit,* Havniae, Typis N. Molleri.

MURGA-ZAMALLOA, C. A., DESAI, N. J., HILDEBRANDT, F. & KHANNA, H. 2010. Interaction of ciliary disease protein retinitis pigmentosa GTPase regulator with nephronophthisis-associated proteins in mammalian retinas. *Mol Vis,* 16, 1373-81.

MURGA-ZAMALLOA, C. A., GHOSH, A. K., PATIL, S. B., REED, N. A., CHAN, L. S., DAVULURI, S., PERANEN, J., HURD, T. W., RACHEL, R. A. & KHANNA, H. 2011. Accumulation of the Raf-1 kinase inhibitory protein (Rkip) is associated with Cep290-mediated photoreceptor degeneration in ciliopathies. *J Biol Chem,* 286, 28276-86.

MURGA-ZAMALLOA, C. A., SWAROOP, A. & KHANNA, H. 2009. RPGR-containing protein complexes in syndromic and non-syndromic retinal degeneration due to ciliary dysfunction. *J Genet,* 88, 399-407.

MYERS, D. C., SEPICH, D. S. & SOLNICA-KREZEL, L. 2002. Convergence and extension in vertebrate gastrulae: cell movements according to or in search of identity? *Trends Genet,* 18, 447-55.

NACHURY, M. V. 2014. How do cilia organize signalling cascades? *Philos Trans R Soc Lond B Biol Sci,* 369.

NACHURY, M. V., LOKTEV, A. V., ZHANG, Q., WESTLAKE, C. J., PERANEN, J., MERDES, A., SLUSARSKI, D. C., SCHELLER, R. H., BAZAN, J. F., SHEFFIELD, V. C. & JACKSON, P. K. 2007. A core complex of BBS proteins cooperates with the GTPase Rab8 to promote ciliary membrane biogenesis. *Cell,* 129, 1201-13.

NAKAYAMA, K. & KATOH, Y. 2018. Ciliary protein trafficking mediated by IFT and BBSome complexes with the aid of kinesin-2 and dynein-2 motors. *J Biochem,* 163**,** 155-164.

NAKAZAWA, Y., HIRAKI, M., KAMIYA, R. & HIRONO, M. 2007. SAS-6 is a cartwheel protein that establishes the 9-fold symmetry of the centriole. *Curr Biol,* 17**,** 2169-74.

NARITA, K., KOZUKA-HATA, H., NONAMI, Y., AO-KONDO, H., SUZUKI, T., NAKAMURA, H., YAMAKAWA, K., OYAMA, M., INOUE, T. & TAKEDA, S. 2012. Proteomic analysis of multiple primary cilia reveals a novel mode of ciliary development in mammals. *Biol Open,* 1**,** 815-25.

NEUMANN, B., WALTER, T., HERICHE, J. K., BULKESCHER, J., ERFLE, H., CONRAD, C., ROGERS, P., POSER, I., HELD, M., LIEBEL, U., CETIN, C., SIECKMANN, F., PAU, G., KABBE, R., WUNSCHE, A., SATAGOPAM, V., SCHMITZ, M. H., CHAPUIS, C., GERLICH, D. W., SCHNEIDER, R., EILS, R., HUBER, W., PETERS, J. M., HYMAN, A. A., DURBIN, R., PEPPERKOK, R. & ELLENBERG, J. 2010. Phenotypic profiling of the human genome by time-lapse microscopy reveals cell division genes. *Nature,* 464**,** 721-7.

NEVERS, Y., PRASAD, M. K., POIDEVIN, L., CHENNEN, K., ALLOT, A., KRESS, A., RIPP, R., THOMPSON, J. D., DOLLFUS, H., POCH, O. & LECOMPTE, O. 2017. Insights into Ciliary Genes and Evolution from Multi-Level Phylogenetic Profiling. *Mol Biol Evol,* 34**,** 2016-2034.

NONAKA, S., TANAKA, Y., OKADA, Y., TAKEDA, S., HARADA, A., KANAI, Y., KIDO, M. & HIROKAWA, N. 1998. Randomization of left-right asymmetry due to loss of nodal cilia generating leftward flow of extraembryonic fluid in mice lacking KIF3B motor protein. *Cell,* 95**,** 829-37.

NOOR, A., WINDPASSINGER, C., PATEL, M., STACHOWIAK, B., MIKHAILOV, A., AZAM, M., IRFAN, M., SIDDIQUI, Z. K., NAEEM, F., PATERSON, A. D., LUTFULLAH, M., VINCENT, J. B. & AYUB, M. 2008. CC2D2A, encoding a coiled-coil and C2 domain protein, causes autosomal-recessive mental retardation with retinitis pigmentosa. *Am J Hum Genet,* 82**,** 1011-8.

NOVARINO, G., AKIZU, N. & GLEESON, J. G. 2011. Modeling human disease in humans: the ciliopathies. *Cell,* 147**,** 70-9.

NUSSE, R. 2003. Wnts and Hedgehogs: lipid-modified proteins and similarities in signaling mechanisms at the cell surface. *Development,* 130**,** 5297-305.

O'DEA, D., PARFREY, P. S., HARNETT, J. D., HEFFERTON, D., CRAMER, B. C. & GREEN, J. 1996. The importance of renal impairment in the natural history of Bardet-Biedl syndrome. *Am J Kidney Dis,* 27**,** 776-83.

OH, E. C. & KATSANIS, N. 2013. Context-dependent regulation of Wnt signaling through the primary cilium. *J Am Soc Nephrol,* 24**,** 10-8.

OSTROWSKI, L. E., DUTCHER, S. K. & LO, C. W. 2011. Cilia and models for studying structure and function. *Proc Am Thorac Soc,* 8**,** 423-9.

OTTO, E. A., SCHERMER, B., OBARA, T., O'TOOLE, J. F., HILLER, K. S., MUELLER, A. M., RUF, R. G., HOEFELE, J., BEEKMANN, F., LANDAU, D., FOREMAN, J. W., GOODSHIP, J. A., STRACHAN, T., KISPERT, A., WOLF, M. T., GAGNADOUX, M. F., NIVET, H., ANTIGNAC, C., WALZ, G., DRUMMOND, I. A., BENZING, T. & HILDEBRANDT, F. 2003. Mutations in INVS encoding inversin cause nephronophthisis type 2, linking renal cystic disease to the function of primary cilia and left-right axis determination. *Nat Genet,* 34**,** 413-20.

OTTO, E. A., TORY, K., ATTANASIO, M., ZHOU, W., CHAKI, M., PARUCHURI, Y., WISE, E. L., WOLF, M. T., UTSCH, B., BECKER, C., NURNBERG, G., NURNBERG, P., NAYIR, A.,

SAUNIER, S., ANTIGNAC, C. & HILDEBRANDT, F. 2009. Hypomorphic mutations in meckelin (MKS3/TMEM67) cause nephronophthisis with liver fibrosis (NPHP11). *J Med Genet,* 46**,** 663-70.

OVALLE, W. K. A. N., P.C. 2013. *Netter's Essential Histology,* Philadelphia, Elsevier.

PAAVOLA, P., SALONEN, R., WEISSENBACH, J. & PELTONEN, L. 1995. The locus for Meckel syndrome with multiple congenital anomalies maps to chromosome 17q21-q24. *Nat Genet,* 11**,** 213-5.

PALA, R., ALOMARI, N. & NAULI, S. M. 2017. Primary Cilium-Dependent Signaling Mechanisms. *Int J Mol Sci,* 18.

PAPAKRIVOPOULOU, E., DEAN, C. H., COPP, A. J. & LONG, D. A. 2014. Planar cell polarity and the kidney. *Nephrol Dial Transplant,* 29**,** 1320-6.

PARISI, M. A. 2009. Clinical and molecular features of Joubert syndrome and related disorders. *Am J Med Genet C Semin Med Genet,* 151C**,** 326-40.

PARISI, M. A., BENNETT, C. L., ECKERT, M. L., DOBYNS, W. B., GLEESON, J. G., SHAW, D. W., MCDONALD, R., EDDY, A., CHANCE, P. F. & GLASS, I. A. 2004. The NPHP1 gene deletion associated with juvenile nephronophthisis is present in a subset of individuals with Joubert syndrome. *Am J Hum Genet,* 75**,** 82-91.

PARISI, M. A., DOHERTY, D., CHANCE, P. F. & GLASS, I. A. 2007. Joubert syndrome (and related disorders) (OMIM 213300). *Eur J Hum Genet,* 15**,** 511-21.

PARK, S. M., JANG, H. J. & LEE, J. H. 2019. Roles of Primary Cilia in the Developing Brain. *Front Cell Neurosci,* 13**,** 218.

PARK, T. J., HAIGO, S. L. & WALLINGFORD, J. B. 2006. Ciliogenesis defects in embryos lacking inturned or fuzzy function are associated with failure of planar cell polarity and Hedgehog signaling. *Nat Genet,* 38**,** 303-11.

PARK, T. J., MITCHELL, B. J., ABITUA, P. B., KINTNER, C. & WALLINGFORD, J. B. 2008. Dishevelled controls apical docking and planar polarization of basal bodies in ciliated epithelial cells. *Nat Genet,* 40**,** 871-9.

PAZOUR, G. J., BAKER, S. A., DEANE, J. A., COLE, D. G., DICKERT, B. L., ROSENBAUM, J. L., WITMAN, G. B. & BESHARSE, J. C. 2002. The intraflagellar transport protein, IFT88, is essential for vertebrate photoreceptor assembly and maintenance. *J Cell Biol,* 157**,** 103-13.

PAZOUR, G. J., DICKERT, B. L., VUCICA, Y., SEELEY, E. S., ROSENBAUM, J. L., WITMAN, G. B. & COLE, D. G. 2000. Chlamydomonas IFT88 and its mouse homologue, polycystic kidney disease gene tg737, are required for assembly of cilia and flagella. *J Cell Biol,* 151**,** 709-18.

PEARSON, C. G., OSBORN, D. P., GIDDINGS, T. H., JR., BEALES, P. L. & WINEY, M. 2009. Basal body stability and ciliogenesis requires the conserved component Poc1. *J Cell Biol,* 187**,** 905-20.

PEEL, N., STEVENS, N. R., BASTO, R. & RAFF, J. W. 2007. Overexpressing centriole-replication proteins in vivo induces centriole overduplication and de novo formation. *Curr Biol,* 17**,** 834-43.

PELISCH, F., RISSO, G. & SREBROW, A. 2013. RNA metabolism and ubiquitin/ubiquitin-like modifications collide. *Brief Funct Genomics,* 12**,** 66-71.

PELLETIER, L., O'TOOLE, E., SCHWAGER, A., HYMAN, A. A. & MULLER-REICHERT, T. 2006. Centriole assembly in Caenorhabditis elegans. *Nature,* 444**,** 619-23.

PERRAULT, I., DELPHIN, N., HANEIN, S., GERBER, S., DUFIER, J. L., ROCHE, O., DEFOORT-DHELLEMMES, S., DOLLFUS, H., FAZZI, E., MUNNICH, A., KAPLAN, J. & ROZET, J. M. 2007. Spectrum of NPHP6/CEP290 mutations in Leber congenital amaurosis and delineation of the associated phenotype. *Hum Mutat,* 28**,** 416.

PIERCE, N. W. & NACHURY, M. V. 2013. Cilia grow by taking a bite out of the cell. *Dev Cell,* 27**,** 126-127.

PLOTNIKOVA, O. V., PUGACHEVA, E. N. & GOLEMIS, E. A. 2009. Primary cilia and the cell cycle. *Methods Cell Biol,* 94**,** 137-60.

PRAVEEN, K., DAVIS, E. E. & KATSANIS, N. 2015. Unique among ciliopathies: primary ciliary dyskinesia, a motile cilia disorder. *F1000Prime Rep,* 7**,** 36.

PRUSKI, M. & LANG, B. 2019. Primary Cilia-An Underexplored Topic in Major Mental Illness. *Front Psychiatry,* 10**,** 104.

PUGACHEVA, E. N., JABLONSKI, S. A., HARTMAN, T. R., HENSKE, E. P. & GOLEMIS, E. A. 2007. HEF1-dependent Aurora A activation induces disassembly of the primary cilium. *Cell,* 129**,** 1351-63.

PURKINJE JE, V. G. 1834. Entdeckung continuerlicher durch wimperhaare einseugter flimmer der bewegungen, als einse allgemeine phanomens in der klassen der aphibien Vogel and Saugetiere. *Műllers Arch Anat Physiol Wissenschaft Med***,** 391–400.

QIAO, R., CABRAL, G., LETTMAN, M. M., DAMMERMANN, A. & DONG, G. 2012. SAS-6 coiled-coil structure and interaction with SAS-5 suggest a regulatory mechanism in C. elegans centriole assembly. *EMBO J,* 31**,** 4334-47.

QIU, N., XIAO, Z., CAO, L., BUECHEL, M. M., DAVID, V., ROAN, E. & QUARLES, L. D. 2012. Disruption of Kif3a in osteoblasts results in defective bone formation and osteopenia. *J Cell Sci,* 125**,** 1945-57.

QUARANTOTTI, V., CHEN, J. X., TISCHER, J., GONZALEZ TEJEDO, C., PAPACHRISTOU, E. K., D'SANTOS, C. S., KILMARTIN, J. V., MILLER, M. L. & GERGELY, F. 2019. Centriolar satellites are acentriolar assemblies of centrosomal proteins. *EMBO J,* 38**,** e101082.

RACHEL, R. A., LI, T. & SWAROOP, A. 2012. Photoreceptor sensory cilia and ciliopathies: focus on CEP290, RPGR and their interacting proteins. *Cilia,* 1**,** 22.

RAMSBOTTOM, S. A. & POWNALL, M. E. 2016. Regulation of Hedgehog Signalling Inside and Outside the Cell. *J Dev Biol,* 4**,** 23.

REDIN, C., LE GRAS, S., MHAMDI, O., GEOFFROY, V., STOETZEL, C., VINCENT, M. C., CHIURAZZI, P., LACOMBE, D., OUERTANI, I., PETIT, F., TILL, M., VERLOES, A., JOST, B., CHAABOUNI, H. B., DOLLFUS, H., MANDEL, J. L. & MULLER, J. 2012. Targeted high-throughput sequencing for diagnosis of genetically heterogeneous diseases: efficient mutation detection in Bardet-Biedl and Alstrom syndromes. *J Med Genet,* 49**,** 502-12.

REITER, J. F., BLACQUE, O. E. & LEROUX, M. R. 2012. The base of the cilium: roles for transition fibres and the transition zone in ciliary formation, maintenance and compartmentalization. *EMBO Rep,* 13**,** 608-18.

REITER, J. F. & LEROUX, M. R. 2017. Genes and molecular pathways underpinning ciliopathies. *Nat Rev Mol Cell Biol,* 18**,** 533-547.

RIGAUT, G., SHEVCHENKO, A., RUTZ, B., WILM, M., MANN, M. & SERAPHIN, B. 1999. A generic protein purification method for protein complex characterization and proteome exploration. *Nat Biotechnol,* 17**,** 1030-2.

ROBERSON, E. C., DOWDLE, W. E., OZANTURK, A., GARCIA-GONZALO, F. R., LI, C., HALBRITTER, J., ELKHARTOUFI, N., PORATH, J. D., COPE, H., ASHLEY-KOCH, A., GREGORY, S., THOMAS, S., SAYER, J. A., SAUNIER, S., OTTO, E. A., KATSANIS, N., DAVIS, E. E., ATTIE-BITACH, T., HILDEBRANDT, F., LEROUX, M. R. & REITER, J. F. 2015. TMEM231, mutated in orofaciodigital and Meckel syndromes, organizes the ciliary transition zone. *J Cell Biol,* 209**,** 129-42.

ROHATGI, R., MILENKOVIC, L., CORCORAN, R. B. & SCOTT, M. P. 2009. Hedgehog signal transduction by Smoothened: pharmacologic evidence for a 2-step activation process. *Proc Natl Acad Sci U S A,* 106**,** 3196-201.

ROHATGI, R., MILENKOVIC, L. & SCOTT, M. P. 2007. Patched1 regulates hedgehog signaling at the primary cilium. *Science,* 317**,** 372-6.

ROHATGI, R. & SNELL, W. J. 2010. The ciliary membrane. *Curr Opin Cell Biol,* 22**,** 541-6.

ROMANI, M., MICALIZZI, A. & VALENTE, E. M. 2013. Joubert syndrome: congenital cerebellar ataxia with the molar tooth. *Lancet Neurol,* 12**,** 894-905.

ROSS, A. J., MAY-SIMERA, H., EICHERS, E. R., KAI, M., HILL, J., JAGGER, D. J., LEITCH, C. C., CHAPPLE, J. P., MUNRO, P. M., FISHER, S., TAN, P. L., PHILLIPS, H. M., LEROUX, M. R., HENDERSON, D. J., MURDOCH, J. N., COPP, A. J., ELIOT, M. M., LUPSKI, J. R., KEMP, D. T., DOLLFUS, H., TADA, M., KATSANIS, N., FORGE, A. & BEALES, P. L. 2005. Disruption of Bardet-Biedl syndrome ciliary proteins perturbs planar cell polarity in vertebrates. *Nat Genet,* 37**,** 1135-40.

RUBINSZTEIN, D. C. 2006. The roles of intracellular protein-degradation pathways in neurodegeneration. *Nature,* 443**,** 780-6.

SABURI, S., HESTER, I., FISCHER, E., PONTOGLIO, M., EREMINA, V., GESSLER, M., QUAGGIN, S. E., HARRISON, R., MOUNT, R. & MCNEILL, H. 2008. Loss of Fat4 disrupts PCP signaling and oriented cell division and leads to cystic kidney disease. *Nat Genet,* 40**,** 1010-5.

SAITO, M., OTSU, W., HSU, K. S., CHUANG, J. Z., YANAGISAWA, T., SHIEH, V., KAITSUKA, T., WEI, F. Y., TOMIZAWA, K. & SUNG, C. H. 2017. Tctex-1 controls ciliary resorption by regulating branched actin polymerization and endocytosis. *EMBO Rep,* 18**,** 1460-1472.

SAITO, S., TAMPE, B., MULLER, G. A. & ZEISBERG, M. 2015. Primary cilia modulate balance of canonical and non-canonical Wnt signaling responses in the injured kidney. *Fibrogenesis Tissue Repair,* 8**,** 6.

SANCHEZ, I. & DYNLACHT, B. D. 2016. Cilium assembly and disassembly. *Nat Cell Biol,* 18**,** 711-7.

SANG, L., MILLER, J. J., CORBIT, K. C., GILES, R. H., BRAUER, M. J., OTTO, E. A., BAYE, L. M., WEN, X., SCALES, S. J., KWONG, M., HUNTZICKER, E. G., SFAKIANOS, M. K., SANDOVAL, W., BAZAN, J. F., KULKARNI, P., GARCIA-GONZALO, F. R., SEOL, A. D., O'TOOLE, J. F., HELD, S., REUTTER, H. M., LANE, W. S., RAFIQ, M. A., NOOR, A., ANSAR, M., DEVI, A. R., SHEFFIELD, V. C., SLUSARSKI, D. C., VINCENT, J. B., DOHERTY, D. A., HILDEBRANDT, F., REITER, J. F. & JACKSON, P. K. 2011. Mapping the NPHP-JBTS-MKS protein network reveals ciliopathy disease genes and pathways. *Cell,* 145**,** 513-28.

SANS-ATXER, L. & JOLY, D. 2018. Tolvaptan in the treatment of autosomal dominant polycystic kidney disease: patient selection and special considerations. *Int J Nephrol Renovasc Dis,* 11**,** 41-51.

SANTOS, N. & REITER, J. F. 2008. Building it up and taking it down: the regulation of vertebrate ciliogenesis. *Dev Dyn,* 237**,** 1972-81.

SASAI, N. & BRISCOE, J. 2012. Primary cilia and graded Sonic Hedgehog signaling. *Wiley Interdiscip Rev Dev Biol,* 1**,** 753-72.

SATIR, P. 2017. CILIA: before and after. *Cilia,* 6**,** 1.

SATIR, P. & CHRISTENSEN, S. T. 2007. Overview of structure and function of mammalian cilia. *Annu Rev Physiol,* 69**,** 377-400.

SATIR, P., PEDERSEN, L. B. & CHRISTENSEN, S. T. 2010. The primary cilium at a glance. *J Cell Sci,* 123**,** 499-503.

SAYER, J. A., OTTO, E. A., O'TOOLE, J. F., NURNBERG, G., KENNEDY, M. A., BECKER, C., HENNIES, H. C., HELOU, J., ATTANASIO, M., FAUSETT, B. V., UTSCH, B., KHANNA, H., LIU, Y., DRUMMOND, I., KAWAKAMI, I., KUSAKABE, T., TSUDA, M., MA, L., LEE, H., LARSON, R. G., ALLEN, S. J., WILKINSON, C. J., NIGG, E. A., SHOU, C., LILLO, C., WILLIAMS, D. S., HOPPE, B., KEMPER, M. J., NEUHAUS, T., PARISI, M. A., GLASS, I. A., PETRY, M., KISPERT, A., GLOY, J., GANNER, A., WALZ, G., ZHU, X., GOLDMAN, D., NURNBERG, P., SWAROOP, A., LEROUX, M. R. & HILDEBRANDT, F. 2006. The centrosomal protein nephrocystin-6 is mutated in Joubert syndrome and activates transcription factor ATF4. *Nat Genet,* 38**,** 674-81.

SCHEIDEL, N. & BLACQUE, O. E. 2018. Intraflagellar Transport Complex A Genes Differentially Regulate Cilium Formation and Transition Zone Gating. *Curr Biol,* 28**,** 3279-3287 e2.

SCHERFT, J. P. & DAEMS, W. T. 1967. Single cilia in chondrocytes. *J Ultrastruct Res,* 19**,** 546-55.

SCHERMER, B., GHENOIU, C., BARTRAM, M., MULLER, R. U., KOTSIS, F., HOHNE, M., KUHN, W., RAPKA, M., NITSCHKE, R., ZENTGRAF, H., FLIEGAUF, M., OMRAN, H., WALZ, G. & BENZING, T. 2006. The von Hippel-Lindau tumor suppressor protein controls ciliogenesis by orienting microtubule growth. *J Cell Biol,* 175**,** 547-54.

SCHMIDTS, M., FRANK, V., EISENBERGER, T., AL TURKI, S., BIZET, A. A., ANTONY, D., RIX, S., DECKER, C., BACHMANN, N., BALD, M., VINKE, T., TOENSHOFF, B., DI DONATO, N., NEUHANN, T., HARTLEY, J. L., MAHER, E. R., BOGDANOVIC, R., PECO-ANTIC, A., MACHE, C., HURLES, M. E., JOKSIC, I., GUC-SCEKIC, M., DOBRICIC, J., BRANKOVIC-MAGIC, M., BOLZ, H. J., PAZOUR, G. J., BEALES, P. L., SCAMBLER, P. J., SAUNIER, S., MITCHISON, H. M. & BERGMANN, C. 2013. Combined NGS approaches identify mutations in the intraflagellar transport gene IFT140 in skeletal ciliopathies with early progressive kidney Disease. *Hum Mutat,* 34**,** 714-24.

SCHOUTEDEN, C., SERWAS, D., PALFY, M. & DAMMERMANN, A. 2015. The ciliary transition zone functions in cell adhesion but is dispensable for axoneme assembly in C. elegans. *J Cell Biol,* 210**,** 35-44.

SEO, S., BAYE, L. M., SCHULZ, N. P., BECK, J. S., ZHANG, Q., SLUSARSKI, D. C. & SHEFFIELD, V. C. 2010. BBS6, BBS10, and BBS12 form a complex with CCT/TRiC family chaperonins and mediate BBSome assembly. *Proc Natl Acad Sci U S A,* 107**,** 1488-93.

SHAH, A. S., BEN-SHAHAR, Y., MONINGER, T. O., KLINE, J. N. & WELSH, M. J. 2009. Motile cilia of human airway epithelia are chemosensory. *Science,* 325**,** 1131-4.

SHAHEEN, R., ALMOISHEER, A., FAQEIH, E., BABAY, Z., MONIES, D., TASSAN, N., ABOUELHODA, M., KURDI, W., AL MARDAWI, E., KHALIL, M. M., SEIDAHMED, M. Z., ALNEMER, M., ALSAHAN, N., SOGATY, S., ALHASHEM, A., SINGH, A., GOYAL, M.,

KAPOOR, S., ALOMAR, R., IBRAHIM, N. & ALKURAYA, F. S. 2015. Identification of a novel MKS locus defined by TMEM107 mutation. *Hum Mol Genet,* 24**,** 5211-8.

SHAHEEN, R., ANSARI, S., MARDAWI, E. A., ALSHAMMARI, M. J. & ALKURAYA, F. S. 2013a. Mutations in TMEM231 cause Meckel-Gruber syndrome. *J Med Genet,* 50**,** 160-2.

SHAHEEN, R., FAQEIH, E., ALSHAMMARI, M. J., SWAID, A., AL-GAZALI, L., MARDAWI, E., ANSARI, S., SOGATY, S., SEIDAHMED, M. Z., ALMOTAIRI, M. I., FARRA, C., KURDI, W., AL-RASHEED, S. & ALKURAYA, F. S. 2013b. Genomic analysis of Meckel-Gruber syndrome in Arabs reveals marked genetic heterogeneity and novel candidate genes. *Eur J Hum Genet,* 21**,** 762-8.

SHAMSELDIN, H. E., SHAHEEN, R., EWIDA, N., BUBSHAIT, D. K., ALKURAYA, H., ALMARDAWI, E., HOWAIDI, A., SABR, Y., ABDALLA, E. M., ALFAIFI, A. Y., ALGHAMDI, J. M., ALSAGHEIR, A., ALFARES, A., MORSY, H., HUSSEIN, M. H., AL-MUHAIZEA, M. A., SHAGRANI, M., AL SABBAN, E., SALIH, M. A., MERIKI, N., KHAN, R., ALMUGBEL, M., QARI, A., TULBA, M., MAHNASHI, M., ALHAZMI, K., ALSALAMAH, A. K., NOWILATY, S. R., ALHASHEM, A., HASHEM, M., ABDULWAHAB, F., IBRAHIM, N., ALSHIDI, T., ALOBEID, E., ALENAZI, M. M., ALZAIDAN, H., RAHBEENI, Z., AL-OWAIN, M., SOGATY, S., SEIDAHMED, M. Z. & ALKURAYA, F. S. 2020. The morbid genome of ciliopathies: an update. *Genet Med*.

SHARMA, M., CASTRO-PIEDRAS, I., SIMMONS, G. E., JR. & PRUITT, K. 2018. Dishevelled: A masterful conductor of complex Wnt signals. *Cell Signal,* 47**,** 52-64.

SHI, X., GARCIA, G., 3RD, VAN DE WEGHE, J. C., MCGORTY, R., PAZOUR, G. J., DOHERTY, D., HUANG, B. & REITER, J. F. 2017. Super-resolution microscopy reveals that disruption of ciliary transition-zone architecture causes Joubert syndrome. *Nat Cell Biol,* 19**,** 1178-1188.

SHINOHARA, K., CHEN, D., NISHIDA, T., MISAKI, K., YONEMURA, S. & HAMADA, H. 2015. Absence of Radial Spokes in Mouse Node Cilia Is Required for Rotational Movement but Confers Ultrastructural Instability as a Trade-Off. *Dev Cell,* 35**,** 236-46.

SHIVANNA, M., ANAND, M., CHAKRABARTI, S. & KHANNA, H. 2019. Ocular Ciliopathies: Genetic and Mechanistic Insights into Developing Therapies. *Curr Med Chem,* 26**,** 3120-3131.

SIMONS, D. L., BOYE, S. L., HAUSWIRTH, W. W. & WU, S. M. 2011. Gene therapy prevents photoreceptor death and preserves retinal function in a Bardet-Biedl syndrome mouse model. *Proc Natl Acad Sci U S A,* 108**,** 6276-81.

SIMONS, M., GLOY, J., GANNER, A., BULLERKOTTE, A., BASHKUROV, M., KRONIG, C., SCHERMER, B., BENZING, T., CABELLO, O. A., JENNY, A., MLODZIK, M., POLOK, B., DRIEVER, W., OBARA, T. & WALZ, G. 2005. Inversin, the gene product mutated in nephronophthisis type II, functions as a molecular switch between Wnt signaling pathways. *Nat Genet,* 37**,** 537-43.

SIMPSON, J. L., MILLS, J., RHOADS, G. G., CUNNINGHAM, G. C., CONLEY, M. R. & HOFFMAN, H. J. 1991. Genetic heterogeneity in neural tube defects. *Ann Genet,* 34**,** 279-86.

SINGLA, V. & REITER, J. F. 2006. The primary cilium as the cell's antenna: signaling at a sensory organelle. *Science,* 313**,** 629-33.

SLAATS, G. G., ISABELLA, C. R., KROES, H. Y., DEMPSEY, J. C., GREMMELS, H., MONROE, G. R., PHELPS, I. G., DURAN, K. J., ADKINS, J., KUMAR, S. A., KNUTZEN, D. M., KNOERS, N. V., MENDELSOHN, N. J., NEUBAUER, D., MASTROYIANNI, S. D., VOGT, J., WORGAN, L., KARP, N., BOWDIN, S., GLASS, I. A., PARISI, M. A., OTTO, E. A., JOHNSON, C. A.,

HILDEBRANDT, F., VAN HAAFTEN, G., GILES, R. H. & DOHERTY, D. 2016. MKS1 regulates ciliary INPP5E levels in Joubert syndrome. *J Med Genet,* 53, 62-72.

SLAATS, G. G., SALDIVAR, J. C., BACAL, J., ZEMAN, M. K., KILE, A. C., HYNES, A. M., SRIVASTAVA, S., NAZMUTDINOVA, J., DEN OUDEN, K., ZAGERS, M. S., FOLETTO, V., VERHAAR, M. C., MILES, C., SAYER, J. A., CIMPRICH, K. A. & GILES, R. H. 2015. DNA replication stress underlies renal phenotypes in CEP290-associated Joubert syndrome. *J Clin Invest,* 125, 3657-66.

SMITH, U. M., CONSUGAR, M., TEE, L. J., MCKEE, B. M., MAINA, E. N., WHELAN, S., MORGAN, N. V., GORANSON, E., GISSEN, P., LILLIQUIST, S., ALIGIANIS, I. A., WARD, C. J., PASHA, S., PUNYASHTHITI, R., MALIK SHARIF, S., BATMAN, P. A., BENNETT, C. P., WOODS, C. G., MCKEOWN, C., BUCOURT, M., MILLER, C. A., COX, P., ALGAZALI, L., TREMBATH, R. C., TORRES, V. E., ATTIE-BITACH, T., KELLY, D. A., MAHER, E. R., GATTONE, V. H., 2ND, HARRIS, P. C. & JOHNSON, C. A. 2006. The transmembrane protein meckelin (MKS3) is mutated in Meckel-Gruber syndrome and the wpk rat. *Nat Genet,* 38, 191-6.

SONG, E. J., WERNER, S. L., NEUBAUER, J., STEGMEIER, F., ASPDEN, J., RIO, D., HARPER, J. W., ELLEDGE, S. J., KIRSCHNER, M. W. & RAPE, M. 2010. The Prp19 complex and the Usp4Sart3 deubiquitinating enzyme control reversible ubiquitination at the spliceosome. *Genes Dev,* 24, 1434-47.

SOROKIN, S. P. 1968. Reconstructions of centriole formation and ciliogenesis in mammalian lungs. *J Cell Sci,* 3, 207-30.

SROUR, M., HAMDAN, F. F., SCHWARTZENTRUBER, J. A., PATRY, L., OSPINA, L. H., SHEVELL, M. I., DESILETS, V., DOBRZENIECKA, S., MATHONNET, G., LEMYRE, E., MASSICOTTE, C., LABUDA, D., AMROM, D., ANDERMANN, E., SEBIRE, G., MARANDA, B., CONSORTIUM, F. C., ROULEAU, G. A., MAJEWSKI, J. & MICHAUD, J. L. 2012. Mutations in TMEM231 cause Joubert syndrome in French Canadians. *J Med Genet,* 49, 636-41.

STASIULEWICZ, M., GRAY, S. D., MASTROMINA, I., SILVA, J. C., BJORKLUND, M., SEYMOUR, P. A., BOOTH, D., THOMPSON, C., GREEN, R. J., HALL, E. A., SERUP, P. & DALE, J. K. 2015. A conserved role for Notch signaling in priming the cellular response to Shh through ciliary localisation of the key Shh transducer Smo. *Development,* 142, 2291-303.

SUGA, A., MIZOTA, A., KATO, M., KUNIYOSHI, K., YOSHITAKE, K., SULTAN, W., YAMAZAKI, M., SHIMOMURA, Y., IKEO, K., TSUNODA, K. & IWATA, T. 2016. Identification of Novel Mutations in the LRR-Cap Domain of C21orf2 in Japanese Patients With Retinitis Pigmentosa and Cone-Rod Dystrophy. *Invest Ophthalmol Vis Sci,* 57, 4255-63.

SUN, S., FISHER, R. L., BOWSER, S. S., PENTECOST, B. T. & SUI, H. 2019. Three-dimensional architecture of epithelial primary cilia. *Proc Natl Acad Sci U S A,* 116, 9370-9379.

SUSPITSIN, E. N. & IMYANITOV, E. N. 2016. Bardet-Biedl Syndrome. *Mol Syndromol,* 7, 62-71.

SZKLARCZYK, D., FRANCESCHINI, A., WYDER, S., FORSLUND, K., HELLER, D., HUERTA-CEPAS, J., SIMONOVIC, M., ROTH, A., SANTOS, A., TSAFOU, K. P., KUHN, M., BORK, P., JENSEN, L. J. & VON MERING, C. 2015. STRING v10: protein-protein interaction networks, integrated over the tree of life. *Nucleic Acids Res,* 43, D447-52.

SZYMANSKA, K., BERRY, I., LOGAN, C. V., COUSINS, S. R., LINDSAY, H., JAFRI, H., RAASHID, Y., MALIK-SHARIF, S., CASTLE, B., AHMED, M., BENNETT, C., CARLTON, R. & JOHNSON, C.

A. 2012. Founder mutations and genotype-phenotype correlations in Meckel-Gruber syndrome and associated ciliopathies. *Cilia,* 1**,** 18.

SZYMANSKA, K., HARTILL, V. L. & JOHNSON, C. A. 2014. Unraveling the genetics of Joubert and Meckel-Gruber syndromes. *J Pediatr Genet,* 3**,** 65-78.

SZYMANSKA, K. & JOHNSON, C. A. 2012. The transition zone: an essential functional compartment of cilia. *Cilia,* 1**,** 10.

TABIN, C. J. & VOGAN, K. J. 2003. A two-cilia model for vertebrate left-right axis specification. *Genes Dev,* 17**,** 1-6.

TAKAO, D. & VERHEY, K. J. 2016. Gated entry into the ciliary compartment. *Cell Mol Life Sci,* 73**,** 119-27.

TAKEDA, S. & NARITA, K. 2012. Structure and function of vertebrate cilia, towards a new taxonomy. *Differentiation,* 83**,** S4-11.

TALLILA, J., JAKKULA, E., PELTONEN, L., SALONEN, R. & KESTILA, M. 2008. Identification of CC2D2A as a Meckel syndrome gene adds an important piece to the ciliopathy puzzle. *Am J Hum Genet,* 82**,** 1361-7.

TAMMACHOTE, R., HOMMERDING, C. J., SINDERS, R. M., MILLER, C. A., CZARNECKI, P. G., LEIGHTNER, A. C., SALISBURY, J. L., WARD, C. J., TORRES, V. E., GATTONE, V. H., 2ND & HARRIS, P. C. 2009. Ciliary and centrosomal defects associated with mutation and depletion of the Meckel syndrome genes MKS1 and MKS3. *Hum Mol Genet,* 18**,** 3311-23.

TANAKA, S., TERADA, K. & NOHNO, T. 2011. Canonical Wnt signaling is involved in switching from cell proliferation to myogenic differentiation of mouse myoblast cells. *J Mol Signal,* 6**,** 12.

THOMA, C. R., FREW, I. J., HOERNER, C. R., MONTANI, M., MOCH, H. & KREK, W. 2007. pVHL and GSK3beta are components of a primary cilium-maintenance signalling network. *Nat Cell Biol,* 9**,** 588-95.

THOMA, C. R., MATOV, A., GUTBRODT, K. L., HOERNER, C. R., SMOLE, Z., KREK, W. & DANUSER, G. 2010. Quantitative image analysis identifies pVHL as a key regulator of microtubule dynamic instability. *J Cell Biol,* 190**,** 991-1003.

TOBIN, J. L. & BEALES, P. L. 2009. The nonmotile ciliopathies. *Genet Med,* 11**,** 386-402.

TOLLENAERE, M. A., MAILAND, N. & BEKKER-JENSEN, S. 2015. Centriolar satellites: key mediators of centrosome functions. *Cell Mol Life Sci,* 72**,** 11-23.

TORRA, R. 2008. [New therapeutic prospects in autosomal dominant polycystic kidney disease]. *Nefrologia,* 28**,** 257-62.

TORRES, V. E., CHAPMAN, A. B., DEVUYST, O., GANSEVOORT, R. T., GRANTHAM, J. J., HIGASHIHARA, E., PERRONE, R. D., KRASA, H. B., OUYANG, J., CZERWIEC, F. S. & INVESTIGATORS, T. T. 2012. Tolvaptan in patients with autosomal dominant polycystic kidney disease. *N Engl J Med,* 367**,** 2407-18.

TORRES, V. E., CHAPMAN, A. B., DEVUYST, O., GANSEVOORT, R. T., PERRONE, R. D., KOCH, G., OUYANG, J., MCQUADE, R. D., BLAIS, J. D., CZERWIEC, F. S., SERGEYEVA, O. & INVESTIGATORS, R. T. 2017. Tolvaptan in Later-Stage Autosomal Dominant Polycystic Kidney Disease. *N Engl J Med,* 377**,** 1930-1942.

TSANG, W. Y., BOSSARD, C., KHANNA, H., PERANEN, J., SWAROOP, A., MALHOTRA, V. & DYNLACHT, B. D. 2008. CP110 suppresses primary cilia formation through its interaction with CEP290, a protein deficient in human ciliary disease. *Dev Cell,* 15**,** 187-97.

TUKACHINSKY, H., LOPEZ, L. V. & SALIC, A. 2010. A mechanism for vertebrate Hedgehog signaling: recruitment to cilia and dissociation of SuFu-Gli protein complexes. *J Cell Biol,* 191**,** 415-28.

TUZ, K., BACHMANN-GAGESCU, R., O'DAY, D. R., HUA, K., ISABELLA, C. R., PHELPS, I. G., STOLARSKI, A. E., O'ROAK, B. J., DEMPSEY, J. C., LOURENCO, C., ALSWAID, A., BONNEMANN, C. G., MEDNE, L., NAMPOOTHIRI, S., STARK, Z., LEVENTER, R. J., TOPCU, M., CANSU, A., JAGADEESH, S., DONE, S., ISHAK, G. E., GLASS, I. A., SHENDURE, J., NEUHAUSS, S. C., HALDEMAN-ENGLERT, C. R., DOHERTY, D. & FERLAND, R. J. 2014. Mutations in CSPP1 cause primary cilia abnormalities and Joubert syndrome with or without Jeune asphyxiating thoracic dystrophy. *Am J Hum Genet,* 94**,** 62-72.

TUZ, K., HSIAO, Y. C., JUAREZ, O., SHI, B., HARMON, E. Y., PHELPS, I. G., LENNARTZ, M. R., GLASS, I. A., DOHERTY, D. & FERLAND, R. J. 2013. The Joubert syndrome-associated missense mutation (V443D) in the Abelson-helper integration site 1 (AHI1) protein alters its localization and protein-protein interactions. *J Biol Chem,* 288**,** 13676-94.

VALENTE, E. M., LOGAN, C. V., MOUGOU-ZERELLI, S., LEE, J. H., SILHAVY, J. L., BRANCATI, F., IANNICELLI, M., TRAVAGLINI, L., ROMANI, S., ILLI, B., ADAMS, M., SZYMANSKA, K., MAZZOTTA, A., LEE, J. E., TOLENTINO, J. C., SWISTUN, D., SALPIETRO, C. D., FEDE, C., GABRIEL, S., RUSS, C., CIBULSKIS, K., SOUGNEZ, C., HILDEBRANDT, F., OTTO, E. A., HELD, S., DIPLAS, B. H., DAVIS, E. E., MIKULA, M., STROM, C. M., BEN-ZEEV, B., LEV, D., SAGIE, T. L., MICHELSON, M., YARON, Y., KRAUSE, A., BOLTSHAUSER, E., ELKHARTOUFI, N., ROUME, J., SHALEV, S., MUNNICH, A., SAUNIER, S., INGLEHEARN, C., SAAD, A., ALKINDY, A., THOMAS, S., VEKEMANS, M., DALLAPICCOLA, B., KATSANIS, N., JOHNSON, C. A., ATTIE-BITACH, T. & GLEESON, J. G. 2010. Mutations in TMEM216 perturb ciliogenesis and cause Joubert, Meckel and related syndromes. *Nat Genet,* 42**,** 619-25.

VALENTE, E. M., SILHAVY, J. L., BRANCATI, F., BARRANO, G., KRISHNASWAMI, S. R., CASTORI, M., LANCASTER, M. A., BOLTSHAUSER, E., BOCCONE, L., AL-GAZALI, L., FAZZI, E., SIGNORINI, S., LOUIE, C. M., BELLACCHIO, E., INTERNATIONAL JOUBERT SYNDROME RELATED DISORDERS STUDY, G., BERTINI, E., DALLAPICCOLA, B. & GLEESON, J. G. 2006. Mutations in CEP290, which encodes a centrosomal protein, cause pleiotropic forms of Joubert syndrome. *Nat Genet,* 38**,** 623-5.

VAN DER HEIDEN, K., HIERCK, B. P., KRAMS, R., DE CROM, R., CHENG, C., BAIKER, M., POURQUIE, M. J., ALKEMADE, F. E., DERUITER, M. C., GITTENBERGER-DE GROOT, A. C. & POELMANN, R. E. 2008. Endothelial primary cilia in areas of disturbed flow are at the base of atherosclerosis. *Atherosclerosis,* 196**,** 542-50.

VAN REEUWIJK, J., ARTS, H. H. & ROEPMAN, R. 2011. Scrutinizing ciliopathies by unraveling ciliary interaction networks. *Hum Mol Genet,* 20**,** R149-57.

VEEMAN, M. T., SLUSARSKI, D. C., KAYKAS, A., LOUIE, S. H. & MOON, R. T. 2003. Zebrafish prickle, a modulator of noncanonical Wnt/Fz signaling, regulates gastrulation movements. *Curr Biol,* 13**,** 680-5.

VIEILLARD, J., PASCHAKI, M., DUTEYRAT, J. L., AUGIERE, C., CORTIER, E., LAPART, J. A., THOMAS, J. & DURAND, B. 2016. Transition zone assembly and its contribution to axoneme formation in Drosophila male germ cells. *J Cell Biol,* 214**,** 875-89.

VIEIRA, O. V., GAUS, K., VERKADE, P., FULLEKRUG, J., VAZ, W. L. & SIMONS, K. 2006. FAPP2, cilium formation, and compartmentalization of the apical membrane in polarized Madin-Darby canine kidney (MDCK) cells. *Proc Natl Acad Sci U S A,* 103**,** 18556-61.

VIERKOTTEN, J., DILDROP, R., PETERS, T., WANG, B. & RUTHER, U. 2007. Ftm is a novel basal body protein of cilia involved in Shh signalling. *Development,* 134**,** 2569-77.

VLADAR, E. K., BAYLY, R. D., SANGORAM, A. M., SCOTT, M. P. & AXELROD, J. D. 2012. Microtubules enable the planar cell polarity of airway cilia. *Curr Biol,* 22**,** 2203-12.

VOGEL, P., GELFMAN, C. M., ISSA, T., PAYNE, B. J., HANSEN, G. M., READ, R. W., JONES, C., PITCHER, M. R., DING, Z. M., DACOSTA, C. M., SHADOAN, M. K., VANCE, R. B. & POWELL, D. R. 2015. Nephronophthisis and retinal degeneration in tmem218-/- mice: a novel mouse model for Senior-Loken syndrome? *Vet Pathol,* 52**,** 580-95.

WALLINGFORD, J. B., FRASER, S. E. & HARLAND, R. M. 2002. Convergent extension: the molecular control of polarized cell movement during embryonic development. *Dev Cell,* 2**,** 695-706.

WALLINGFORD, J. B. & HABAS, R. 2005. The developmental biology of Dishevelled: an enigmatic protein governing cell fate and cell polarity. *Development,* 132**,** 4421-36.

WALLINGFORD, J. B. & MITCHELL, B. 2011. Strange as it may seem: the many links between Wnt signaling, planar cell polarity, and cilia. *Genes Dev,* 25**,** 201-13.

WALLINGFORD, J. B., ROWNING, B. A., VOGELI, K. M., ROTHBACHER, U., FRASER, S. E. & HARLAND, R. M. 2000. Dishevelled controls cell polarity during Xenopus gastrulation. *Nature,* 405**,** 81-5.

WANG, X. & ROBBINS, J. 2014. Proteasomal and lysosomal protein degradation and heart disease. *J Mol Cell Cardiol,* 71**,** 16-24.

WANG, Y., WONG, L. B. & MAO, H. 2010. Creation of a long-lifespan ciliated epithelial tissue structure using a 3D collagen scaffold. *Biomaterials,* 31**,** 848-53.

WANG, Z., IIDA, A., MIYAKE, N., NISHIGUCHI, K. M., FUJITA, K., NAKAZAWA, T., ALSWAID, A., ALBALWI, M. A., KIM, O. H., CHO, T. J., LIM, G. Y., ISIDOR, B., DAVID, A., RUSTAD, C. F., MERCKOLL, E., WESTVIK, J., STATTIN, E. L., GRIGELIONIENE, G., KOU, I., NAKAJIMA, M., OHASHI, H., SMITHSON, S., MATSUMOTO, N., NISHIMURA, G. & IKEGAWA, S. 2016. Axial Spondylometaphyseal Dysplasia Is Caused by C21orf2 Mutations. *PLoS One,* 11**,** e0150555.

WANN, A. K. & KNIGHT, M. M. 2012. Primary cilia elongation in response to interleukin-1 mediates the inflammatory response. *Cell Mol Life Sci,* 69**,** 2967-77.

WARE, S. M., AYGUN, M. G. & HILDEBRANDT, F. 2011. Spectrum of clinical diseases caused by disorders of primary cilia. *Proc Am Thorac Soc,* 8**,** 444-50.

WATANABE, D., SAIJOH, Y., NONAKA, S., SASAKI, G., IKAWA, Y., YOKOYAMA, T. & HAMADA, H. 2003. The left-right determinant Inversin is a component of node monocilia and other 9+0 cilia. *Development,* 130**,** 1725-34.

WATERS, A. M. & BEALES, P. L. 2011. Ciliopathies: an expanding disease spectrum. *Pediatr Nephrol,* 26**,** 1039-56.

WATNICK, T. & GERMINO, G. 2003. From cilia to cyst. *Nat Genet,* 34**,** 355-6.

WEN, X., LAI, C. K., EVANGELISTA, M., HONGO, J. A., DE SAUVAGE, F. J. & SCALES, S. J. 2010. Kinetics of hedgehog-dependent full-length Gli3 accumulation in primary cilia and subsequent degradation. *Mol Cell Biol,* 30**,** 1910-22.

WESTLAKE, C. J., BAYE, L. M., NACHURY, M. V., WRIGHT, K. J., ERVIN, K. E., PHU, L., CHALOUNI, C., BECK, J. S., KIRKPATRICK, D. S., SLUSARSKI, D. C., SHEFFIELD, V. C.,

SCHELLER, R. H. & JACKSON, P. K. 2011. Primary cilia membrane assembly is initiated by Rab11 and transport protein particle II (TRAPPII) complex-dependent trafficking of Rabin8 to the centrosome. *Proc Natl Acad Sci U S A,* 108**,** 2759-64.

WHEWAY, G., MITCHISON, H. M. & GENOMICS ENGLAND RESEARCH, C. 2019. Opportunities and Challenges for Molecular Understanding of Ciliopathies-The 100,000 Genomes Project. *Front Genet,* 10**,** 127.

WHEWAY, G., NAZLAMOVA, L. & HANCOCK, J. T. 2018. Signaling through the Primary Cilium. *Front Cell Dev Biol,* 6**,** 8.

WHEWAY, G., SCHMIDTS, M., MANS, D. A., SZYMANSKA, K., NGUYEN, T. T., RACHER, H., PHELPS, I. G., TOEDT, G., KENNEDY, J., WUNDERLICH, K. A., SORUSCH, N., ABDELHAMED, Z. A., NATARAJAN, S., HERRIDGE, W., VAN REEUWIJK, J., HORN, N., BOLDT, K., PARRY, D. A., LETTEBOER, S. J. F., ROOSING, S., ADAMS, M., BELL, S. M., BOND, J., HIGGINS, J., MORRISON, E. E., TOMLINSON, D. C., SLAATS, G. G., VAN DAM, T. J. P., HUANG, L., KESSLER, K., GIESSL, A., LOGAN, C. V., BOYLE, E. A., SHENDURE, J., ANAZI, S., ALDAHMESH, M., AL HAZZAA, S., HEGELE, R. A., OBER, C., FROSK, P., MHANNI, A. A., CHODIRKER, B. N., CHUDLEY, A. E., LAMONT, R., BERNIER, F. P., BEAULIEU, C. L., GORDON, P., PON, R. T., DONAHUE, C., BARKOVICH, A. J., WOLF, L., TOOMES, C., THIEL, C. T., BOYCOTT, K. M., MCKIBBIN, M., INGLEHEARN, C. F., CONSORTIUM, U. K., UNIVERSITY OF WASHINGTON CENTER FOR MENDELIAN, G., STEWART, F., OMRAN, H., HUYNEN, M. A., SERGOUNIOTIS, P. I., ALKURAYA, F. S., PARBOOSINGH, J. S., INNES, A. M., WILLOUGHBY, C. E., GILES, R. H., WEBSTER, A. R., UEFFING, M., BLACQUE, O., GLEESON, J. G., WOLFRUM, U., BEALES, P. L., GIBSON, T., DOHERTY, D., MITCHISON, H. M., ROEPMAN, R. & JOHNSON, C. A. 2015. An siRNA-based functional genomics screen for the identification of regulators of ciliogenesis and ciliopathy genes. *Nat Cell Biol,* 17**,** 1074-1087.

WHITE, J. J., MAZZEU, J. F., HOISCHEN, A., BAYRAM, Y., WITHERS, M., GEZDIRICI, A., KIMONIS, V., STEEHOUWER, M., JHANGIANI, S. N., MUZNY, D. M., GIBBS, R. A., BAYLOR-HOPKINS CENTER FOR MENDELIAN, G., VAN BON, B. W. M., SUTTON, V. R., LUPSKI, J. R., BRUNNER, H. G. & CARVALHO, C. M. B. 2016. DVL3 Alleles Resulting in a -1 Frameshift of the Last Exon Mediate Autosomal-Dominant Robinow Syndrome. *Am J Hum Genet,* 98**,** 553-561.

WIEGERING, A., DILDROP, R., KALFHUES, L., SPYCHALA, A., KUSCHEL, S., LIER, J. M., ZOBEL, T., DAHMEN, S., LEU, T., STRUCHTRUP, A., LEGENDRE, F., VESQUE, C., SCHNEIDER-MAUNOURY, S., SAUNIER, S., RUTHER, U. & GERHARDT, C. 2018a. Cell type-specific regulation of ciliary transition zone assembly in vertebrates. *EMBO J,* 37.

WIEGERING, A., RUTHER, U. & GERHARDT, C. 2018b. The ciliary protein Rpgrip1l in development and disease. *Dev Biol,* 442**,** 60-68.

WILLIAMS, C. L., LI, C., KIDA, K., INGLIS, P. N., MOHAN, S., SEMENEC, L., BIALAS, N. J., STUPAY, R. M., CHEN, N., BLACQUE, O. E., YODER, B. K. & LEROUX, M. R. 2011. MKS and NPHP modules cooperate to establish basal body/transition zone membrane associations and ciliary gate function during ciliogenesis. *J Cell Biol,* 192**,** 1023-41.

WILLIAMS, C. L., WINKELBAUER, M. E., SCHAFER, J. C., MICHAUD, E. J. & YODER, B. K. 2008. Functional redundancy of the B9 proteins and nephrocystins in Caenorhabditis elegans ciliogenesis. *Mol Biol Cell,* 19**,** 2154-68.

WILSON, C. W. & STAINIER, D. Y. 2010. Vertebrate Hedgehog signaling: cilia rule. *BMC Biol,* 8**,** 102.

WODARZ, A. & NUSSE, R. 1998. Mechanisms of Wnt signaling in development. *Annu Rev Cell Dev Biol,* 14**,** 59-88.

WOLF, M. T., SAUNIER, S., O'TOOLE, J. F., WANNER, N., GROSHONG, T., ATTANASIO, M., SALOMON, R., STALLMACH, T., SAYER, J. A., WALDHERR, R., GRIEBEL, M., OH, J., NEUHAUS, T. J., JOSEFIAK, U., ANTIGNAC, C., OTTO, E. A. & HILDEBRANDT, F. 2007. Mutational analysis of the RPGRIP1L gene in patients with Joubert syndrome and nephronophthisis. *Kidney Int,* 72**,** 1520-6.

YAMAMOTO, S. & KITAGAWA, D. 2019. Self-organization of Plk4 regulates symmetry breaking in centriole duplication. *Nat Commun,* 10**,** 1810.

YANG, T. T., SU, J., WANG, W. J., CRAIGE, B., WITMAN, G. B., TSOU, M. F. & LIAO, J. C. 2015. Superresolution Pattern Recognition Reveals the Architectural Map of the Ciliary Transition Zone. *Sci Rep,* 5**,** 14096.

YEE, L. E., GARCIA-GONZALO, F. R., BOWIE, R. V., LI, C., KENNEDY, J. K., ASHRAFI, K., BLACQUE, O. E., LEROUX, M. R. & REITER, J. F. 2015. Conserved Genetic Interactions between Ciliopathy Complexes Cooperatively Support Ciliogenesis and Ciliary Signaling. *PLoS Genet,* 11**,** e1005627.

YIN, Y., BANGS, F., PATON, I. R., PRESCOTT, A., JAMES, J., DAVEY, M. G., WHITLEY, P., GENIKHOVICH, G., TECHNAU, U., BURT, D. W. & TICKLE, C. 2009. The Talpid3 gene (KIAA0586) encodes a centrosomal protein that is essential for primary cilia formation. *Development,* 136**,** 655-64.

YODER, B. K. 2007. Role of primary cilia in the pathogenesis of polycystic kidney disease. *J Am Soc Nephrol,* 18**,** 1381-8.

YOSHIBA, S. & HAMADA, H. 2014. Roles of cilia, fluid flow, and Ca2+ signaling in breaking of left-right symmetry. *Trends Genet,* 30**,** 10-7.

YOUN, Y. H. & HAN, Y. G. 2018. Primary Cilia in Brain Development and Diseases. *Am J Pathol,* 188**,** 11-22.

YUAN, X., CAO, J., HE, X., SERRA, R., QU, J., CAO, X. & YANG, S. 2016. Ciliary IFT80 balances canonical versus non-canonical hedgehog signalling for osteoblast differentiation. *Nat Commun,* 7**,** 11024.

ZAHN-ZABAL, M., MICHEL, P. A., GATEAU, A., NIKITIN, F., SCHAEFFER, M., AUDOT, E., GAUDET, P., DUEK, P. D., TEIXEIRA, D., RECH DE LAVAL, V., SAMARASINGHE, K., BAIROCH, A. & LANE, L. 2020. The neXtProt knowledgebase in 2020: data, tools and usability improvements. *Nucleic Acids Res,* 48**,** D328-D334.

ZAKI, M. S., SATTAR, S., MASSOUDI, R. A. & GLEESON, J. G. 2011. Co-occurrence of distinct ciliopathy diseases in single families suggests genetic modifiers. *Am J Med Genet A,* 155A**,** 3042-9.

ZHU, B., ZHU, X., WANG, L., LIANG, Y., FENG, Q. & PAN, J. 2017. Functional exploration of the IFT-A complex in intraflagellar transport and ciliogenesis. *PLoS Genet,* 13**,** e1006627.

ZILBER, Y., BABAYEVA, S., SEO, J. H., LIU, J. J., MOOTIN, S. & TORBAN, E. 2013. The PCP effector Fuzzy controls cilial assembly and signaling by recruiting Rab8 and Dishevelled to the primary cilium. *Mol Biol Cell,* 24**,** 555-65.

ZIMMERMANN, K. W. 1898. Beitrage zur Kenntniss einiger Drusen und Epithelien. *Archiv fur Mikroskopische Anatomie* 52**,** 552-706.

ZIMMERMANN, R., EYRISCH, S., AHMAD, M. & HELMS, V. 2011. Protein translocation across the ER membrane. *Biochim Biophys Acta,* 1808**,** 912-24.

ZINCHUK, V., WU, Y. & GROSSENBACHER-ZINCHUK, O. 2013. Bridging the gap between qualitative and quantitative colocalization results in fluorescence microscopy studies. *Sci Rep,* 3**,** 1365.

ZINCHUK, V., ZINCHUK, O. & OKADA, T. 2007. Quantitative colocalization analysis of multicolor confocal immunofluorescence microscopy images: pushing pixels to explore biological phenomena. *Acta Histochem Cytochem,* 40**,** 101-11.